博士論文

Enhancement of energy harvesting from nonlinearly vibrating systems under harmonic and random excitations

（調和およびランダム励振による非線形振動系からのエナジーハーベスティングの性能向上）

蘇　東旭

Contents

Abstract

Different energy sources exist in the environment, in which the vibration sources can be found everywhere in daily life, and hence the concept of electrical energy harvesting from ambient vibration sources has been of popular interest of research in recent years. Due to recent advancements in microelectromechanical systems, the power consumption of electrics had been dramatically decreased. It becomes a considerable application to use small-scale low powered wireless sensors in inaccessible or hostile environments. On the other hand, the vibrations in many situations can be very large; for example, the vibrations of vehicle systems, can be 100 W or more. Up to new, linear resonant energy harvesters had been one of the most common type of energy harvesters with the limited response bandwidth. Many efforts were made to overcome this problem, covering resonance frequency tuning techniques, multimodal energy harvesting, frequency up-conversion, and so on. However, those well-known methods are still restricted in the field of linear energy harvesting, which already studied by many researchers.

The energy harvesting by application of self-excited vibration also attracted some attentions; however, its applicable area for energy harvesting is generally limited to a certain field. For example, the energy harvester subjected to a uniform and steady flow. Another apparent issue is that the performance of the energy harvester is significantly limited by the fundamental frequency of the device. One typical case is the beam-type wind energy harvester using the theory of Karman Vortex Street.

As a result of those problems, a large body of work has been, and still is being, devoted to investigating the energy harvesting performance by introducing dynamic nonlinearities into devices - this forms the main focus of this thesis. Therefore, the present work in this thesis is to enhance the energy harvesting efficiency applying nonlinearly vibrating systems, which can be divided into two parts based on the excitation types: harmonic and random excitations.

For the case of the harmonic excitation, it is mainly focused on the monostable energy harvester with Duffing-type nonlinearity. It is validated that at relatively high excitation levels, both low- and high-energy solutions can coexist for the same combinations of parameters, and the existence of the high-energy orbit can achieve higher energy harvesting effectiveness with wider bandwidth applications. It is certainly favourable to maintain the high-energy orbit for boosting the response and a larger output power. However, if the operating point falls down to the low-energy orbit, the wider bandwidth compared with the linear energy harvester will be impaired. The frequency or amplitude sweeps of the excitation is usually used in order to reach a desirable high-energy orbit and investigate the influence of the nonlinearity by many researchers.

This gives a limitation on practical implementation, because the external vibration source cannot be arbitrarily controlled.

Another approach is to add disturbance or initial conditions for the energy harvesters, but no physically feasible mechanism has been fabricated and tested. To solve this problem, a stiffness tunable nonlinear vibrational energy harvester is proposed, whose nonlinearity emerges from the interaction forces with two neighbouring permanent magnets facing with opposing poles. The hypothesis is that the jump from the low-energy orbit to the high-energy orbit can be triggered by tuning the stiffness of the system, without changing the frequency or the amplitude of the excitation. Theoretical investigations show a methodology for tuning stiffness, and experimental tests also validated that the proposed method can be used to trigger a jump to the desirable state, and also tune the resonant frequency when the external ambient vibration varies; thereby, this can broaden the bandwidth of the energy harvester. Considering the tuning procedure of the stiffness, it means the additional energy consumption, though it does not require the constant energy supply. Another improved approach is further investigated to stabilise the high-energy orbit. The equivalent linear stiffness of the energy harvester can be varied by tuning the damping level of the device. Same as the stiffness tunable nonlinear energy harvester, from this adjustment the variation of the equivalent stiffness generates a corresponding shift in the frequency-amplitude response curve, which can trigger a jump and stabilise the high-energy orbit. The approach has been observed to require little additional energy supply for the adjustment and stabilisation, because it needs less energy for tuning the damping than the direct stiffness tuning by mechanical method.

Having stabilised on the high-energy orbit, it is necessary to further optimise the system for maximum power output. However, there has been much recent interest in the response analysis of the monostable nonlinear energy harvesters and comparison with their linear counterpart, but few literatures about the optimisation of the nonlinear energy harvester. Same as the linear energy harvester, the Duffing monostable energy harvester can also be optimised to maximise the available electrical power. With the consideration of the unconstrained and constrained electrical damping and stroke of the energy harvester, the analytical optimisation and numerical studies are demonstrated under the different conditions with the designed harvesting devices. The optimisation works can comprehensively provide the design rules of the monostable nonlinear energy harvester under harmonic excitations.

Furthermore, this thesis also focuses on the nonlinear energy harvesting techniques to random excited energy harvesting scenarios, because the vibration sources in the environment usually present time-varying properties, even completely random.

It is firstly concentrated on the influence of the stiffness nonlinearity on the transduction of the energy harvester, and the relative performance of linear, monostable hardening-type and

bistable energy harvesters are comparatively investigated with the careful consideration of the constrained electrical damping and stroke of the device. General conclusions are drawn based on the numerical and experimental observations, which provide the guidance for the design of the randomly excited energy harvesting devices.

In spite of the comparative performance study of different kinds of energy harvesters, it is the passive energy harvesting approach by using several kinds of existing typical configurations. Then, motivated by how to actively enhance energy harvesting efficiency from random excitations, another novel approach is proposed and improved based on the theory of stochastic resonance. Stochastic resonance is a physical phenomenon through which the throughput of energy within an oscillator excited by a stochastic source can be boosted by adding a small modulating excitation. The hypothesis is that such stochastic resonance can be efficiently realised in a bistable mechanism, and the feasibility of implementing stochastic resonance is investigated for energy harvesting. Experimental results confirm that the addition of a small-scale force to the bistable system, excited by a random signal apparently, leads to a corresponding amplification of the response. Thereby, the proposed approach is a promising way to improve the energy harvesting performance under certain forms of random excitations.

Nomenclature

A_0	Amplitude of the periodic force
A_1, B_1	Fourier coefficient of the displacement
A_2, B_2	Fourier coefficient of the displacement
$\mathbf{B}$	Magnetic flux density
B	Replacement symbol
C	Capacitance
D	Noise density
D_{31}	Piezoelectric constant of the transducer
E	Young's modulus
E_c	Consumed energy
E_f	Electric field
E_{net}	Net energy
F	Amplitude of the periodic fore
F_E	Force of the electrical magnet
F_M, F_{Mb}, F_V	Interaction force between permanent magnets
F_r	Restoring force of a schematic hardening type energy harvester
G	Gain
I	Moment of inertia
$\mathbf{M}_f$, $\mathbf{M}_c$	Magnetisation amplitude
M_{fx}, M_{cx}	Magnetisation amplitude in x direction
M_{fy}, M_{cy}	Magnetisation amplitude in y direction
N	Noise excitation
P, P_{Xl}	Power
P_c	Consumed power
P_{net}	Net power
P_d	Dissipated power
Q	Electrical displacement
Q_a, Q_b	Replacement symbol
R	Sum of the internal resistance and the load resistance
R_i	International resistance
R_l	Load resistance
R_{lopt}	Optimum load resistance
S	Strain

T_s	Stress
T	Period
T_0	Length of time
U_0, U_{0u}, U_{0d}	Non-dimensional displacement amplitude
U	Potential
U_m, U_{mb}	Potential between permanent magnets
V	Voltage
$\boldsymbol{V}$	Laplace transform of the volatge
V_l	Induced voltage on the load resistance
X	Displacement amplitude
$\boldsymbol{X}$	Laplace transform of displacement
X_{max}	Maximum displacement amplitude
X_l	Displacement amplitude limit
a_1, b_1	Fourier coefficient of the displacement
a_2, b_2	Fourier coefficient of the voltage
b_t	Width of the piezoelectric transducer
c	Sum of the mechanical damping and the electrical damping
c_1	Electrical damping coefficient
c_2	Tunable electrical damping coefficient
c_e	Electrical damping coefficient
c_m	Mechanical damping
d	Distance between the permanent magnets
d_0	Distance between the mass and frame of the hardening type energy harvester
d_{31}	Piezoelectric constant of material
f	Induced force by the piezoelectric transducer
h	Distance between the permanent magnets
i	Current
k_0, k_1, k_2, k_3	Stiffness of springs
k_c	Stiffness of the beam
l	Length of the beam
l_0	Length of the spring
l_t	Length of the transducer
m	Mass
$\mathbf{m}_f$, $\mathbf{m}_c$	Magnetic moment
m_{opt}	Optimum mass
n	Transmission ratio

p	Ratio between the deflection of the piezoelectric transducer and the beam
q	Electrical charge
rms	Root mean square
$\mathbf{r}_c$, $\mathbf{r}_f$, $\mathbf{r}_{c/f}$	Magnet positon vector
r_K	Kramers rate
s^E	Mechanical compliance
t, t_0	Time
t_b	Thickness of the beam
t_t	Thickness of the piezoelectric transducer
v	Volume of the permanent magnets
x, x_p	Displacement
x_m	Equilibrium position of bistable system
x_0	Deflection formula for a cantilever beam
y_t	Deflection of the piezoelectric transducer along the direction of the beam
α	Nonlinear stiffness
β	Non-dimensional nonlinear stiffness
ω	Excitation frequency
ω_d	Jump-down frequency
ω_n	Natural frequency
ω_u	Jump-up frequency
Ω	Non-dimensional excitation frequency
Ω_d	Non-dimensional jump-down frequency
Ω_u	Non-dimensional jump-up frequency
ε	Permittivity under constant stress
γ	Additional periodic force
γ_a	Additional periodic force
ζ	Total damping ratio
ζ_m	Mechanical damping ratio
κ	Electromechanical coupling factor
μ_0	Permeability of free space
φ	Phase angle between the input and response
ϕ	Electromechanical constant related to velocity
τ	Non-dimensional time
θ	Electromechanical coupling coefficient of piezoelectric energy harvester
ψ	Magnetic force angle
υ , $\overline{\upsilon}$	Variable of the index

λ	Constant
δ	Root mean square of power
σ	Root mean square of excitation
Θ , Φ , Γ	Replacement symbol acceleration

Acknowledgements

I deeply thank my supervisor, Dr. Kimihiko Nakano, Associate Professor in The University of Tokyo. for his guidance, patience and encouragement. His enthusiasm and attention to details will continue to influence my research career in the future.

I greatly thank Professor Shigehiko Kaneko, Professor Yoshihiro Suda, Professor Yuji Suzuki, and Professor Hiroshi Yabuno. As referees of my dissertation, all of their valuable comments and constructive suggestions help me to complement my study and improve the dissertation.

I also thank Dr. Rencheng Zheng, the project research associate of K. Nakano Laboratory. He supported me in my experiments and helped me so much not only in my research but also in my daily life. I convey my sincere thanks to Professor Matthew P. Cartmell, he gave me important guidance in the theory of energy harvesting.

I appreciate Dr. Tsutomu Kaizuka, the research associate and Dr. Keisuke Shimono, the project researcher of K. Nakano Laboratory, they gave me much advice about the purchase and use of experimental devices.

I also would like to express my heartfelt gratitude to Ms. Atusko Hasegawa, Dr. SeungYong Lee, Yunshun Zhang, Bo Yang, Antonin Joly, Zheng Wang, Shu Wakabayashi, and all the other members of K. Nakano Laboratory, they gave me their help with their kindness in my research and daily life.

I am also thankful to China Scholarship Council, this work may have not been possible without the provided finical support.

Finally, I am deeply indebted to my family for their continuous support and encouragement.

August 5, 2015

Dongxu Su

Chapter 1

Introduction

1.1 Background

Efficient energy harvesting from environmental ambient vibration is of great current interest as a means of self-powering for small-scale electronics. Especially modern electronic devices have become increasingly efficient. For instance, a wireless sensor can require the power as little as 100μW [1]. Currently, the wireless sensing applications and portable electronics are powered by batteries; however, the improvement of batteries energy density remains stagnant, as compared with the other computing hardware. Another limitation for the use of batteries is in inaccessible or hostile environments. It becomes inconvenient for the usual miniaturisation and replacement. There are a lot of sources that can be used as an energy source, such as thermal gradient, wind, solar, mechanical vibration, and so on. Among these several workable energy sources, ambient vibration has promising potential to be a power source, since it can be found almost everywhere in the environment.

Up to now, there are three kinds of common methods to convert mechanical energy to electrical energy, termed as electromagnetic, piezoelectric and electrostatic. One of the earliest vibrational energy harvesters was designed by Amirtharajah et al. [2]. It is a simple single-degree-of-freedom (SDOF) system comprised by a mass, spring and damper. An electromagnetic transducer, composed of a coil and magnetic core, is used in this device. One obvious benefit of the electromagnetic transduction is that it usually has very small mechanical damping because of little contact between the magnet and coil. However, the voltage generated by the electromagnetic transducer is relatively low, and the level of the electrical damping strongly depends the magnetic strength. In the same case, piezoelectric-type transducer can produce relatively high voltage. Electrostatic transduction is capacitive and offers the most promising potential for the application to microelectronics. Relatively high voltage can be easily provided using the technology with the advantage that it does not require smart materials to operate, whilst it is required for the piezoelectric-type transducer. Therefore, the requirement of the initial external source to charge is the main limitation.

Among those single degree-of-freedom mechanical systems for transferring mechanical vibration energy into electrical energy, the beam-type system is one of the most popular type [3][4][5][6]. The main limitation of this kind of energy harvester is that it can provide maximum output power, only when the natural frequency of the system is same as the external excitation frequency. However, considering the practical cases, the environmental vibration is normally frequency-varying or totally stochastic. Therefore, how to broaden the bandwidth of the energy harvesters becomes one of the most important topics for the practical implementation. In addition, because the performance decreases dramatically under the non-resonance conditions, many researchers have concentrated on overcoming such disadvantages in linear devices.

The recent advances in this field are briefly introduced in the following parts, covering the resonance frequency tuning methods, multimodal energy harvesting, frequency up-conversion, and nonlinear energy harvesting.

1.2 Linear energy harvesting

(1) Resonance frequency tuning methods

The most of the existing literature are related with linear devices, and a natural frequency tuning mechanism can be adopted to increase its functionality. According to different tuning mechanisms, the frequency tuning methods can also be divided into mechanical and piezoelectric methods [7][8][9][10]. To tune the natural frequency of the device, either the stiffness or the mass of the devices can be varied. However, it is more feasible to tune the stiffness rather than the mass. Generally, mechanical tuning methods can achieve the largest tuning range. However, it is difficult to tune the device automatically. For instance, Eichhorn et al. [11] proposed and fabricated a beam-type tunable energy harvester based on natural frequency variation using pre-stress. The preload of the cantilever beam is tuned by a screw, which is the most common method for mechanical tuning. Figure 1.1 shows the generator and the schematic of the entire setup.

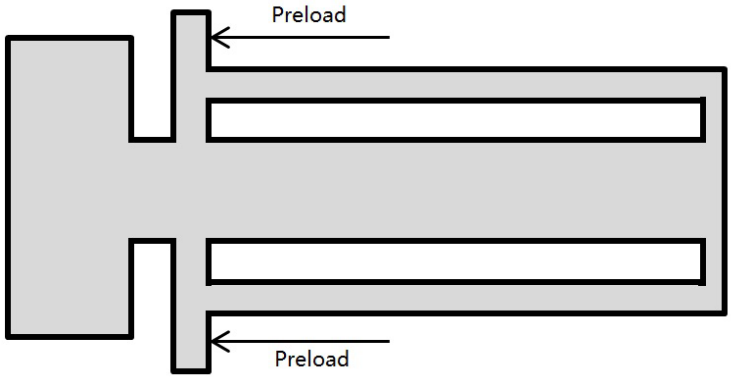

Figure 1.1. Schematic of the beam-type stiffness tunable energy harvester

Researchers also used the permanent magnets as the actuator, for example, by varying the distance between the permanent magnets as shown in Figure 1.2 [12]. Compared with the mechanical method, a much smaller frequency tuning range is presented by the piezoelectric tuning method. However, it consumes much less energy for the tuning process. Wu et al. [13] reported that the consumed power is only the level of micro-Watt. Thus the enhanced net power can be achieved. However, when the frequency of the excitation shows the frequent variation

property, it becomes difficult to follow it, which limits its implementation.

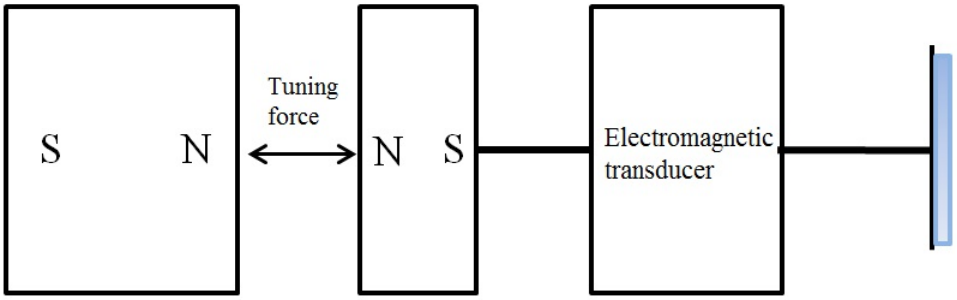

Figure 1.2. Schematic of the tuning mechanism

(2) Multimodal energy harvesting

Several natural frequencies can coexist when the energy harvester is designed as a multi-degree-of-freedom system. The frequency response curves can overlap. Therefore broaden the bandwidth of the energy harvester. Shahruz [14][15] designed an energy harvester, which is composed of piezoelectric beams with different lengths and tip masses attached to a same base. Each beam had a unique natural frequency. That is why it is called multimodal energy harvester. The schematic diagram is presented in Figure 1.3. However, such an arrangement will increase the size of the device. Therefore, the energy density will be reduced. Another problem is that it requires more complex circuit because of the use of multi-energy transform-mechanism.

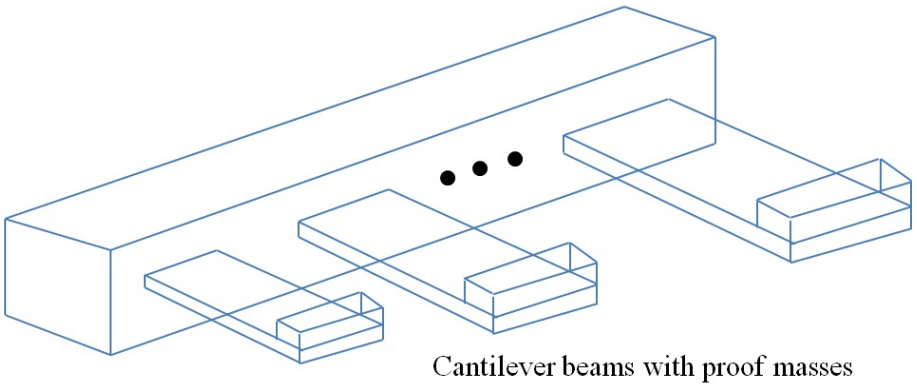

Figure 1.3. Schematic of the band-pass filters energy harvester

(3) Frequency up-conversion

In most cases, the natural frequency of the micro-energy harvester is relatively high. However, it is common for the ambient vibration occurs at low frequency, for example in human motion. Frequency up-conversion is therefore adopted for the frequency amplification of the ambient vibration source. As long as the resonance frequency of the energy harvester is much higher than the vibration source, their energy harvesting performances are less sensitive to the variation of the excitation frequency. Therefore, this characteristic improves the robustness of the energy harvester. Figure 1.4 depicts an example of a frequency up-conversion energy harvester [16]. Another similar study can be found in the literature [17]. An apparent problem of this configuration is that there is energy loss because of the impact between the mass and beam. Therefore, Külah, et al. used two permanent magnets as the actuator to overcome this problem [18]. However, this kind of configuration requires a minimum distance between the two magnets, because the interaction force between the magnets should be small enough at a certain time for the realisation of the free vibration of the beam.

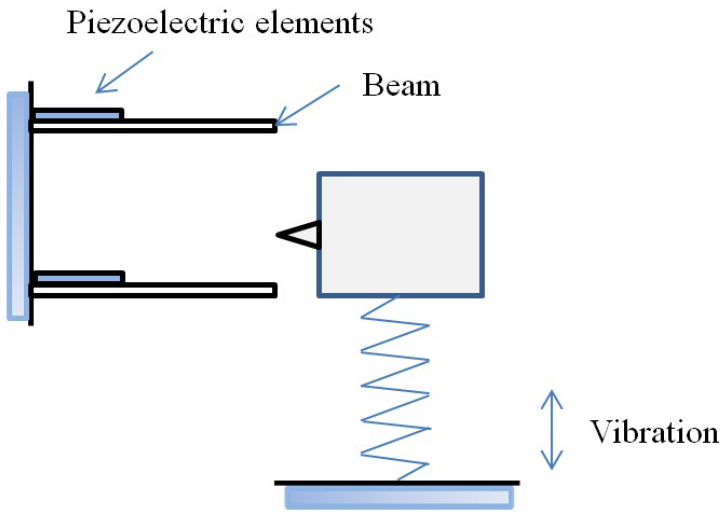

Figure 1.4. Schematic of the two-stage vibration energy harvester

Those studies are still restricted in the field of linear energy harvesting, which is well-known and already done by many researchers.

1.3 Self-excited vibrational energy harvesting

The self-excited vibration can also be employed as an approach for energy harvesting. Although the phenomenon of the self-excited vibration can be very common in the daily life,

such as clock pendulum, vibration caused by the friction, and cutting process of the machine. However, for its application in the field of energy harvesting, it is mainly about the piezoelectric energy harvester subjected to a uniform and steady flow. Akaydin et al. designed a harvester that consists of a cylinder attached to the free end of a cantilevered beam for wind energy harvesting, where the cylinder induced self-vibration is the most common type [19]. Several similar devices were presented in references [20][21][22][23]. Other configurations include flutter and beam with an attack angle [24] [25].

It can be noted that different kinds of parts were used to achieve the vortex induced vibration but with the similar principle. One common advantage of the energy harvesting using self-excited vibration is that the performance of the harvester is not limited by its fundamental frequency. However, for the application of self-excited vibration in the field of energy harvesting, it is mainly constrained in the fluidic energy harvesting.

1.4 Parametric resonance energy harvesting

The amount of literature about the parametric resonance energy harvesting is relatively small. However, Yu. et al. [26] validated that the parametric resonant technique theoretically promises better power and frequency response in contrast to the conventional directly excited harvesters. However, a list of strict initiation criteria, such as a damping dependent minimum excitation amplitude threshold, needs to be fulfilled, which limits it practical implementation.

1.5 Nonlinear energy harvesting

As a result of the issues highlighted in the previous sections, a large body of work has been, and still is being, devoted to investigating the energy harvesting performance by introducing dynamic nonlinearities into devices - this forms the main focus of this thesis. For the nonlinear energy harvester, it has the functionality of self-frequency-tuning. Therefore, it is more insensitive to the variation of the excitation frequency. The nonlinearity of the system itself can improve the performance of the energy harvester over a wider bandwidth. According to the type of nonlinearity, the nonlinear energy harvesters can be classified into monostable and bistable cases. Under certain harmonic excitation conditions, both the bistable and the hardening-type monostable nonlinearities can provide enhanced energy harvesting over that of the conventional linear energy harvester. However, it shows more complex phenomenon under random excitations.

1.5.1 Monostable energy harvester

(1) Harmonic excitation

The nonlinearities were firstly employed to study and test its influence on the performance by Burrow et al. [27] and Barton et al. [28]. The hardening-type nonlinearity of the energy harvester was achieved by using a tip magnetic mass attached to a beam and a steel stator.

Following the work of Burrow et al. and Barton et al., a hardening-type oscillator was investigated by Mann et al. [29] and the schematic diagram of the magnetic levitation system is shown in Figure 1.5. Two outer permanent magnets were used in this device and were attached to a threaded support. The threaded supports were installed to the ends of a teflon tube for varying the distance between the permanent magnets. A centre magnet was inserted between the two outer magnets and with opposite polarity with the outer magnets. Thus levitate the centre magnet with a nonlinear restoring force. In their work it was shown that the magnetic restoring force of the centre magnet could be accurately modelled by a cubic order nonlinear spring. This gave the system similar properties to that of the Duffing hardening-type monostable oscillator which has a governing equation of the form as

$$m\ddot{x} + c\dot{x} + kx + \alpha x^3 = F\cos\omega t \tag{1.1}$$

where m is the mass, c is the viscous damping, $F\cos\omega t$ is the excitation force, and k and α are linear and nonlinear stiffness, respectively.

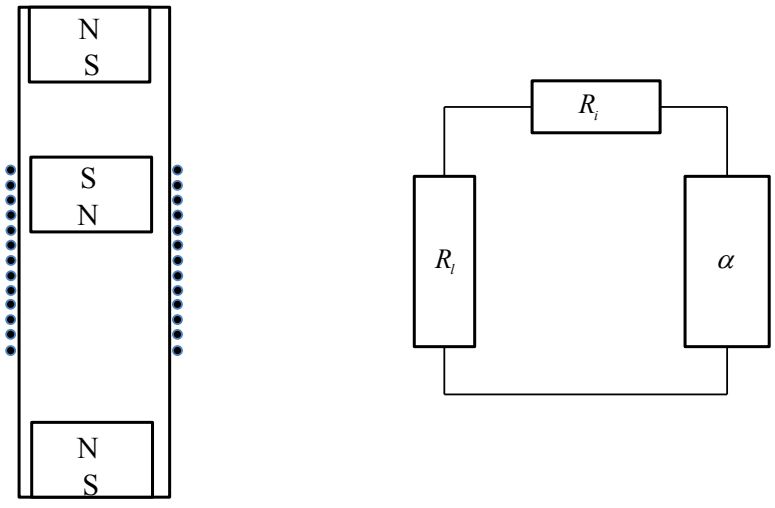

Figure 1.5. Schematic of the magnetic levitation system

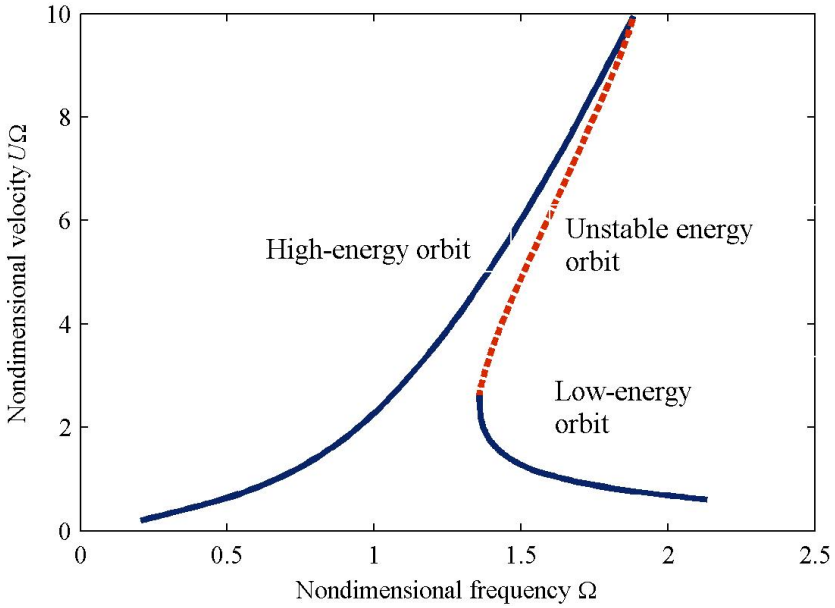

Figure 1.6. Frequency response curve of hardening-type Duffing oscillator demonstrating area of coexisting solutions.

It was found that the nonlinear stiffness term lead to a skew effect on the frequency response curve of the system. An example of this effect is shown in Figure 1.6, where one can find that the frequency response curve becomes skewed that a area of coexisting solutions has been achieved, called the high-energy orbit (upper solution) and the low-energy orbit (lower solution). In practice, there exists the third unstable energy orbit, and the steady-state of the oscillator will converge to either the high- or low-energy orbit. By using the device shown in Figure 1.5, Mann and Sims tested the responses under different excitation amplitudes. It is found that only at relatively high sinusoidal excitation levels, both low- and high-energy responses can coexist for the same parameter combinations. When compared with a linear oscillator using similar parameters the effectiveness of a nonlinear energy harvester can be dramatically enhanced over certain frequency ranges if one can stabilise the high-energy orbit. However, the operating branch is determined by the basins of attraction of the coexisting solutions, the probabilistic method for estimating the steady-state response were investigated by Quinn et al. [30] in the area where multiple solutions coexist. For the steady-state response, a weighted average value is used with the weights calculated using the basins of attraction under physically reasonable initial conditions. It was found that as the frequency moves away from the linear natural frequency, the probabilistic response shifts to the lower branch of solutions.

Based on the device of Mann and Sims and by comparing with experimental data, a more reliable and extensively validated mathematical model of the energy device was developed by

Green et al. [31]. With regards to device dynamics the first important contribution from this investigation was the discovery that one must include friction effects to accurately model the system dynamics. Only viscous damping is used to model mechanical losses of the energy harvesters for the majority of works. However, after an extensive investigation using several different friction models it was found that the relatively simple Coulomb damping model could be used to accurately model friction in the device.

Other monostable devices with Duffing nonlinearities have also been analysed [32] [33][34][35][36]. In [34], the operating principle of this device was similar to that of the Mann and Sims device, but with an advantage that when the centre magnet approached the ends of the device, the beams could flex away thereby reducing the magnet colliding chance with the beams.

In addition to this technique, a monostable nonlinear device using the piezoelectric effect was proposed by Stanton et al. [32]. The response of this system showed an increase in bandwidth and a distinct capability for outperforming the linear approach.

Another detailed investigation to evaluate the performance of a monostable Duffing-type harvester was carried out by Sebald et al. [37]. Especially the influence of the time-constant ratio on the performance was investigated.

In addition to the macroscale examples, several monostable energy harvesters were fabricated for microscale applications [38][39][40][41].

Thus far, the literature focused upon in this section has been concerned with the use of Duffing-type nonlinearities in monostable energy harvesters.

⑵ Random excitation

The stochastic nature of many ambient vibration sources led to several authors focusing on the performance of nonlinear energy harvesters to random excitations.

For the white noise excitation, the influence of nonlinearity on the performance of Duffing-type monostable energy harvesters has been investigated by many researchers [42][43][44][45][46]. Gammaitoni et al. [42] numerically and experimentally studied the response of a monostable piezoelectric energy harvester under random excitations. It is validated that, when the linear stiffness is held constant, the root mean square (rms) output voltage always decreases with the nonlinearity when the time constant ratio is very large. Subsequently, in [43] the response of a similar device to a Gaussian white noise excitation was analysed using the Fokker-Planck-Kolmogorov (FPK) equation. It is found that the nonlinear stiffness has no effect on the velocity probability density function (PDF) of the system thus it did not enhance power output when the time constant is very large. By approximating a solution for the corresponding FPK equation, the response of the device to colored noise excitations was

also analysed. It was concluded that, the nonlinearities are not beneficial to improve the performance of the system for most cases. After that, in [44], the FPK equation was also used to find the stationary joint probability density of the system by Green et al., however, it was shown that the Duffing hardening-type nonlinearities are beneficial to reduce the size of the device without effecting its power output.

Daqaq [45] also showed that, for both capacitive and inductive harvesters, even when the time-constant ratio is not very large, the output voltage also decreases with the increasing of the nonlinearity as long as the stiffness is the hardening-type. It was verified that, the performance of the hardening-type energy harvester always cannot outperform its linear counterpart.

In a recent study, Halvorsen [46] also demonstrated that the rms voltage of the harvester has no relationship with the nonlinearity when the time constant of the harvesting circuit is very small. Moreover, it was found that, it is impossible for the voltage variance of a monostable energy harvester with the hardening-type nonlinearity be larger than that of its linear counterpart harvester when the time constant is at intermediate levels.

For the band-limited random excitations, Barton et al. [28] experimentally investigated the response of a monostable energy harvester with Duffing-type nonlinearities under random excitations with very limited bandwidth. In this paper it was concluded that the limitations of a linear energy harvester (a limited response bandwidth) indeed can be overcome by introducing the nonlinearity. However, the nonlinear energy harvester can only present a wider response bandwidth when it is subjected to a consistent vibrating environment. For instance, the harvester is attached to the rotating machinery. Especially, random excitations appear to average out the high- and low-energy states thus impairing the advantage of the nonlinear stiffness. In [43], Daqaq also investigated the response of Duffing-type monostable inductive harvesters to band-limited random excitations. For obtaining the approximate analytical solutions for the FPK equation governing the response statistics, the Van Kampen expansion is adopted. It is concluded that, when the natural frequency of the harvester match the centre frequency of the noise, the output power always decreases with the increasing of the nonlinearity

1.5.2 Bistable energy harvester

(1) Harmonic Excitation

For the case of bistablility, it has been initially proposed by Cottone et al. [47] and later studied by several researchers [48][49][50], is based on the well-known bi-stable magneto-elastic structure of Moon and Holmes [51]. However, the main operation principle is very similar while several variations of the device were proposed. As shown in Figure 1.7, the device is composed of a ferroelectric and piezoelectric beam oscillating between two permanent

magnets. By adjusting the distance between those permanent magnets, the system becomes bistable system with two stable equilibriums.

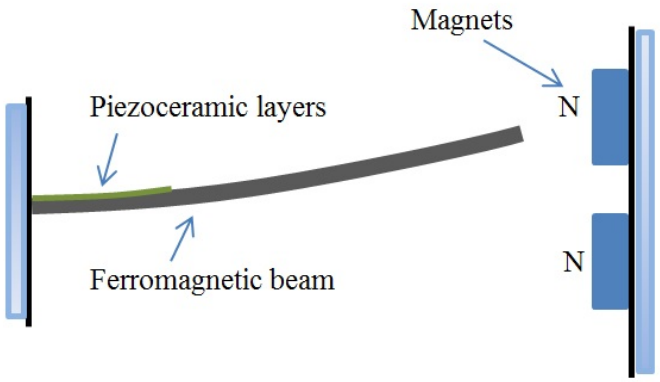

Figure 1.7. The piezomagnetoelastic generator.

Another form of bistable device was proposed in [52] - a schematic of which is shown in Figure 1.8. The device consisted of a series of magnets that were positioned to make the system bistable. Based on the device of Mann and Sims, four permanent magnets were placed symmetrically around the tube's middle position to make it become a bistable device.

Among the research to investigate the performance of bistable energy harvesters to harmonic excitations, the work of Erturk et al. [50][53] were the earliest one. It is concluded that the bistable energy harvester is beneficial because of the occurrence of the interwell oscillation which can be triggered under certain excitations. The interwell oscillations can yield apparently larger power output over a wider frequency bandwidth when compared with its linear counterpart. After the investigation of the amplitude and frequency bifurcations of a bistable piezoelectric energy harvester, Stanton et al. [49] arrived at similar conclusions. The analytical model of the system was presented. Similarly, it is observed both the large- and small-orbit periodic and chaotic responses for different levels of harmonic excitations.

Under certain excitation levels, the operating point can stabilise either on the high- or the lower energy orbit, which is determined by the basin of attraction of the solutions. However, the mechanism for adding the disturbance for stabilising the high-energy orbit has not yet physically designed.

Another approach to solve the problem is to extend the frequency response bandwidth where the unique large energy-orbit exists. This is a rather complex problem, and several researchers had employed some analytical methods for investigation. The harmonic balancing method is used by Stanton et al. [54] and Harne et al. [55] to derive the analytical solutions of the

responses. Thus, it provides a better understanding of the influence of the parameters on the final response states.

In [56] work was undertaken with the specific aim of comparing the response of monostable and bistable devices to chirp excitations. In this work it was concluded that the bistable device was only effective if the interwell chaotic response could be activated. Furthermore, it was found that the shape of the potential energy well required for such behavior to occur was very sensitive to the amplitude of excitation. It is also noted that even if the input acceleration is increased to a large enough value, one can only find that the bistable energy harvester outperforms the monostable one in the vicinity of the frequencies where the secondary resonances occur. Figure 1.9 shows the schematic diagram of the experimental device, an axial preload is applied to the beam to achieve the monostable and bistable configurations.

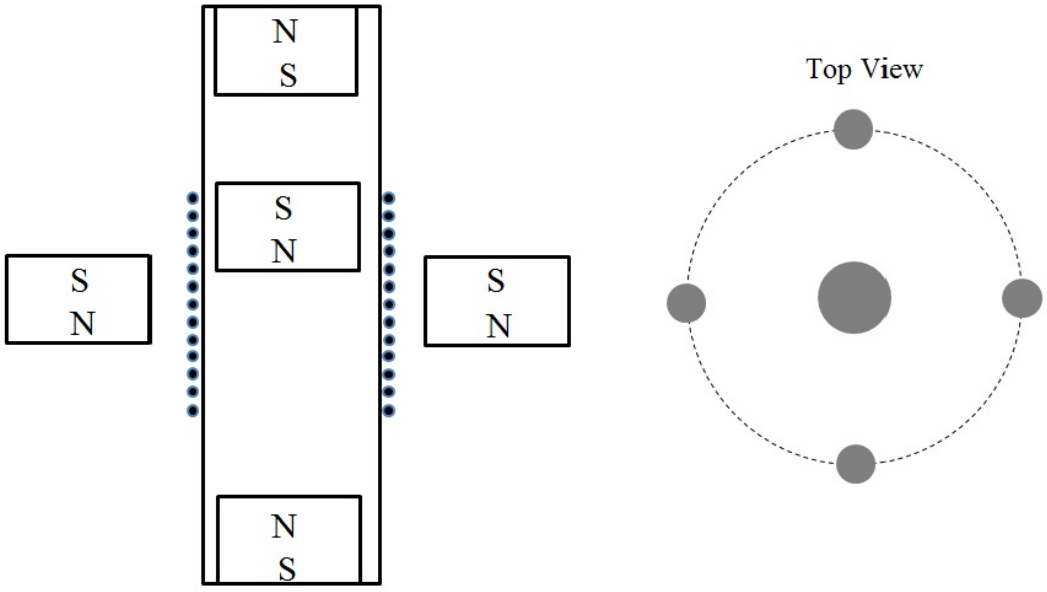

Figure 1.8. Illustrations of the bistable generator.

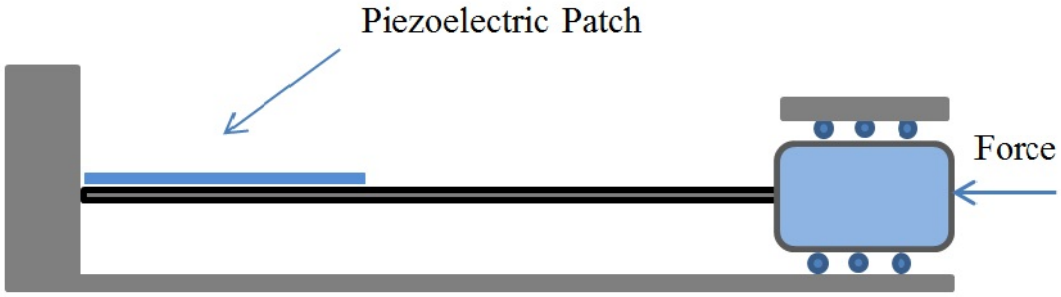

Figure 1.9. Schematic of an axially loaded energy harvester.

(2) Random excitation

Several works have focused on the response of bistable devices to random excitations [42][57][58].

For the white noise excitation, Cottone et al. [47] analysed the response of a bistable piezoelectric energy harvester. They illustrated that a bistable device can provide performance improvement in the output power under white Gaussian noise only when the time constant of the harvesting circuit is very large. By solving the FPK equation, Daqaq [45] corroborated these findings and showed that, when the time constant ratio is large, the mean power becomes independent of the nonlinearity and equals that obtained using an equivalent linear device. The same result was also concluded by Daqaq in another literature [58].

For the band-limited random excitations, Daqaq [58] studied the approximating the solution of the FPK equation for the case of exponentially correlated noise, it was shown that maximum power could be extracted from a bistable device if interwell dynamics were activated.

1.6 Motivation

This thesis focused on how to enhance the energy harvesting performance under two kinds of the most common excitations: harmonic and random excitations, by using nonlinearly vibrating system.

Based on the previous discussions, it is apparent that nonlinear energy harvesters have presented potential advantages for improving the performance of the device, and the intentional inclusion of nonlinearities makes the devices more tolerant to variations in the excitation frequency. However, there are still some apparent issues exist.

The performance of different energy harvesters under both the harmonic and the random are

briefly summarised in Table 1.1, where the bold part indicates the focused investigation in this thesis.

(1) How to guarantee operation of the Duffing-type monostable energy harvesters on the favorable high-energy orbit for energy harvesting, thereby widening the response width and boosting the response under harmonic excitation:

The nonlinearity of the Duffing-type monostable oscillator provides a wider bandwidth and a higher energy harvesting capability under harmonic excitations because of the high-energy orbit solution. However, the high-energy orbit favorable for energy harvesting is always accompanied by a lower energy orbit. The ability of the harvester to operate on the higher orbit of solutions is determined by the initial conditions and its basin of attraction. Due to its larger basin of attraction away from resonance, probabilistic studies seem to suggest that, on average, the output voltage will be closer to the lower orbit of solutions as the frequency shifts away from the linear resonance value, which diminishes the importance of the higher orbit of solutions [59]. If the oscillator's response happens to coincide with the low-energy orbit then the improved performance achieved by the nonlinear oscillator over that of its linear counterpart, could be impaired. This is the main motivation for stabilising the high-energy orbit.

It should be mentioned that because the monostable configuration can show higher performance compared with the bistable one as presented in [56], and also because of the complicated dynamics characteristic of the bistable oscillator, the approach to stabilise the high-energy orbit of the monostable configuration is investigated in this thesis.

(2) Optimisation of the nonlinear monostable energy harvester for maximum power output and design guidance under harmonic excitation:

There has been much recent interest in the response analysis and optimisation of the linear energy harvester under ambient vibrations. To transfer maximum power to an electrical load in a resonant system, the load resistance should be equal to the sum of the electrical analogue of mechanical damping and internal resistance. However, there is little literature on the optimisation of the nonlinear energy harvester. The motivating hypothesis has been that the nonlinear monostable energy harvester can also be optimised to maximise the available electrical power. This thesis presents theoretically analytical optimisation and numerical studies under three different conditions for the designed Duffing-type monostable devices, by taking the practical application into account. Meanwhile, the su-boptimisation of the energy harvesters is also conducted when the excitation frequency changes.

Table 1.1. Concise performance summary of the energy harvesters with different configurations

Configuration / Excitation	Duffing-type monostable	Bitsable	Linear
Harmonic	Wider bandwidth and higher energy harvesting capability [29] **(with a precondition that the high-energy orbit must be stabilised); Optimisation work for maximum power delivery is still needed**.	Can't outperform the monostable one under many scenarios, and the performance is sensitive to the excitation amplitude. [56]	Narrow response bandwidth
White noise	Similar mean output power with the linear one but with the smaller mean displacement. [43] [44]	Similar mean output power with the linear one. [58]	
Band-limited noise	Comparative numerical or experimental studies were incompletely made by some researchers and with some contradictory conclusions [28][43][58][60][61], **a comprehensive investigation is still needed**. **To actively enhance the noised excited energy harvesting using the theory of stochastic resonance instead of just using the existing passive nonlinear mechanisms.**		

(3) Performance analysis in random vibratory environment for random excitation:

Nonlinear systems have shown increase in the bandwidth of the device and the capability to outperform linear resonance under harmonic excitations. However, the excitation force is not always periodic, it was realised that many ambient vibrations sources can actually be somewhat stochastic in nature. While many environmental excitations exhibit the characteristics of white excitations, many others have most of their energy trapped within a narrow bandwidth possessing the characteristics of a band-limited (Colored) noise excitation.

Several incomplete theoretical or experimental works have studied the effect of nonlinearities on the performance but with some conclusions conflicting with each other. Thus, a full performances comparison and analysis between different kinds of energy harvesters is presented in this thesis for the clearly interpreting the role of the nonlinearities and providing an optional design guidance of the energy harvesters for random excitations with certain bandwidth and centre frequency. Moreover, it should be mentioned that the parameters optimisation were also discussed and conducted for fair comparison

(4) Enhanced energy harvesting for random excitation for random excitation:

A bistable device may outperform the linear equivalent in random environments, this conclusion draws on the assumption that the bistable harvester exhibits inter-well vibrations. Should inter-well vibrations be observed, it has been proposed to utilise the random excitation component in tandem with small coherent sinusoidal excitation to induce stochastic resonance. This provides a potential of further performance improvement of the bistable energy harvester. This thesis aims to adopt stochastic resonance as an effective way for energy harvesting and takes this a further step by introducing a novel approach to enhance the random excited energy harvesting with experimental demonstration.

Chart 1.1 Structure of the thesis

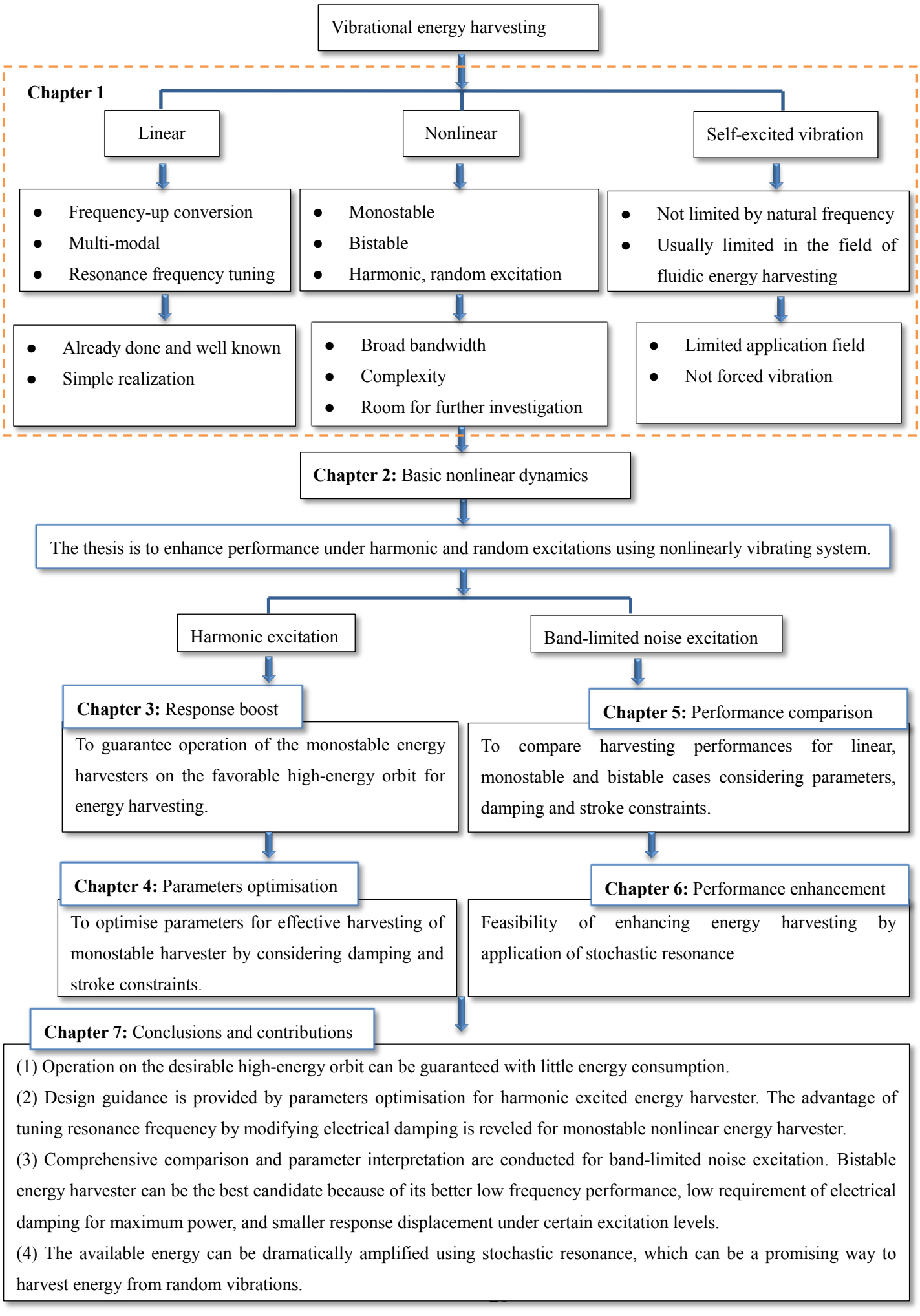

1.7 Objectives

This thesis is focused on enhancement of the energy harvesting performance from nonlinearly vibration system under harmonic and random excitations. The main objectives of this thesis are as follows:

(1) Guaranteeing operation of the Duffing-type monostable energy harvesters on the favorable high-energy orbit for energy harvesting.

(2) Investigating the optimised condition for maximum delivered power from the harmonic vibrating source using the Duffing-type monostable energy harvester.

(3) Making clear interpretation of the effect of nonlinearities on performance under band-limited noise excitations and give the guidance for the design of the energy harvesting device.

(4) Investigation of the feasibility of actively enhancing the available energy from the randomly vibrating sources by using a proposed and improved novel approach - stochastic resonance.

1.8 Overview

As presented in Chart 1.1, structure of the thesis is clearly interpreted corresponding the studying motivation, and the further introduction is given in the following parts.

In Chapter 1, an overview was executed about the developing techniques to increase the bandwidth of vibration-based energy harvesters. The broadband vibration-based energy harvesting solutions are introduced covering resonance tuning, multimodal energy harvesting, frequency up-conversion, self-excited and parametric resonance energy harvesting, which are summarised with regard to their merits and shortcomings. Moreover, the techniques exploiting non-linear oscillations are especially addressed.

In Chapter 2, the basic dynamics characteristics of the typical Duffing oscillators are presented, including the principle of the theory of stochastic resonance.

The main work of Chapter 3 is focused on how to guarantee operation of the monostable nonlinear energy harvesters on the favorable high-energy orbit for energy harvesting, thereby widening the response bandwidth and boosting the response. Two kinds of approaches with the prototyping are presented to trigger a jump from the low- to the high-energy orbits by tuning the stiffness of the system, without changing the frequency or the amplitude of the excitation. One configuration is designed as a stiffness tunable nonlinear energy harvester, whose stiffness can be tuned directly. Meanwhile, another configuration is also proposed to change the equivalent stiffness of the energy harvesting device using damping variation. One obvious advantage of this method is that it requires little extra energy input for stiffness tuning, which is different from the directly mechanical tuning method.

The Chapter 4 presents the parameters optimisation work under harmonic excitations for maximum electrical delivery, with the assumption that the energy harvesting device operates on the high-energy orbit. By the consideration of the implemental environments, theoretical and analytical optimisation under unconstrained and constrained conditions (i.e. electrical damping and stroke of the device) is investigated. This work provides the guidance for the design of the monostable nonlinear harvesters.

In Chapter 5, for the random excitation, the parameters interpretation is processed for the influence of the nonlinearities on the transduction of the energy harvester, and the comprehensive performance comparisons of different energy harvesters. Meanwhile, the performance comparison is also conducted with the consideration of the constrained electrical damping and displacement amplitude conditions

In Chapter 6, instead of only making using of the existing typical passive devices (i.e. including linear, monostable nonlinear and bistable configurations), a novel method of actively enhancing energy harvesting effectiveness is investigated under random excitations based on the theory of stochastic resonance. Meanwhile, another method to achieve stochastic resonance is also presented, which indicates that an easier approach may be a promising way to improve the performance of energy harvesting under random excitations. After that, by using the bistable configuration, the method using the theory of stochastic resonance is demonstrated for enhancing the energy harvesting effectiveness.

In Chapter 7, the conclusions are drawn mainly about contributions and significance of the above work.

Chapter 2

Basic Nonlinear Dynamics

2.1 Introduction

In this chapter, the basic dynamics and its characteristics are introduced for the monostable and bistable Duffing oscillators under harmonic excitations, which will be used for the theoretical derivation in the following chapters. Moreover, the nonlinear influences on the responses under random excitations are also briefly discussed, which is followed by the introduction of a novel method to further enhance the performance using the theory of stochastic resonance, and its details will be presented in Chapter 6.

2.2 Harmonic excitation

2.2.1 Monostable oscillator

The equation of motion of a force-excited Duffing monostable oscillator can be written as

$$m\ddot{x} + c\dot{x} + kx + \alpha x^3 = F\cos(\omega t + \varphi) \tag{2.1}$$

where x is the relative displacement, and m is the seismic mass which is coupled with a restoring force with cubic nonlinearity and an energy transducer with damping coefficient c, excited by a harmonic force $F\cos(\omega t + \varphi)$, φ is the phase angle between the excitation and the response. The positive and negative nonlinearity α indicate a hardening and softening system, respectively. Equation (2.1) can be expressed in non-dimensional form as

$$u'' + 2\zeta u' + u + \beta u^3 = \cos(\Omega\tau + \varphi) \tag{2.2}$$

where $u = \frac{kx}{F}$, $\Omega = \frac{\omega}{\omega_n}$, $\omega_n = \sqrt{\frac{k}{m}}$, $\zeta = \frac{c}{2m\omega_n}$, $\beta = \frac{\alpha F^2}{k^3}$ and $(\bullet)' = \frac{d}{d\tau}$.

To analyse the response of the oscillator, the frequency-amplitude relationship needs to be derived. The analytical approach includes using classical perturbation methods, which are quite accurate for predicting the jump-up frequency, but less so for the jump-down frequency under a strong nonlinearity. Another approach to obtain the analytical solution of the equation is the method of harmonic balancing method. The harmonic balancing method can be applied to the weakly and strongly nonlinear systems, which gives an advantage of this method over the perturbation methods. It is assumed that the harvester response can be modelled by a truncated Fourier series, where the number of terms dictates the accuracy of the intended solution. In the existing literature different numbers of terms in the Fourier series have been used to compute

the critical jump frequencies in the frequency response curve of the Duffing oscillator. Friswell and Penny [62], and Worden [63] computed the jump-up and jump-down frequencies of the Duffing oscillator linear damping using the HBM. Friswell and Penny [62] used a numerical approach based on Newton's method to compute the jump frequencies, including terms up to the ninth harmonic, while Worden used a first order expansion to solve the resulting equation numerically. Brennan et al. [64] made a comparison based on the results. Remarkably the difference between Friswell and Penny's results and Worden's first order approximation never exceeded 0.34% for the parameters chosen in Brennan's study [64]. Carrella [65] used the HBM for a first order expansion to find closed form expressions that, with the parameters used in [62][63], yield values which differ from those found by Friswell and Worden by less than 1%. However, a relatively weak nonlinearity was used in Friswell and Penny' study. Peng et al. [66] investigated the case of a Duffing oscillator with a stronger nonlinearity using third order expansion HBM. However, the frequency response curve was only numerically computed because it they failed to find analytical solutions, even by using appropriate software.

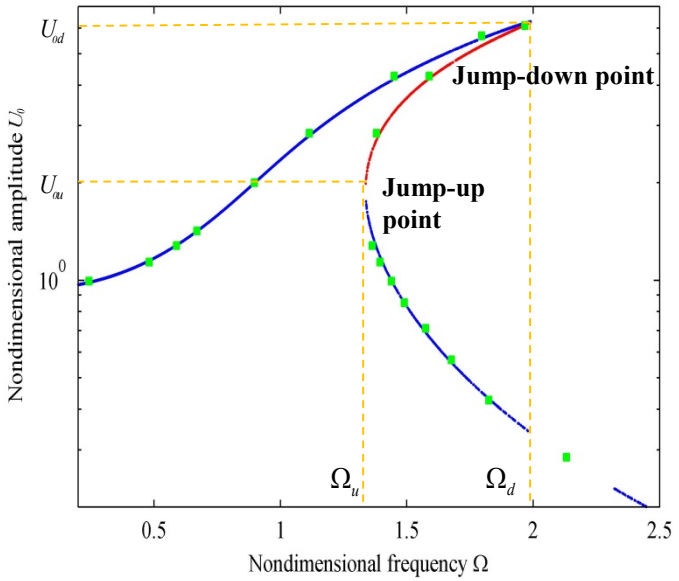

Figure 2.1. Frequency response comparison between the first order expansion HBM (dotted line) and the third order expansion HBM (square).

To validate the accuracy of the first order HBM approximation the parameters chosen by Peng et al. [66] are employed to make a comparison ($\zeta = 0.04$, $\beta = 0.1$) by simulation, which is presented in Figure 2. 1. It is validated that the fundamental harmonic of the response is dominant over higher harmonics and it shows sufficient accuracy.

It is assumed that the steady state solution of Equation (2.2) is of the form

$$u = U_0 \cos \Omega \tau \tag{2.3}$$

so that the velocity and acceleration are respectively given by

$$\dot{u} = -U_0 \Omega \sin \Omega \tau \tag{2.4}$$

and

$$\ddot{u} = -U_0 \Omega^2 \cos \Omega \tau \tag{2.5}$$

Substituting Equations (2.3), (2.4) and (2.5) into the Equation (2.2), it becomes

$$\begin{aligned} &-U_0 \Omega^2 \cos \Omega \tau - 2\zeta \Omega U_0 \sin \Omega \tau + U_0 \cos \Omega \tau + \beta {U_0}^3 \cos^3 \Omega \tau \\ &\quad = \cos \varphi \cos \Omega \tau - \sin \varphi \sin \Omega \tau \end{aligned} \tag{2.6}$$

The coefficient of β is then expanded using elementary trigonometric relations. By ignoring the superharmonics, it gives

$$\beta {U_0}^3 \cos^3 \Omega \tau = \frac{3}{4} \beta {U_0}^3 \cos \Omega \tau + \frac{1}{4} \beta {U_0}^3 \cos 3\Omega \tau \tag{2.7}$$

Substituting the approximation into Equation (2.6), and equating the coefficients of $\sin \Omega \tau$ and $\cos \Omega \tau$, gives

$$-U_0 \Omega^2 + U_0 + \frac{3}{4} \beta {U_0}^3 = \cos \varphi \tag{2.8a}$$

$$2\zeta \Omega U_0 = \sin \varphi \tag{2.8b}$$

Squaring and summarizing Equations (2.8a) and (2.8b) to obtain

$$\frac{9}{16} \beta^2 {U_0}^6 + \frac{3}{2} \beta \left(1 - \Omega^2\right) {U_0}^4 + \left(\left(1 - \Omega^2\right)^2 + \left(2\zeta \Omega\right)^2\right) {U_0}^2 = 1 \tag{2.9}$$

This equation represents the frequency-amplitude response relationship of the oscillator. The

solution of this sixth order polynomial can be found using the Matlab *solve* command.

However, the expressions of the jump-up and jump-down points of the oscillator should be derived, which are necessary for the high-energy orbit stabilisation and optimisation in the following chapters. For convenience, the modal coupling coefficient ε is neglected.

Solving Equation (2.9) for the positive solutions as

$$\Omega_1 \approx \sqrt{\frac{3\beta U_0^{\,2}}{4} + 1 - 2\zeta^2 + \frac{\sqrt{1 - 4\zeta^2 U_0^{\,2}\left(1\text{-}\zeta^2\right) - 3\beta\zeta^2 U_0^{\,4}}}{U_0}} \tag{2.10a}$$

$$\Omega_2 \approx \sqrt{\frac{3\beta U_0^{\,2}}{4} + 1 - 2\zeta^2 - \frac{\sqrt{1 - 4\zeta^2 U_0^{\,2}\left(1 - \zeta^2\right) - 3\beta\zeta^2 U_0^{\,4}}}{U_0}} \tag{2.10b}$$

Assuming that $\zeta^2 << 1$, the above solutions can be reduced to

$$\Omega_1 = \sqrt{\frac{3\beta U_0^{\,2}}{4} + 1 + \frac{\sqrt{1 - 4\zeta^2 U_0^{\,2} - 3\beta\zeta^2 U_0^{\,4}}}{U_0}} \tag{2.11a}$$

$$\Omega_2 = \sqrt{\frac{3\beta U_0^{\,2}}{4} + 1 - \frac{\sqrt{1 - 4\zeta^2 U_0^{\,2} - 3\beta\zeta^2 U_0^{\,4}}}{U_0}} \tag{2.11b}$$

The jump-down point can be regarded as the resonance point of the nonlinear oscillator and it approximately equal to the point where the response amplitude is maximum. In this thesis, the approach taken by Magnus [67] and Hagedorn [68] is followed to derive the jump-down point. The jump-down frequency can be found by equating the two values in Equations (27) to yield

$$1 - 4\zeta^2 U_0^{\,2} - 3\beta\zeta^2 U_0^{\,4} = 0 \tag{2.12}$$

and rearranging the expression gives

$$U_{0d} \approx \sqrt{\frac{2}{3\beta}\left(\sqrt{1+\frac{3\beta}{4\zeta^2}}-1\right)} \tag{2.13}$$

Substituting Equation (2.13) into Equation (2.11) yields the jump-down frequency of the frequency-amplitude curve as

$$\Omega_d \approx \sqrt{\frac{1}{2}\left(\sqrt{1+\frac{3\beta}{4\zeta^2}}+1\right)} \tag{2.14}$$

To determine the jump-up frequency, it is noted that when the jump-up phenomenon occurs, this frequency is weakly dependent upon the damping ratio. Thus, by setting $\zeta = 0$ and finding the point at $\frac{d\Omega_{1,2}}{dU_0} = 0$, the non-dimensional displacement amplitude of the jump-up frequency can be given as

$$U_{0u} \approx \left(\frac{2}{3\beta}\right)^{1/3} \tag{2.15}$$

Substituting Equation (2.15) into Equations (2.11) gives the jump-up frequency

$$\Omega_u \approx \sqrt{1+\frac{3}{2}\left(\frac{3\beta}{2}\right)^{1/3}} \tag{2.16}$$

2.2.2 Bistable oscillator

The equation motion of the bistable oscillator can be expressed in non-dimensional form as

$$u'' + 2\zeta u' - u + \beta u^3 = \cos\left(\Omega\tau + \varphi\right) \tag{2.17}$$

The steady state solution of Equation (2.17) is that of the form

$$u = B + U_0 \cos\Omega\tau \tag{2.18}$$

where B is a constant. The frequency-amplitude response equation can also be obtained using the harmonic balance method, which can be expressed as
when $B = 0$

$$\frac{9}{16}\beta^2 {U_0}^6 - \frac{3}{2}\beta\left(1+\Omega^2\right){U_0}^4 + \left(\left(1+\Omega^2\right)^2 + \left(2\zeta\Omega\right)^2\right){U_0}^2 = 1 \tag{2.19}$$

and when $B^2 = 1 - \frac{3}{2}{U_0}^2$

$$9\beta^2 {U_0}^6 + 6\beta\left(\Omega^2 - 2\right){U_0}^4 + \left(\left(\Omega^2 - 2\right)^2 + \left(2\zeta\Omega\right)^2\right){U_0}^2 = 1 \tag{2.20}$$

It can be noted that the response of the bistable oscillator is more complex compared with the monostable one. However, as mentioned previously, in [56], the performance of the monstable oscillator was experimentally compared, it is demonstrated that in contrast to the common understanding that the bistable energy harvester has a wider bandwidth, it is is very much dependent on the level of the input acceleration and the shape of the bistable potential function. And, many of the presented scenarios clearly demonstrate that the monostable harvester can outperform the bi-stable one.

On the other hand, considering the complexity of the bistable oscillator, it is mainly focused on the investigation of the monostable configuration for the harmonic excitations in this thesis, including how to trigger a jump from the low- to the high-energy orbit thereby boost the response and the optimisation work for maximum power output, which will be presented in Chapter 3 and Chapter 4, respectively.

2.3 Random excitation

2.3.1 Effect of the nonlinearity

Nonlinear energy harvesters, in particular the hardening monostable oscillator with a cubic nonlinearity [69][70], and bistable devices with double-well potential [53][71] have shown an increase in the bandwidth of the device and the capability to outperform linear resonance under harmonic excitations. However, the excitation force is not always periodic in reality and in fact most ambient vibrations sources can actually be somewhat stochastic in nature.

The influence of the nonlinearity on the performance of energy harvesters under random excitations has been investigated in some of the literature [72][73][74][75]. However, it was

demonstrated that under Gaussian white noise excitation both the nonlinearity of the hardening-type monostable oscillator and the bistabilities in the potential did not provide any enhancement of energy harvesting over that of the traditional linear generator with a single well [43][58]. Different conclusions can be found when the value of the constant of the harvesting circuit is taken into consideration [47][42]. While many environmental excitations exhibit characteristics of white noise excitations, many others have most of their energy trapped within a narrow bandwidth possessing the characteristics of a band-limited coloured excitation. Notably, Daqaq [43] analysed the responses of linear and hardening-type monostable systems subjected to band-limited noise by computing the probability density function (PDF) and made certain comparisons. It was shown that the nonlinearity can adversely influence the mean output power under band-limited noise excitations, but it can be noted that experimental validation was not involved in this particular study. Sebald et al. [37][76] arrived at a similar conclusion for a hardening-type monostable harvester. After that, by applying a static compressive axial load at one end of a beam, Masana et al. [77] experimentally investigated the performance of a monostable hardening-type energy harvester in the pre-buckling condition, and a bistable energy harvester in the post-buckling condition, when the harvesters were subjected to random base excitations of different levels, bandwidths, and centre frequencies. The bistable harvester has been shown to outperform the monostable design.

On the other hand, Meimukhin el al. [60] made a comparison of a bistable energy harvester and its linear counterpart and showed that nonlinear bistable oscillators generally perform better than the linear one under band-limited noise excitation, in certain regions. This was only under the condition that a random excitation with a cut-off frequency was analysed, and without considering the independent influence of the various centre frequencies. However, Joo et al. [61] numerically demonstrated that under coloured noise excitations the linear energy harvester outperformed the monostable nonlinear harvester, while the bistable energy harvester showed the lowest performance, and this rather conflicts with the conclusions discussed above.

Therefore, a full performance comparison between the monostable hardening-type configuration, the bistable configuration, and the linear counterpart, under a band-limited base force will be presented in the thesis which will be shown in Chapter 5. The influences of various excitations levels, bandwidths and centre frequencies are all taken into account. Moreover, the influence of damping and displacement constraint on the performance is also analysed.

2.3.2 Method for performance enhancement

The enhanced method presented in this thesis is based on the theory of stochastic resonance, which is an intriguing and counter-intuitive phenomenon. It has been demonstrated and

considered for several fields such as signal processing, electrical circuit development and image visualization [78][79]. Ongoing work exploits stochastic resonance as a way of harvesting the energy within the random excitation.

Stochastic resonance applied to harvesting requires three basic ingredients: firstly an energetic activation barrier such as the double well potential of a bistable system, a weak but coherent control input in the form of a periodic signal, which is a means of controlling the potential well's threshold of a bistable system, and finally a source of ambient vibration that is inherent to the system to be harvested. In satisfying the above requirements the response of the system undergoes resonance-like behaviour as a function of the ambient (noise) excitation, hence the term stochastic resonance [80][81]. Stochastic resonance can be thought of as resulting from the synchronisation of a stochastic time-scale determined by the transition rate over the barrier, and a deterministic time-scale determined by the time-scale of periodic modulation. The system is seen to exhibit stochastic resonance when the noise strength is appropriately tuned to ensure the synchronisation of these two time scales.

An excellent review which clearly identifies the advantages of bistable energy harvesters was provided by Cammarano et al. [82]. Reports on experimental studies confirm the necessity for inter-well motion through which the system oscillates by switching between two stable equilibria, and show that more energy can be throughput than for intra-well motion where the system simply oscillates around one stable equilibrium. Consequently, for a suitably designed nonlinear mechanical system, the ambient noise is the source of excitation, and it is this which can excite the stochastically resonant system into a bistable nonlinear response. The presence of bistability makes the system capable of rapidly switching between stable states and if even a relatively weak periodic excitation is also applied to the system then the double well potential can periodically raise and lower the potential barrier, and so noise-induced hopping between the potential wells can become synchronised with the periodic excitation, leading to stochastic resonance. McInnes et al. [83] first proposed the possibility of enhancing the performance of a bistable mechanism with stochastic resonance, and provided a numerical analysis to support this. By adding a periodic modulating excitation to a random excited bistable mechanism, the power available from the device was found to be enhanced over that of the same device without the periodic excitation. In this thesis, the motivation is to propose and validate a design for a novel nonlinear bistable harvester in which the principles of stochastic resonance are applied.

A basic model is proposed by initially considering a hypothetical nonlinear system with one single degree of freedom comprising an oscillating mass m undergoing response x from forces determined by an overall damping coefficient c, and stiffness coefficients k and α the determine a third-order polynomial $-kx+\alpha x^3$ that is required for bistability. Subjected also to random excitations, $N(t)$, this system is described by

$$m\ddot{x} + c\dot{x} - kx + \alpha x^3 = N(t) \tag{2.21}$$

The potential governing the particle dynamics is of the standard double well type, and defined as,

$$U(x) = -\frac{1}{2}kx^2 + \frac{1}{4}\alpha x^4 \tag{2.22}$$

The doubly degenerate minima of the double well potential are located at $x_m = \pm(k/\alpha)^{1/2}$ and the barrier height is given by $\Delta U = k^2/(4\alpha)$.

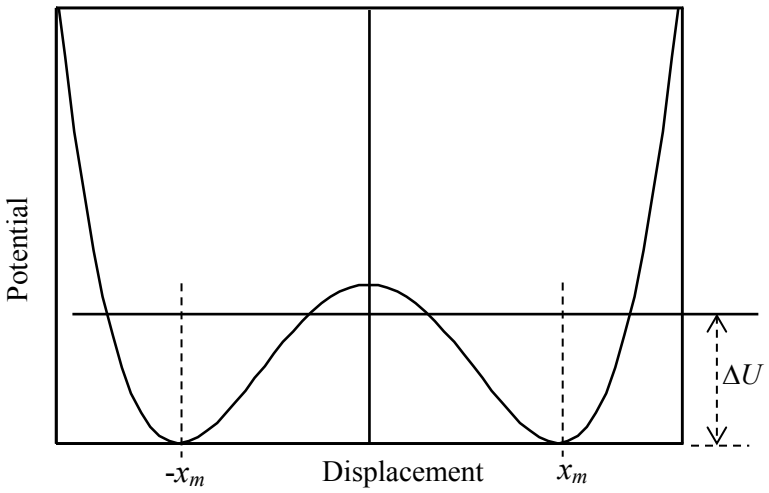

Figure 2.2. The potential well of bistable system.

In addition to the system being excited by the ambient vibration force, when the low-level additional periodic force $A_0\cos(t)$, is applied to the right hand side of Equation (2.21), the system's dynamics is described as

$$m\ddot{x} + c\dot{x} - kx + \alpha x^3 - A_0\cos\omega t = N(t) \tag{2.23}$$

The potential associated with the system described by Equation (2.23) can be correspondingly expressed as

$$U(x,t) = -\frac{1}{2}kx^2 + \frac{1}{4}\alpha x^4 - A_0 x\cos\omega t \tag{2.24}$$

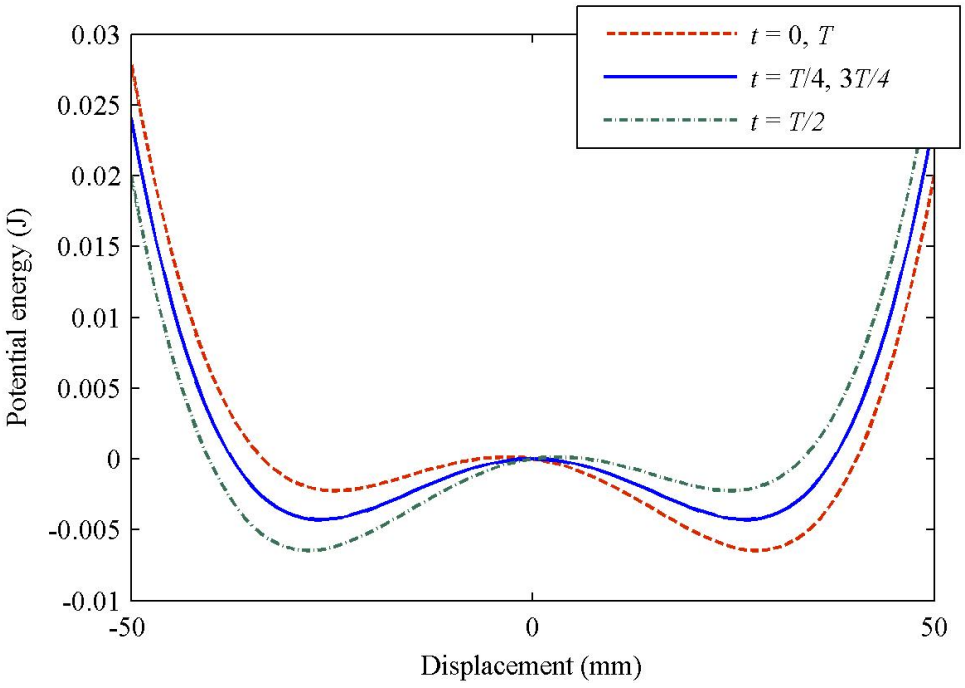

Figure 2.2. Variation of the potential wells with the periodic force ($k = -24.5\,\mathrm{N/m}$, $\alpha = 35000\,\mathrm{N/m^3}$ and $T = 2\pi/\omega$).

The presence of bistability makes the system capable of switching between stable states. From Figure 2.2, it can be noted that the double-well potential can be tilted asymmetrically up and down, so that the potential-well barrier can be lowered. Although the additional periodic excitation is maybe too weak to continually make the system move from one side of the double-well potential into the other, it becomes relatively easy for the random excitation to overcome this barrier and a noise-induced hopping between the wells can still take place through synchronisation with the small-scale additional excitation. In short, stochastic resonance can be generated in a bistable system through synchronisation of hopping between the potential minima with the imposed small-scale periodic excitation. When the condition for stochastic resonance is fulfilled, the response will be amplified because the inter-well dynamics are activated from the intra-well motion, thereby enhancing the energy harvesting from the random excitation.

2.4 Summary

By the analysis of the basic dynamics and its characteristics of the Duffing type oscillators, under the harmonic excitation, the bistable oscillator presents a more complex characteristic than that of the monostable configuration. However, it is validated that the monostable energy harvester can outperform the bistable one under many scenarios. Therefore, the monostable configuration is mainly investigated for the harmonic excited energy harvesting in this thesis.

For the case of random excitation, it gives a brief review of the performances of several typical energy harvesters, and presents the necessities of further investigation. Thereby, the comprehensive study under band-limited excitations will be introduced in Chapter 5, including the constrained electrical damping and displacement conditions.

Moreover, it is briefly introduced about the theory of the stochastic resonance in this chapter, and its implementation and the improved method for achieving stochastic resonance will be investigated in detail in Chapter 6.

Chapter 3

Response Boost for Harmonic Excitation

3.1 Introduction

As mentioned previously, a hardening type oscillator was investigated by Mann and it was

found that at relatively high excitation levels, both low- and high-energy responses can coexist for the same parameter combinations [29]. When compared with a linear oscillator using similar parameters, the effectiveness of a nonlinear energy harvesting device can apparently be increased over a certain frequency range. However, this conclusion is obtained with the precondition that the energy harvester is always operated on the high-energy orbit within the frequency range, where the low-energy orbit coexists. However, it is not always the case. Furthermore, in the numerical and experimental investigations of the former studies, many researchers only used the slow forward or backward sweeps of the excitation frequency for the performance of the monostable nonlinear energy harvester, despite the implementation challenge that this offers in practice, and in fact this is a formidable requirement for the satisfication of the ideal harvesting conditions.

The hardening type device, proposed by Mann [29], is an electromagnetic energy harvester, which contains a moving magnet suspended between two magnets with opposing poles, and whose nonlinearity is identical to that of the monostable Duffing oscillator. This current study improves upon that work to produce a design for a stiffness tunable nonlinear vibrational energy harvester. The device is constructed in the hope that the jump from a low-energy orbit to a high-energy orbit, which can be triggered by tuning the stiffness of the device.

However, it should be mentioned that the linear DC motor, utilised to tune the stiffness, will result in the energy consumption for this form of mechanical tuning, and it was the main shortcoming. A similar effort to tune the stiffness of a linear vibration-based generator was reported by Zhu et al. [12].

The self-excitation method was also proposed by Masuda et al. [84] to stabilise the high-energy orbit. A load circuit was adopted in this design, with a switch between the conventional load, a negative resistance circuit, and a switching control law dependent on the amplitude of the oscillator's response. However, besides the additional electrical energy required to drive the circuit and switch, it also consumes part of the harvested energy in order to destabilise the low-energy orbit and trigger the jump. Although the technique can work well, it is not ideal in the context of the self-sustainability and overall efficiency for the energy harvester.

Inspired by a linear vibration isolation system with variable stiffness as proposed by Liu et al. [85], in this thesis, the method of damping variation is used to change the equivalent linear stiffness of a nonlinear harvester for stabilising the high-energy orbit. It provides an advantage for practical implementation, because of the fact that it consumes much less energy to vary the damping, compared with directly tuning the stiffness using the mechanical method, especially when an electromagnetic damper is adopted. It should be noted that this kind of electrical damper was successfully used for a self-powered vehicle suspension by Nakano el al. [86], in

which the electrical damping was tuned by varying the load resistance in the electrical drive circuit. For a further improvement, a nonlinear vibrational energy harvester is also designed, in which the equivalent linear stiffness can be changed by only varying the damping.

The proposed principles are demonstrated for stabilising the high-energy orbit and boosting the response, through the analysis of the variation in the frequency-amplitude response curves during the tuning process; thereby, its effectiveness is validated for both of the tuning methods.

3.2 Stiffness tuning method

3.2.1 Apparatus illustrations

A schematic diagram for an energy harvester is given in Figure 3.1 in which three permanent magnets of the same dimensions and parameters are arranged in a repulsive configuration, and where the magnetic end mass of the piezoelectric cantilever is aligned with respect to the fixed top and bottom permanent magnets [87]. The top magnet is fixed and the bottom magnet is attached to a slider on a rail to allow the equilibrium distance h to be adjusted by a DC motor. The initial positions of the top magnet and bottom magnet are symmetric about the equilibrium position of magnetic end mass under the action of the cantilever and the gravity. However, it should be noted that the magnetic end mass will deviate the middle position between the other two permanent magnets when only the bottom magnets is tuned to change the stiffness of the system because of the existence of the cantilever. Hence, the equivalent stiffness of the cantilever is chosen to be low enough to minimise its influence on the magnetic interaction force between the permanent magnets.

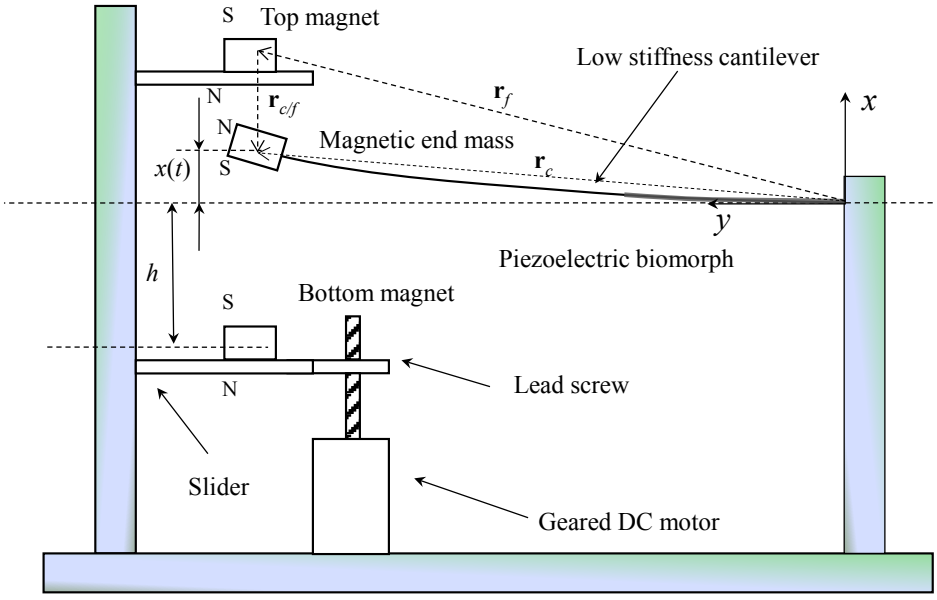

Figure 3.1. Schematic diagram of the stiffness tunable hardening type energy harvester.

3.2.2 Model of energy harvester

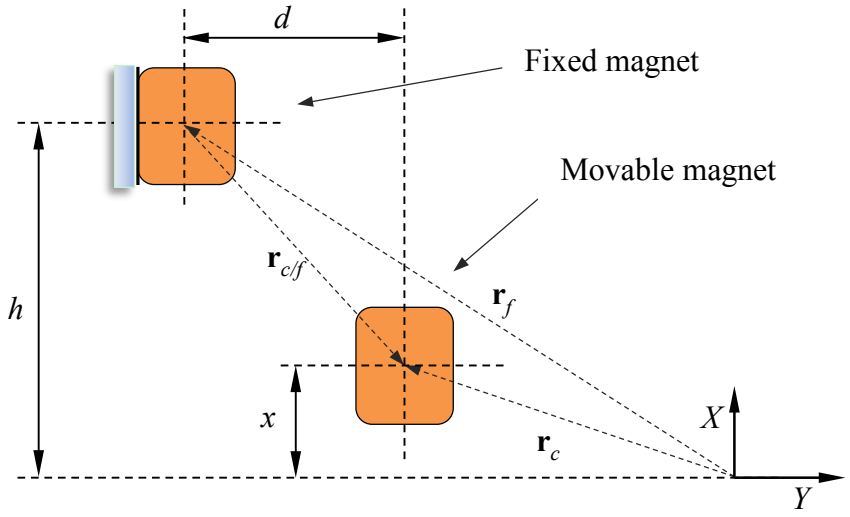

Figure 3.2. Schematic diagram of the interaction between two permanent magnets.

To obtain the restoring force between the permanent magnets, the mathematical model of the interaction forces between two permanent magnets shown in Figure 3.2 is firstly derived. The dipole model [52][88][89] is used to represent the interaction forces. The magnetic flux density at the location $\mathbf{r}_c$ due to the top magnet located at $\mathbf{r}_f$ can be defined by

$$\mathbf{B} = -\frac{\mu_0}{4\pi}\nabla\frac{\mathbf{m}_f \cdot \mathbf{r}_{c/f}}{\left|\mathbf{r}_{c/f}\right|^3} \tag{3.1}$$

where $\mathbf{B}$ is the magnetic flux density, ∇ is the vector gradient, $\mu_0 = 4\pi\times10^{-7}\ \mathrm{H/m}$ is the permeability of free space, $\mathbf{r}_{c/f}$ is the position vector from the fixed magnet to the movable magnet, and $\left|\mathbf{r}_{c/f}\right|$ is the scalar distance between the two permanent magnets. The magnetic moment of the fixed magnet is defined by $\mathbf{m}_f = \mathbf{M}_f v$, where $\mathbf{M}_f$ and v are the magnetisation amplitude and volume of the magnet, respectively. The potential energy of the movable magnet at $\mathbf{r}_c$ in the field generated by the fixed magnet at $\mathbf{r}_f$ is defined by

$$U_M = -\mathbf{m}_c \cdot \mathbf{B} \tag{3.2}$$

where the magnetic moment of the movable magnet is defined by $\mathbf{m}_c = \mathbf{M}_c v$. The magnetisation amplitudes of the movable and the fixed magnet are defined by $\mathbf{M}_c = (M_{cx}, M_{cy})$ and $\mathbf{M}_f = (M_{fx}, M_{fy})$, respectively. Using Equations. (3.1) and (3.2), the potential energy of the magnetic end mass can be expressed as

$$U_M = \frac{\mu_0 v^2}{4\pi} \Phi(h+x) \tag{3.3}$$

where h is the vertical distance between the equilibrium position of the movable magnet and the fixed magnet, and the function $\Phi(x)$ is defined by

$$\Phi(x) = -\frac{3\left(dM_{cy} + xM_{cx}\right)\left(dM_{fy} + xM_{fx}\right)}{\left(d^2 + x^2\right)^{5/2}} + \frac{M_{fy}M_{cy} + M_{fx}M_{cx}}{\left(d^2 + x^2\right)^{3/2}} \tag{3.4}$$

where d is the lateral distance between the movable magnet and the fixed magnets. Equation (3.4) can be substituted into Equation (3.3) to get the analytic expression of the potential energy of the movable magnet.

Restoring forces are conventionally obtained from the negative of the spatial derivative of the potential energy, as follows

$$F_M(x) = \frac{\mu_0 v^2}{4\pi} \Theta(h+x) \tag{3.5}$$

where the function $\Theta(x)$ is defined by

$$\Theta(x) = \frac{3\left(M_{cy}\left(dM_{fx} + xM_{fy}\right) + M_{cx}\left(dM_{fy} + 3xM_{fx}\right)\right)}{\left(d^2 + x^2\right)^{5/2}} - \frac{15x\left(xM_{fx} + dM_{fy}\right)\left(xM_{cx} + dM_{cy}\right)}{\left(d^2 + x^2\right)^{7/2}} \tag{3.6}$$

The analytic expression of the restoring forces of the movable magnet can also be got by substituting Equation (3.6) into Equation (3.5).

The corresponding magnetisation strengths of the magnets are chosen to be $M_{cx} = M_{fx} = 9 \times 10^5$ A/m and $M_{fy} = -M_{cy} = 8 \times 10^5$ A/m, where the signs indicate polarity. The length, width and height of these permanent magnets with same dimensions are chosen to be 30 mm, 10 mm and 10 mm, respectively. Those parameters are used to depict the magnetoelastic force. Figures 3.3 to 3.8 show the restoring force and the corresponding potential energy as function of displacement of the movable magnet under various distance *d* and *h*.

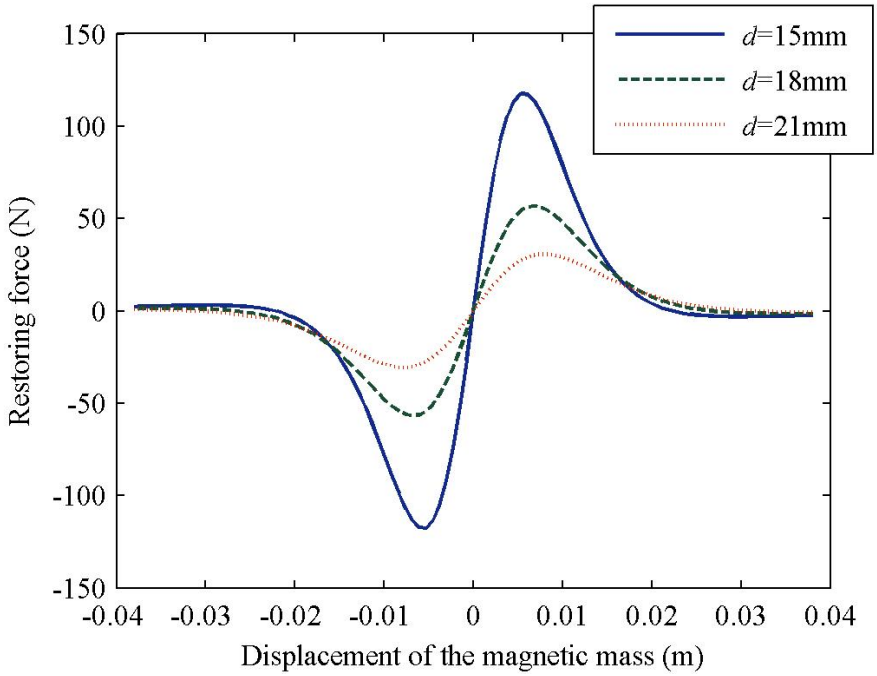

Figure 3.3. The restoring force plotted as a function of displacement of the movable magnet (*h*=15 mm).

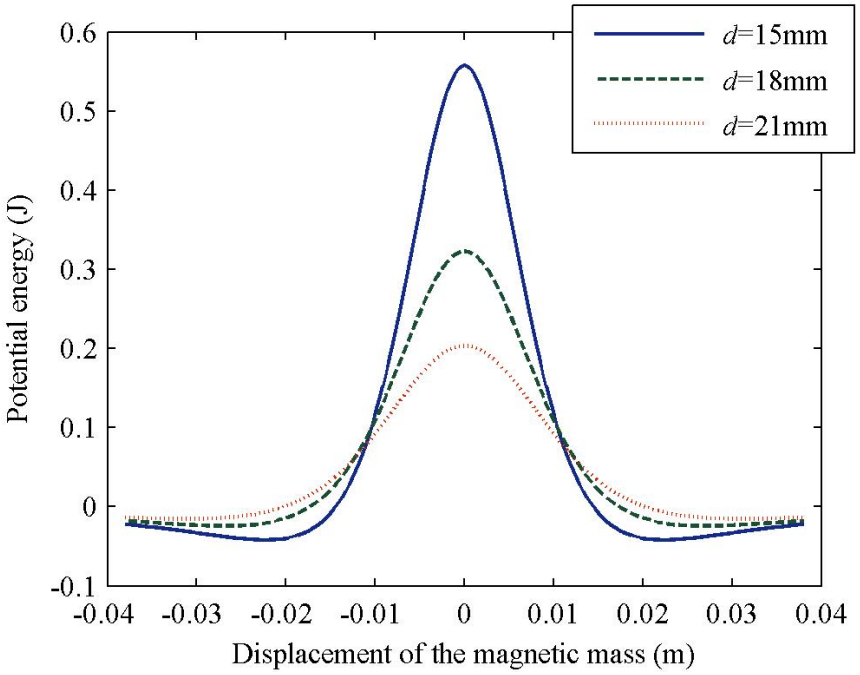

Figure 3.4. The potential energy plotted as a function of displacement of the movable magnet (h=15 mm).

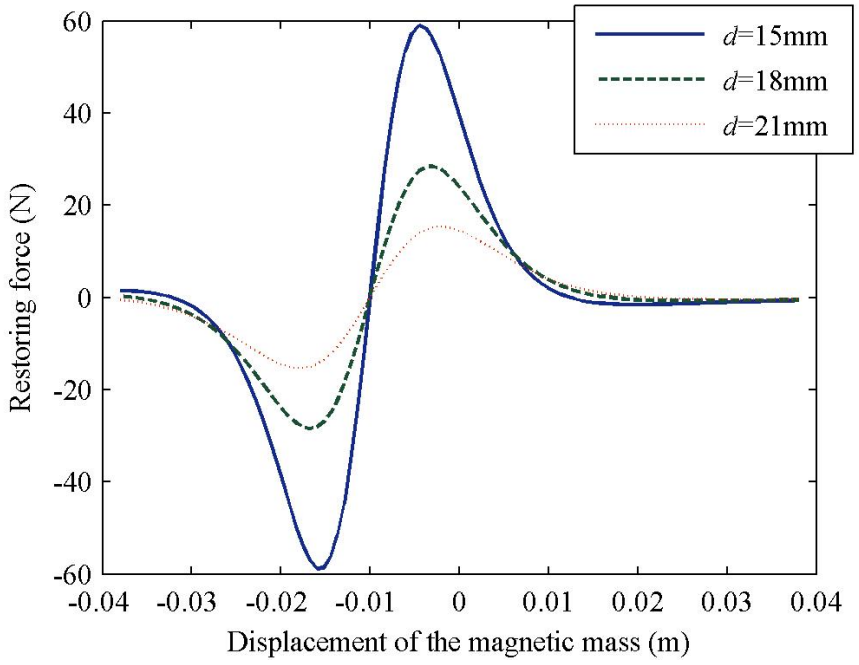

Figure 3.5. The restoring force plotted as a function of displacement of the movable magnet (h=18 mm).

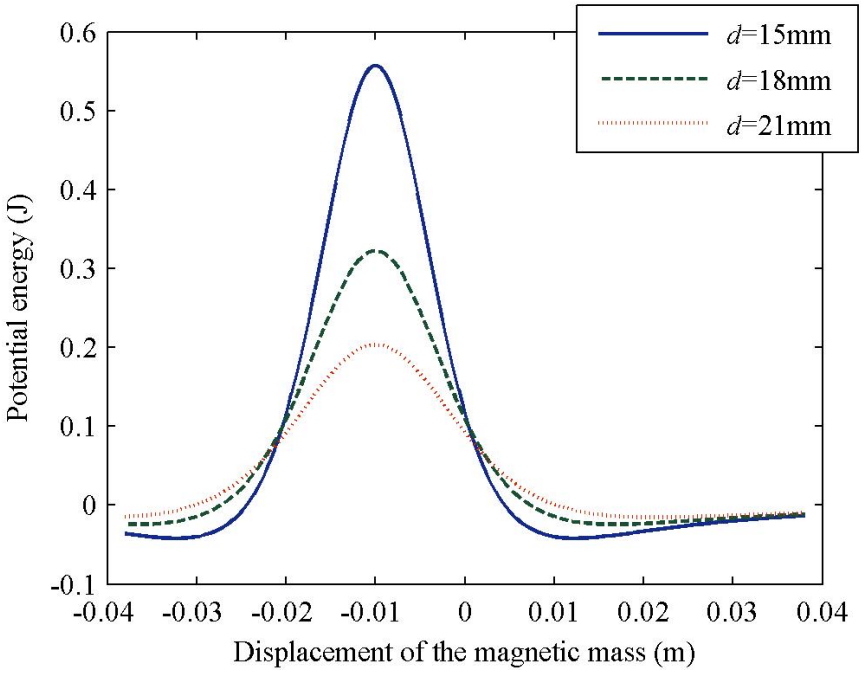

Figure 3.6. The potential energy plotted as a function of displacement of the movable magnet (h=18 mm).

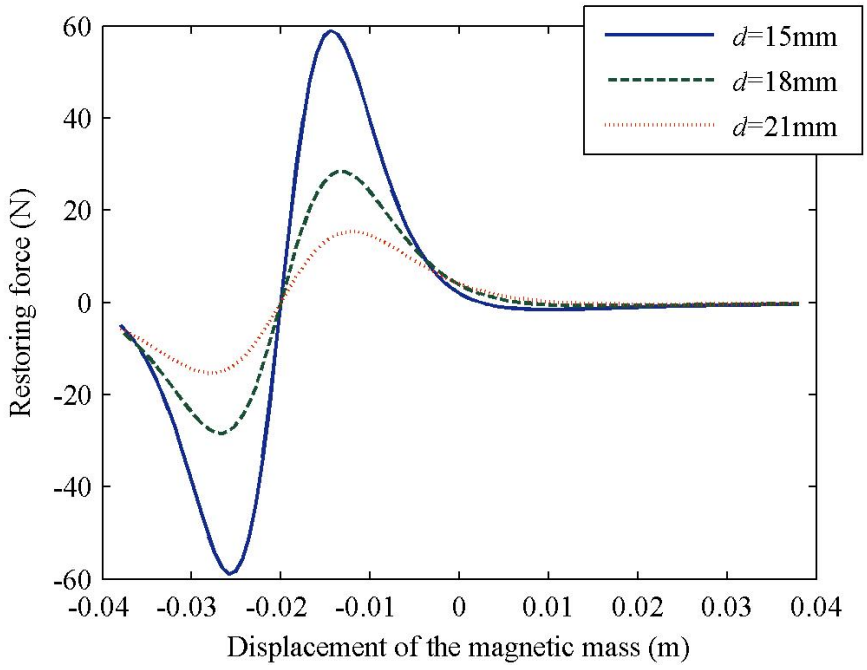

Figure 3.7. The restoring force plotted as a function of displacement of the movable magnet (h=21 mm).

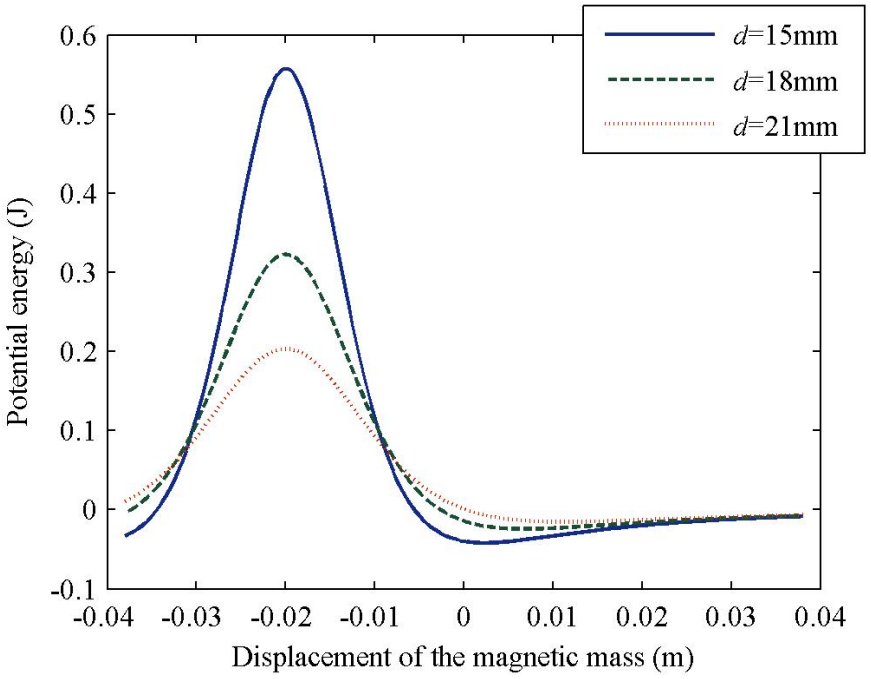

Figure 3.8. The potential energy plotted as a function of displacement of the movable magnet (h=21 mm).

The movable magnet can be regarded as the magnetic end mass on the cantilever, and the fixed magnet represents the top magnet or bottom magnet as shown in Figure 3.2. Using Equations (3.3) and (3.4), considering the effect of the bottom magnet and cantilever, and setting the distance d to be zero, the potential energy of the magnetic end mass can be expressed as

$$U_{Mb}(x) = -\frac{3\mu_0 v^2 M_f M_c}{4\pi}\left(\frac{1}{(h+x)^3}+\frac{1}{(h-x)^3}\right)-\frac{1}{2}k_c x^2 \tag{3.7}$$

where h is the vertical distance between the equilibrium position of the magnetic end mass and the top and bottom magnets.

The restoring forces are conventionally obtained from the negative of the spatial derivative of the potential energy, as follows

$$F_{Mb}(x)=\frac{3\mu_0 v^2 M_f M_c}{4\pi}\left(\frac{3}{(h-x)^4}-\frac{3}{(h+x)^4}\right)-k_c x \tag{3.8}$$

By choosing the same magnetisation strengths, the diameter and height of these three permanent magnets with same dimensions are chosen to be $20\,\text{mm}$ and $8\,\text{mm}$, respectively, which are also representative of the experimental system. The magnetic force and the beam elastic force can all be plotted against the magnetic mass displacement, as shown in Figure 3.9.

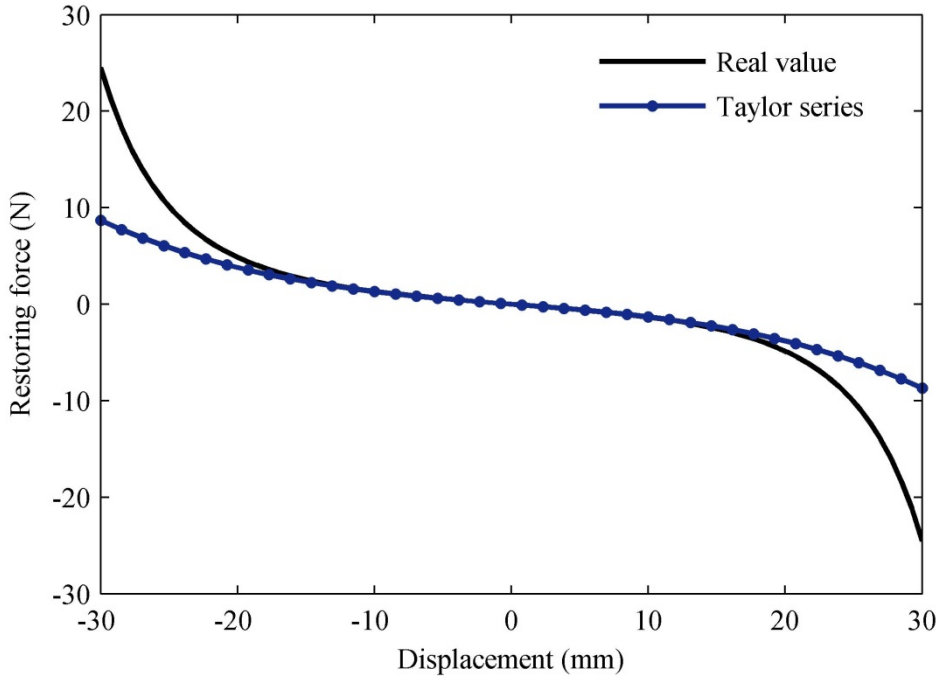

Figure 3.9. The restoring force plotted as a function of displacement of the magnetic end mass.

3.2.3 Tuning stiffness

This section describes the method of tuning the stiffness, and the analysis of charactering the response of the energy harvester to a wide range of frequencies for stiffness variations. In this paper, in order to investigate the influence of linear stiffness and nonlinear stiffness on the frequency response curve, respectively, the Taylor series is used to get the stiffness coefficients. Thus, Equation (3.8) can be expanded as

$$F_{Mb}(x) \approx -\frac{\mu_0 v^2 M_f M_c}{\pi}\left(\frac{12}{h^5}x + \frac{60}{h^7}x^3\right) - k_c x \tag{3.9}$$

Then the linear stiffness and the nonlinear stiffness coefficients can both be expressed as

$$k = \frac{12\mu_0 v^2 M_f M_c}{\pi h^5} + k_c \tag{3.10a}$$

and

$$\alpha = \frac{60\mu_0 v^2 M_f M_c}{\pi h^7} \tag{3.10b}$$

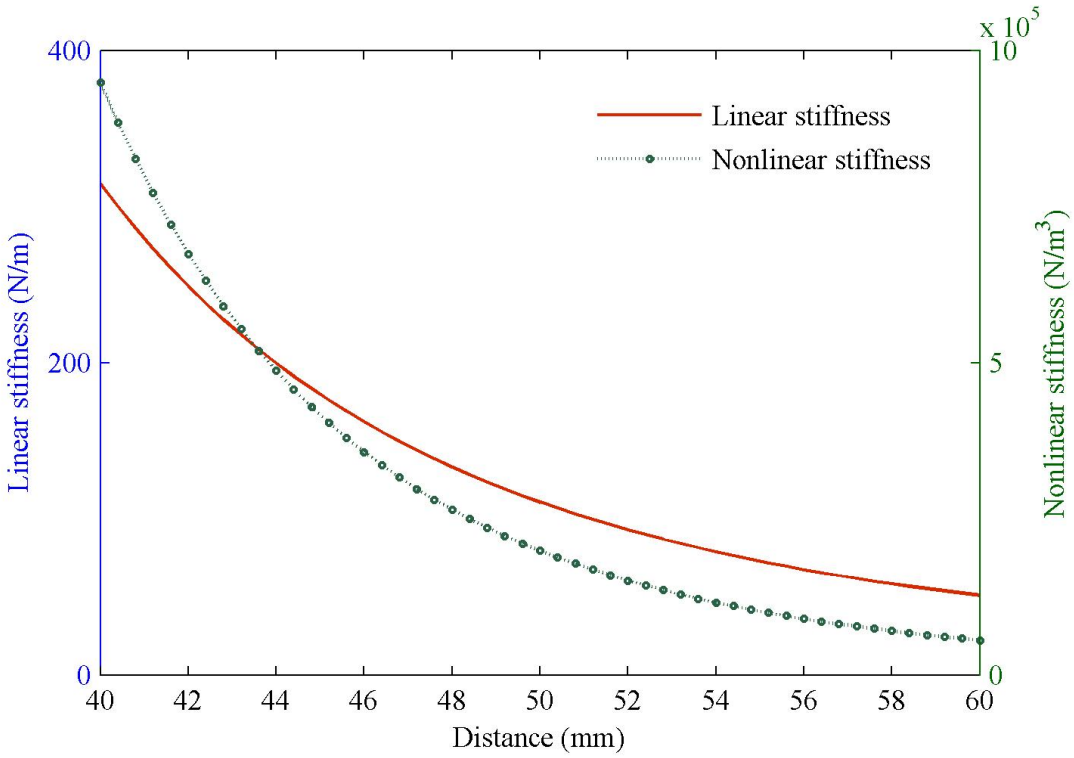

Figure 3.10. Linear stiffness and nonlinear stiffness as function of the distance between the magnetic end mass and the top magnet.

Table 3.1. Parameters used in the investigations of stiffness calculation.

Parameter	Value	Unit

M_f, M_c	9×10^5	A/m
μ_0	4×10^{-7}	H/m
v	2.8×10^{-6}	m^3
k_c	11.2	N/m

The restoring force calculated by the Taylor series is also presented in Figure 3.9. It can be seen that the error can be neglected when the displacement amplitude of the magnetic end mass is smaller than 20 mm. As shown in Equation (3.10), the nonlinear restoring force can enable both the linear stiffness and nonlinear stiffness to be tuned for changes in distance h. Figure 2.10 shows the relationship between the stiffness and the distance.

In order to find the influence of the stiffness variations on the frequency response, the frequency-amplitude relationship should be derived. As mentioned previously, the classical perturbation methods which can be quite accurate for predicting the jump-up frequency, but less so for the jumping down frequency under a strong nonlinearity [67]. The harmonic balanced method is used again to derive the frequency response-amplitude relationship when the electromechanical coupling is considered.

To derive the motion equation of the energy harvester coupled with the piezoelectric transducer. The model of the piezoelectric transducer is shown first.

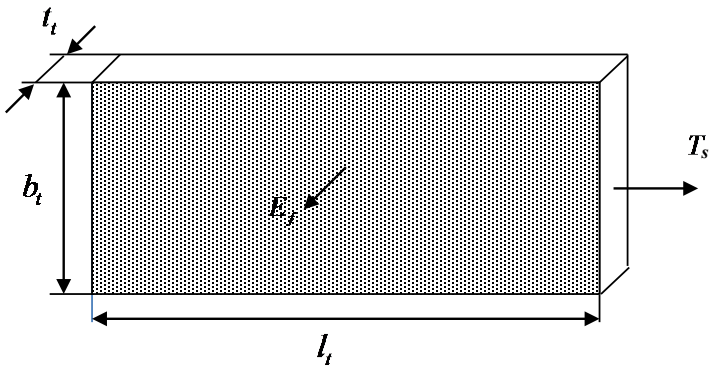

Figure 3.11 A laminar design piezoelectric transducer.

In a piezoelectric transducer, electric charge is generated by a displacement, while a force is produced when the voltage is applied. A constitutive equation for a uniaxial piezoelectric transducer whose piezoelectric material constant is d_{31} can be written as [90]

$$\begin{bmatrix} Q \\ S \end{bmatrix} = \begin{bmatrix} \varepsilon & d_{31} \\ d_{31} & s^E \end{bmatrix} \begin{bmatrix} E_f \\ T_s \end{bmatrix} \tag{3.11}$$

where Q, S, E_f, T_s are electrical displacement, strain, electric field and stress, respectively. The symbol ε represents permittivity under constant stress and s^E is the mechanical compliance of the material when the electric field is constant. Figure 3.11 illustrates a laminar design piezoelectric transducer. The length, width and thickness of the transducer are l_t, b_t, and t_t, respectively.

Then the constitutive equation can be written as

$$f = -D_{31} q \tag{3.12a}$$

and

$$-D_{31} y_t = \frac{q}{C} + V \tag{3.12b}$$

where f is the induced force by the piezoelectric transducer, q is the electrical charge, C is the capacitance of the piezoelectric film, y_t is the deflection of piezoelectric transducer, V is the voltage, and D_{31} is the piezoelectric constant of a transducer, and C and D_{31} can be defined as

$$\frac{1}{C} = \frac{1}{1-\kappa^2} \frac{t_t}{l_t b_t \varepsilon} \tag{3.12c}$$

$$D_{31} = -\frac{d_{31} b_t}{s^E C} \tag{3.12d}$$

where

$$\kappa = -\frac{|d_{31}|}{\sqrt{s^E \varepsilon}} \tag{3.12e}$$

Then, by introducing the harmonic excitation $F\cos\omega t$, the equation of motion for the piezoelectric energy harvester directing powering a resistive load can be written as

$$m\ddot{x} + c_m \dot{x} + kx + \alpha x^3 + \theta q = F\cos\omega t \tag{3.13a}$$

and

$$\theta x = \frac{q}{C} + R\dot{q} \tag{3.13b}$$

where m is the equivalent mass of the permanent magnet attached to the beam, c_m is the mechanical damping, $R = R_i + R_l$, and R_i and R_l are the internal and load resistances, and θ is the electromechanical coupling coefficient, which can be obtained by using D_{31} by considering the relationship between the deflection at the tip of the beam and the deflection of the piezoelectric transducer, it can be expressed as

$$\theta = pD_{31} \tag{3.14a}$$

where p is the ratio between the deflection of the piezoelectric transducer along the beam and the deflection of the tip of the beam in the x direction, and it is given as

$$p = \frac{y_t}{x} = \frac{\int_0^{l_t} \frac{t_b}{2} \frac{d^2 x_0(y,t)}{dy^2} dy}{x_0(l,t)} \tag{3.14b}$$

where l_t is the length of the piezoelectric transducer, and the l is the length of the beam, y is the horizontal location along the beam axis in Figure 3.1, and x_0 is the deflection formula for a cantilever beam at the first bend mode, it is shown as follows

$$x_0(y,t) = \left(\frac{3y^2}{2l^2} - \frac{y^3}{2l^3} \right) x(l,t) \tag{3.14c}$$

The model consists of a mechanical oscillator coupled to an electric circuit through a piezoelectric transducer. The equivalent electrical circuit model of the piezoelectric transducer is shown in Figure 3.12. It is a voltage source in series with its capacitance and resistance.

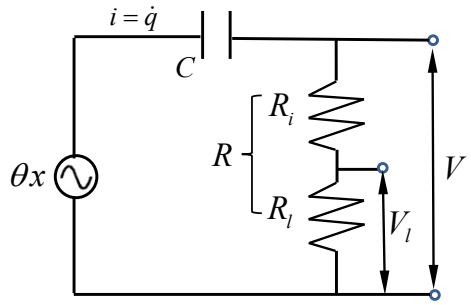

Figure 3.12. Equivalent electrical circuit of the piezoelectric transducer modelled as a voltage source.

Moreover, another kind of equivalent model is the piezoelectric transducer can be regarded as a current source, it can be obtained by the transformation of Equation (3.11b) as follows.

Multiplying both sides of Equation (3.13b) by capacitance C gives

$$\theta C x = q + CR\dot{q} \tag{3.15}$$

Then, Equation (3.15) can be written as

$$\theta C x = q + CV \tag{3.16}$$

where $V = R\dot{q}$ is the induced voltage. Taking the derivative of each term in Equation (3.16) with respect to the time, it can be written as

$$\theta C\dot{x} = \dot{q} + C\dot{V} \tag{3.17}$$

Equation (3.17) can be further repressed as

$$\theta C\dot{x} = \frac{V}{R} + C\dot{V} \tag{3.18}$$

Equations (3.13b) and (3.18) represent the same model but with different methods of expression. In Equation (3.13b), the piezoelectric transducer is regarded as a voltage source, while it is expressed as a current source in Equation (3.18). The corresponding electrical circuit is show in Figure 3.13.

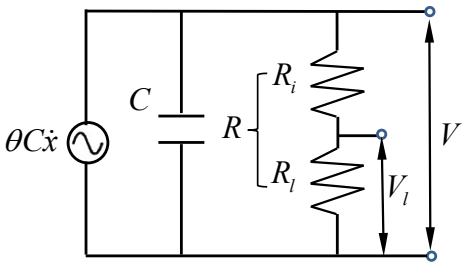

Figure 3.13. Equivalent electrical circuit of the piezoelectric transducer modelled as a current source.

In references [32][42][59][91], the expression of Equation (3.18) was adopted to model the piezoelectric nonlinear energy harvester.

Thus, the equation of motion for the piezoelectric energy harvester directing powering a resistive load can be re-written as

$$m\ddot{x} + c_m\dot{x} + kx + \alpha x^3 + \theta CV = F\cos\omega t \tag{3.19a}$$

and

$$\theta C\dot{x} = \frac{V}{R} + C\dot{V} \tag{3.19b}$$

In order to explain how the piezoelectric operates in the mechanical system, Equation (3.18b) can be repressed s

$$\boldsymbol{V} = \frac{\theta s}{s + 1/RC}\boldsymbol{X} \tag{3.20}$$

where s is Laplace transform, and $\boldsymbol{V}$ and X are the Laplace transform of V and x. Now, it can be seen that the piezoelectric transducer operates as an electrical damping related to the velocity and a spring element when the electrical circuit is connected and disconnected, respectively.

It is assumed that the higher order harmonics are negligible and the steady state solution of Equations (3.19a) and (3.19b) can be modelled as

$$x = a_1\sin\omega t + b_1\cos\omega t \tag{3.21a}$$

and

$$V = a_2 \sin \omega t + b_2 \cos \omega t \tag{3.21b}$$

Then

$$\dot{x} = a_1 \omega \cos \omega t - b_1 \omega \sin \omega t \tag{3.22a}$$

$$\dot{V} = a_2 \omega \cos \omega t - b_2 \omega \sin \omega t \tag{3.22b}$$

and

$$\ddot{x} = -a_1 \omega^2 \sin \omega t - b_1 \omega^2 \cos \omega t \tag{3.22c}$$

Substituting Equations (3.21), (3.22) into Equation (3.19a), collecting coefficients with the same structure and neglecting the high order items, it gives

$$b_1 Q_a + Q_b a_1 - \theta C b_2 = F \tag{3.23a}$$

and

$$a_1 Q_a - Q_b b_1 - \theta C a_2 = 0 \tag{3.23b}$$

where

$$Q_a = k - m\omega^2 + \frac{3\alpha}{4} X^2 \tag{3.23c}$$

$$Q_b = c_m \omega \tag{3.23d}$$

Similarly, substituting the steady state solutions of Equations (3.21b) and (3.22) into Equation (3.19b), it is given that

$$a_2 = \frac{\theta C \omega \left(-b_1 / R + C \omega a_1 \right)}{1/R^2 + C^2 \omega^2} \tag{3.24a}$$

and

$$b_2 = \frac{\theta C\omega\left(a_1/R + C\omega b_1\right)}{1/R^2 + C^2\omega^2} \tag{3.24b}$$

By and squaring and adding Equations (3.23a) and (3.23b), it can be obtained as

$$Q_a X^2 + Q_b X^2 + \left(\theta C\right)^2 V^2 - 2\theta C a_2\left(Q_a a_1 - Q_b b_1\right) - 2\theta C b_2\left(Q_a b_1 - Q_b a_1\right) = F^2 \tag{3.25a}$$

where

$$X^2 = a_1^2 + b_1^2 \tag{3.25b}$$

$$V^2 = a_2^2 + b_2^2 = \frac{\left(\theta\omega X\right)^2}{\omega^2 + 1/R^2C^2} \tag{3.25c}$$

Substituting Equation (3.24) into Equation (3.25), the items of $a_1 b_1$ can be cancelled. Then by adding the items of a_1^2 and b_1^2 using Equation (3.25b), Equation (3.25a) can be expressed by an algebraic equation about X as

$$X^2\left[\left(k - m\omega^2\right)\left(1 - \frac{\theta^2 C}{m\left(\omega^2 + 1/R^2C^2\right)}\right) + \frac{3}{4}\alpha X^2\right]^2$$

$$+\left[c_m + \frac{\theta^2}{R\left(\omega^2 + 1/R^2C^2\right)}\right]^2 \omega^2 X^2 = F^2 \tag{3.26}$$

Equation (3.26) represents the equation for the steady-state motion of the piezoelectric energy harvesters.

Moreover, Equation (3.25c) can be rewritten as

$$V = \frac{\theta}{\sqrt{1 + 1/\omega^2 R^2 C^2}} X \tag{3.27a}$$

The physical interpretation is the induced voltage by the piezoelectric material cannot be completely delivered to the resistance because of the existence of the capacitance. From Equation (3.27a), it can be noted that the delivered voltage on the resistance increases with the increasing of the excitation frequency because of the high-frequency-pass property of the capacitance.

Equation (3.27b) can also be rearranged as

$$V = \frac{\theta}{\sqrt{\omega^2 + \frac{1}{R^2 C^2}}} \omega X \tag{3.27b}$$

It can be found that Equation (3.27b) expresses the induced voltage on the resistance and the velocity amplitude of the seismic mass, which is similar to the inductive model. Therefore, the equivalent electromechanical constant related to the velocity can be written as

$$\phi = \frac{\theta}{\sqrt{\omega^2 + \frac{1}{R^2 C^2}}} \tag{3.28}$$

It should be mentioned that the coupling between the oscillator and the piezoelectric transducer also has influence on the frequency response curve of the energy harvester. The standard form of the frequency response curve without the consideration of the electromechanical coupling can be expressed as

$$X^2 \left[\left(k - m\omega^2 \right) + \frac{3}{4} \alpha X^2 \right]^2 + {c_m}^2 \omega^2 X^2 = F^2 \tag{3.29}$$

By comparing Equations (3.26) and (3.29), it can be found that the piezoelectric transducer can be regarded as an electrical damping item from the second term on the left side of the equations. For the first item on the left side, it has little influence on the frequency response because the fact that $\theta^2 C \Big/ \left(m\omega^2 + m \Big/ R^2 C^2 \right) \ll 1$.

Table 3.2 shows the parameters which were used to investigate the influence of stiffness on the frequency response, which will be used for the experiments. It should be mentioned that the proportion between the displacement of the magnetic end mass and the deflection of the piezoelectric film is considered for calculating the coupling coefficient θ.

Table 3.2. Parameters used in the investigations of stiffness on the frequency response.

Parameter	Value	Unit
m	0.022	kg
c_m	0.008	Ns/m
θ	645	V/m
C	110	nF
R_i	115	KΩ
F	0.06	N
ω	11.2	Hz

As shown in Equation (3.10), the stiffness can be tuned by increasing or decreasing the distance between the permanent magnets. To illustrate this for energy harvesting considerations, a series of frequency-relative velocity amplitude curves under different stiffness are presented in Figure 3.14, according to Equation (3.26). While Figures 3.14(a) and 3.14(b) show the independent influence of the linear stiffness and the nonlinear stiffness on the frequency response respectively, Figure 3.14(c) depicts the effect of varying the distance *h*. It should be mentioned that Mann [29] compared the relative velocity responses of the hardening-type monostable device with a linear device with similar parameters.

An observation is that the response for both systems scales almost linearly within the regime of low level amplitude of excitations. In this study, the case that the nonlinearities are sufficiently engaged is discussed.

Variations in the linear stiffness have an influence on both the jump-up and jump-down

frequency. By increasing the linear stiffness, the frequency response curve shows a movement to the right. Varying the value of the nonlinear stiffness, a similar tendency is observed. For the practical experimental system, Figure 3.14(c) is used to illustrate the process of triggering the jump. It is assumed that the energy harvester is oscillating at point A, which is located on the low-energy orbit, and then by starting to decrease the distance between the permanent magnets, the operating point moves slowly to the jump up point. A further decrease in the distance h, shows that the frequency of the excitation will exceed the jump up frequency. Hence, the operating point jumps to B. The oscillator is now operating in the desirable orbit. However, variation of the stiffness also decreases the amplitude of the response. So following the high-energy orbit mean that the operating point moves to C by increasing the distance h.

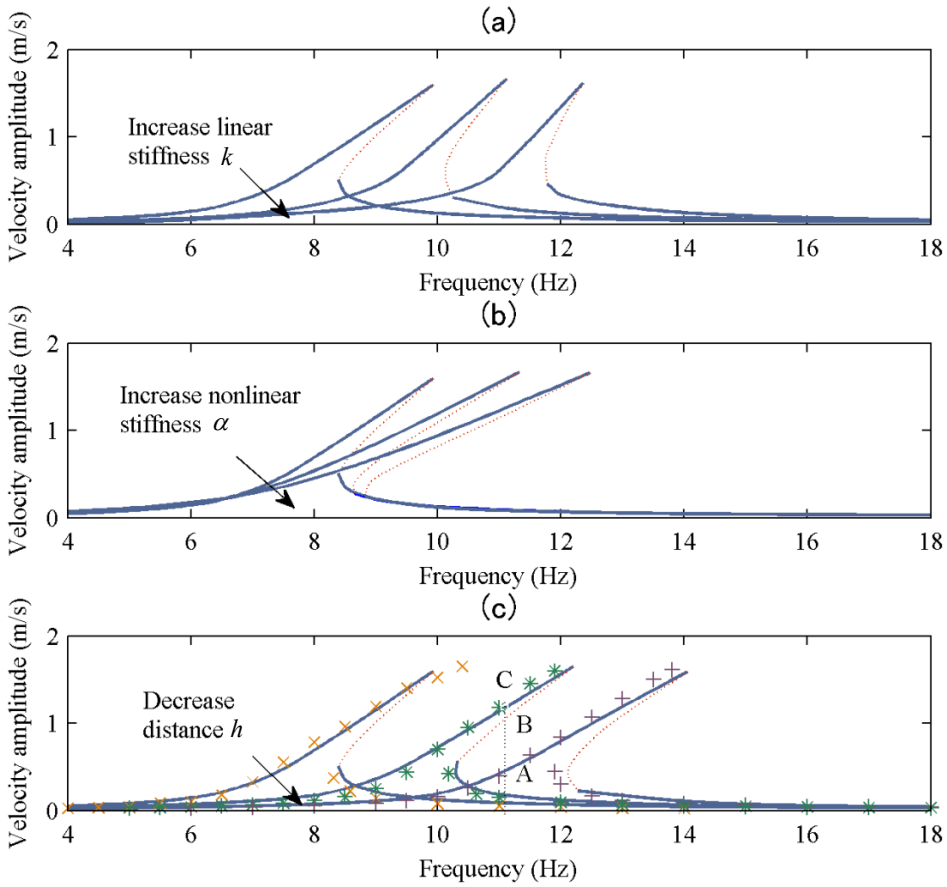

Figure 3.14. Influence of the stiffness on the frequency response curve: (a) k = [50.3, 77.5, 109] N/m versus h = [60, 54, 50] mm and $\alpha = 5.44\times10^4$ N/m^3, (b) k = 50.3 N/m and α = [5.44×10^4, 1.14×10^5, 1.95×10^5] N/m^3 versus h = [60, 54, 50] mm, and (c) h = [60, 54, 50] mm versus k = [50.3, 77.5, 109] N/m and α = [5.44×10^4, 1.14×10^5, 1.95×10^5] N/m^3 (solid lines: stable solutions, and unstable solutions: dashed lines; Scatter points: experimental results).

Moreover, the scatter points in Figure 3.14(c) represent the experimental results for comparing with the theoretical frequency response curve. Figures 3.15(a) and 3.15(b) show the time domain experimental results when the distance h is chosen to be 60 mm. A base acceleration of 2.7 m/s^2 was used so that multiple periodic attractors could appear, and it is same as the excitation amplitude for the numerical simulation. In Figure 3.15(a)，the excitation frequency starts from 4 Hz, and with the upward frequency sweep of 0.03 Hz/s to 14 Hz, which corresponds to Figure 3.15 (c), where the horizontal axis is re-expressed using frequency.

Similarly, in Figure 3.15(b), the excitation frequency starts from 14 Hz with the downwards frequency sweeps of 0.03 Hz/s to 4 Hz, which corresponds the results shown in Figure 3.15(d).

From the results presented in Figures 3.15(c) and 3.15(d). The experimental scatter data for the case of the distance h is set to be 60 mm shown in Figure 3.14(c) can be obtained by using the response amplitude data at different frequencies. Similarly, in Figure 3.14(c), the experimental scatter data when h is set to be 54 mm and 50 mm can be obtained from Figures 3.16 and 3.17, respectively.

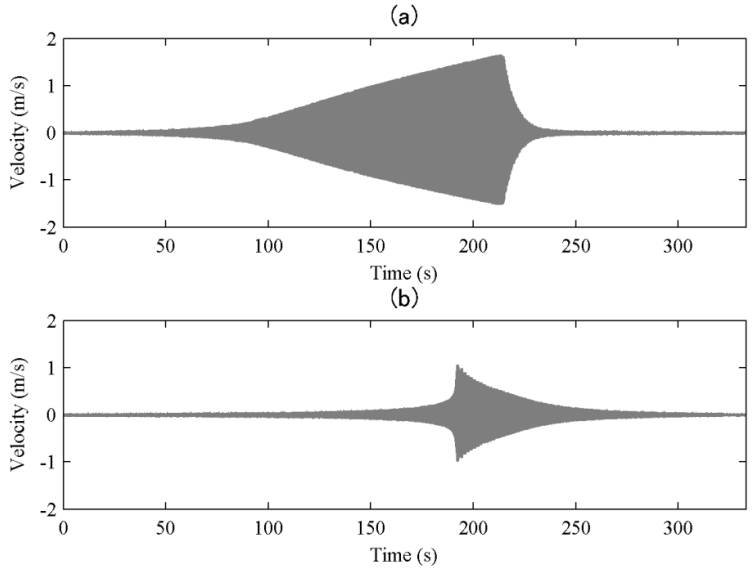

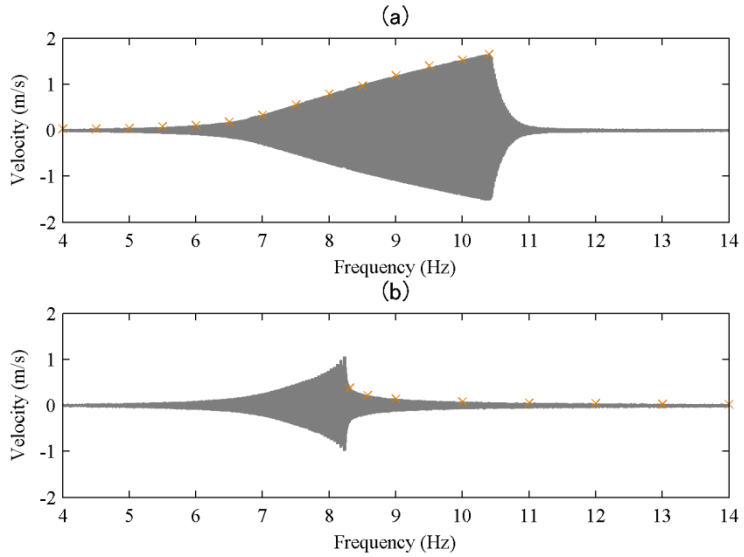

Figure 3.15. Experimental velocity responses under the excitation amplitude of 2.7 m/s^2 when the magnets distance h is 60 mm: (a) the time domain data when the excitation frequency linearly increased at the rate of 0.03 Hz/s, (b) the time domain data when the excitation frequency linearly decreased at the rate of 0.03 Hz/s, (c) the relationship between the excitation frequency and the response amplitude when the excitation frequency linearly increased at the rate of 0.03 Hz/s, and (d) the relationship between the excitation frequency and the response amplitude when the excitation frequency linearly decreased at the rate of 0.03 Hz/s. (The marked points corresponds to the scatter data in Figure 3.14(c)).

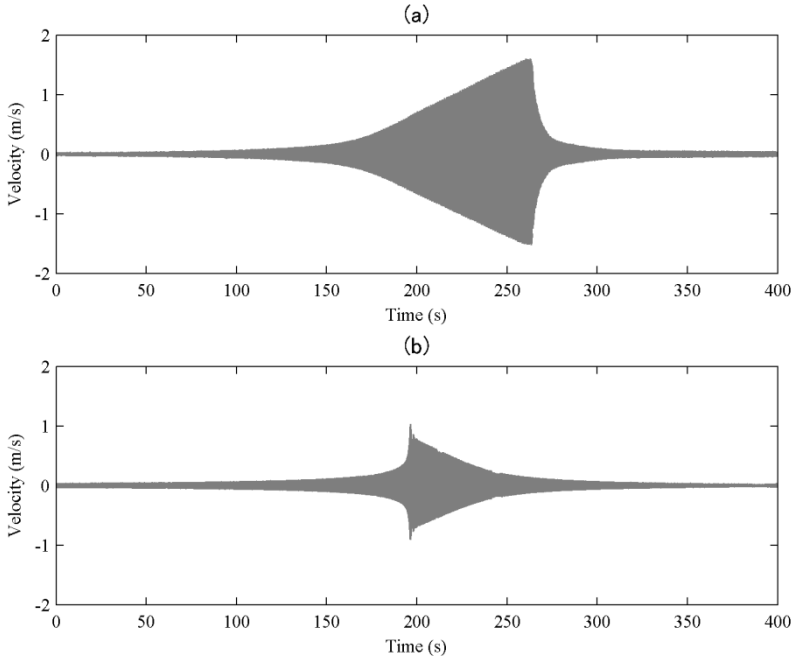

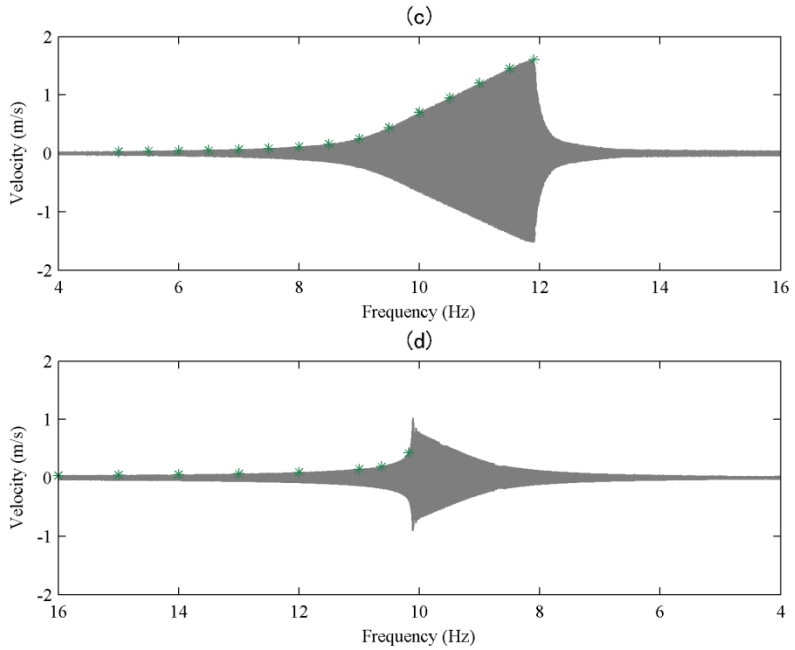

Figure 3.16. Experimental velocity responses under the excitation amplitude of 2.7 m/s^2 when the magnets distance h is 54 mm: (a) the time domain data when the excitation frequency linearly increased at the rate of 0.03 Hz/s, (b) the time domain data when the excitation frequency linearly decreased at the rate of 0.03 Hz/s, (c) the relationship between the excitation frequency and the response amplitude when the excitation frequency linearly increased at the rate of 0.03 Hz/s, and (d) the relationship between the excitation frequency and the response amplitude when the excitation frequency linearly decreased at the rate of 0.03 Hz/s. (The marked points corresponds to the scatter data in Figure 3.14(c)).

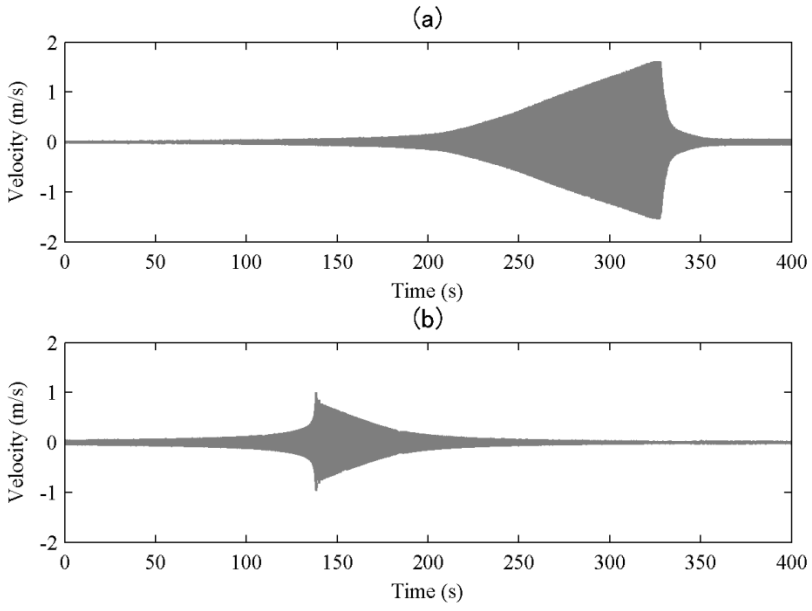

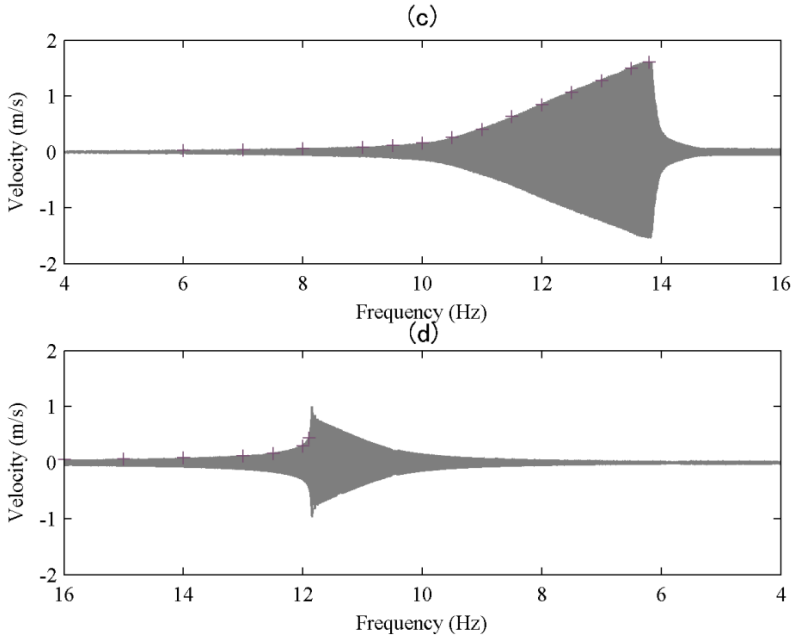

Figure 3.17. Experimental velocity responses under the excitation amplitude of 2.7 m/s^2 when the magnets distance h is 50 mm: (a) the time domain data when the excitation frequency linearly increased at the rate of 0.03 Hz/s, (b) the time domain data when the excitation frequency linearly decreased at the rate of 0.03 Hz/s, (c) the relationship between the excitation frequency and the response amplitude when the excitation frequency linearly increased at the rate of 0.03 Hz/s, and (d) the relationship between the excitation frequency and the response amplitude when the excitation frequency linearly decreased at the rate of 0.03 Hz/s. (The marked points corresponds to the scatter data in Figure 3.14(c)).

To trigger a jump to the high-energy orbit, the dimensional jump-up frequency ω_u should be higher than the excitation frequency ω.

Rewriting Equation (2.16) with the dimensional form of the jump-up frequency as

$$\omega_u = \sqrt{1+\frac{3}{2}\left(\frac{3\alpha F^2}{2k^3}\right)^{\frac{1}{3}}} \tag{3.30}$$

Substituting Equations (3.10) into Equation (3.30), it gives

$$\omega_u = \left(\frac{1}{m}\left(\frac{12\mu_0 v^2 M_f M_c}{\pi h^5}+\left(\frac{3}{2}\right)^{\frac{4}{3}}\left(\frac{12F^2\mu_0 v^2 M_f M_c}{\pi h^7}\right)^{\frac{1}{3}}\right)\right)^{\frac{1}{2}} \tag{3.31}$$

and

$$\omega_u > \omega \tag{3.32}$$

As mentioned previously, after the operating point jumps to the high-energy orbit, it is necessary to increase the distance between the magnets to make it moves toward to the peak response point, rewriting Equation (2.14) with the dimensional form of the jump-down frequency as

$$\omega_d = \sqrt{\frac{1}{2}\left(\sqrt{1+\frac{3m\alpha F^2}{k^2c^2}}\right)+1} \tag{3.33}$$

By substituting Equations (3.10) into Equation (3.33), the corresponding jump-down frequency can be written as

$$\omega_d = \left(\frac{6\mu_0 v^2 M_f M_c}{\pi m h^5}\left(1+\left(1+\frac{5\pi m F^2 h^3}{3\mu_0 c^2 v^2 M_f M_c}\right)^{\frac{1}{2}}\right)\right)^{\frac{1}{2}} \tag{3.34}$$

and

$$\omega_d \geq \omega \tag{3.35}$$

It is still necessary to estimate the consumed energy for the tuning process. When the distance between the permanent magnets decreases, part of the electrical energy is transfer into the potential energy, which can be expressed as

$$E_c = \frac{3\mu_0 v^2 M_f M_c}{32\pi\eta}\left(\frac{1}{h^3}-\frac{1}{h_0^3}\right) \tag{3.36}$$

where h_0 is half of the original distance between the top and bottom magnets, and η is the electric-to-mechanical conversion efficiency.

3.2.4 Power delivered to the load resistance

A primary interest is the electrical power delivered to the electrical load. An expression for the power is derived in this section.

Using Equation (3.27a), the stable response voltage across the load resistance can be expressed as

$$V_l = \frac{R_l}{R_i + R_l} V = \frac{R_l \theta}{\sqrt{\omega^2 \left(R_i + R_l\right)^2 + \frac{1}{C^2}}} \omega X \tag{3.37}$$

Then the power amplitude delivered to the load resistance can be written as

$$P = \frac{V_l^2}{R_l} = \frac{R_l \theta^2}{\omega^2 \left(R_i + R_l\right)^2 + 1/C^2} \omega^2 X^2 \tag{3.38}$$

3.2.5 Numerical simulation

The parameters of a hardening-type energy harvester shown in Table 6.2 are used to conduct the numerical simulation, which are also representative of the experimental parameters. An array of numerical simulation was performed to validate the theoretical predictions, the harmonic excitation amplitude and excitation frequency is kept constant while changing both the stiffness and nonlinear stiffness of the system.

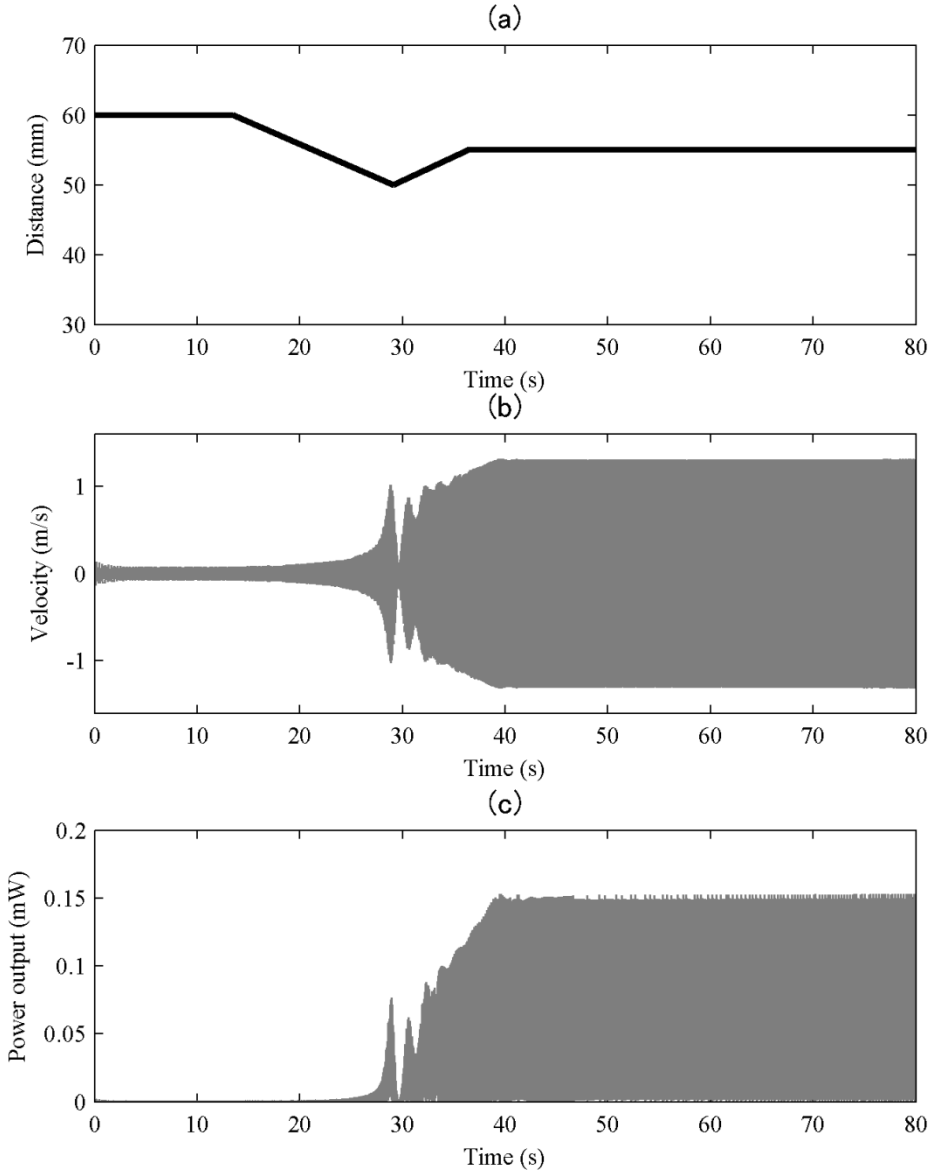

Figure 3.18. Influence on the responses for energy harvesting by tuning the stiffness under constant excitation: (a) the changing of the distance between the magnets, (b) the velocity response of the magnetic end mass, and (c) the power delivered to the load resistance.

Figures 3.18 (a) shows the variation of the distance between the magnetic end mass and the bottom magnet during the tuning process, which is equivalent to the tuning of the distance between the magnetic end mass and the top or bottom magnet and it corresponds to the changing of the frequency response curve shown in Figure 3.14.

Figure 3.18(b) presents the influence of the changing of stiffness on the responses of velocity of the magnetic end mass. It can be observed that the energy harvester is operated on the low-energy orbit at first, and then jump to the branch with higher solutions with the increasing

of the stiffness. The response amplitude shows a continuous decrease tendency if the stiffness is further increased. Conversely, the operating point moves towards to the peak response point on the high-energy orbit with the decreasing of the stiffness. The power delivered to the load resistance of $51K\Omega$ is presented in Figure 3.18(c).

3.2.6 Experimental validation of stiffness tunable harvester

- Instrumentation and measurement

A laboratory scale experimental device has been designed and manufactured to illustrate the theory described previously. A photograph of the experimental rig is shown in Figure 3.19. The energy harvester is mounted on an IMV m060 modal shaker to provide harmonic base excitations. The accelerometer can be attached to the table of the shaker to measure its acceleration. The displacement of the bottom permanent magnets and velocity of the magnetic end mass are measured by a laser displacement sensor and a directly mounted velocity micro-sensor.

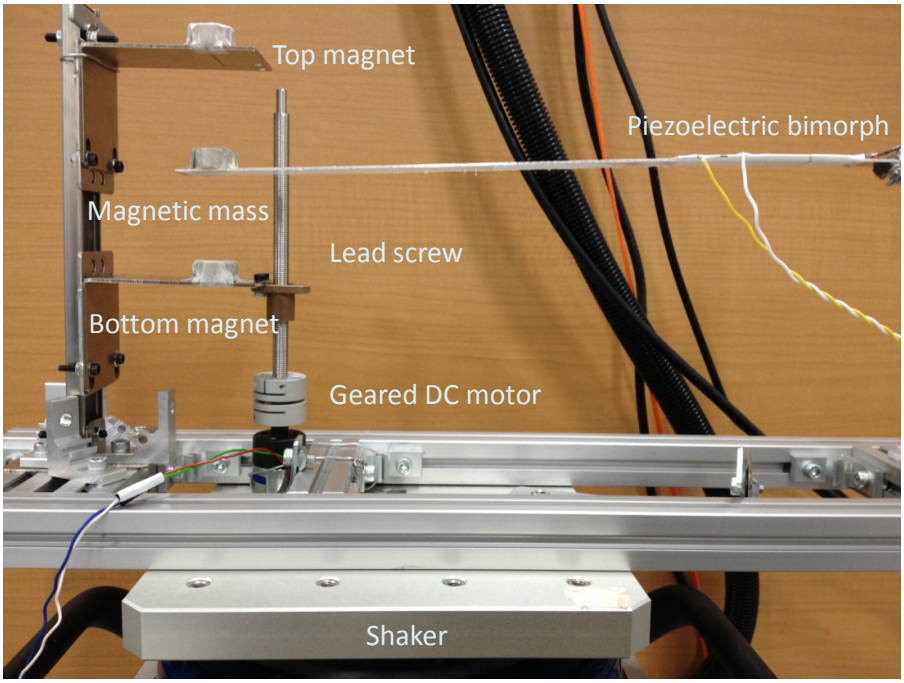

Figure 3.19. Photograph of the experimental system.

- Experimental results

The experimental tests was performed to compare the experimental behavior and theoretical predictions, the permanent magnets distance of the energy harvester is tuned with no variation of the excitation frequency and amplitude. The initial distance h is chosen to be $60\,\text{mm}$.

The experimental test results are displayed in Figure 3.20. It shows the influence on the responses for energy harvesting by tuning the stiffness under the harmonic excitation with the acceleration amplitude of 2.7 m/s^2, where the frequency of the excitation is 11.2 Hz and held constant. It can be noted that the excitation frequency is higher than the jump-down frequency. The variations of *h*, the velocity of the magnetic end mass and the power delivered to the load resistance of $51\text{K}\Omega$ are presented, respectively. It is noted that a jump from the low-energy orbit to the high-energy orbit can be triggered by tuning the stiffness of the energy harvester.

The finally stabilised responses in Figure 3.20 and compared with the numerical simulation results in Figure 3.18, where the black color represents the experimental results and the light blue color represents the simulation results. It can be noted that the experimental results meet the simulation well. An index shown in Equation (3.39) for the quantitative comparison between the numerical and experimental results:

$$Index = \frac{\sqrt{\frac{1}{T_0}\int_0^{T_0}\left[\upsilon(t)-\overline{\upsilon}(t)\right]^2 dt}}{\sqrt{\frac{1}{T_0}\int_0^{T_0}\upsilon(t)^2 dt}} \tag{3.39}$$

where υ is the numerical simulation, $\overline{\upsilon}$ is the experimental data, and T_0 is the selected length of time. The calculated error of the velocity is 4.3% by using the stabilised data in Figures 3.20(b) and 3.20(c). Similarly, the error for the delivered power is estimated to be 6.7% by form Figures 3.20(d) and 3.20(e).

Moreover, it can be noted that the jump-up phenomenon occurs when the distance between the permanent magnets is around 51 mm, which corresponds to the estimation results using Equation (3.31). It is a little earlier than the experimental results because of the estimation error of the interaction force between the permanent magnets.

If the electric-to-mechanical energy conversion is chosen to be 0.8, the consumed energy during the distance decreasing process is estimated to be around 0.0026 J by using Equation (3.36). The mean delivered power to the load resistance is about 0.11 mW after it is stabilised on

the high-energy orbit, which indicts the required time for compensating for the consumed energy is around 24 s.

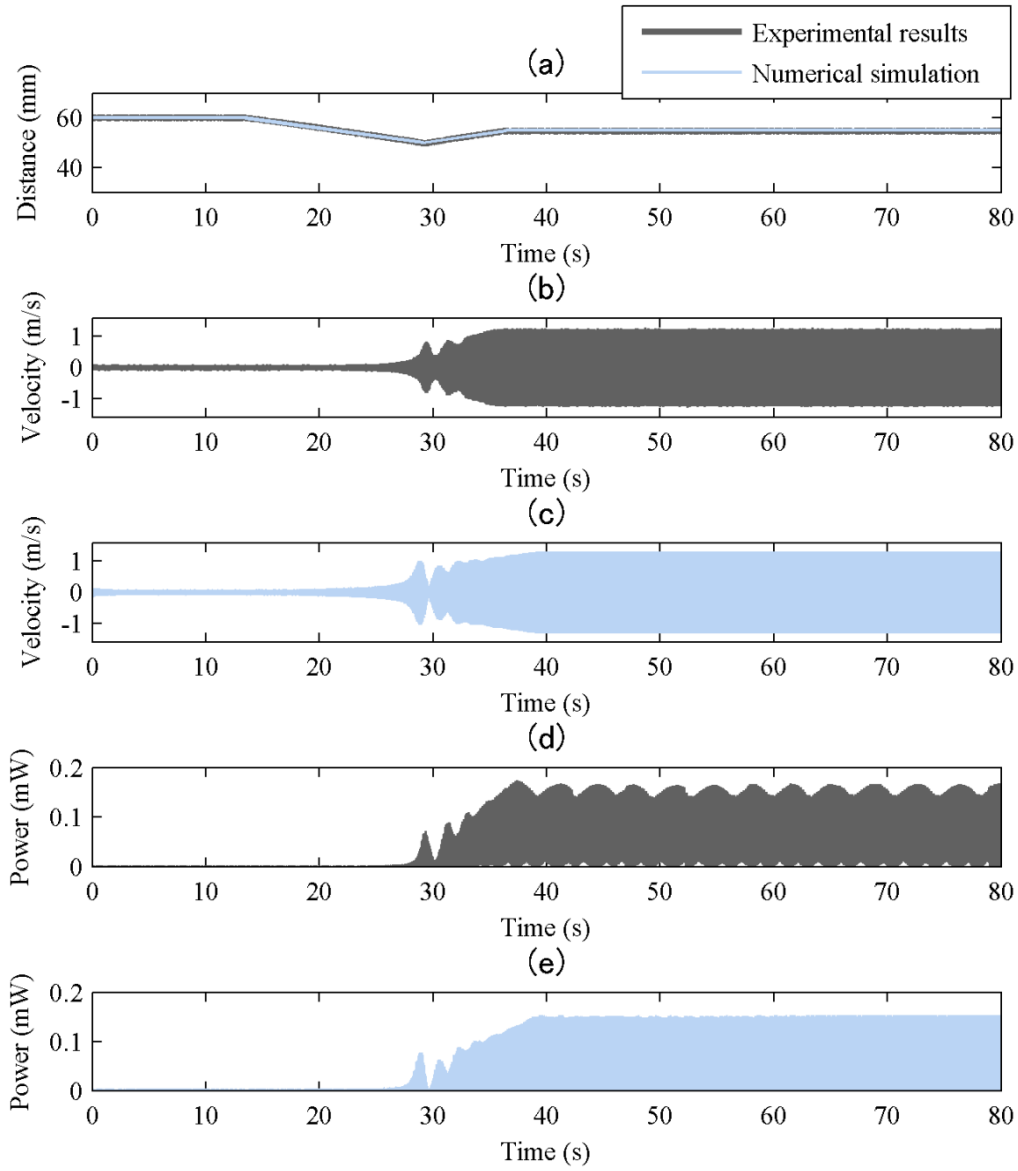

Figure 3.20. Influence on the responses for energy harvesting by tuning the stiffness under constant excitation: (a) the distance between the equilibrium position of magnetic end mass and the bottom magnet, (b) the experimental velocity response of the magnetic end mass, (c) the numerically obtained velocity response of the magnetic end mass (d) the experimental power delivered to the load resistance. (e) the numerical obtained power delivered to the load resistance.

3.3 Damping tuning method

3.3.1 Apparatus illustrations

A schematic diagram for an energy harvester is shown in Figure 3.21. It is composed of two linear springs connected in series, with two dampers in parallel with the springs, and a third order nonlinear spring. It should be noted that the model is a one-degree-of-freedom system because the linear springs are connected at a node which is an effectively massless point. The equivalent linear stiffness of the system can be tuned by adjusting the damping coefficient of controllable damper c_2. The right side of the Figure 3.21 shows the electrical circuit for tuning the damping level c_2. If a linear DC motor is adopted to achieve the required relatively high damping level for the tuning process, the dimension of the device might become impractically large. A transmission mechanism, e.g. ball screw or gear rack, and a micro DC motor can be used as an alternative. Thus the linear motion of the mass can be transferred into the rotational motion of the motor, and the damping level is also amplified. The damping can be changed by tuning the load resistance of the circuit. It can be noticed that different from the directly mechanical tuning method which needs extra energy consumption, electrical energy still can be harvested during the tuning process.

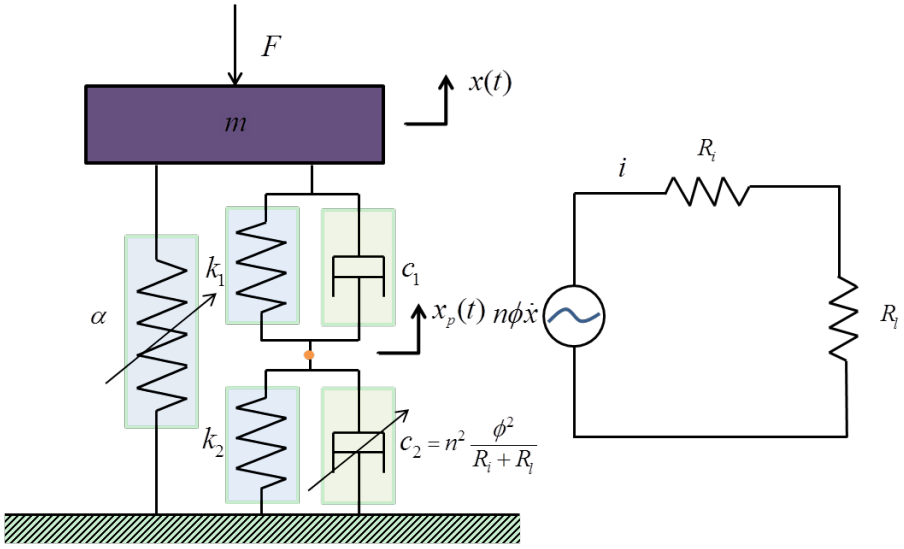

Figure 3.21. Schematic diagram of the stiffness, tunable, hardening-type energy harvester.

3.3.2 Model of the energy harvester

The governing equations for the motion of the system shown can be stated as

$$m\ddot{x} = -k_2\left(x - x_p\right) - c_2\left(\dot{x} - \dot{x}_p\right) - \alpha x^3 + F_0 \cos\omega t \tag{3.40a}$$

$$k_1 x_p + c_1 \dot{x}_p = k_2\left(x - x_p\right) + c_2\left(\dot{x} - \dot{x}_p\right) \tag{3.40b}$$

where m is the mass, k_1, k_2 are the linear stiffness coefficients of the springs and c_1, c_2 are the damping shown in Figure 3.21. x and x_p are the displacements of the mass and the connection point of the springs, respectively, α is the nonlinear stiffness coefficient. The single frequency harmonic excitation is given by $F\cos\omega t$.

The harmonic balance method is applied to generate the responses. The harvester response is presumed to be accurately modelled by a truncated Fourier series, where the number of terms dictates the accuracy of the intended solution [92]. This type of motion maintains a dominant fundamental frequency at the frequency of excitation. Hence, Equations (3.40a) and (3.40b) can represent the assumed Fourier series expansion of the displacements of the mass, and connection point, respectively.

$$x = A_1 \sin\omega t + B_1 \cos\omega t \tag{3.41a}$$

$$x_p = A_2 \sin\omega t + B_2 \cos\omega t \tag{3.41b}$$

where $X^2 = A_1^2 + B_1^2$ and $X_p^2 = A_2^2 + B_2^2$. X and X_p therefore represent the corresponding displacement amplitudes. Equations (3.41a) and (3.41b), and the time derivatives, are substituted into Equations (3.40a) and (3.40b). It should be mentioned that for convenient derivation, the third order item is neglected first. Equating the coefficients of the harmonic terms $\cos\omega t$ and $\sin\omega t$, four equations are obtained as follows

$$k_1 A_2 - c_1 B_2 \omega = k_2\left(A_1 - A_2\right) - c_2\left(B_1 - B_2\right)\omega \tag{3.42a}$$

$$k_1 B_2 - c_1 A_2 \omega = k_2\left(B_1 - B_2\right) - c_2\left(A_1 - A_2\right)\omega \tag{3.42b}$$

$$-mA_1\omega^2 + k_2\left(A_1 - A_2\right) - c_2\left(B_1 - B_2\right)\omega = 0 \tag{3.42c}$$

$$-mB_1\omega^2 + k_2\left(B_1 - B_2\right) + c_2\left(A_1 - A_2\right)\omega = F \tag{3.42d}$$

Equations (3.42a) and (3.42b) are solved in terms of A_2 and B_2, then substituted into Equations (3.42c) and (3.42d). The latter are squared and summed to produce the following equation as

$$\left\{\left[\frac{k_1^2k_2 + k_2^2k_1 + \left(c_1^2k_2 + c_2^2k_1\right)\omega^2}{\left(k_1 + k_2\right)^2 + \left(c_1 + c_2\right)^2\omega^2} - m\omega^2\right]^2 + \left[\frac{k_1^2c_2 + k_2^2c_1 + \left(c_2^2c_1 + c_1^2c_2\right)\omega^3}{\left(k_1 + k_2\right)^2 + \left(c_1 + c_2\right)^2\omega^2}\right]^2\right\}X^2 = F^2 \tag{3.43}$$

From Equation (3.43), the equivalent linear stiffness and equivalent damping can be expressed as

$$k_{eq} = \frac{k_1k_2\left(k_1 + k_2\right) + \left(c_1^2k_2 + c_2^2k_1\right)\omega^2}{\left(k_1 + k_2\right)^2 + \left(c_1 + c_2\right)^2\omega^2} \tag{3.44a}$$

$$c_{eq} = \frac{k_1^2c_2 + k_2^2c_1 + c_1c_2\left(c_1 + c_2\right)\omega^2}{\left(k_1 + k_2\right)^2 + \left(c_1 + c_2\right)^2\omega^2} \tag{3.44b}$$

For the equivalent model of the system, the corresponding relationship between the frequency and amplitude of the response can be given as [64]

$$\begin{aligned}&\frac{9}{16}\alpha^2X^6 + \frac{3}{2}\alpha\left[\frac{k_1^2k_2 + k_2^2k_1 + \left(c_1^2k_2 + c_2^2k_1\right)\omega^2}{\left(k_1 + k_2\right)^2 + \left(c_1 + c_2\right)^2\omega^2} - m\omega^2\right]X^4 \\ &+\left\{\left[\frac{k_1^2k_2 + k_2^2k_1 + \left(c_1^2k_2 + c_2^2k_1\right)\omega^2}{\left(k_1 + k_2\right)^2 + \left(c_1 + c_2\right)^2\omega^2} - m\omega^2\right]^2 + \left[\frac{k_1^2c_2 + k_2^2c_1 + \left(c_2^2c_1 + c_1^2c_2\right)\omega^3}{\left(k_1 + k_2\right)^2 + \left(c_1 + c_2\right)^2\omega^2}\right]^2\right\}X^2 = F_0^2\end{aligned} \tag{3.45}$$

A set of physically reasonable parameters used for simulation is shown in Table 3.3, where ϕ, n and R_i are back EMF constants, transmission ratio and internal resistance of the DC motor, respectively. This data is also used for the numerical examples afterwards.

Table 3.3. Parameters of the vibrational energy harvester.

Parameter	m	c_1	k_1	α	F	ω	n	ϕ	R_i
Value	1kg	1 Nm/s	1000 N/m	2.45×10^6 N/m^3	1N	5.2Hz	6283	0.003 Vs/rad	6Ω

The equivalent stiffness and damping coefficients as functions of c_2 and the stiffness coefficient ratio k_2/k_1 are plotted in Figures 3.22 and 3.23, respectively. It is noted that the equivalent stiffness increases with increasing c_2 and that it can be tuned within a larger range when k_2/k_1 is smaller, as shown in Figure 3.22. However, from Figure 3.23, it can be shown that the equivalent damping increases first, then decrease with increasing c_2, and that smaller k_2/k_1 can cause a greater equivalent damping when a certain value of the damping coefficient c_2 is applied.

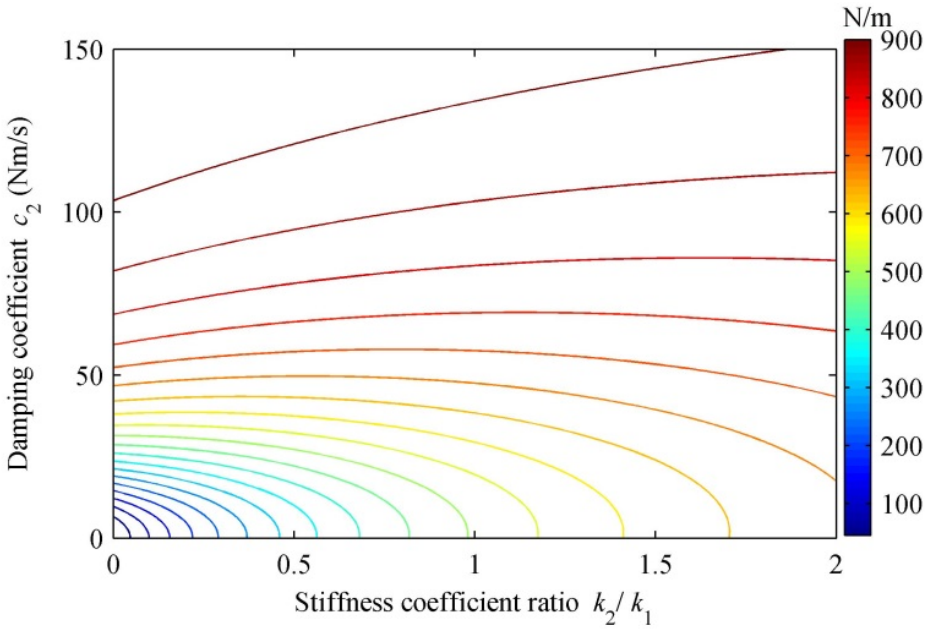

Figure 3.22. Equivalent stiffness coefficient as a function of c_2 and stiffness coefficient ratio k_2/k_1.

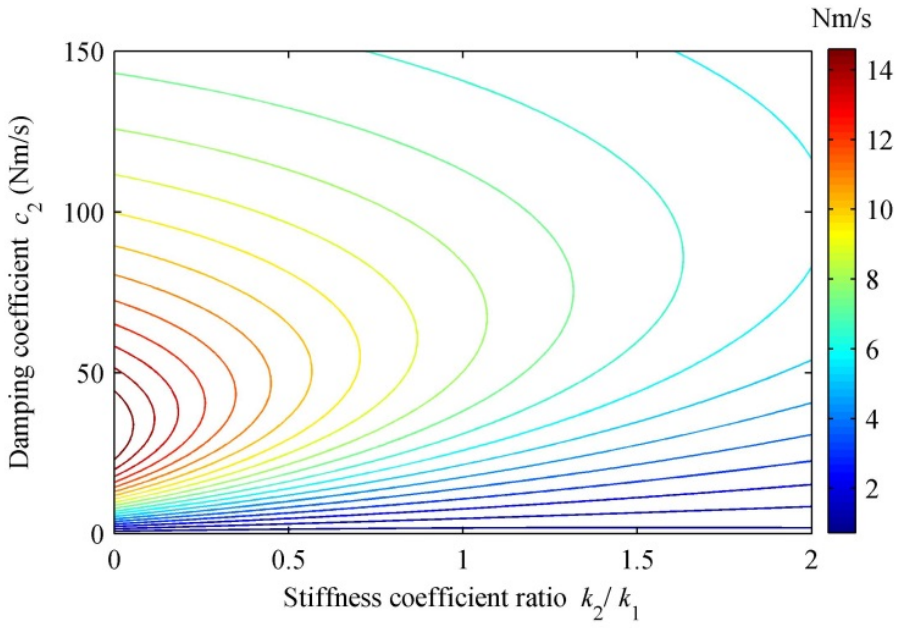

Figure 3.23. Equivalent damping coefficient as a function of c_2 and stiffness coefficient ratio k_2/k_1.

3.3.3 Tuning damping

The tuning of the damping coefficient can cause a change in the equivalent stiffness, and then a further influence on the frequency-amplitude response curve of the oscillator. The detailed principle of the proposed method is presented in this section. Figure 3.24 shows the frequency response curves under different values of damping coefficient c_2 according to Equation (3.36), while the other parameters shown in Table 3.3 are kept constant. Variations in the damping coefficient have an influence on both the jump-up and jump-down frequencies. By increasing the linear stiffness, the frequency response curve shows a movement to the right.

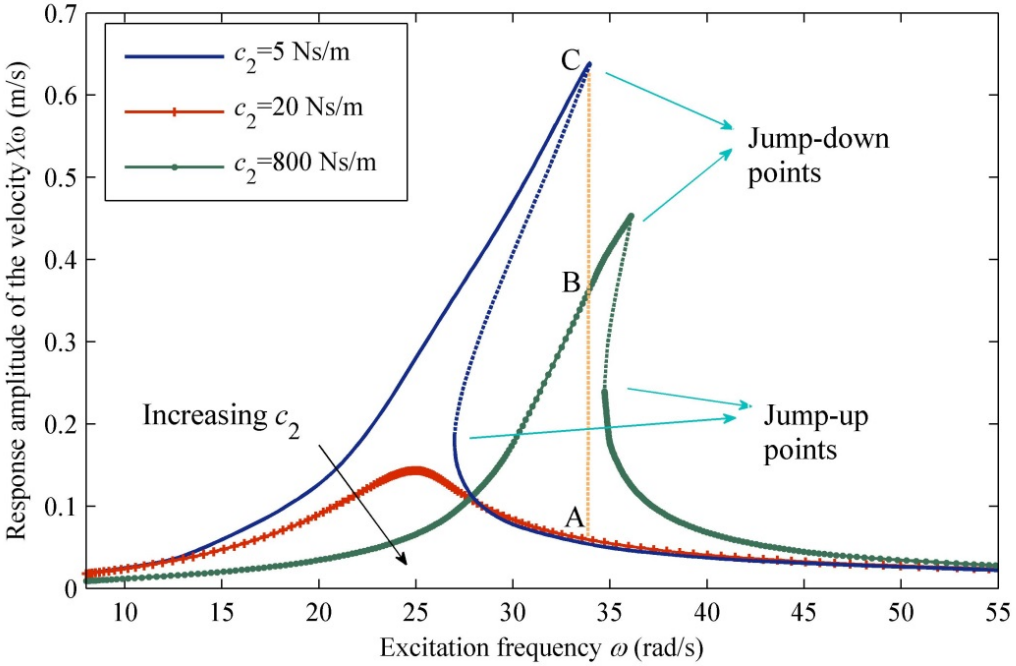

Figure 3.24. Frequency response curve of a hardening-type system.

The process of triggering the jump is also illustrated in Figure 3.24. It is assumed that the energy harvester is oscillating at point A when c_2 is equal to 5 Ns/m, with this point located in the low-energy orbit, and then by starting to increase c_2, the shape of the frequency response curve slowly varies, as shown in Figure 3.24 . The operating point jumps to point B when the frequency of the excitation exceeds the jump-up frequency. The oscillator is now operating in the preferred orbit. However, variation in the stiffness also decreases the amplitude of the response. Thus, following the high-energy orbit, the operating point subsequently moves to C by decreasing the damping coefficient c_2. It is noted that in the process of tuning the damping coefficient there is a possibility that the multi-valued frequency response curve disappears (for c_2 = 20 Ns/m) because the equivalent damping coefficient initially increases with c_2, as shown in Figure 3.23. This phenomenon does not influence the jump from point A to B, but the movement from point B to C and this is further discussed below.

To trigger a jump to the high-energy orbit, the dimensional jump frequency ω_u should be higher than the excitation frequency ω. Hence, from Equation (3.30), the minimum equivalent stiffness coefficient for triggering a jump is defined by

$$k'_{eq} = m\omega^2 - \left(\frac{3}{2}\right)^{4/3} \left(\alpha F^2\right)^{1/3} \tag{3.46}$$

It is assumed that the electrical damping is small and $c_1 << c_2$. By setting $c_1 = 0$, the corresponding minimum control damping coefficient can be given by Equation (3.44a) as

$$c_{2u} = \sqrt{\frac{k'_{eq}\left(k_1 + k_2\right)^2 - k_1 k_2\left(k_1 + k_2\right)}{\omega^2\left(k_1 - k'_{eq}\right)}} \tag{3.47}$$

Using Equation (3.47), and substituting Equation (3.46) into Equation (3.44b), the required equivalent damping coefficient to get the target equivalent stiffness can be expressed as

$$c_{equ} = \frac{\sqrt{\left(k'_{eq}\left(k_1 + k_2\right)^2 - k_1 k_2\left(k_1 + k_2\right)\right)\left(k_1 - k'_{eq}\right)}}{\omega\left(k_1 + k_2\right)} \tag{3.48}$$

To increase the jump-up frequency tuning range as much as possible it is necessary to analyse the influence of the parameters k_2/k_1 and αF^2 on the ratio between the maximum and minimum jump-up frequencies, and this can be expressed as the following frequency ratio

$$\frac{\omega_{u\max}}{\omega_{u\min}} = \frac{\sqrt{k_{\max} + \left(3/2\right)^{4/3}\left(\alpha F^2\right)^{1/3}}}{\sqrt{k_{\min} + \left(3/2\right)^{4/3}\left(\alpha F^2\right)^{1/3}}} \tag{3.49}$$

where $k_{\max} = k_1$ when $c_1 = c_2 = 0$ and $k_{\min} = k_1 k_2/\left(k_1 + k_2\right)$ when $c_2 \to \infty$.

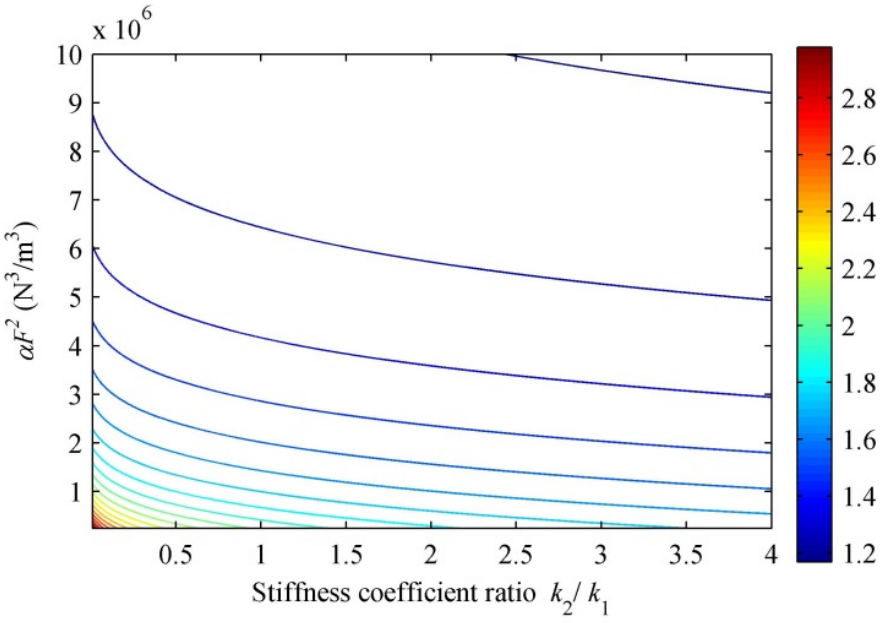

Figure 3.25. Jump-up frequency ratio as a function of k_2/k_1 and αF^2.

Assuming that $k_1 = 1000\,\mathrm{N/m}$, the jump-up frequency ratio as a function of k_2/k_1 and αF^2 is shown in Figure 3.25, where αF^2 governs the degree of nonlinearity and the excitation amplitude.

It is noted that a smaller stiffness coefficient ratio k_2/k_1 is propitious for increasing the tuning range. Additionally, the weaker nonlinearity and smaller excitation amplitude can achieve a similar effect for increasing the jump-up frequency tuning range.

As analysed above, it is possible to trigger a jump to the high-energy orbit by tuning the damping until the jump-up frequency exceeds the frequency of the excitation. However, under some conditions it is necessary to continue to decrease the equivalent stiffness to close to the jump-down frequency, which is the peak response point of the oscillator. It should be noted that the equivalent damping of the system also varies besides the equivalent stiffness in the process of damping variation, as shown in Figure 3.23, which has strong influence on the occurrence of the multi-valued frequency-amplitude curve and the value of the jump-down frequency. Thus, excessive equivalent damping during the tuning process (point B to point C shown in Figure 3.24 may again lead to an undesirable jump-down to the low-energy orbit.

The condition for the multi-valued frequency-amplitude curve to occur is defined as [64]

$$\frac{\alpha F^2}{k^3} \geq \frac{2^5}{3^{5/2}} \frac{c^3}{(mk)^{3/2}} \tag{3.50}$$

Equation (3.50) can be combined with Equations (3.46) and (3.48) to give

$$\alpha F^2 \geq \frac{2^5}{3^{5/2}} \left(\frac{{c_{equ}}^2 k'_{eq}}{m} \right)^{3/2} \tag{3.51}$$

It can be seen that the stronger nonlinearity and higher level of excitation amplitude are beneficial for meeting the requirement determined by Equation (3.51) for an inflexion to occur. However, this will decrease the tuning range of the jump-up frequency.

Another condition is that the jump-down frequency should be kept higher than the excitation frequency. As shown in Figure 3.23, a maximum equivalent damping exists when the damping c_2 is large enough. Substituting Equations (3.44a) and (3.44b) into Equation (3.33) leads to the corresponding damping c_2 versus the minimum jump-down frequency being obtained from $\frac{d\omega_d}{dc_2} = 0$, which leads to the following expression:

$$c_{2d} = \frac{k_1 + k_2}{\omega} \sqrt{\frac{k_2 \left(\sqrt{9k_1^2 + 4k_1k_2 + 4k_2^2} - 3k_1 \right)}{2k_1k_2 - 3k_1\sqrt{9k_1^2 + 4k_1k_2 + 4k_2^2} + 9k_1^2 + 2k_2^2}} \tag{3.52}$$

The corresponding equivalent stiffness coefficient and damping coefficient can then be obtained by substituting Equation (3.52) into Equations (3.44a) and (3.44b), respectively. Thus, the condition for keeping the oscillating point on the high-energy point can be expressed as

$$\omega_{d\min} \geq \omega \tag{3.53}$$

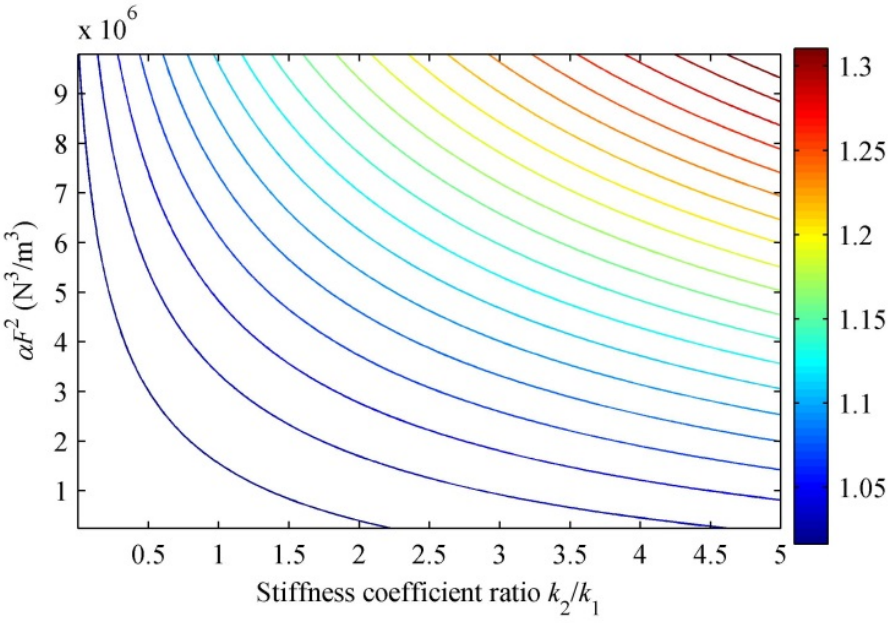

Figure 3.26. Non-dimensional minimum jump-down frequency as a function of k_2/k_1 and αF^2.

Using the same values of k_1 and αF^2 as previously obtained, and setting the mass at $m = 1\text{kg}$, Figure 3.26 shows the minimum jump-down frequency $\Omega_{d\min}$ as a function of the stiffness coefficient ratio k_2/k_1 and αF^2. It is obvious that the higher values of k_2/k_1 and αF^2 can increase the available minimum jump-down frequency of the system, which also indicates that the jump-down frequency can also be increased by employing a greater nonlinearity in the stiffness and excitation amplitude. However, as discussed above, this will decrease the tunable jump-up frequency range. Therefore, the parameters k_2/k_1 and αF^2 should be appropriately selected.

3.3.4 Numerical simulation

The parameters in Table 3.3 are used for simulation but under different excitation level *F* and stiffness coefficient k_2. Figures 3.27 present the tuning process for the damping coefficient c_2, and the corresponding velocity vs displacement phase trajectories of the magnetic end mass. As shown in Figure (3.27b), the oscillating point jumps to the high-energy orbit with the increase in the damping coefficient, and then moves further towards the maximum response point by decreasing c_2 and by setting *F* and k_2 equal to 3 N and 1000 N/m , respectively.

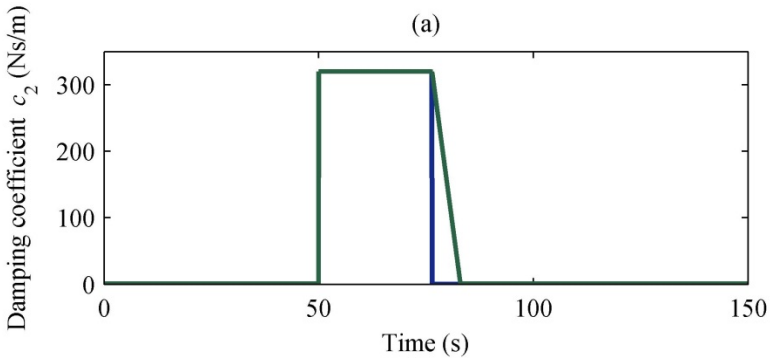
(a)
Damping coefficient c_2 (Ns/m)
300
200
100
0
0
50
100
150
Time (s)

(b)

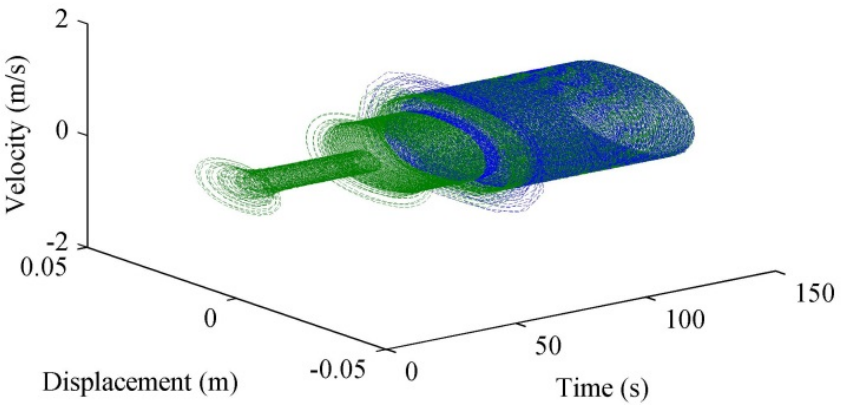
Velocity (m/s)
2
0
-2
0.05
0
-0.05
Displacement (m)
0
50
100
150
Time (s)

(c)

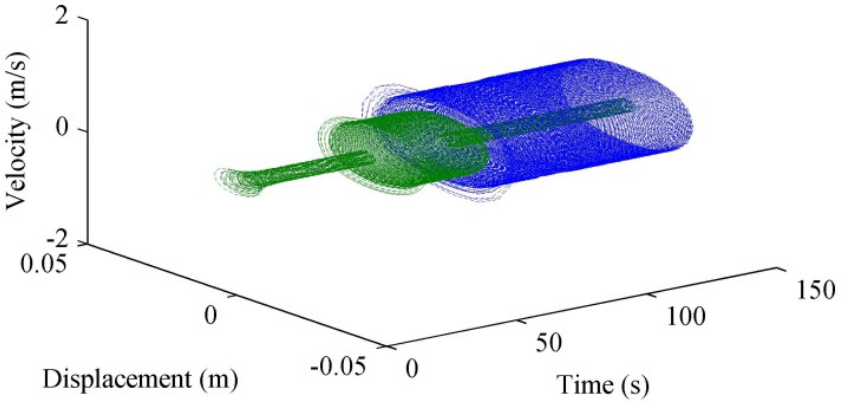
Velocity (m/s)
2
0
-2
0.05
0
-0.05
Displacement (m)
0
50
100
150
Time (s)

(d)

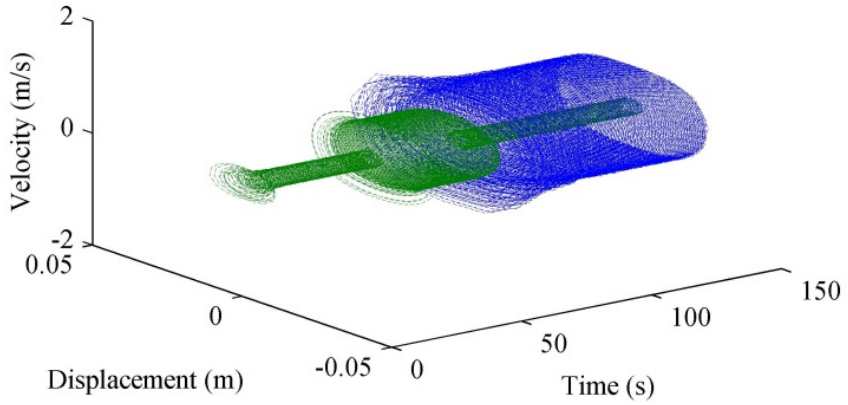

Figure 3.27. Variation of the damping coefficient and velocity vs displacement phase trajectories of the magnetic end mass (blue line: damping coefficient instantaneously tuned, and green line: damping coefficient slowly tuned): (a) changing the damping coefficient c_2, (b) response with F and k_2 set to 3N and $1000\,\mathrm{N/m}$, respectively, (c) response with F and k_2 set to 2N and $1000\,\mathrm{N/m}$, respectively, and (d) response with F and k_2 set to 3N and $500\,\mathrm{N/m}$, respectively.

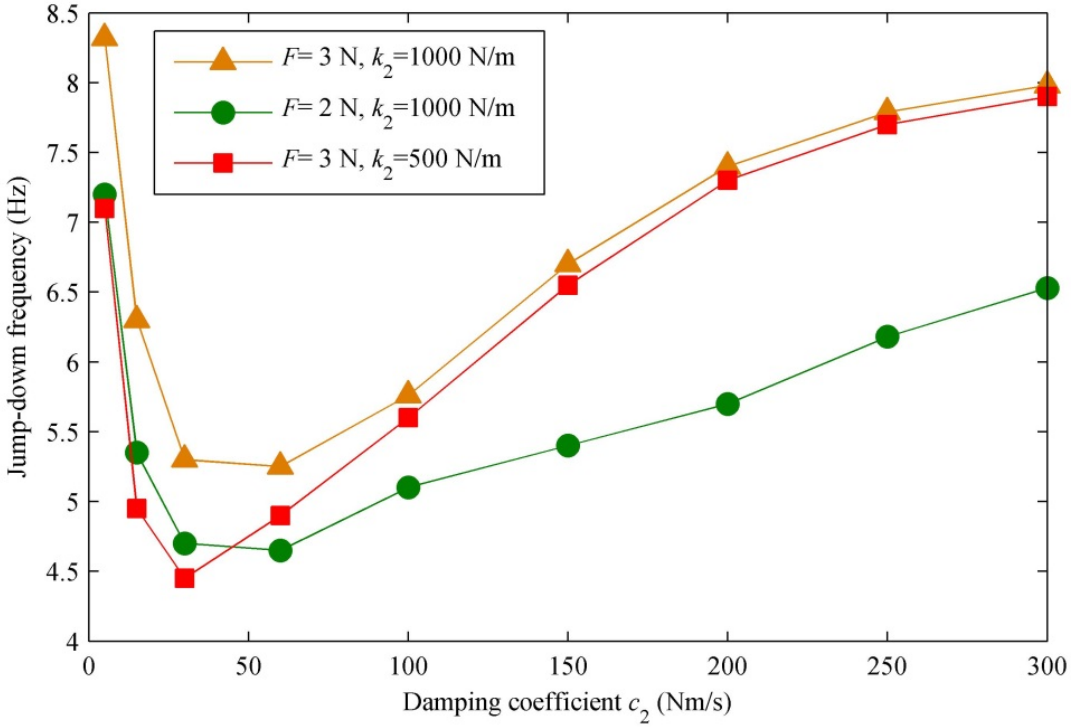

Figure 3.28. Jump-down frequency as a function of damping coefficient c_2 under various excitation levels F and stiffness coefficients k_2.

However, when the excitation amplitude F is set to $2\mathrm{N}$, the condition defined by Equation (3.53) cannot be satisfied, as shown in Figure 3.28, the minimum jump-down frequency is smaller than the excitation frequency of 5.2 Hz. The oscillating point jumps to the low-energy orbit again during a decrease in the damping coefficient, which is shown in Figure 3.27(c) (green line). A similar response can be seen in Figure 3.27(d) (green line) when the stiffness coefficient k_2 is set to $500\,\mathrm{N/m}$. The corresponding jump-down frequency as a function of the damping coefficient c_2 is also presented in Figure 3.28 by numerical simulation. It establishes that the smaller value of k_2/k_1 can decrease the available minimum jump-down frequency of the system in the process of damping variation.

The condition defined by Equation (3.53) provides a limitation on the tuning procedure. However, from Figures 3.27(c) and 3.27(d) (blue line), it is interesting to find that another approach to triggering a jump to the high-energy orbit is by instantaneously decreasing the damping coefficient c_2, when the condition defined by Equation (3.53) is not satisfied. It is known that the steady-state orbit is also significantly dependent upon the initial conditions. This is evaluated by using the basin of attraction obtained by choosing the initial conditions from the lattice points in the phase plane and then solving the equation of motion numerically until the trajectory converges to one of the steady-state solutions [84]. As mentioned previously, by increasing the controllable damping c_2, the operating point can jump to the high-energy orbit (see point B in Figure 3.24). Then, when c_2 instantaneously decreases to the initial value this could be regarded as an initial condition to be applied to the oscillator, and this initial condition is caused by the response of the oscillator at point B in Figure 3.24. If the initial conditions can lead to the basin of attraction for the high-energy solution then the oscillator will stabilise on the corresponding high-energy orbit. This approach gives a possible solution to the limitation problem defined by Equation (3.53).

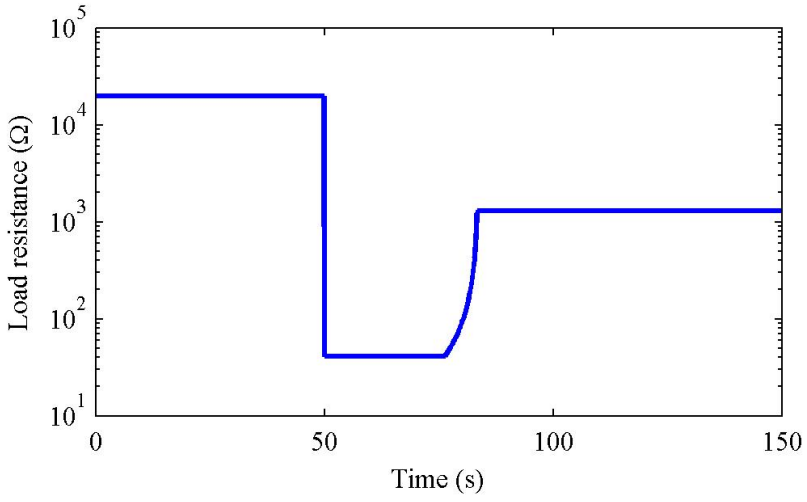

Figure 3.29. Variation of the load resistance. (F and k_2 set to 3N and $1000\,\mathrm{N/m}$, respectively)

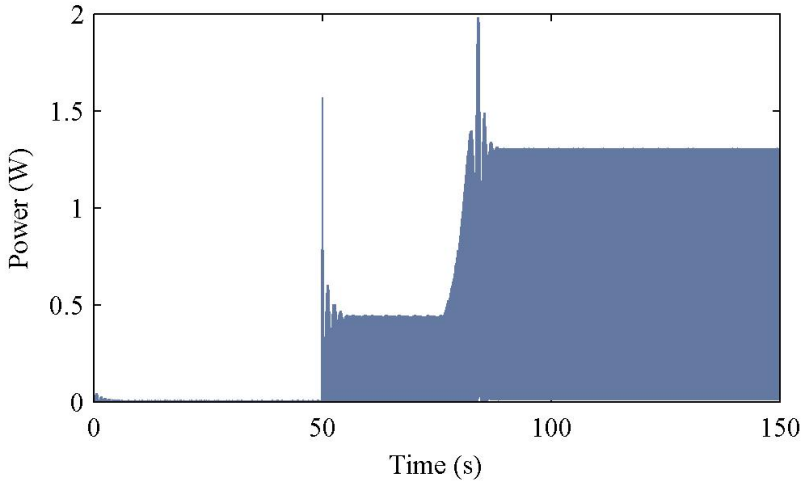

Figure 3.30. Delivered power with the changing of the load resistance. (F and k_2 set to 3N and $1000\,\mathrm{N/m}$, respectively)

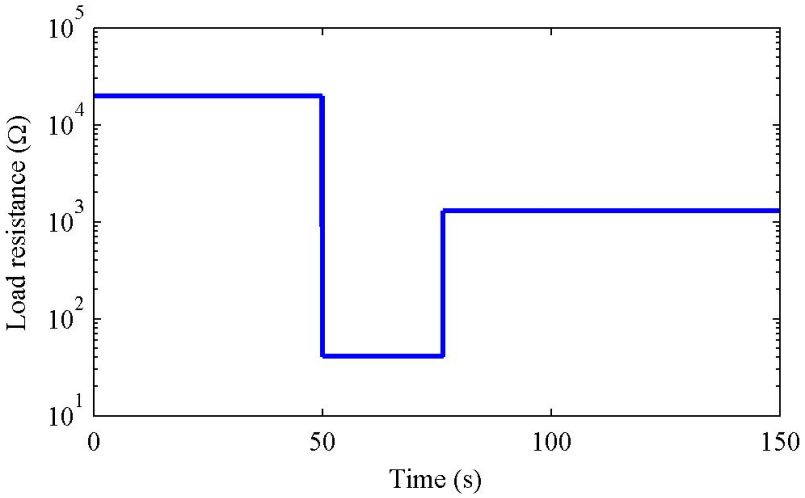

Figure 3.31.Variation of the load resistance. (F and k_2 set to 2N and $1000\,\mathrm{N/m}$, respectively)

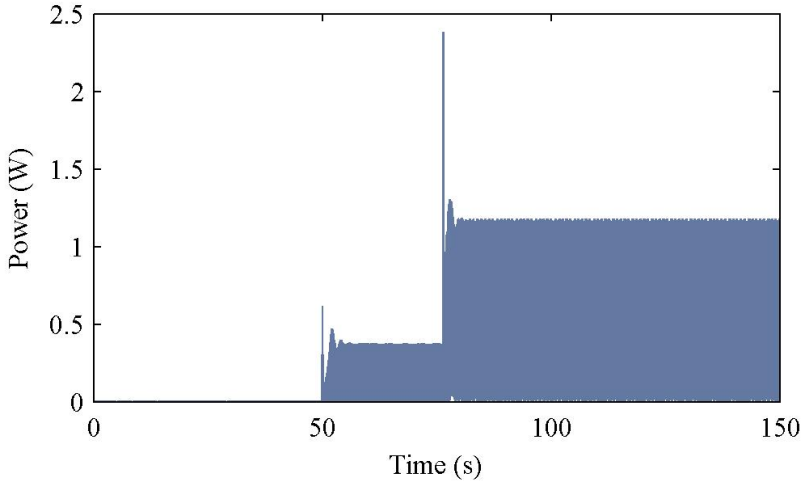

Figure 3.32. Delivered power with the changing of the load resistance. (F and k_2 set to 2N and $1000\,\text{N/m}$, respectively)

Figures 3.29 to 3.32 present the changing of the load resistance and the corresponding delivered power, which can be expressed as

$$P(t)=\frac{R_l\left(n\phi\dot{x}_p\right)^2}{\left(R_i+R_l\right)^2} \tag{3.54}$$

The load resistance plays not only the role of the power delivery but also the high-energy orbit stabilisation. Considering that it is much easier to tuning the load resistance compared with the direct stiffness adjustment, it can be concluded that net energy can still be harvested during the tuning process, which provides an apparent advantage for the application of the energy harvester.

3.3.5 Numerical and experimental validation of a simplified model

This section describes the experimental test, also with the numerical simulation performed to validate the proposed method using a simplified model because of the difficulty of the engineering design problem. More detailed description is shown as follows.

An electrical damper is favorable for the experiment and that it can be fabricated using a linear DC motor or a DC generator coupled with a transmission mechanism so that it can produce a high level of damping. The damping could be tuned using a variable resistance [86], with the advantage that electrical energy can be harvested by the controllable damper, even

during the tuning process. However, because of the mass of the linear DC motor and the equivalent mass of the transmission mechanism, it becomes rather difficult to achieve a very high damping ratio, as expected in an ideal experimental device. As an alternative, a small piece of ferrous metal is attached to the beam and an electromagnetic restraining device is placed under it with a small gap between them. And the gap is set small enough to minimise the influence on the response caused by the initial displacement when the beam is released. The piezoelectric beam can be regarded as two springs connected at the location of the small piece of ferrous metal. The electromagnetic restraining device is used to simulate the conditions that $c_2 \to 0$ and $c_2 \to \infty$ by restraining and releasing the beam, respectively. This is the so called simplified model.

On the other hand, the piezoelectric bimorph provides the electrical damper c_1 for energy harvesting. A schematic diagram of the ideal energy harvester is also presented in Figures 3.33 (b).

A picture of the fabricated energy harvester attached to the shaker table (m060, IMV Corp., Japan) is shown in Figure 3.33(a), in which three permanent magnets are arranged in a repulsive configuration to provide the cubic nonlinear stiffness [29], and where the magnetic end mass attached to the piezoelectric beam is aligned with respect to the symmetrically fixed permanent magnets (top and bottom magnets) in the vertical direction. The top and bottom magnets are symmetrically attached to sliders on a rail and this configuration allows the distance to be adjusted equally on each side, and so the natural frequency of the device is set to 16.3 Hz. The parameters of the device are shown in Table 3.4.

(a)

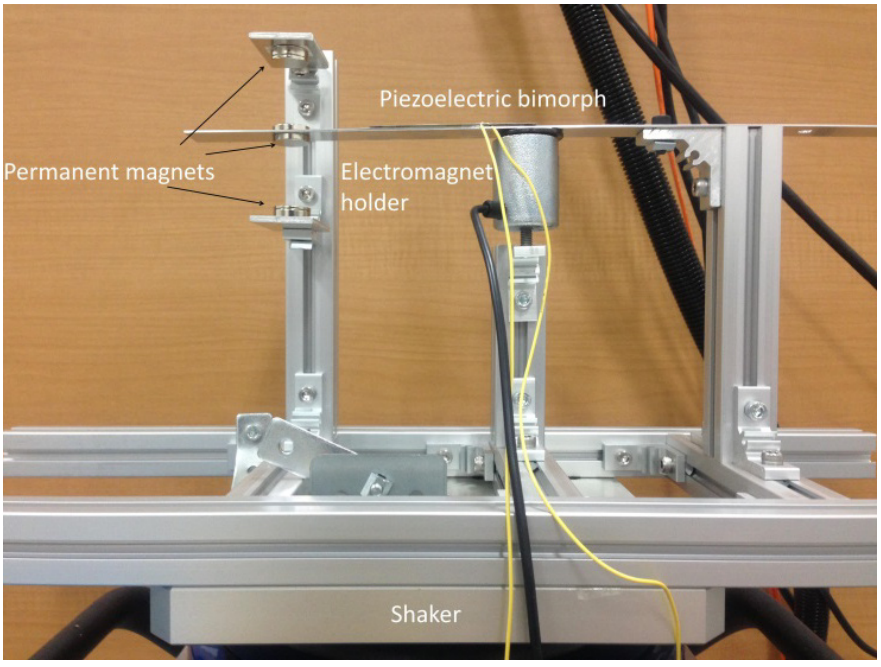

(b)

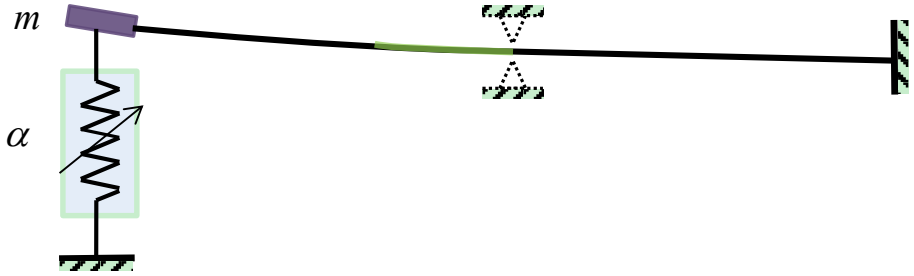

Figure 3.33. Experimentation setup: (a) photo of the experimental device and (b) the corresponding schematic diagram.

Table 3.4. Parameters of the experimental device and used for numerical simulation.

Parameter	Value	Unit
mass	0.01	kg
Linear stiffness (Released)	105	N/m
Linear stiffness (Stuck by EM)	213	N/m
Nonlinear stiffness	4.6×10^{5}	N/m^3
Mechanical damping	0.007	Ns/m
Coupling coefficient	472	V/m
PZT capacitance	110	nF
Internal resistance	115	KΩ

(a)

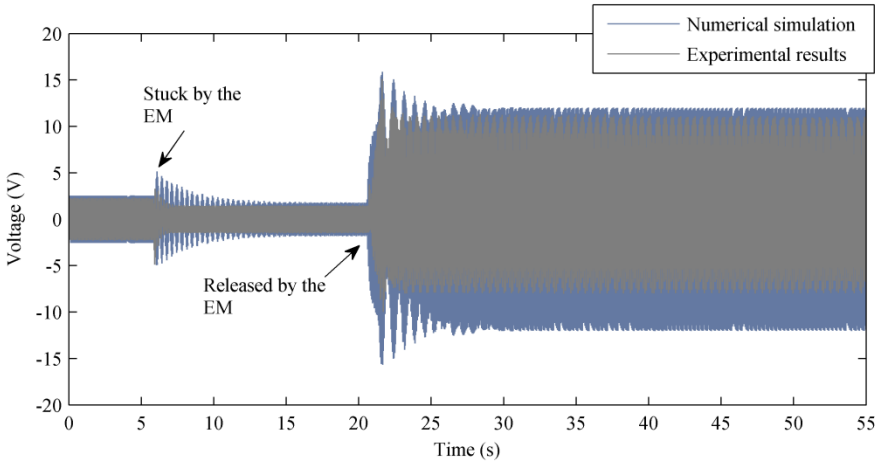

(b)

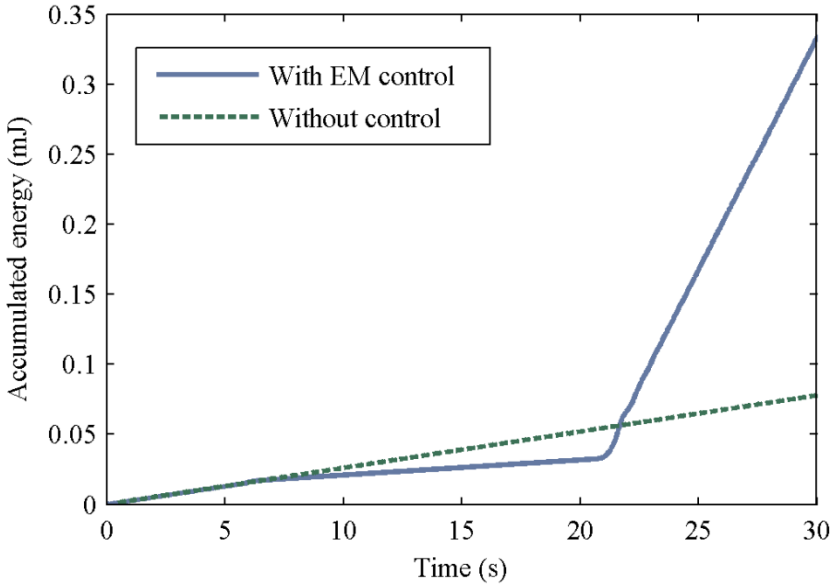

Figure 3.34. (a) Delivered output voltage on the load resistance (Blue color: Simulation results; Black color: Experimental results), (b) Experimentally cumulative energy on the load resistance.

Figure 3.34(a) presents the delivered voltage on a load resistance of 1MΩ when the energy harvester is subjected to a base excitation of 0.62 m/s^2 at 18 Hz. Both the measured results and the simulated results are shown in this figure, by using the index defined in Equation (3.39), the error after the response is stabilized is around 15.2%. Moreover, it is noted that the output voltage for the experiment is not symmetric because the influence of the electrical magnets. Moreover, it can be seen that the output voltage decreases when the beam is held by the electromagnet restraining device, because the oscillating point moves to the lower frequency side of the frequency response curve, and the natural frequency of the system is measured to be 23.25 Hz. When the beam is released by the electromagnet it can be seen that it jumps to the oscillating point which is close to the jump-down point on the high-energy orbit, and this validates the proposed solution to the limitation defined by Equation (3.53).

Figure 3.34(b) compares the cumulative generated energy when the harvester is operated on the low-energy orbit and the condition with damping variation for the experimental results.

3.4 Summary

This chapter investigated the methods to boost the response by stabilise the high-energy orbit using the ways of stiffness tuning and damping variation, respectively. The mathematical

models of the designed schematic devices were derived to interpret the principles of the proposed methods. For the former method, the analytical expressions of the key points, such as the permanent magnets distance that makes the excitation frequency equal the jump-up or jump-down frequency, are obtained through analysing the frequency response curve. Moreover, it is known that the resonant frequency of the monostable nonlinear oscillator is also dependent on the damping， and the optimum energy harvesting cannot always be achieved by only tuning the damping, when other physical parameters of the energy harvester are fixed. Thus, besides the function of high-energy orbit stabilisation, it also becomes possible for the stiffness tuning method to vary the resonant frequency of the device for the maximum energy harvesting, when the excitation frequency varies.

The method of the damping variation has a identical principle to the stiffness tuning method, except the stiffness is indirectly tuned by varying the damping. Considering the fact that it is much easier to tune the damping compared with that of the stiffness, it requires much less energy consumption for the tuning process.

Chapter 4

Parameters Optimisation for Harmonic Excitation

4.1 Introduction

This chapter presents the optimisation rule for the harmonic excited monostable energy harvester, with the consideration of two kinds of transducers, i.e. inductive and piezoelectric transducers.

In first, the full optimisation of the general model is considered, in where both of the fundamental frequency and electrical damping are selected as the optimisation variables. A hardening-type monostable energy harvester is adopted for the numerical validation. It should be mentioned that the influence on the performance is also considered about the electromechanical coupling coefficient. In general, the higher electromechanical coupling coefficient is beneficial to enhancing the available energy; however, the maximum electromechanical coupling coefficient is often limited by the dimension and weight of the transducer. It is a feasible approach to overcome this problem by application of the transmission mechanism. The available electrical damping level can be amplified, and is proportional to the square of the transmission ratio. The related studies using the transmission mechanism can be found in references [93] [94] [95].

After that, a single parameter optimisation of the energy harvester is introduced, in which only the electrical damping can be varied for the maximum power output. For a system with the fixed fundamental frequency, when the excitation frequency moves away, it cannot follow this frequency variation for the linear energy harvester; however, this can be completed by changing the damping level for the monostable nonlinear energy harvester, because of the existence of the nonlinear stiffness term. However, it cannot achieve the full optimisation.

In addition, in the practical implementations, several parameters of the energy harvesting device are constrained. For example, the maximum displacement of the seismic mass could be constrained on the maximum amount of stretch of the spring [96]. There is also a limitation for the available electrical damping of the damper. The optimisation rule is also suggested under this constrained condition.

4.2 General model with two parameters optimization

In this section, the parameters of the fundamental frequency and the load resistance are selected as the optimisation variables to maximizse the maximum power output.

4.2.1 Inductive model

It is known that the Duffing oscillator has frequencies at which the vibration jumps up or down. The frequencies at which these jumps occur are dependent on whether the nonlinearity is hardening or softening [64]. To conventionally derive the optimisation, the motion equation of a single degree-of-freedom Duffing oscillator with a inductive transducer is rewritten as

$$m\ddot{x} + c\dot{x} + kx + \alpha x^3 = F\cos(\omega t + \varphi) \tag{4.1}$$

where x is the relative displacement, and m is the seismic mass which is coupled with a restoring force with cubic nonlinearity and the inductive energy transducer with damping coefficient c, excited by a harmonic force $F\cos(\omega t + \varphi)$. The positive and negative nonlinearity indicate a hardening and softening system, respectively. The simplest form of electromechanical coupling, as typified by a permanent magnetic linear DC motor, is assumed in this section, Figure 4.1 shows the schematic circuit, the effect of the electrical inductance is assumed to be neglected because of the relatively low frequency. Thus, in the case of an electromagnetic transducer, the relationship between the induced coupling force and the current can be written as

$$F_e = \phi i \tag{4.2}$$

where ϕ is the electromechanical constant, it can be the back EMF constants for a linear DC motor.

And the value of i can be evaluated by using Kirchhoff's second law as

$$\phi\dot{x} = (R_i + R_l)i \tag{4.3}$$

where R_i and R_l are the internal resistance and load resistance, respectively. Then, the electrical damping coefficient is defined by [97]

$$c_e = \frac{\phi^2}{(R_i + R_l)} \tag{4.4}$$

The total damping can be expressed as

$$c = c_m + c_e \tag{4.5}$$

where c_m is the mechanical damping coefficient.

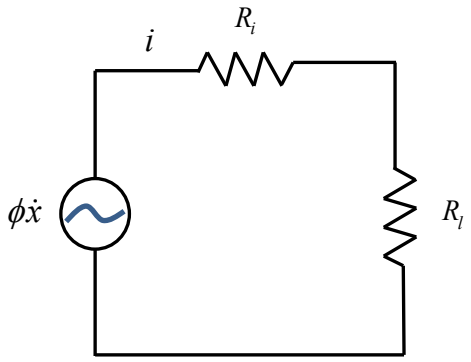

Figure 4.1. Schematic circuit of the energy harvester with a purely resistive load.

The case without any constraint is analysed first. The instantaneous current passing through the electrical load is expressed as:

$$i(t) = -\frac{\phi X_d \omega_d}{R_i + R_l} \sin\left(\omega_d t\right) \tag{4.6}$$

where X_d and ω_d are the amplitude and frequency at the jump-down point, and X_d can be rewritten from Equation (2.13) as

$$X_d = \frac{F}{k}\sqrt{\frac{2k^3}{3\alpha F^2}\left(\sqrt{1+\frac{3m\alpha F^2}{c^2k^2}}-1\right)} \tag{4.7}$$

Thus, the instantaneous delivered power is:

$$P(t) = \frac{\phi^2 {X_d}^2 {\omega_d}^2 R_l}{\left(R_i + R_l\right)^2} \sin^2\left(\omega_d t\right) \tag{4.8}$$

Substituting Equations (3.33), (4.4), (4.5) and (4.7), into Equation (4.8), the amplitude of the power is given by

$$P \approx \frac{\phi^2 F^2 R_l}{\left[\phi^2 + c_m\left(R_i + R_l\right)\right]^2} \tag{4.9}$$

The optimum load resistance is then obtained from $\frac{\partial P_d}{\partial R_l} = 0$, which gives

$$R_{lopt} = R_i + \frac{\phi^2}{c_m} \tag{4.10}$$

It is assumed that the seismic mass is selected as the design variable so that the jump-down frequency is equal to the source excitation frequency while maximising the available electrical power. For the hardening or softening-type Duffing energy harvester, from Equation (2.14), we have

$$\frac{\omega}{\omega_n} = \sqrt{\frac{1}{2}\left(\sqrt{1 + \frac{3m\alpha F^2}{c^2 k^2}} + 1\right)} \tag{4.11}$$

Substituting Equations (4.4), (4.5) into Equation (4.11), the selected mass is derived as

$$m = \frac{k}{\omega^2} + \frac{3\alpha F^2\left(R_i + R_{lopt}\right)^2}{4\omega^4\left[\phi^2 + c_m\left(R_i + R_{lopt}\right)\right]^2} \tag{4.12}$$

For the Duffing oscillator there is always the potential for an essentially nonlinear system where the linear stiffness k equals zero. From Equation (4.10) it can be noted that the optimal resistance at the peak point is not dependent upon the stiffness. Moreover, for the essentially nonlinear system, the selected seismic mass can be obtained by setting k in Equation (4.12) to zero.

A hardening-type Duffing energy harvester is selected for the numerical validation in this section, and the load resistance, mass as the design variable, is derived at the peak response point of the system.

A schematic diagram of the energy harvester is shown in Figure 4.2. It consists of a single lumped mass with two horizontally placed linear springs of stiffness k_3 and natural length l_0,

providing a restoring force, and another linear spring of stiffness k_0 in the vertical direction to counteract the influence of gravity.

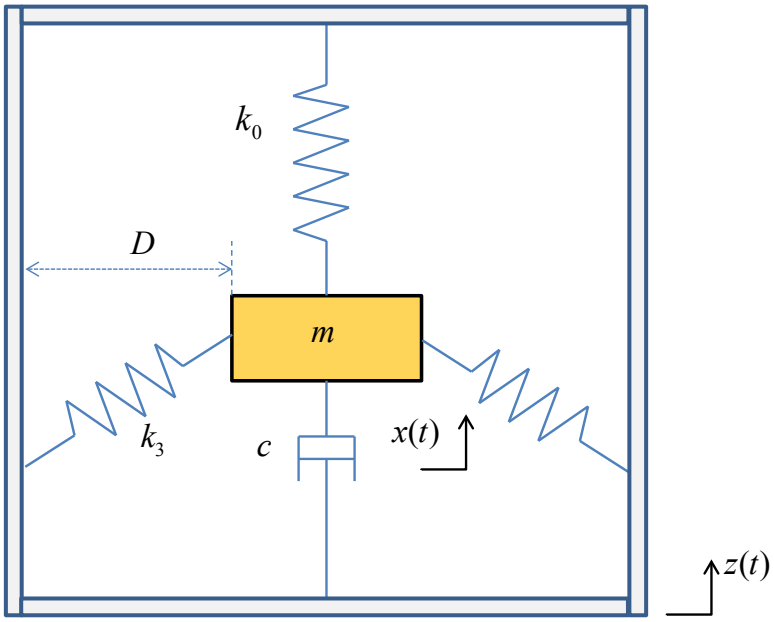

Figure 4.2. Schematic diagram for a hardening-type Duffing energy harvester.

Dissipation of the mechanical damping and electrical transducer is modelled using a single linear damper c. It is noted that the horizontal springs are unstretched with l_0 = D. The restoring force in the vertical direction is then expressed by

$$F_r = 2k_3 x\left(\frac{l_0}{\sqrt{x^2 + l_0^2}} - 1\right) - k_0 x \tag{4.13}$$

Using the Taylor-series expansion to the third order, Equation (4.13) is rewritten as

$$F_r = -k_0 x - \frac{k_3}{l_0^2} x^3 \tag{4.14}$$

Thus, the linear stiffness and nonlinear coefficients k and α are equal to k_0 and k_3/l_0^2, respectively.

Table 4.1. Parameters of the hardening-type Duffing energy harvester.

Parameter	k	α	c_m	R_i	ϕ	F	ω
Value	30 N/m	2×10^5 N/m^3	0.05 Ns/m	8 Ω	0.3 Vs/m	0.08 N	11 Hz

Table 4.1 shows a group of parameters used for the numerical simulation. This data represents the majority of current research in which milliwatt levels of power are obtained usually for applications in self-powered wireless sensors and low-power electronics.

It is assumed that the parameters in Table 4.1 are to be used. Based on Equations (4.10) and (4.12), the optimum values for the load resistance and selected mass are $9.8\,\Omega$ and 0.02kg, and with the maximum delivered power of 5.9 mW. Figure 4.3 shows the delivered power as a function of load resistance.

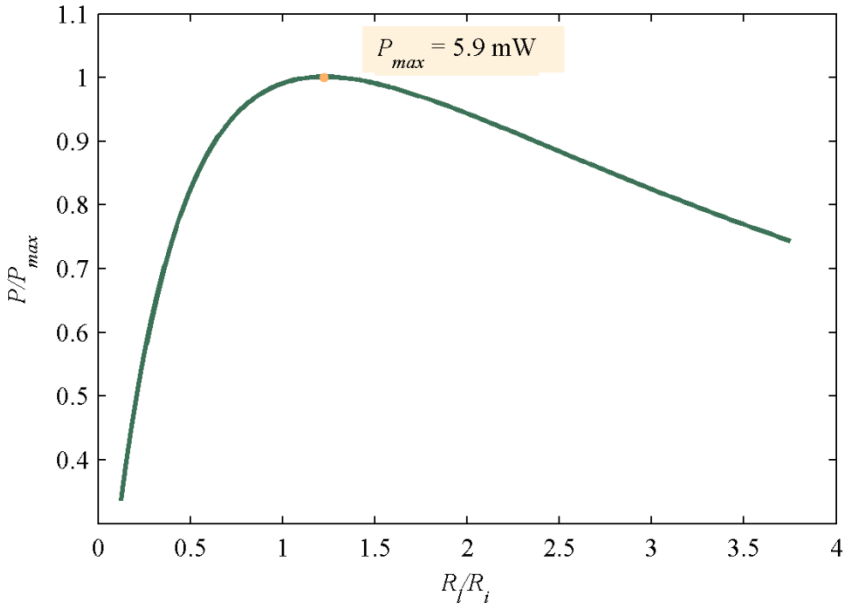

Figure 4.3. The delivered power as a function of load resistance.

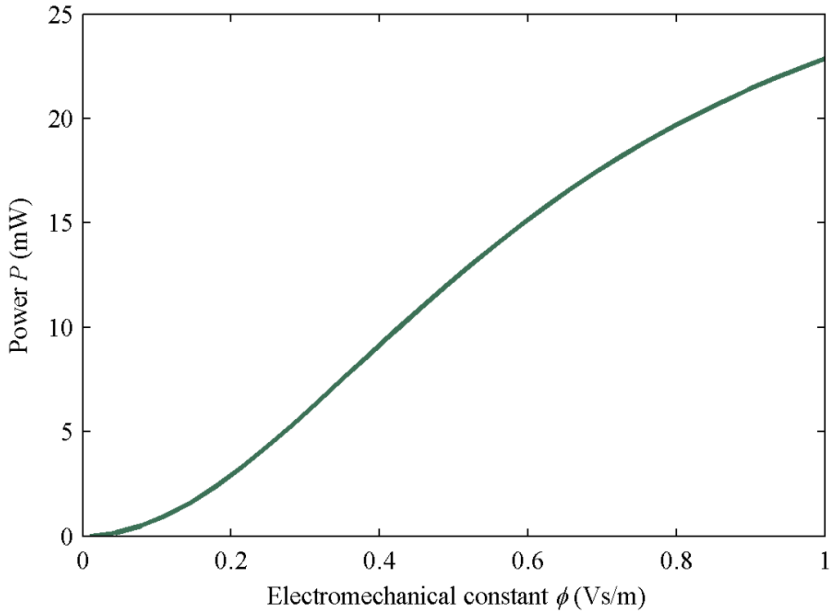

Figure 4.4. The delivered optimum power as a function of the electromechanical constant.

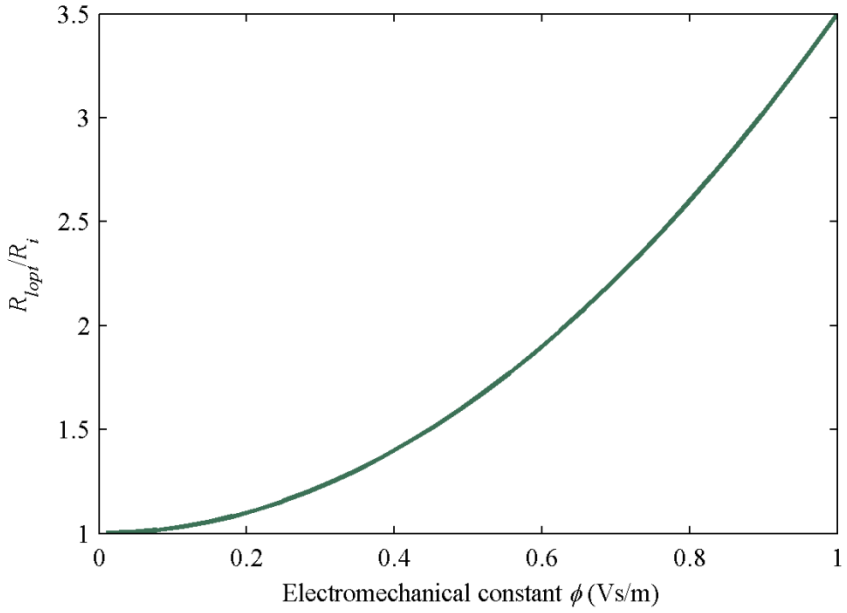

Figure 4.5. The optimum load resistance as a function of the electromechanical constant.

In practice, form Equation (4.10), it can be noted that it has the same form with the linear energy harvester, in other words, the available power from the monostable nonlinear energy harvester is same to that of the linear energy harvester at the resonance point.

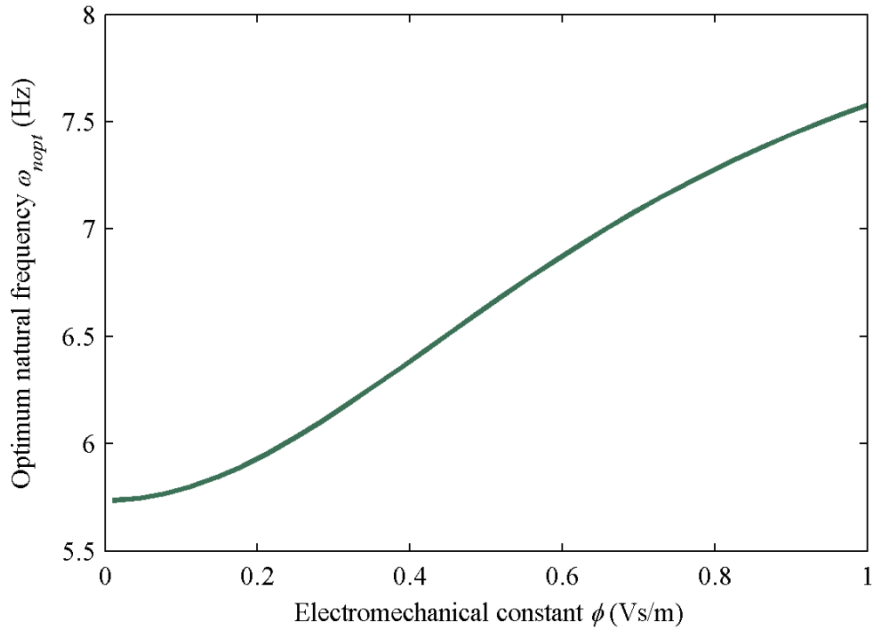

Figure 4.6. The optimum fundamental frequency as a function of the electromechanical constant.

Moreover, the effect of the electromechanical constant on the optimum delivered power on the load resistance is shown in Figure 4.4. The corresponding results for the optimum load resistance and the fundamental frequency is shown in Figures 4.5 and 4.6. It is predictable that with the increasing of the electromechanical constant, the load resistance shows the monotonous increasing tendency, which indicts higher power delivery efficiency. Also, the increasing of the optimum fundamental frequency indicted the smaller seismic mass.

For practical implementation, in order to achieve the high electromechanical constant, a transmission mechanism can be used to amplify the electromechanical constant of the linear DC motor, e.g. ball screw and gear rack. Usually, some of them have extremely transmission efficiency [98].

The equation of motion of the system under this condition is similar to Equation (4.1), but with a total damping coefficient as

$$c = c_m + n^2 c_e \tag{4.15}$$

where n is the transmission ratio. The available electrical damping level of the energy harvester can be dramatically amplified by using a transmission mechanism.

Moreover, some additional benefits of the transmission mechanism are for the low frequency

vibration conditions:

(1) When the excitation frequency is low but with the large amplitude, it might require an inacceptable large size transducer if the linear DC motor is directly used when the excitation amplitude is big. It can be replaced by a transmission mechanism and a small size rotational DC motor.

(2) If the energy harvester is excited by a low amplitude vibration source, where the low frequency also indicts the low velocity. It will decrease the mechanical-to-electric conversion efficiency, because conversion efficiency of the practical motor also depends on the motion or rotation speed for a practical motor, the difference of the available DC motor conversion efficiency can be more than 35% under different speed [99].

4.2.2 Piezoelectric model

The condition for the piezoelectric model is more complicated compared with the inductive model. Substituting Equations (3.33) and (4.7) (4.18) into Equation (3.38), the steady state power delivered to the load resistance can be expressed as

$$P = \frac{F^2 R_l \theta^2 \Big/ \left(\omega^2 + \dfrac{1}{R^2 C^2} \right)}{\left[\theta^2 \Big/ \left(\omega^2 + \dfrac{1}{R^2 C^2} \right) + c_m \left(R_i + R_l \right) \right]^2} \tag{4.16}$$

The optimum load resistance R_l is then obtained from $\dfrac{\partial P}{\partial R_l} = 0$. However, because of its complexity, it is rather difficult to obtain the analytical expression even if using computer. Therefore, numerical analysis will be carried out for validation.

When the mass is selected as the optimum variable, the expression is same as the inductive model, by substituting Equation (3.28) to Equation (4.12) as

$$m = \frac{k}{\omega^2} + \frac{3\alpha F^2 \left(R_i + R_{lopt} \right)^2}{4\omega^4 \left[\theta^2 \Big/ \left(\omega^2 + \dfrac{1}{R^2 C^2} \right) + c_m \left(R_i + R_{lopt} \right) \right]^2} \tag{4.17}$$

Table 4.2. Parameters of the piezoelectric hardening-type energy harvester.

Parameter	k	α	c_m	R_i	θ	C	F	ω
Value	30 N/m	2×10^5 N/m^3	0.05 Ns/m	110 KΩ	2745 V/m	110 nF	0.08 N	11 Hz

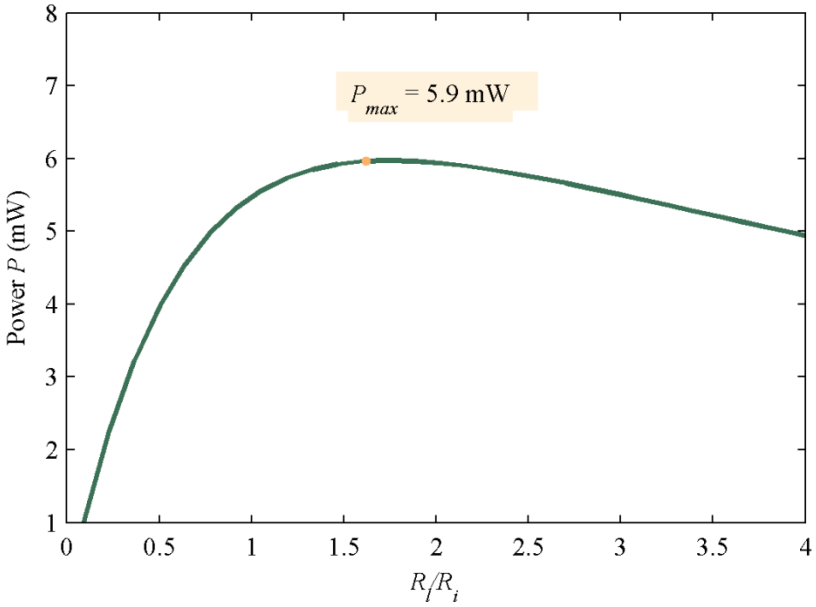

Figure 4.8. The delivered power as a function of load resistance.

It is assumed that the parameters in Table 4.2 are to be used. Based on Equations (4.16) and (4.17), the optimum values for the load resistance and selected mass are 192 KΩ and 0.02 kg, and with the maximum delivered power of 5.9 mW. Figure 4.8 shows the delivered power as a function of load resistance.

Moreover, the corresponding results are presented in Figures 4.9 to 4.11 when the electromechanical coupling coefficient θ varies, the same tendency as the inductive model can be observed. However, in general, for the practical piezoelectric transducer, the maximum available electromechanical coupling coefficient or electrical damping is smaller compared to the inductive transducer.

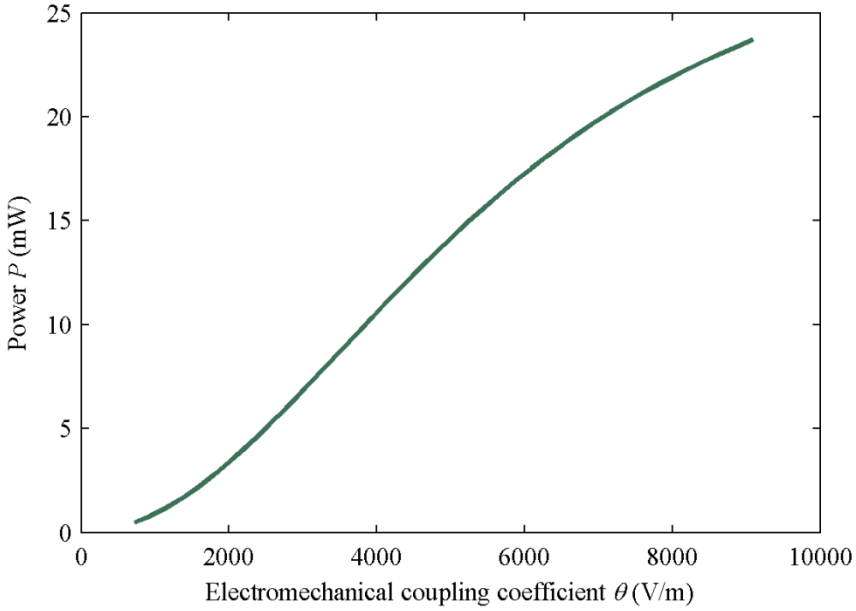

Figure 4.9. The delivered optimum power as a function of the electromechanical coupling constant.

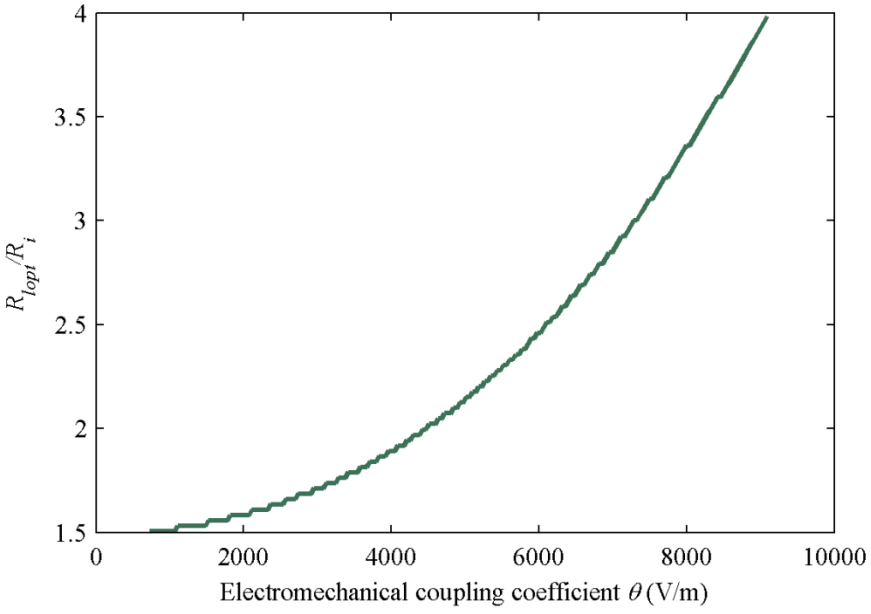

Figure 4.10. The optimum load resistance as a function of the electromechanical coupling constant.

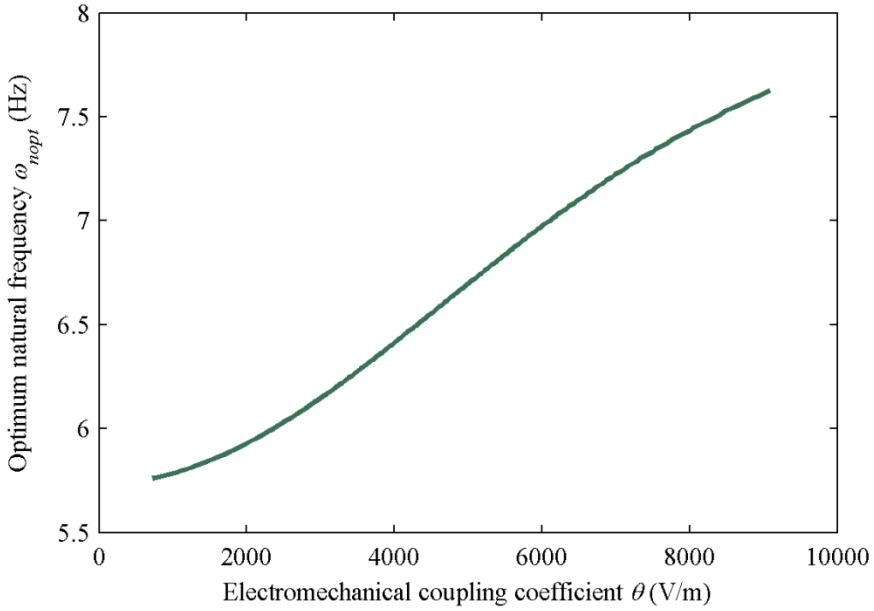

Figure 4.11. The optimum fundamental frequency as a function of the electromechanical coupling constant.

4.3 General model with single parameter optimisation

The above section introduced the optimisation method of the basic general model, this optimisation work is based on the assumption that there are two parameters can be varied for the optimization, i.e. the fundamental frequency and the electrical damping (load resistance).

However, if one considers the fundamental frequency of the device are already determined, only the single parameter of the electrical damping can be tuned and optimised when the excitation amplitude and frequency changes, it is termed as 'single parameter optimisation'.

There is a beneficial property for the nonlinear energy harvester compared with the linear one, which is because the frequency of the resonance point of the nonlinear energy harvester, can changes under different damping level, in other words, the resonance frequency is a function of the damping, which is shown in Equation (2. 14) in Chapter 2. However, for the linear energy harvester, the changing of the damping has little influence on the resonance frequency when the damping ratio is relatively small. One cannot make the resonance frequency follow the excitation frequency by tuning damping.

In order to understand the optimisation method, the frequency-amplitude response relationship is analysed first, it is shown in Equation (4.18) as

$$U_0{}^2\left(1-\Omega^2++\frac{3}{4}\beta U_0{}^2\right)^2+\left(2\zeta\right)^2\left(\Omega U_0\right)^2=1 \tag{4.18}$$

It can be noted that the first term on the left side of Equation (4.18) is the conservative term, and the second part is the damping force, which is the non-conservative term. The right side of the equation represents the external force. The maximum power can be obtained when the external force and damping force can be in phase. Thus, it can be obtained the following equation as

$$\left(2\zeta\Omega U_0\right)^2=1 \tag{4.19}$$

and

$$-U_0\Omega^2+U_0+\frac{3}{4}\beta U_0{}^3=0 \tag{4.20}$$

Rearranging Equation (4.20), the relationship between the response amplitude and the excitation frequency can be expressed as

$$U_0=\sqrt{\frac{4}{3\beta}\left(\frac{\omega^2}{\omega_n^2}-1\right)} \tag{4.21}$$

It can be noted that it is the backbone curve, it indicts that the optimum operating point of the energy harvester occurs at the jump-down point, which is at resonance. However, it should be mentioned that this conclusion is based on the condition that the energy consumed by the internal resistance is relatively small compared with the power delivered to the load resistance.

This is an advantage of the monostable nonlinear energy harvester compared with the linear configuration, because the resonance frequency can be tuned by changing the damping without the need to employ reactive loads as required for linear energy harvesters.

4.3.1 Inductive model

It is considered that the linear, nonlinear stiffness and the seismic mass of the oscillator are given, by combining Equations (4.4), (4.5) and (4.11), the expression for optimum load resistance at the given excitation frequency can be written as

$$R_{lopt} = \frac{\phi^2}{\sqrt{\frac{3\alpha F^2 m^2 \omega^2}{k\left(2m\omega^2 - k\right)^2 - k^3}} - c_m} - R_i \tag{4.22}$$

It indicts the electrical damping is tuned to make the excitation frequency be equal to that of the peak response point of the frequency response curve. The corresponding maximum power can be obtained by substituting Equation (4.22) into Equation (4.9).

By using the parameters in Table 4.1, a three-dimensional graph is depicted in Figure 4.12 to show the relationship between the delivered power, the non-dimensional excitation frequency and the electrical damping ratio under different values of electromechanical constant. The non-dimensional electrical damping ratio is defined as follows

$$\frac{\zeta_e}{\zeta_{e0}} = \frac{c_e}{c_{e0}} = \frac{\phi^2 / \left(R_i + R_l\right)}{\phi^2 / R_i} \tag{4.23}$$

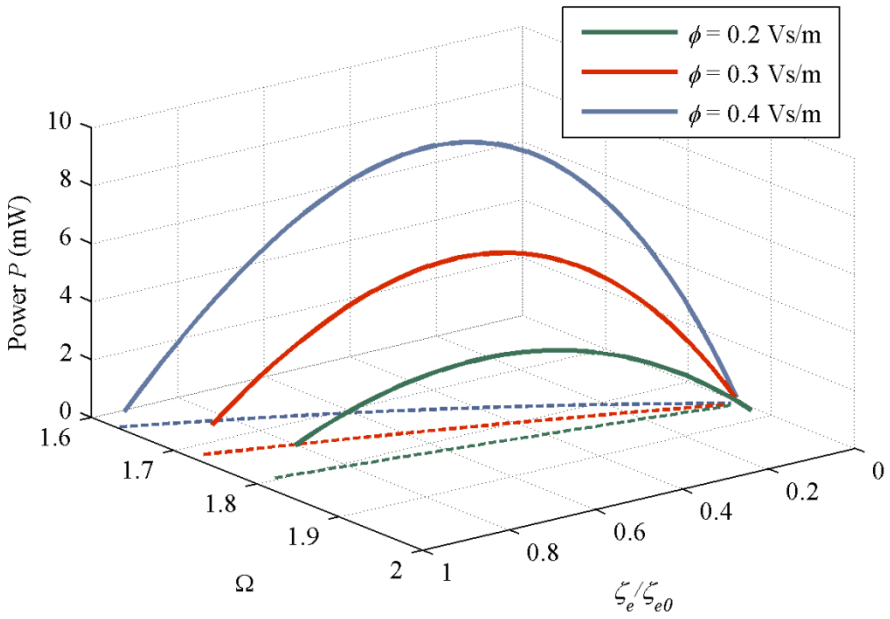

Figure 4.12. The delivered power as a function of the non-dimensional excitation frequency ($\Omega = \omega/\omega_n$) and the non-dimensional electrical damping ratio under different values of electromechanical constant, (solid line); the non-dimensional electrical damping ratio as a function of the non-dimensional excitation frequency and under different values of electromechanical constant. (dashed line)

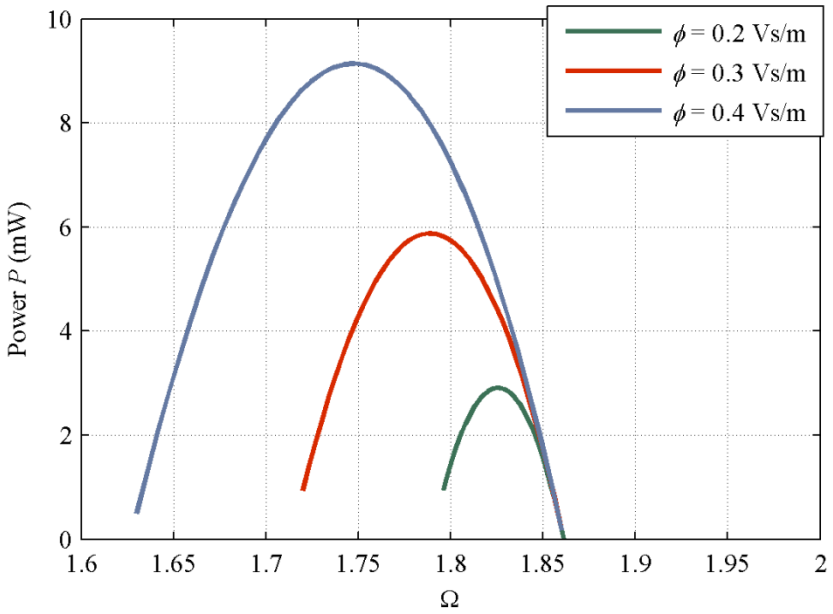

Figure 4.13. The delivered power as a function of the non-dimensional excitation frequency under different values of electromechanical constant.

For clearance, the results on the excitation frequency and the delivered power plan of Figure 4.12 are plotted in Figure 4.13. The peak point is 5.9 mW at 11 Hz for the red line, which corresponds to the two parameters optimisation condition as shown in Section 4.2.1, and for the energy harvester with the fixed fundamental frequency, there is the optimised excitation frequency exists, the maximum available power decreases when the excitation frequency varies.

4.3.2 Piezoelectric model

Same as the inductive model, the linear, nonlinear stiffness and the seismic mass of the oscillator are assumed to be given, by substituting Equations (3.28) (4.4), (4.5) into (4.11), the expression for optimum load resistance at the given excitation frequency can be written as

$$R_{lopt} = \frac{C\theta^2 + \sqrt{\Gamma^4 - 4\Gamma^2\omega^2}}{2C\omega^2\Gamma^4} - R_i \tag{4.24a}$$

where

$$\Gamma = \frac{1}{2\omega}\sqrt{\frac{3\alpha F^2}{m\omega^2 - k}} \tag{4.24b}$$

The corresponding maximum power can be obtained by substituting Equations (4.4) and (4.24) into Equation (4.9).

The delivered power as a function of the non-dimensional excitation frequency and the electrical damping ratio under different values of electromechanical constant are plotted in Figure 4.14 using Equations (4.9) and (4.24) and the parameters in Table 4.2. The corresponding projection on the excitation frequency and power plan is shown in Figure 4.15. The similar tendency to inductive model can be observed.

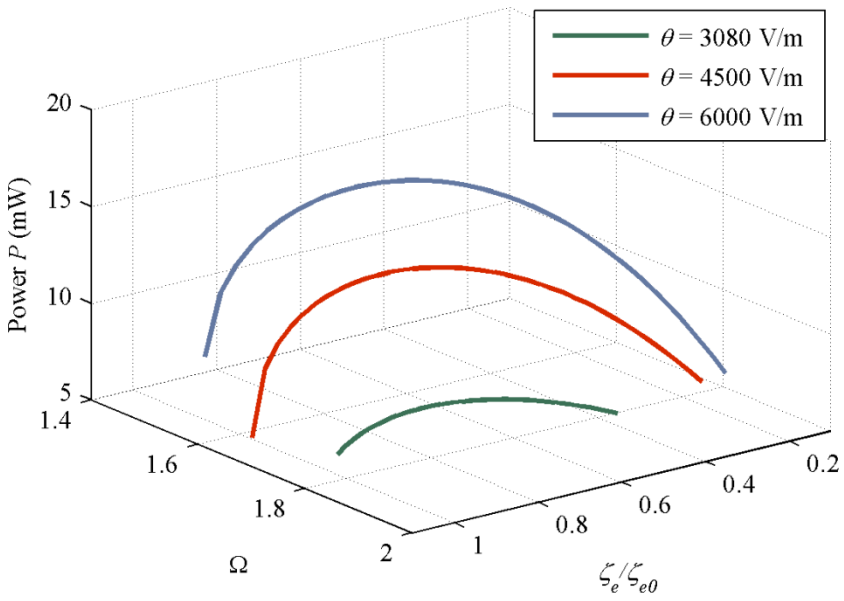

Figure 4.14. The delivered power as a function of the non-dimensional excitation frequency ($\Omega = \omega/\omega_n$) and the non-dimensional electrical damping ratio under different values of electromechanical constant, (solid line); the non-dimensional electrical damping ratio as a function of the non-dimensional excitation frequency and under different values of electromechanical constant. (dashed line)

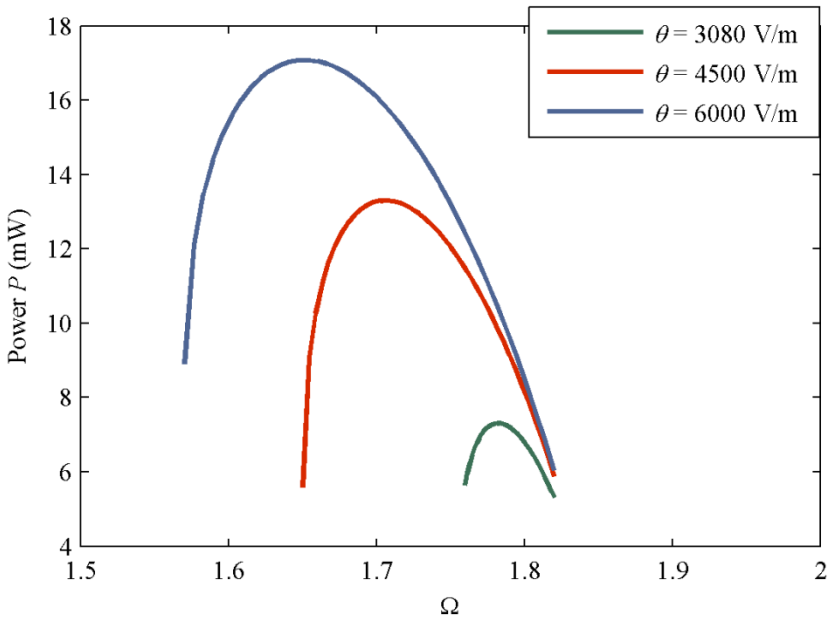

Figure 4.15. The delivered power as a function of the non-dimensional excitation frequency under different values of electromechanical constant.

4.4 Constrained displacement model analysis

4.4.1 Inductive model

A design principle with the constrained relative displacement is suggested in this section. The allowed dimensional displacement amplitude of the seismic mass, X_l, is assumed. From Equation (4.7), it can be obtained as

$$X_l = \frac{F}{k}\sqrt{\frac{2k^3}{3\alpha F^2}\left(\sqrt{1+\frac{3m\alpha F^2}{c^2k^2}}-1\right)} \tag{4.25}$$

Combining Equations (4.11) and (4.25) yields the expression for the selected mass as

$$m_{opt} = \frac{k}{\omega^2} + \frac{3X_l^2\alpha}{4\omega^2} \tag{4.26}$$

It can be seen that different from the previous cases, the selected mass does not depend on the damping coefficient.

Substituting Equations (4.4) and (4.5) into Equation (4.25) and rearrange it, the optimum load resistance can be given as

$$R_{lopt} = \frac{\phi^2}{\sqrt{\frac{12m_{opt}F^2\alpha}{\left(2k+3\alpha X_l^2\right)^2-4k^2}}-c_m} - R_i \tag{4.27}$$

and the corresponding delivered power is given as

$$P_{X_l} = \frac{R_{lopt}\phi^2}{\left(R_{lopt}+R_i\right)^2}X_l^2\omega^2 \tag{4.28}$$

By using the parameters in Table 4.1, the maximum displacement amplitude X_l under the

complete optimised condition is X_{max} = 0.021 m. Then, based on Equations (4.27) and (4.28), the non-dimensional load resistance as a function of the electromechanical constant is depicted under various displacement amplitude limits. It can be noted that the smaller displacement constraint requires the higher minimum electromechanical constant, because the small displacement limit indicts higher level of the electrical damping. It is known that this can be done by decreasing the load resistance. However, there is the possibility of reaching zero before achieving the required electrical damping. Therefore, the higher electromechanical constant becomes necessary.

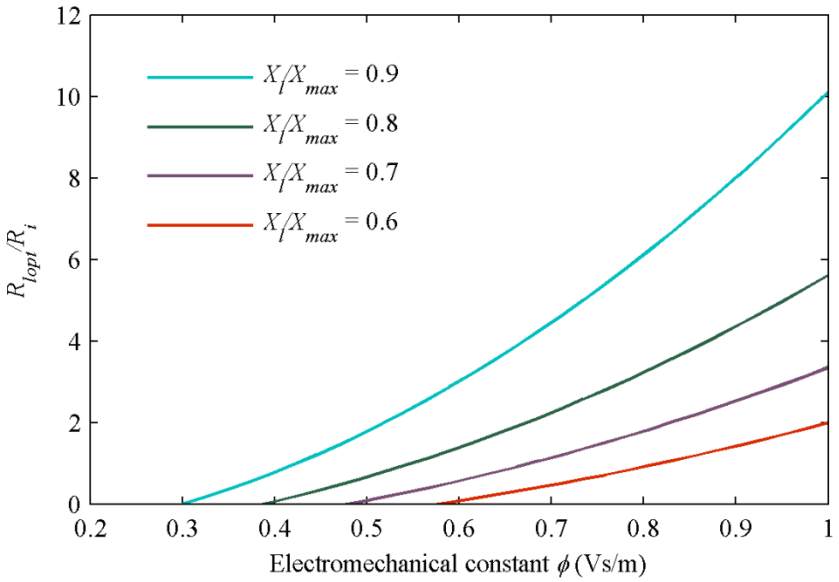

Figure 4.16. The optimum non-dimensional load resistance as a function of the electromechanical constant (X_{max} = 0.021 m, R_i = 8 Ω).

The corresponding delivered power as a function of the electromechanical constant is presented in Figure 4.17. Although the higher minimum electromechanical constant is needed with the decreasing of the displacement amplitude limit, it does not inevitably lead to the higher delivered power.

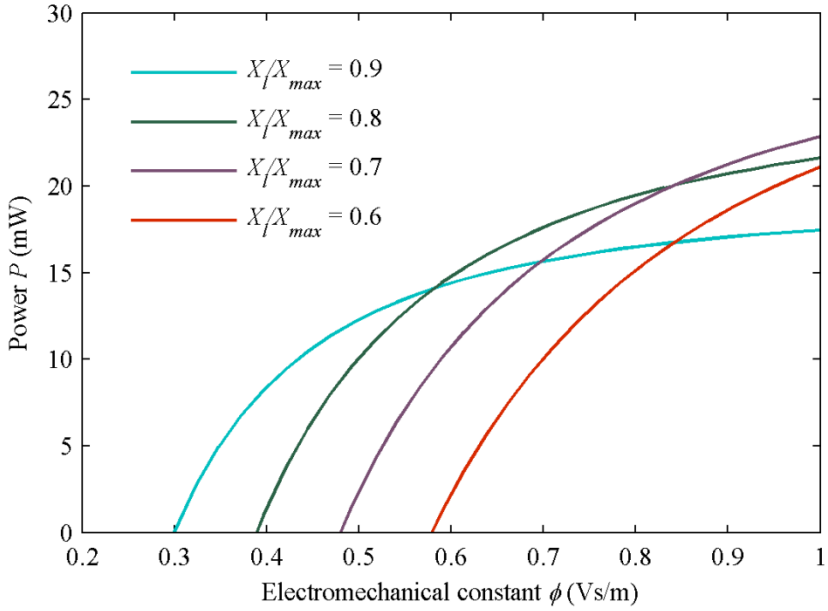

Figure 4.17. The delivered power as a function of the electromechanical constant (X_{max} = 0.021 m, $R_i = 8\,\Omega$).

4.4.2 Piezoelectric model

Because the optimum mass shown in Equation (4.26) has no relationship to the electrical damping, it is still applicable for the piezoelectric model.

Substituting Equations (3.28), (4.4) and (4.5) into Equation (4.7) and rearrange it, the optimum load resistance can be given as

$$R_{lopt} = \frac{C\Phi + \sqrt{C^2\Phi^2 - 4\omega^2}}{2C\omega^2} - R_i \tag{4.29a}$$

where

$$\Phi = \frac{\theta^2}{\sqrt{\frac{12 m_{opt} F^2 \alpha}{\left(2k + 3\alpha X_l^2\right)^2 - 4k^2}} - c_m} \tag{4.29b}$$

and the corresponding delivered power is the same expression as Equation (4.28).

By using the parameters in Table 4.2, the optimum load resistance and the delivered power as

a function of the electromechanical constant are presented in Figures 4.17 and 4.18, respectively. The similar results to the inductive model can be observed.

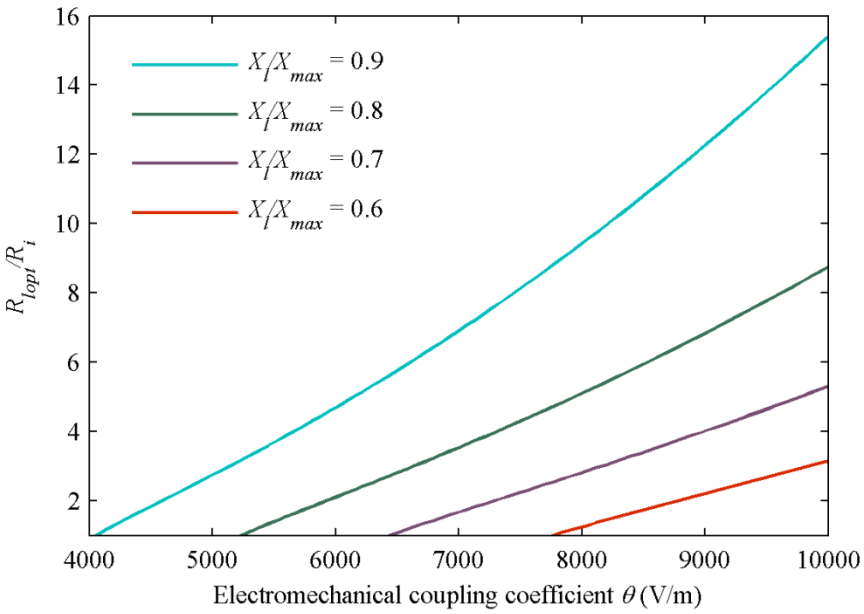

Figure 4.18. The optimum non-dimensional load resistance as a function of the electromechanical constant (X_{max} = 0.021 m, R_i = 110 K Ω).

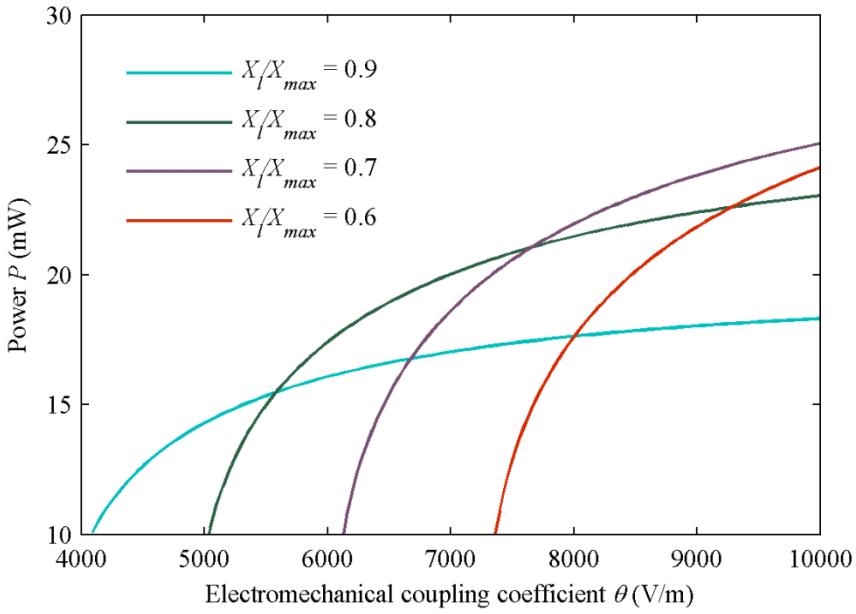

Figure 4.19. The delivered power as a function of the electromechanical constant (X_{max} = 0.021 m, R_i = 110 K Ω).

4.5 Constrained electrical damping model analysis

In this section, the influence of the electrical damping limit on the performance is considered. In previous sections, it is already validated that the piezoelectric transducer can also be regarded as an equivalent electrical damper likes the inductive transducer, but the difference is the equivalent effective electromechanical coupling coefficient is not a constant, because it is a function of the excitation frequency. However, the influence is small due to the frequency just varies within restricted range in this study. Also for clearance, it is assumed that all the dissipated energy by the electrical damping is harvested.

It is assumed that the parameters in Table 4.3 are given. The performance comparison under the constrained and the unconstrained conditions is conducted first. The maximum available electrical damping is set to be different values.

Table 4.3. Parameters of the hardening-type Duffing energy harvester.

Parameter	Value	Unit
m	0.02	kg
k	30	N/m
α	2×10^5	N/m^3
c_m	0.05	Ns/m
F	0.04	N

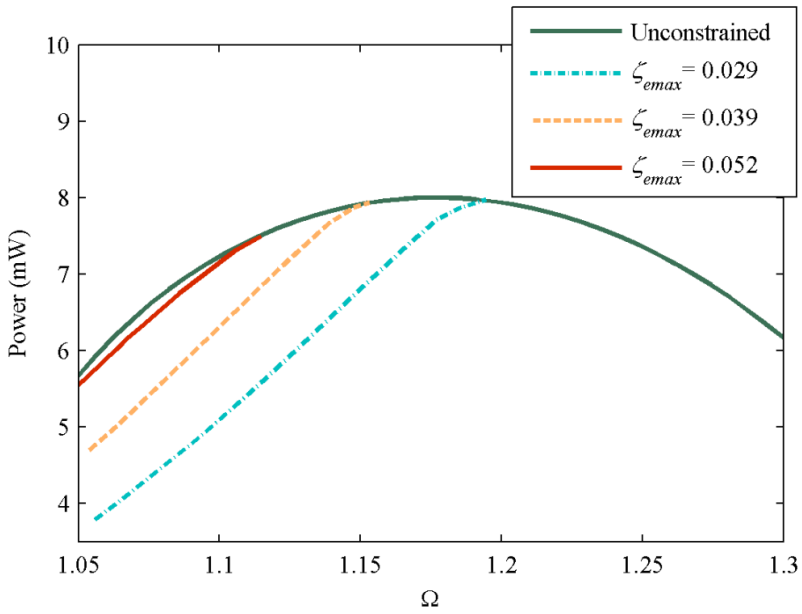

Figure 4.20 Comparison of the output power under the unconstrained and constrained conditions

Figure 4.20 shows the comparison under the ideal condition and the electrical damping constrained case. Under the unconstrained condition, the electrical damping can be arbitrary tuned to make the resonance point of the system be equal to the excitation frequency for achieving the maximum output power, which corresponds to the single parameter optimisation condition of the general shown in Section 4.3.

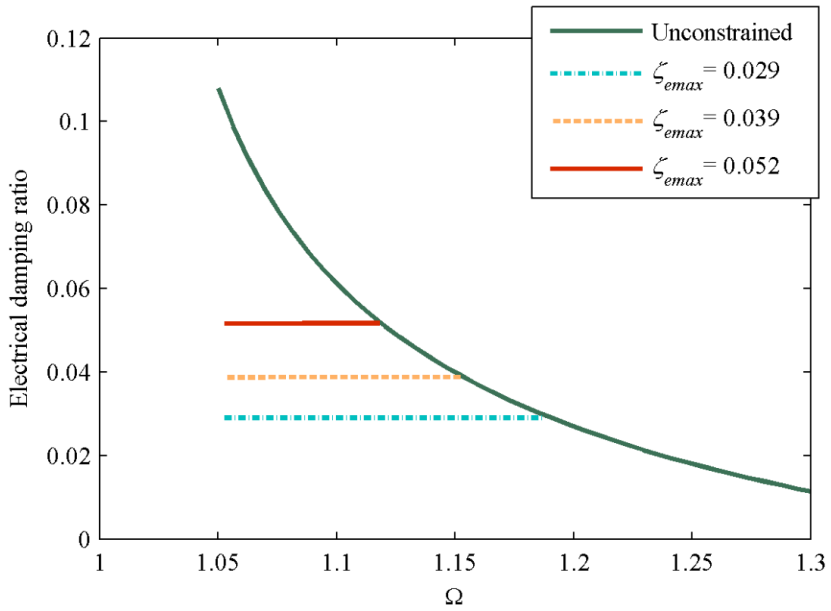

Figure 4.21 Variation of the electrical damping under the unconstrained and constrained conditions

The corresponding value of the electrical damping ratio with the variation of the excitation frequency is plotted in Figure 4.21，with the decreasing of the excitation frequency, the required electrical damping increases until it reach the limit, after that the operating point of the system moves away from the peak resonance point.

However, the above discussion is about the condition that all the parameters of the device are given except for the electrical damping, thus, the problem is how to appropriately determine the value of the parameters for a given excitation. It is assumed that the energy harvester achieves a complete optimisation and there is no electrical damping limit. Similar to Equation (4.9), the amplitude of the dissipated power by the electrical damper can be expressed as

$$P_d = \frac{c_e F^2}{\left(c_m + c_e\right)^2} \tag{4.30}$$

The optimum electrical damping is then obtained from $\frac{\partial P_d}{\partial c_e} = 0$, which gives:

$$c_{eopt} = c_m \tag{4.31}$$

Therefore, a constrained electrical damping smaller than the mechanical damping is selected for the parameters optimisation, the seismic mass of the device is selected as the design variable for a given excitation, while the other parameters are held constant.

Equation (4.12) can be rearranged to get the optimum mass as

$$m_{opt} = \frac{k}{\omega^2} + \frac{3\alpha F^2}{4c^2\omega^4} \tag{4.32}$$

Table 4.4. Parameters of the hardening-type Duffing energy harvester for optimisation

Parameter	Value	Unit
k	30	N/m
α	2×10^5	N/m^3
c_m	0.05	Ns/m
c_{emax}	0.03	Ns/m
F	0.04	N
ω	7.5	Hz

It is assumed that the parameters in Table 4.4 are given for the validation of the optimisation. The calculated optimum seismic mass according to Equation (4.32) is 0.021 kg.

To validate the result, the amplitude of power when the selected mass varies should also be analysed. By recalling the frequency-amplitude response relationship in Equation (3.29), the amplitude of the power can be expressed as

$$P = c_e \left(X\omega \right)^2 \tag{4.33}$$

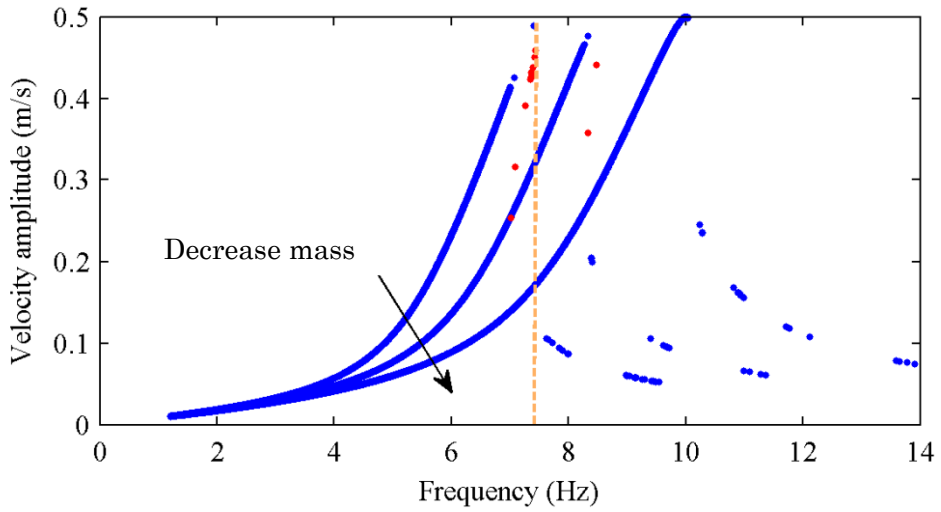

Figure 4.22 Frequency response curves under different seismic mass

By substituting Equations (4.18) into(4.29), the implicit function of the amplitude of the power can be obtained. Then, the roots of this function can be solved. However, because of its complexity, numerical calculation is conducted by using the parameters in Table 4.4. Figure

4.22 shows frequency response curves under different seismic mass, the value of the mass decrease from 0.21 kg (optimum value) to 0.1 kg with the direction of the arrow. The dashed line is the excitation frequency, it can be noted that the amplitude of the response velocity shows the decreasing tendency.

The power as a function of the seismic mass is depicted in Figure 4.23. The power shows a sharp decrease when the mass exceeds the optimum value due to the operation point jump down to the low energy orbit.

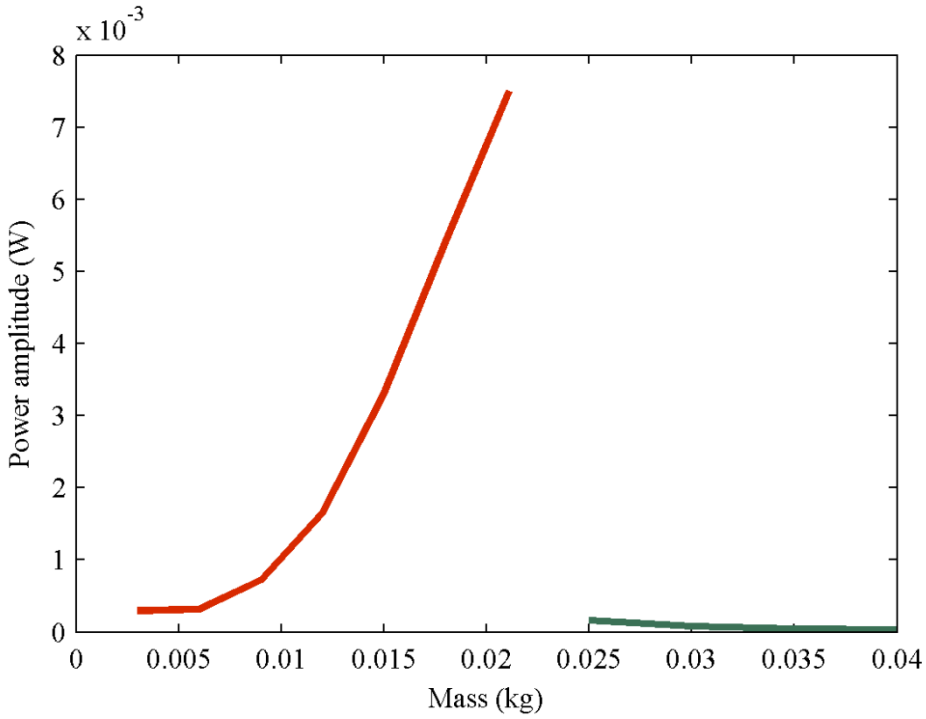

Figure 4.23 Power as a function of the seismic mass

4.6 Summary

In this chapter, parameter optimisation of the Duffing energy harvester under a harmonic vibrating environment has been analysed with the consideration of two kinds of typical transducer models.

Under the two parameters optimisation condition, for the form of inductive transduction, as embodied by a permanent magnetic linear DC generator, the maximum power is delivered to an electrical load, when its resistance is equal to the sum of the internal resistance and the electrical analogue of the mechanical damping coefficient. For the piezoelectric transducer model, the expression of the equivalent electromechanical coupling coefficient is derived for the inductive transducer, which depends on the excitation frequency and the load resistance because of the

exist of the capacitance. Based on this work, the corresponding parameters optimisation is conducted.

Moreover, for the single parameter optimisation, only the load resistance can be tuned for maximum power outputting, and the corresponding analytical expression of the load resistance is also derived.

In the practical applications, the relative displacement of the seismic mass is usually constrained. Furthermore, there is the limit for the available electrical damping of the transducer. Both of the conditions are discussed. The energy harvester can still keep normal operation under the certain constraints.

The common point of the different conditions is that the optimised operating point of the energy harvester is always closed to the point, at which the backbone curve intersects the frequency response, i.e. the jump-down point of the frequency response curve.

However, it should be mentioned that, when an optimum energy harvesting system is designed, the parameters should be optimised according to the design principle of the unconstrained case in the first step. And, if the amplitude of the relative displacement response exceeds the allowed maximum value, it will be valid for the constrained optimisation principle.

Chapter 5

Comparative Analysis for Random Excitation

5.1 Introduction

As mentioned in Chapter 1, related to literature review of the random excitation, it was already validated that the nonlinearities do not tend to provide the performance enhancement of the energy harvesting under ideal Gaussian white noise excitations. On the other hand, in fact, the environmental excitations have most of their energy trapped within a narrow bandwidth, namely possessing the characteristics of a band-limited noise excitation.

Therefore, it becomes necessary for the comparative analysis among the linear, hardening-type monostable, and bistable configurations under the band-limited noise excitations, which is conducted to provide the guidance for the practical design of the randomly excited energy harvester.

For rational comparison of the different configurations, the parameters optimisation should be indetical for each system. Therefore, the parameters interpretation is presented first for appropriately determining the optimisation variable for the performance comparison, including the role of the linear stiffness and nonlinear stiffness on the performance of the hardening-type monostable- and bistable energy harvesters.

Then, the comparative analysis of the three different configurations is carried out under both of the conditions of the constant and optimised electrical damping levels.

Finally, the performance comparison is also conducted among the different configurations under the constrained electrical damping and displacement, considering the practical limit of the electrical damper and the maximum stroke of the device.

5.2 Interpretation of the parameters

For a give band-limited noise excitation, in order to make a fair comparison of different configurations, the parameters should be optimised for each case, e.g. stiffness and electrical damping. It should be mentioned that because of the generally higher available electrical damping level of the electromagnetic-type transducer compared with the piezoelectric-type, which is beneficial for achieving the required optimised electrical damping, the electromagnetic-type transducer is adopted for the numerical parameters interpretation. The general governing equation of the energy harvesters can be written as

$$m\ddot{x} + c\dot{x} \pm kx + \alpha x^3 = N(t) \tag{5.1}$$

where c is the total damping, and it is the sum of the mechanical damping c_m and the electrical damping c_e, $N(t)$ is the band-limited noise excitation.

It can be found that either the stiffness or the electrical damping can be selected as the parameters for optimisation while the other parameters are held constant. Thus, the influence of the stiffness on the performance of the energy harvester under certain excitation will be discussed firstly.

Table 5.1. Parameters of the energy harvesters for parameters interpretation

Parameter	m	c_m	σ_{acc}^2	Bandwidth
Value	0.028 kg	0.036 Ns/m	2.49 m^2s^{-4}	10-20 Hz

Table 5.1 shows the parameters for the numerical studies. The variance of the excitation acceleration is set to be 2.49 m^2s^{-4}, and the bandwidth of the noise excitation is 10-20 Hz with the centre frequency of 15 Hz.

It should be mentioned that the selected bandwidth is physically reasonable, and it is also considered about the fundamental frequency of the experimental device in the next section, which is 15 Hz. All the other parameters shown in Table 5.1 are the represent of the experimental parameters.

Moreover, it is more concise to use the non-dimensional expression of the bandwidth. However, because the stiffness of the energy harvester is varied for parameters interpretation, the non-dimensional cannot be adopted in this section.

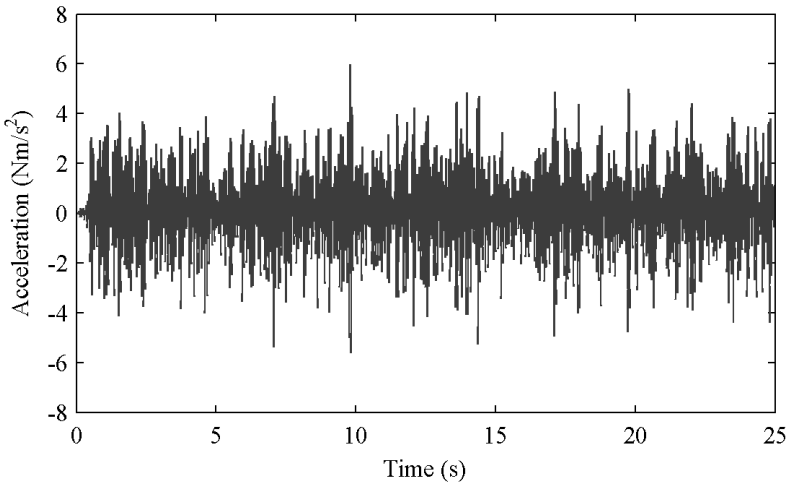

Figure 5.1. Time domain data of the band-limited noise excitation shown in Table 5.1.

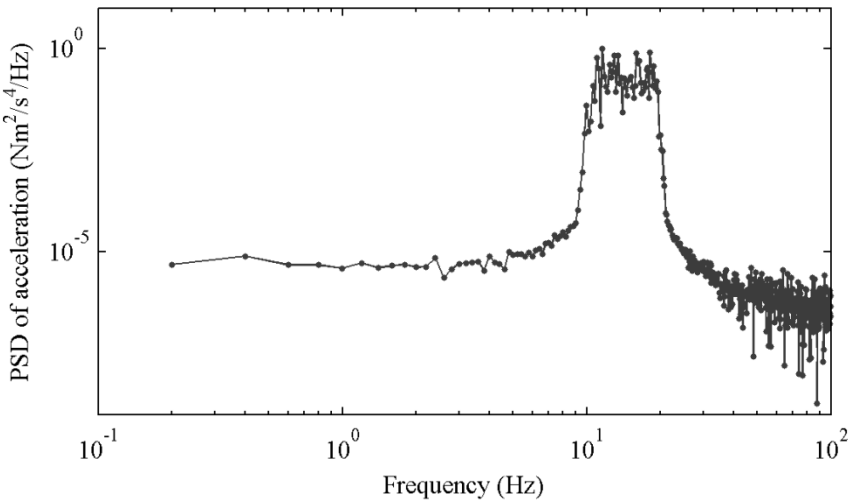

Figure 5.2. PSD (Power Spectrum Density) of the band-limited noise excitation shown in Table 5.1.

The band-limited noise signals are created by applying the band-pass filters to the original Gaussian white noise signal. Figure 5.1 shows time domain of the band-limited white noise, while the PSD (Power Spectrum Density) of the filtered band-limited noise is presented in Figures 5.2.

- Hardening-type monostable configuration

By using parameters in Table 5.1, Figures 5.3, 5.5 to 5.7 show the corresponding simulation results of the hardening-type monostable energy harvester subjected to a noise excitation with the bandwidth of 10-20 Hz by varying the other parameters, i.e. the rms output power of the energy harvester is simulated as a function of the linear stiffness and nonlinear stiffness under different electrical damping levels.

(a) Side view

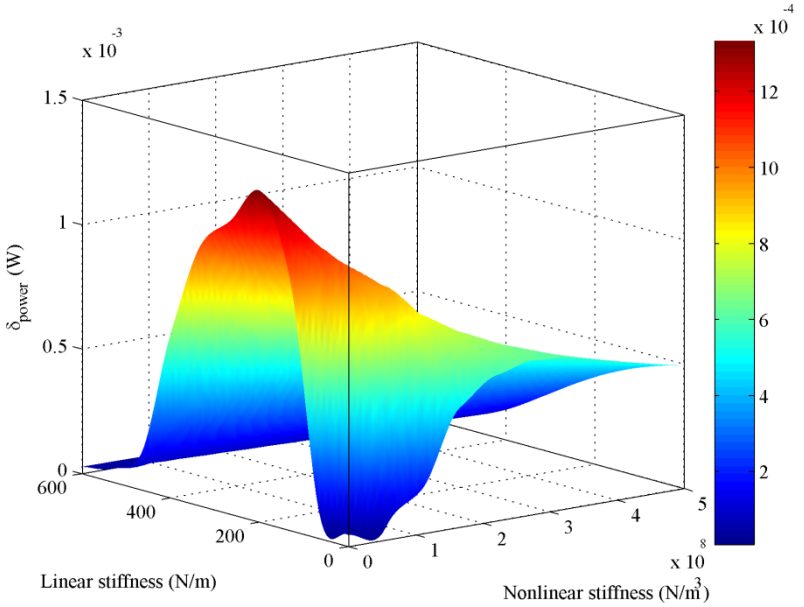

(b) Top view

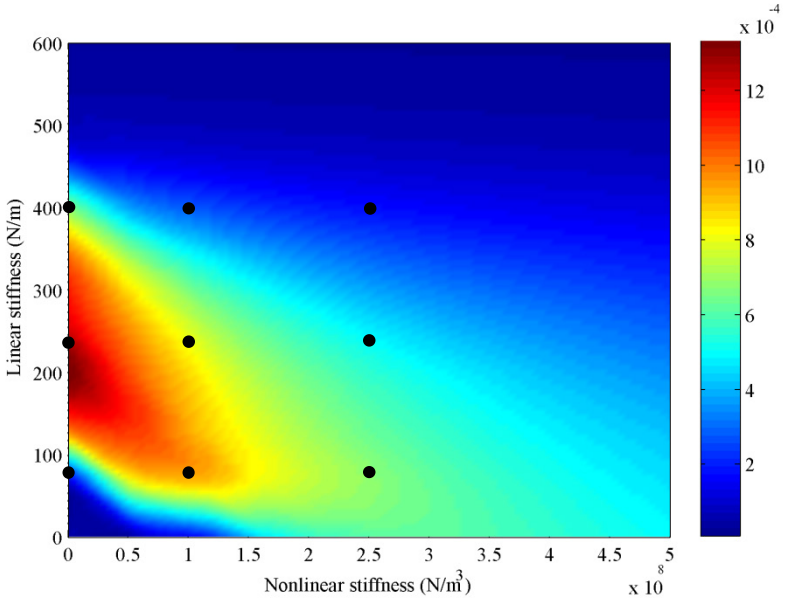

Figure 5.3. The rms power (W) as a function of the linear stiffness and nonlinear stiffness. ($c_e = 0.15\,\mathrm{Ns/m}$ Hardening-type monostable oscillator)

For better understanding and interpretation of the observation in Figure 5.3, the frequency response curves of different linear- and nonlinear stiffness (corresponds to the black points in Figure 5.3(b)) under the noise excitation with the bandwidth of (10-20Hz) are shown in Figure 5.4, where the red line represents the unstable energy orbit. And the frequency axis is plotted using the non-dimensional form for concise expression. When the linear stiffness k is 80 N/m as shown in Figure 5.4(a), with the increasing of nonlinear stiffness α, the peak response area is included by the bandwidth of the noise excitation, thereby showing the increasing tendency of the harvested power as shown in Figure 5.3(b). However, if one further increases the nonlinear stiffness, it presents the decrease of the performance. This is because the operating point of the energy harvester cannot stablisied on the high energy orbit under random excitations.

In Figure 5.4 (b), the linear stiffness is set to be 240 N/m, the corresponding fundamental frequency near to the centre frequency (i.e. 15 Hz) of the band-limited noise excitation. The continues decreasing tendency of the performance can be observed with the increasing of the nonlinear stiffness as presented in Figure 5.3(b), due to the frequency response curve skew towards to the higher frequency area and also the unstable high-energy orbit. The results when the linear stiffness is 400 N/m can also be interpreted from Figure 5.4 (c).

The similar results can be observed in Figures 5.5 to 5.7.

(a)

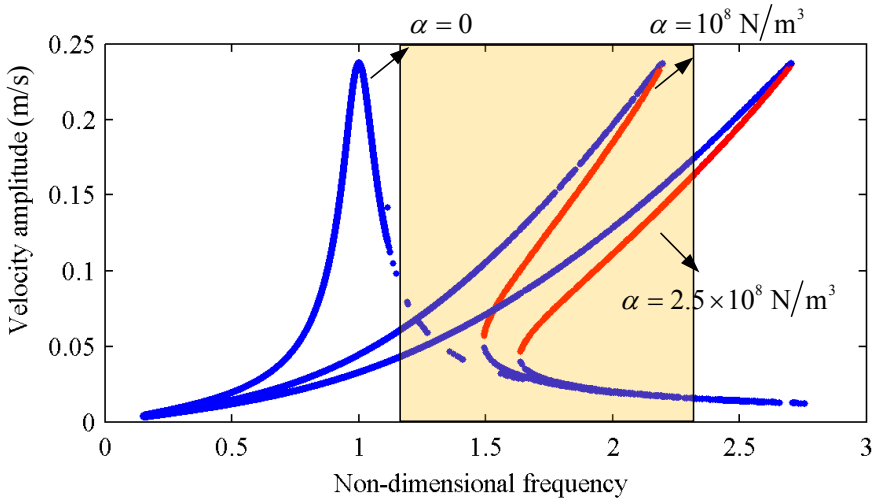

(b)

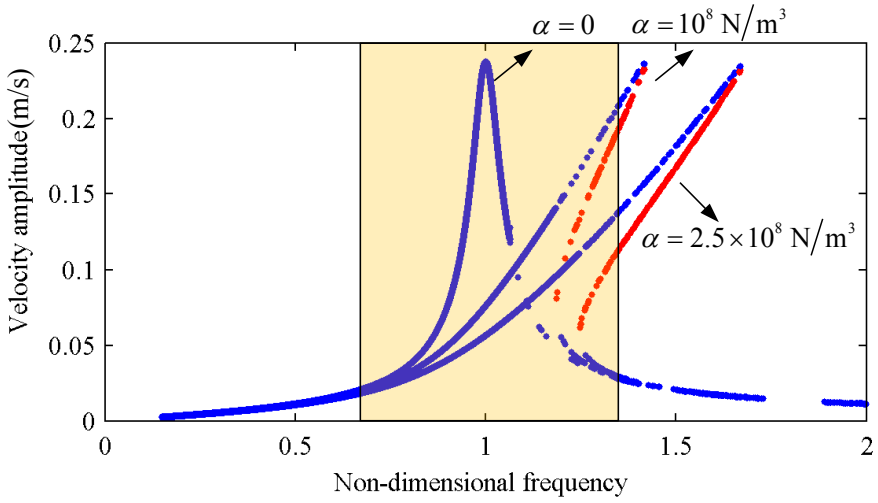

(c)

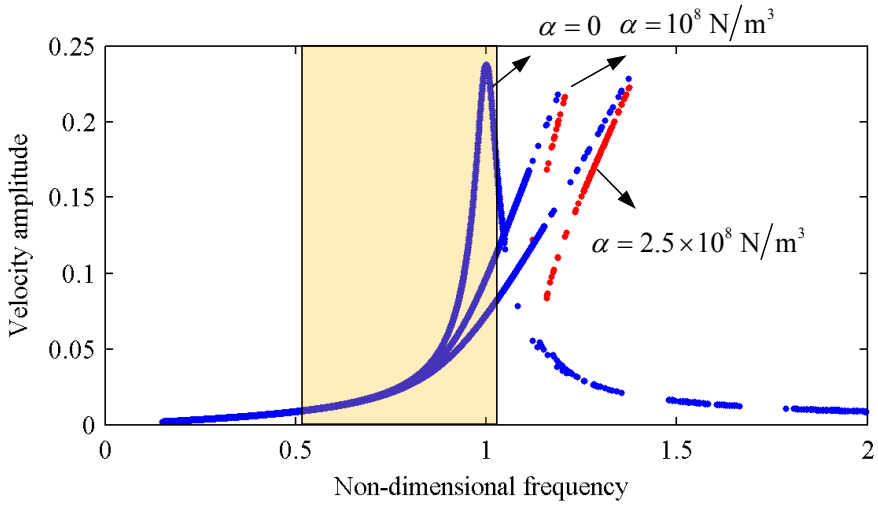

Figure 5.4. Frequency response curves under different linear stiffness and nonlinear stiffness and the non-dimensional bandwidth of the noise excitation (10-20 Hz, yellow area): (a) linear stiffness k = 80N/m, (b) linear stiffness k = 240N/m, and (c) linear stiffness k = 400N/m.

(a) Side view

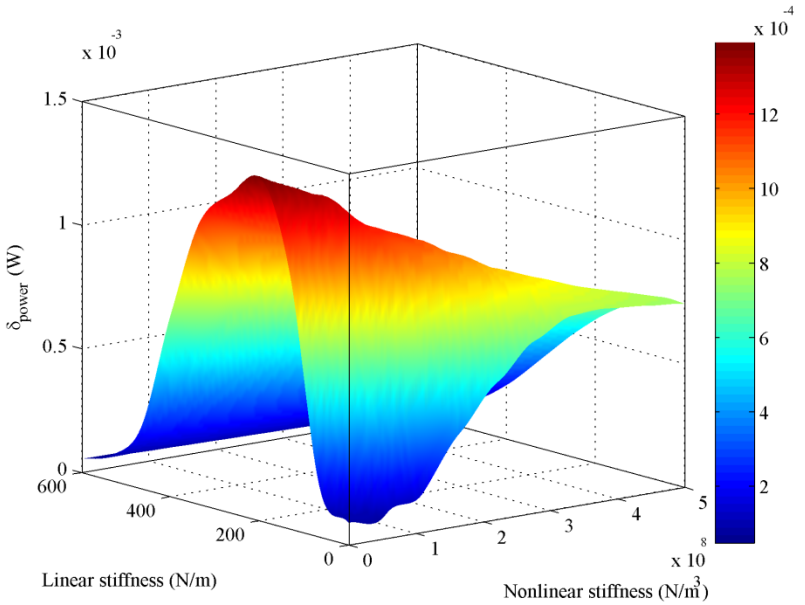

(b) Top view

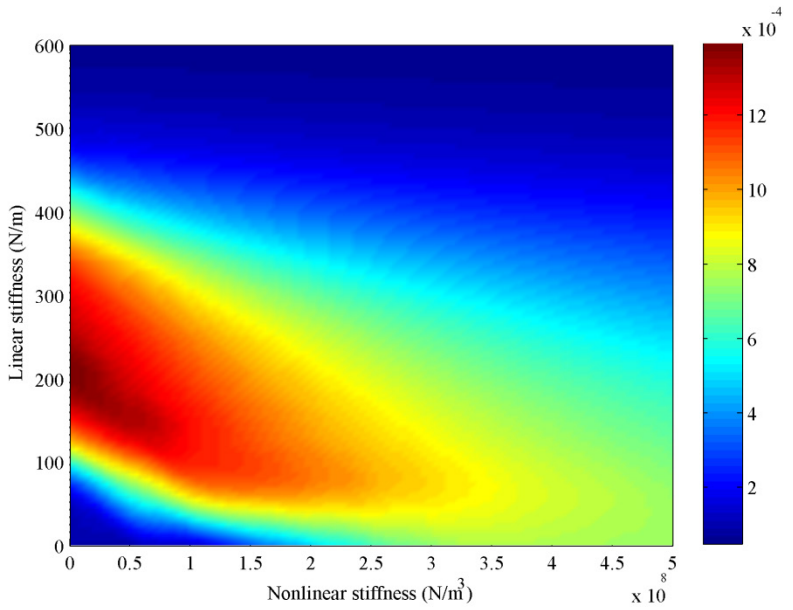

Figure 5.5. The rms power (W) as a function of the linear stiffness and nonlinear stiffness. ($c_e = 0.3\,\mathrm{Ns/m}$ Hardening-type monostable oscillator)

(a) Side view

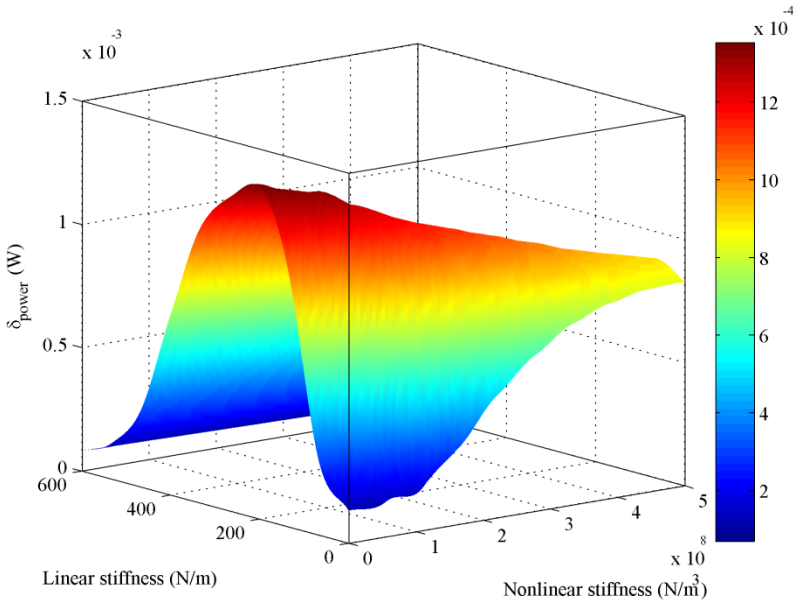

(b) Top view

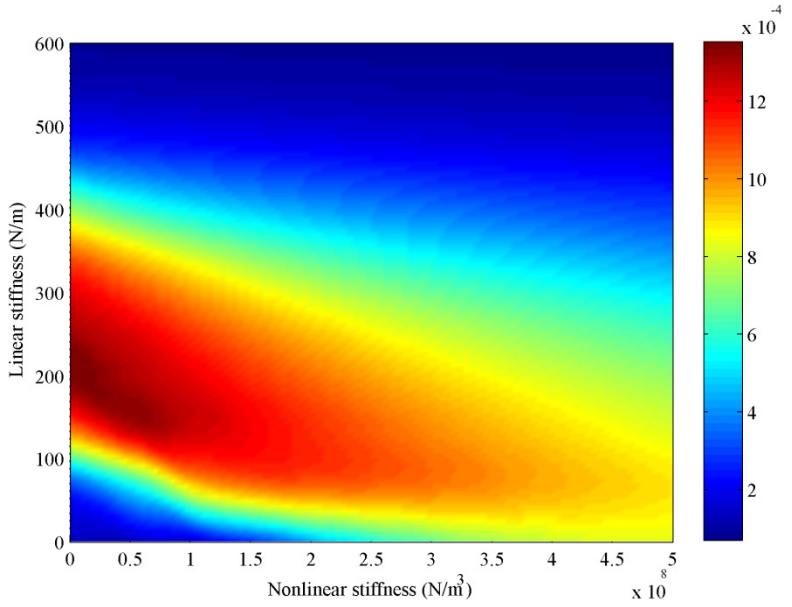

Figure 5.6. The rms power (W) as a function of the linear stiffness and nonlinear stiffness. ($c_e = 0.45\,\mathrm{Ns/m}$ Hardening-type monostable oscillator)

(a) Side view

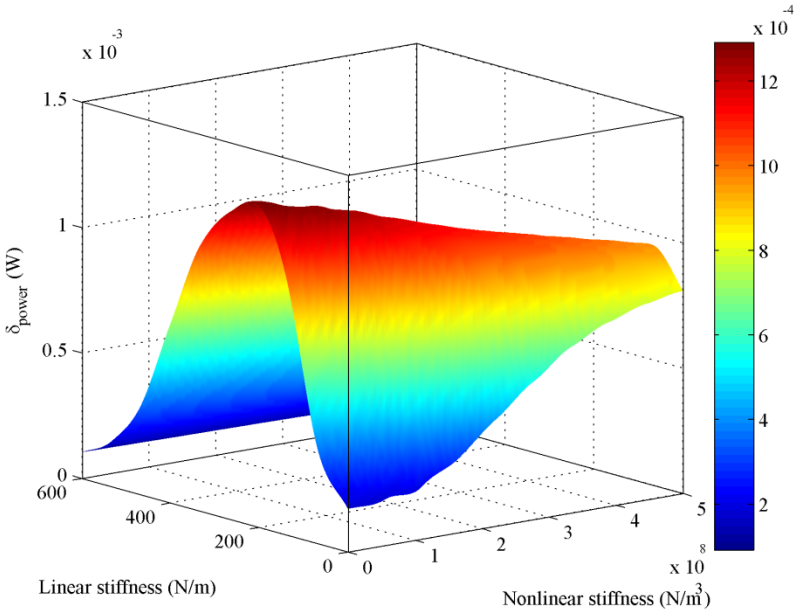

(b) Top view

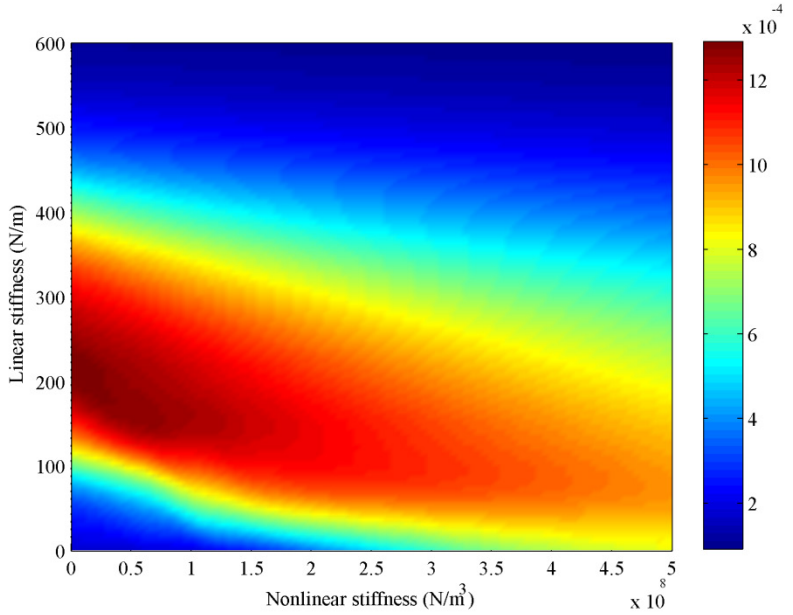

Figure 5.7. The rms power (W) as a function of the linear stiffness and nonlinear stiffness. ($c_e = 0.6\,\mathrm{Ns/m}$ Hardening-type monostable oscillator)

From the above simulation results, it can be noted that it presents similar tendency under different electrical damping levels, the peak response point moves towards to the lower linear stiffness with the increasing of the nonlinear stiffness, which is due to the hardening effect.

However, the most high output power is when the nonlinear stiffness is equal to zero, which indicts a linear energy harvester. Moreover, the corresponding linear stiffness at the peak response point is around 240 N/m, where the fundamental frequency is around 15 Hz. It is same as the centre frequency of the band-limited noise.

- Bistable configuration

Similar to the hardening-type monostable configuration, the rms output power of the bistable energy harvester is also simulated as a function of the linear stiffness and nonlinear stiffness under various electrical damping levels.

(a) Side view

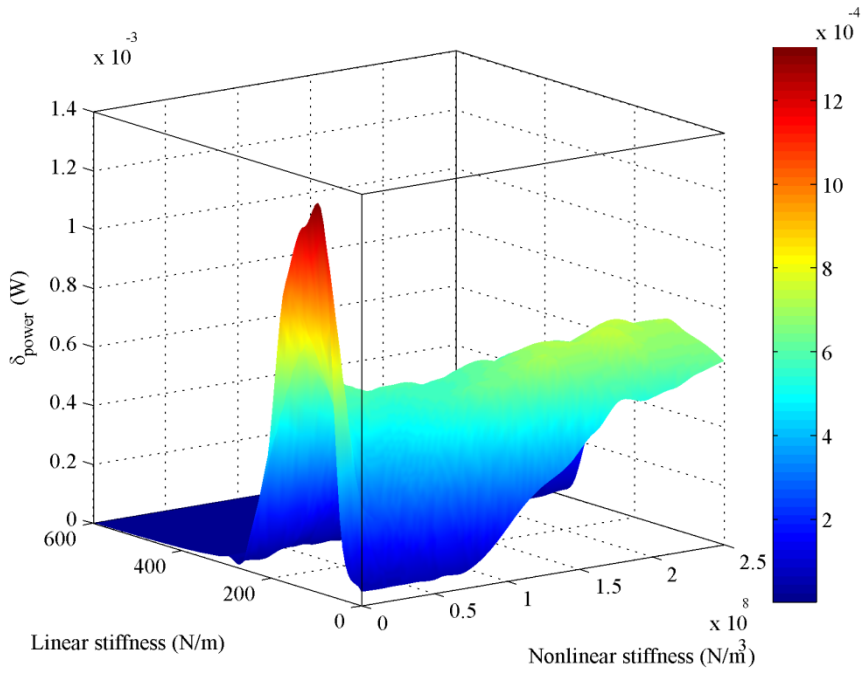

(b) Top view

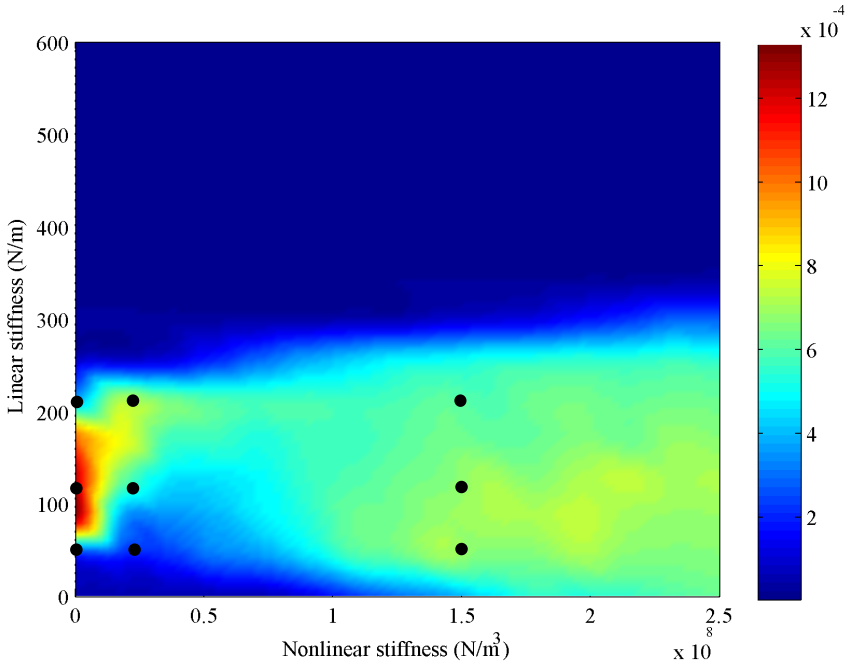

Figure 5.8 The rms power (W) as a function of the linear stiffness and nonlinear stiffness. ($c_e = 0.15\,\mathrm{Ns/m}$ Bistable oscillator)

To interpret the results shown in Figure 5.8, the frequency response curves of different linear- and nonlinear stiffness (corresponds to the black points in Figure 5.8(b)) under the noise excitation with the bandwidth of (10-20Hz) are shown in Figures 5.9 to 5.11. Similar to the hardening-type case, the frequency axis is plotted using the non-dimensional form for concise expression.

When the linear stiffness k is 120 N/m as shown in Figure 5.9, when the nonlinear stiffness α is very small, the energy harvester operate as the linear case as shown in Figure 5.9 (a), because the potential ($\Delta U = k^2/4\alpha$) is very large, and the energy harvester only oscillate within one potential well and nears to the equilibrium point, with the increasing of the nonlinear stiffness, the frequency response curve skew towards to the lower frequency side because of the softening effect of the potential well of the bistable system, and as presented in Figure 5.9(b), there is another highest energy orbit exists, which indicts the inter-well motion of the energy harvester. However, it is not covered by the bandwidth of the noise excitation under this condition. Thus, in Figure 5.9(b) the energy harvester tends to oscillate within one potential well and cannot stabilise on the high-energy orbit of the frequency response curve skews to the low frequency sider. That't why the performance decreases compared with that of Figure 5.9(a).

Then, with the further increase of the nonlinear stiffness, as shown in Figure 5.9(c), the highest energy orbit is included by the bandwidth of the noise excitation. Although it cannot be stabilised, the large-amplitude inter-well motion can be sometimes triggered, thereby increasing the performance.

From Figures 5.10 and 5.11, the conditions when the linear stiffness equals to 50 N/m and 210 N/m as shown in Figure 5.8(b) can be interpreted using the same principle.

(a)

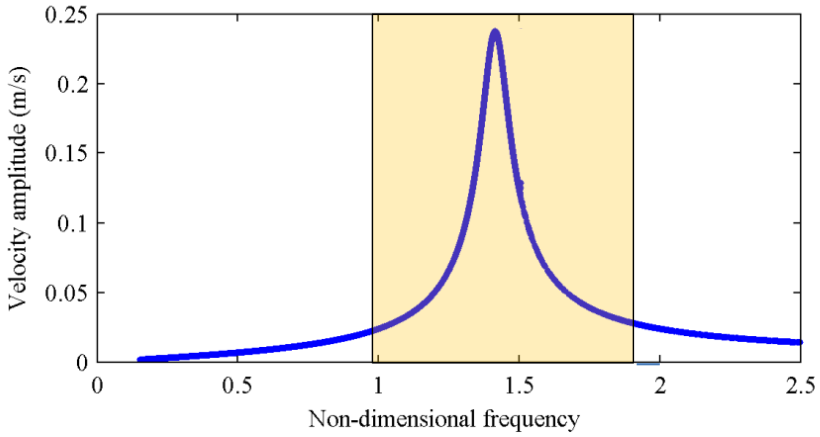

(b)

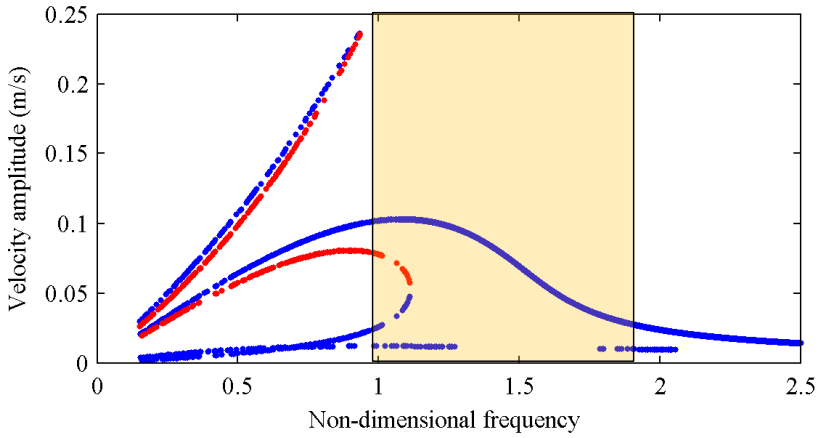

(c)

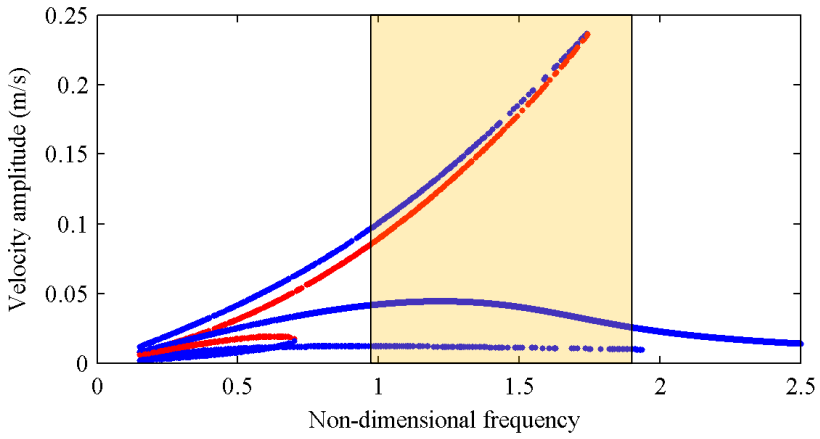

Figure 5.9. Frequency response curves under the constant linear stiffness (k = 120 N/m) and different nonlinear stiffness and the non-dimensional bandwidth of the noise excitation (10-20 Hz, yellow area): (a) nonlinear linear stiffness $\alpha = 1$ N/m^3, (b) nonlinear stiffness $\alpha = 2\times10^7$ N/m^3, and (c) nonlinear stiffness $\alpha = 1.5\times10^8$ N/m^3.

(a)

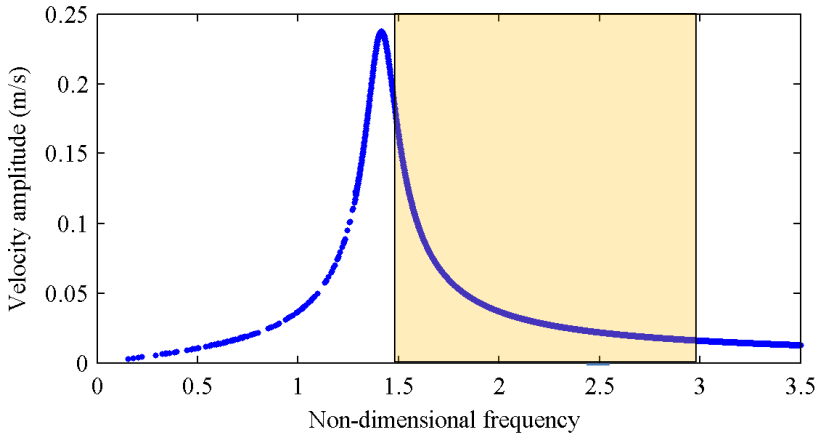

(b)

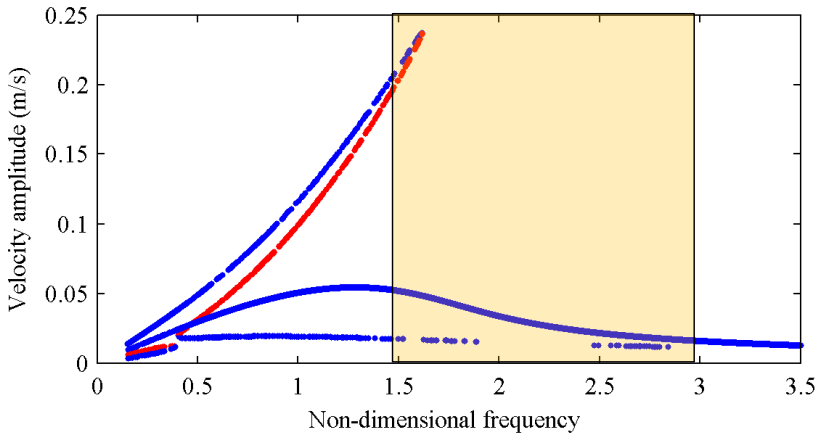

(c)

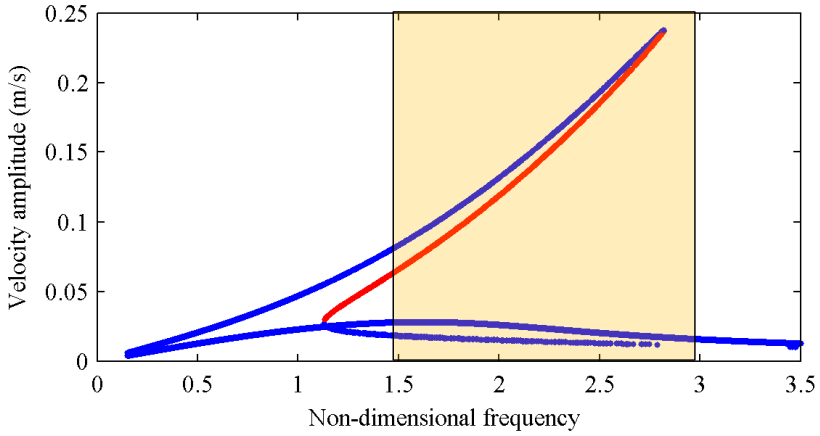

Figure 5.10. Frequency response curves under the constant linear stiffness (k = 50 N/m) and different nonlinear stiffness and the non-dimensional bandwidth of the noise excitation (10-20 Hz, yellow area): (a) nonlinear linear stiffness $\alpha =$ N/m^3, (b) nonlinear stiffness $\alpha = 2\times10^7$ N/m^3, and (c) nonlinear stiffness $\alpha = 1.5\times10^8$ N/m^3.

(a)

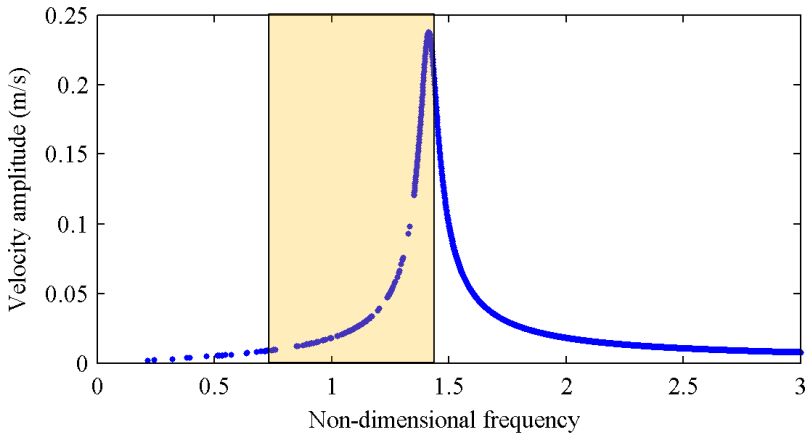
Velocity amplitude (m/s)
0.25
0.2
0.15
0.1
0.05
0
0
0.5
1
1.5
2
2.5
3
Non-dimensional frequency

(b)

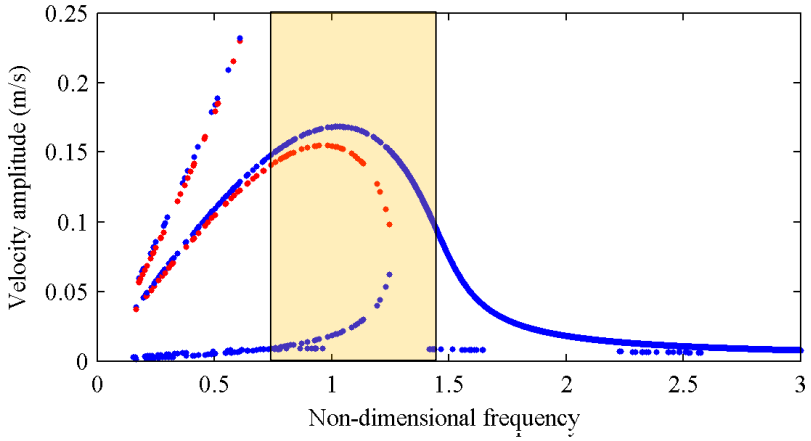
Velocity amplitude (m/s)
0.25
0.2
0.15
0.1
0.05
0
0
0.5
1
1.5
2
2.5
3
Non-dimensional frequency

(c)

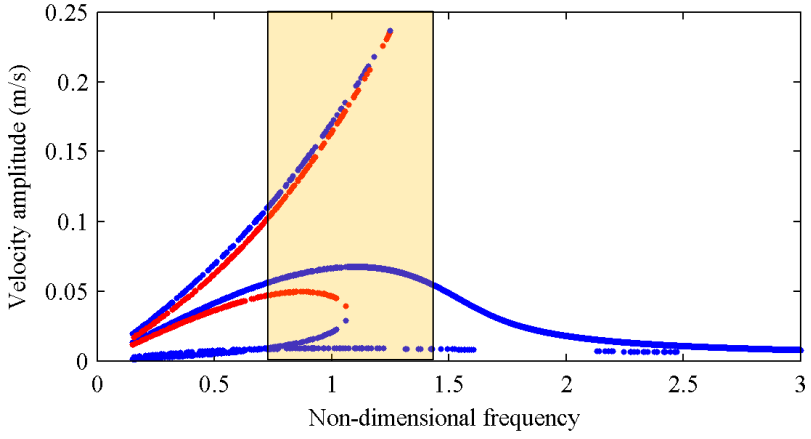
Velocity amplitude (m/s)
0.25
0.2
0.15
0.1
0.05
0
0
0.5
1
1.5
2
2.5
3
Non-dimensional frequency

Figure 5.11. Frequency response curves under the constant linear stiffness (k = 210 N/m) and different nonlinear stiffness and the non-dimensional bandwidth of the noise excitation (10-20 Hz, yellow area): (a) nonlinear linear stiffness α = N/m^3, (b) nonlinear stiffness $\alpha = 2\times10^7$ N/m^3, and (c) nonlinear stiffness $\alpha = 1.5\times10^8$ N/m^3.

(a) Side view

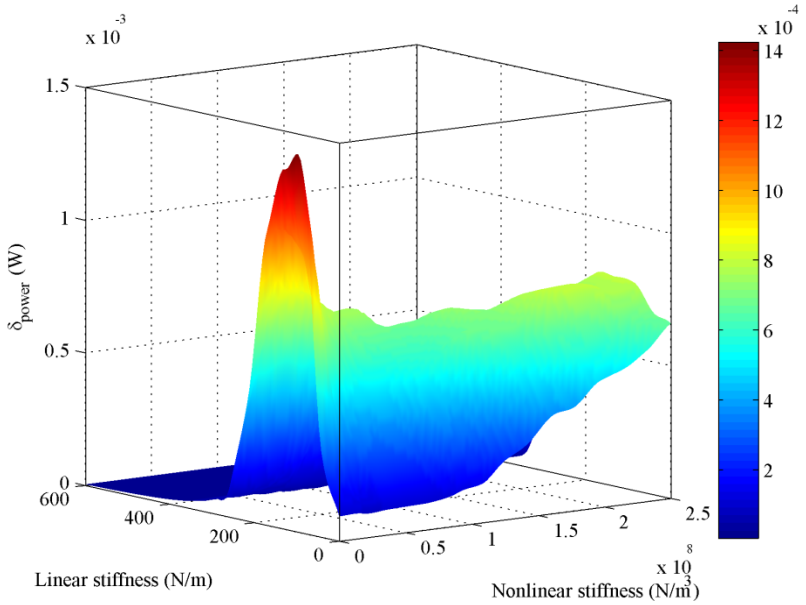

(b) Top view

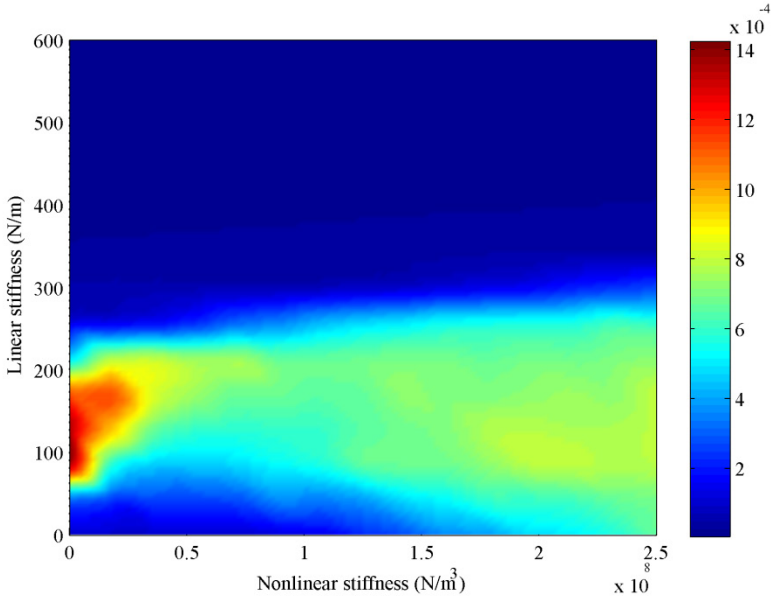

Figure 5.12 The rms power (W) as a function of the linear stiffness and nonlinear stiffness. ($c_e = 0.3\,\mathrm{Ns/m}$ Bistable oscillator)

(a) Side view

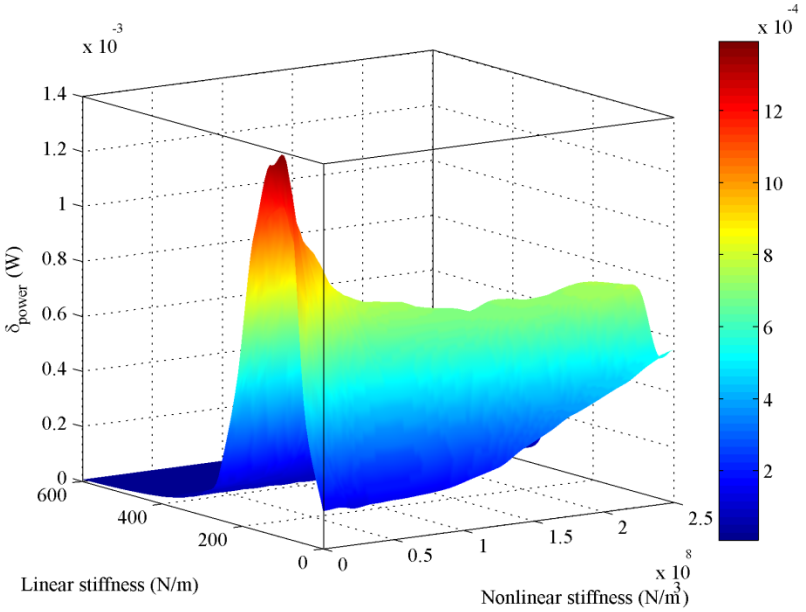

(b) Top view

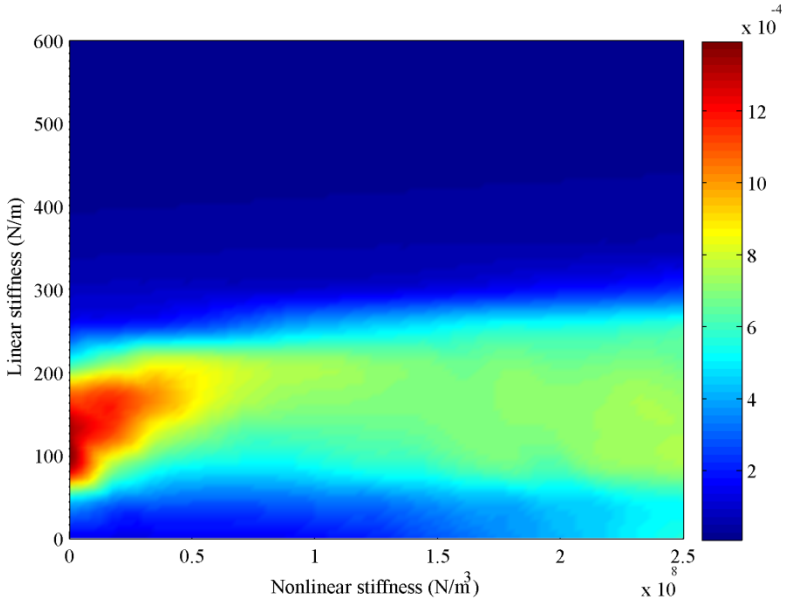

Figure 5.13 The rms power (W) as a function of the linear stiffness and nonlinear stiffness. ($c_e = 0.45\,\mathrm{Ns/m}$ Bistable oscillator)

(a) Side view

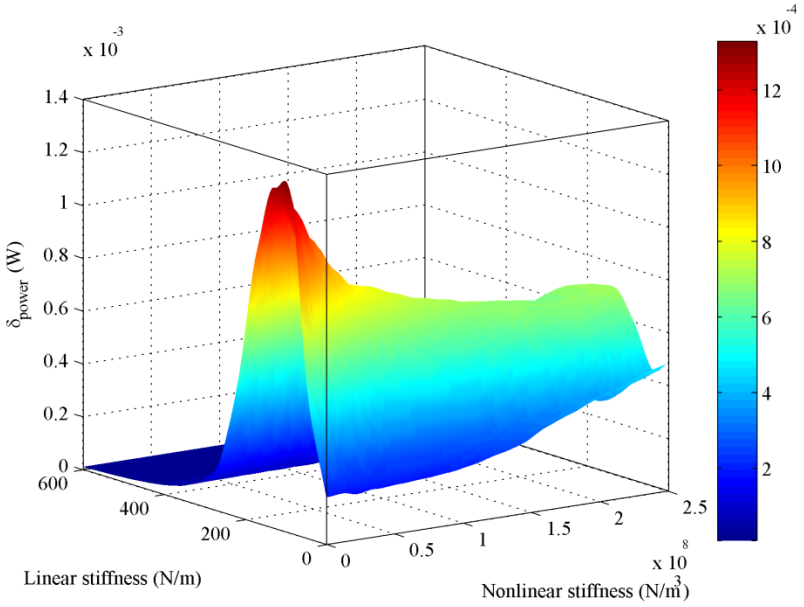

(b) Top view

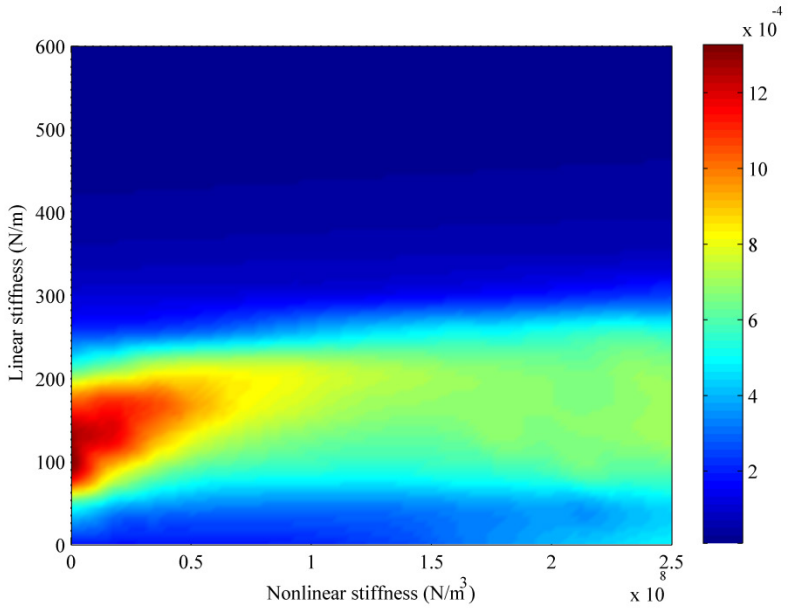

Figure 5.14 The rms power (W) as a function of the linear stiffness and nonlinear stiffness. ($c_e = 0.6\,\mathrm{Ns/m}$ Bistable oscillator)

Similar results are also observed in Figures 5.12 to 5.14 for the bistable case, but the optimised linear stiffness is nearly half of the hardening-type monostable case, that is because the stiffness around the equilibrium point with in one potential well of the bsitable system is

obtained as *2k*. Thus, it is fundamental frequency is also located at the around the midpoint of the frequency bandwidth of the excitation. Moreover, the peak response point is obtained when the nonlinear stiffness α is very small, it indicts a very deep potential well (potential $\Delta U = k^2/4\alpha$), the oscillator only operate around the equilibrium point, which is similar to a linear energy harvester with the natural frequency of $\sqrt{2k/m}$.

From the observation results, it can be concluded as:

Hardening-type monostable configurations:

(1) For a given noise excitation with certain bandwidth, if both the linear stiffness and nonlinear stiffness can be tuned for optimisation, the maximum power output always occur at the point, where the nonlinear stiffness equals zero.

(2) The optimised linear stiffness exists, when the fundamental frequency is equal to the centre frequency of the band-limited noised excitation.

(3) Under the optimised condition, the energy harvester becomes a linear energy harvester.

Bistable configurations:

(1) For a given noise excitation with certain bandwidth, if both the linear stiffness and nonlinear stiffness can be tuned for optimisation, the maximum power output always occurs at the point, where the nonlinear stiffness is extremely small (can't be zero).

(2) The optimised linear stiffness exists, when the fundamental frequency at the equilibrium point is equal to the centre frequency of the band-limited noised excitation.

(3) Under the optimised condition, the energy harvester operates like a linear energy harvester.

5.3 Comparative analysis

From the discussion in Section 5.2, the following conclusions can be obtained as:

(1) If the linear and nonlinear stiffness are selected as the optimisation parameters, the linear configuration can be directly employed, for a given band-limited noise excitation with the fixed centre frequency, because the optimised peak output power point is always at when the nonlinear stiffness is zero (for hardening-type monostable configuration) or extremely small

(for bistable configuration), and operated as a linear energy harvester.

(2) When the excitation presents the time-varying property of the frequency bandwidth or centre frequency, if the stiffness can be tuned, the linear energy harvester can be directly employed, in other words, there is no necessary to conduct the performance comparison.

Thus, the stiffness is kept as constant but the electrical damping should be optimised for more fair comparison under different centre frequencies and bandwidths of the band-limited excitations. The maximum bandwidth of the band-limited noise excitation will be selected large enough (i.e. around two times larger than the fundamental frequency) to make the effect of the nonlinearities on the performance become not obvious anymore, which is similar to the white noise condition.

However, before the performance with optimised electrical damping level, the comparison with the constant electrical damping is also conducted in the following Section 5.3.1.

5.3.1 Comparative analysis with constant electrical damping

- Energy harvester configurations

To compare the performance of the energy harvesters, linear, nonlinear monostable and bistable configurations were designed to undertake the work reported here. By considering a cantilever beam it is possible to create an appropriate nonlinearity by positioning a magnetic mass on the cantilever tip which moves relative to externally fixed permanent magnet(s). The dependence of the restoring force on the tip deflection can be changed by controlling the distance between the magnets and also through their polarities.

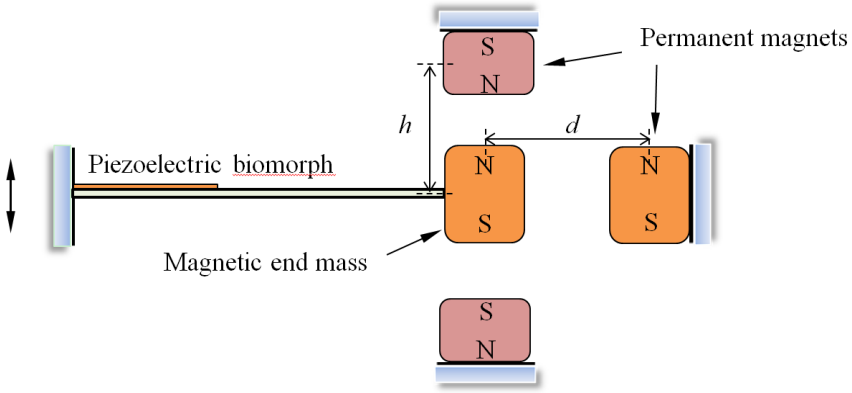

Figure 5.15. Schematic diagram of the energy harvesters in different configurations.

Figure 5.15 presents a schematic diagram from which two types of energy harvester can be synthesised by means of intentionally introduced nonlinearities. Bistability can be created by positioning two permanent magnets with opposite polarities, respectively on the piezoelectric cantilever tip and on another fixed support at a distance d in the horizontal direction. The corresponding expression for the interaction force can be obtained by setting h to zero in Equation (3.5).

To achieve the monostable nonlinear configuration, another two permanent magnets are fitted symmetrically at an equilibrium distance h at either side of the magnetic end mass, and the magnets are arranged in a repulsive configuration to produce the hardening-type nonlinearity.

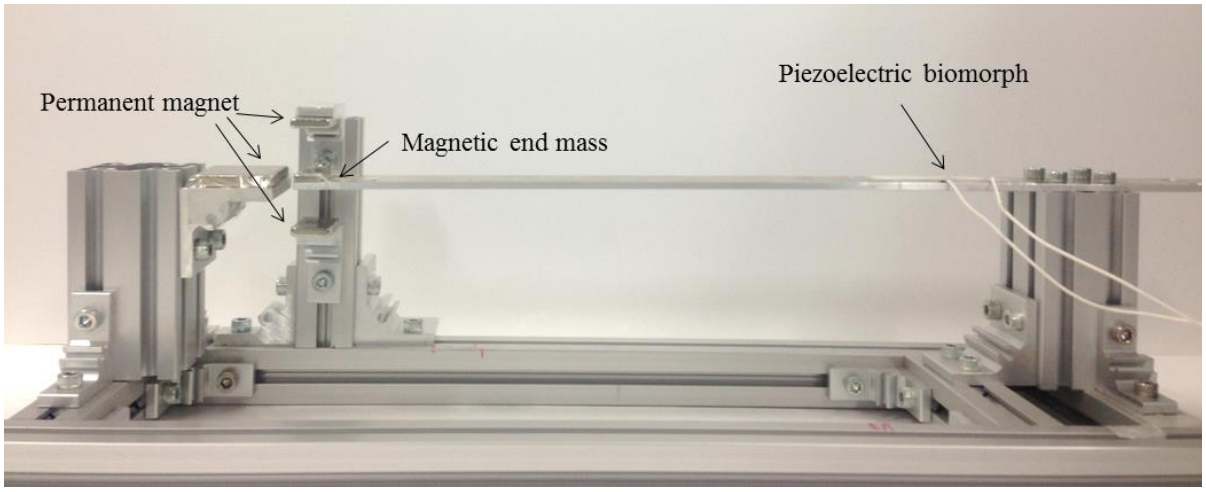

Figure 5.16. Photo of the energy harvesters in different configurations.

A photograph of the experimental device is shown in Figure 5.16. The permanent magnets are attached to sliders on rails that allow the distance to be adjusted. In order to conduct a convenient comparison, the fundamental frequencies in different configurations are set to be equal to 15 Hz by adjusting the mass on the cantilever tip and changing the distances h and d.

The general motion equation of the system can be written as [32][42][59][91]

$$m\ddot{x} + c_m\dot{x} + kx + \alpha x^3 + \theta q = F\cos\omega t \tag{5.2a}$$

and

$$\theta x = \frac{q}{C} + R\dot{q} \tag{5.2b}$$

where c_m is the mechanical damping, m is the equivalent mass of the permanent magnet attached to the beam, θ is the modal coupling coefficient, C is the capacitance of the piezoelectric film, q is the electrical charge, $R = R_i + R_l$, and R_i and R_l are the internal and load resistances. Table 5.2 shows the parameters of the system.

Table 5.2. Parameters used in the investigations of stiffness on the frequency response.

Parameter	Value	Unit
m	0.028	kg
c_m	0.036	Ns/m
θ	645	V/m
C	110	nF
R_i	115	KΩ
R_l	1	MΩ

The experiments were conducted using a seismic shaker (IMV corporation, m060) controlled by a dSPACE 1103 controller. The main objective was to make a comparative performance study in the linear, monostable and bistable configurations under colored noise excitations. These devices allow for the chosen harvester system to be subjected to random base acceleration at specified excitation levels, frequency bandwidths and centre frequencies. The shaker table acceleration is measured by a vibrometer then the root-mean-square value is calculated by the dSPACE controller, and this is kept approximately equal for noise excitations with different bandwidths and centre frequencies by tuning the amplifier gain (noting that a constant power spectral density of the excitation produced by the shaker cannot be guaranteed under different bandwidths and centre frequencies using a fixed gain because of the dynamic characteristics of the shaker). The rms power of the piezoelectric bimorph attached on the cantilever can be obtained in a similar way, and used for comparison.

Tests consist of response comparisons under various centre frequencies and excitation levels at a constant bandwidth, and the influence of the bandwidth on the performance is assessed under several centre frequencies by keeping the same excitation level.

- Comparison under different centre frequencies and excitation levels

The responses are investigated with the change of centre frequency in different configurations in this section. Figures 5.17-5.19 show the comparison of the output voltage variance in the open-circuit configuration with band-limited noise excitation (using a bandwidth of 4 Hz) of several levels. The sampling window of the output voltage is kept wide enough for accuracy.

The results in Figure 5.17 show that at a small excitation level the peak of the output voltage occurs when the centre frequency nears the fundamental frequency for both of the monostable hardening-type monostable- and bistable configurations, and this is similar to the linear configuration. There is also not a great deal of difference for the amplitude of the peak output voltage between the results, and this indicates that these energy harvesters are operating near their equilibrium positions and do not obviously exert strong nonlinear effects.

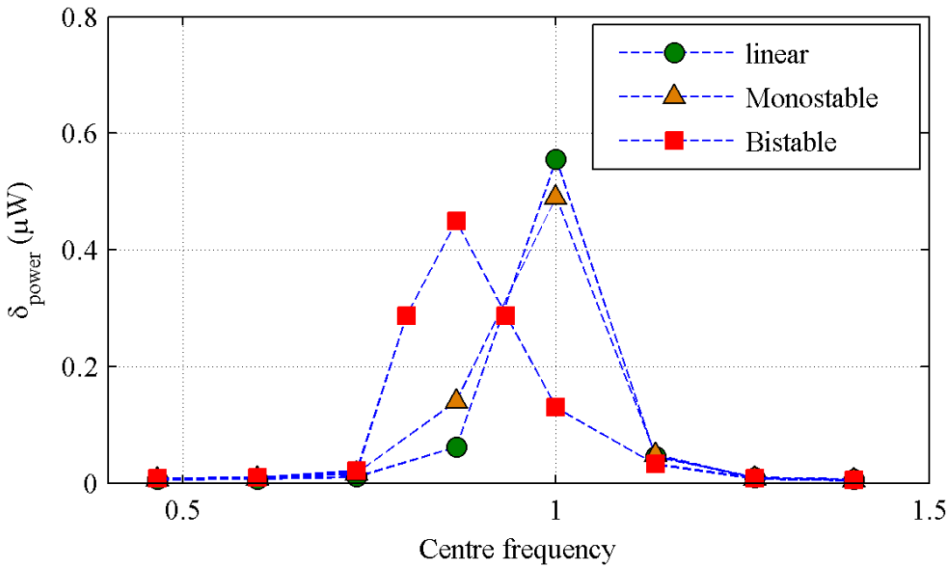

Figure 5.17. Variation of the experimental voltage variance with the excitation's centre frequency. ($\sigma_{acc}^2 = 0.0286\,m^2s^{-4}$ bandwidth $\Delta = 4\,Hz$)

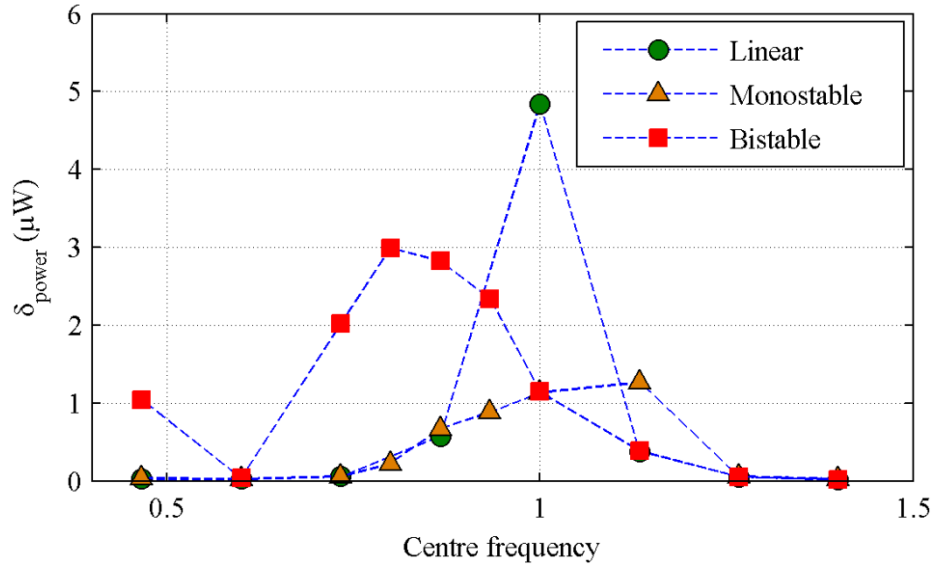

Figure 5.18. Variation of the experimental voltage variance with the excitation's centre frequency. ($\sigma_{acc}^2 = 2.49\,m^2s^{-4}$ bandwidth $\Delta = 4\,Hz$)

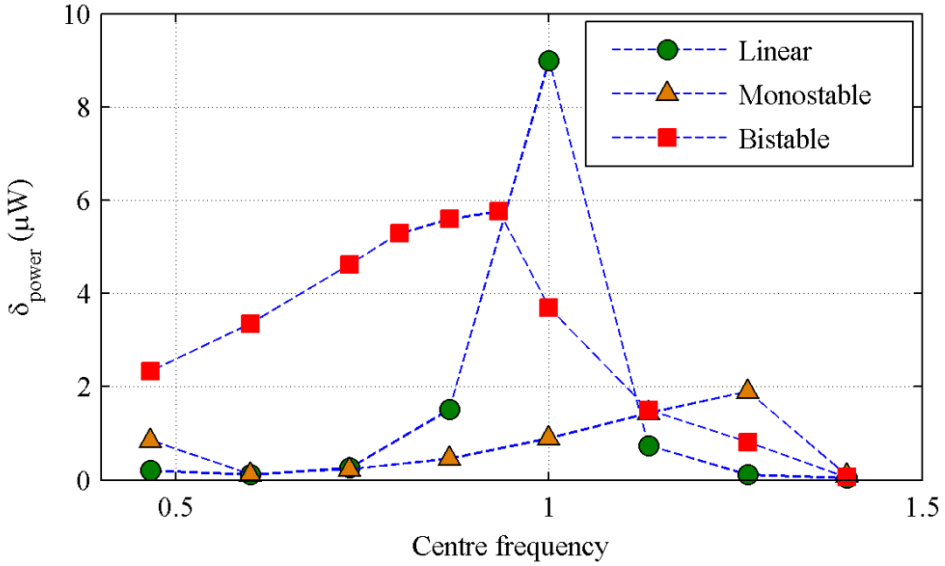

Figure 5.19. Variation of the experimental voltage variance with the excitation's centre frequency. ($\sigma_{acc}^2 = 7.38\,m^2s^{-4}$ bandwidth $\Delta = 4\,Hz$)

With the increase of the acceleration level the peak output voltage of the monostable energy harvester shifts towards higher frequencies because of the hardening effect of the stiffness, as shown in Figure 5.18. However, it can be noted that the amplitude of the peak voltage is lower when compared with the linear configuration. It is known that for a monostable hardening-type

monostable oscillator, both low- and high-energy responses can coexist for the same parameter combinations at relatively high harmonic excitation levels. This indictates that when the energy harvester is randomly excited, the high-energy orbit cannot be maintained. The performance decreased due to a noticeable hopping between the different energy orbits with the variation in excitation level. On the other hand the peak voltage of the bistable configuration shifted towards to the lower frequency away from the fundamental frequency. This phenomenon is caused by asymmetric stiffness softening effect within one potential well. Figure 5.20 shows the stiffness as a function of displacement in different configurations. It should be mentioned that for the case of the bistable energy harvester one of the equilibrium positions is set as the origin for the coordinate system. The softening effect can be observed at the side of the equilibrium position for the bistable configuration.

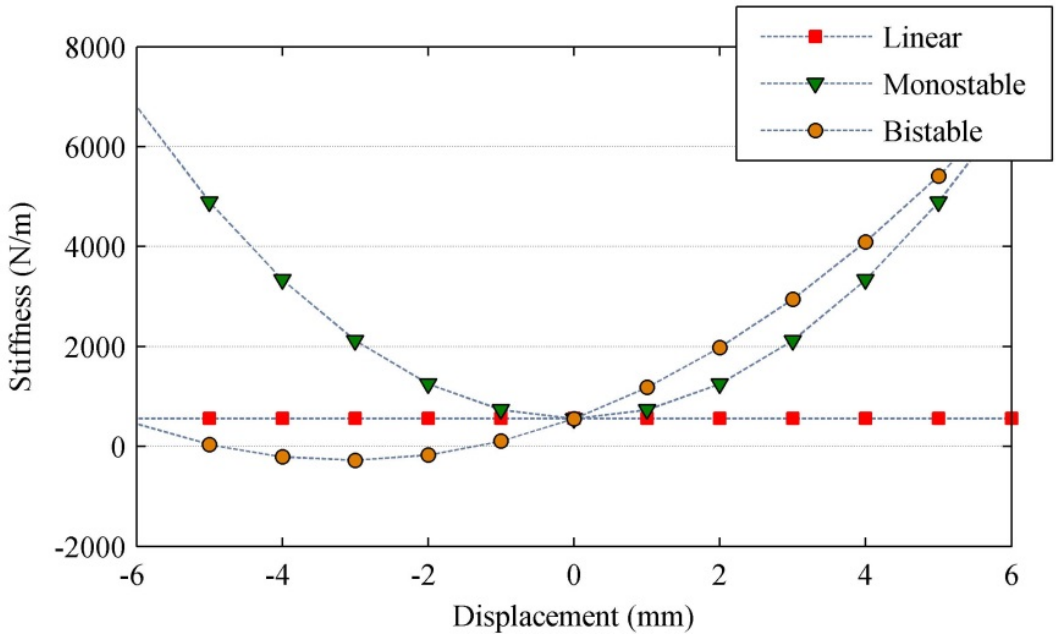

Figure 5.20. Stiffness as function of displacement in different configurations.

The peak output voltage of the monostable energy harvester shifts further to the high frequency side as the excitation level is increased, as presented in Figure 5.19. However, the tendency of the bistable configuration is to show a reversion and to start to move to the higher frequency side. The increase of the excitation makes it relatively easy to overcome this barrier and hop between the two potential wells. In this condition the hardening-effect, as shown in Figure 5.20 with larger amplitude motions, starts to become the dominant factor at higher centre frequencies. For a bistable energy harvester the presence of the hopping oscillation between the

double potential wells yields a substantially larger power output. However the large amplitude hopping oscillation is considerably dependent upon the excitation level. Figure 5.21 shows the displacement responses under different accelerations levels. The number of occurrences of hopping between the potential wells increases as the excitation level increases.

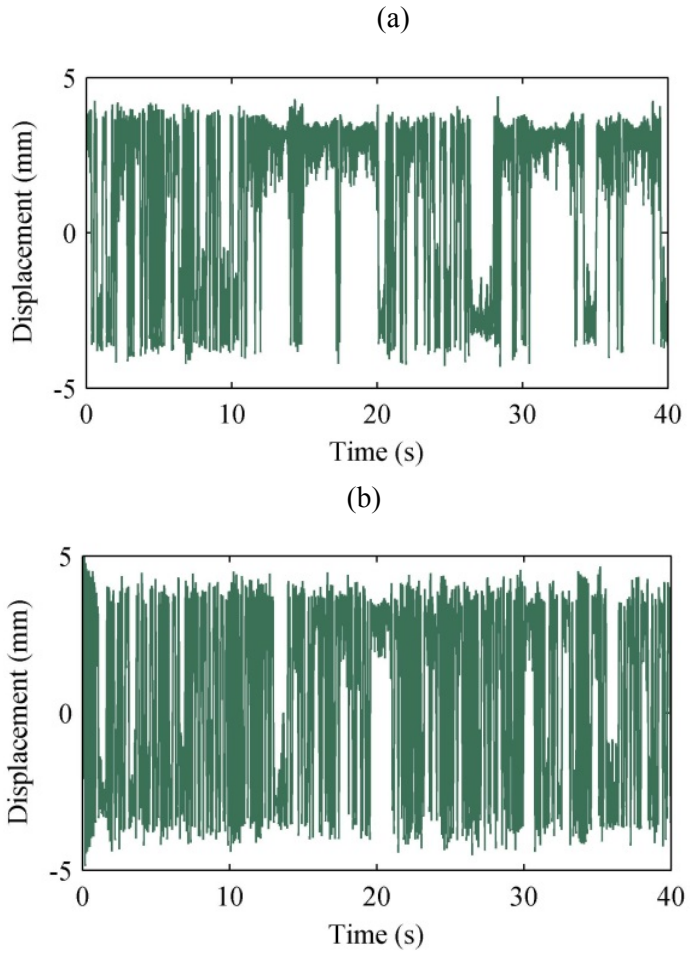

Figure 5.21. Displacement responses of the bi-stable harvester at the input acceleration variance of (a) $2.49\,m^2s^{-4}$ and (b) $7.38\,m^2s^{-4}$ when the centre frequency and bandwidth are set as 15 Hz and 4 Hz, respectively.

- Comparison under different bandwidths

The objective of this section was to study the performance of both of the linear and nonlinear configurations with the change of bandwidth, and at different centre frequencies while keeping a moderate level of excitation. The bandwidth of more than two times of the fundamental frequency is considered, which is large enough for the comparison. The centre frequencies are set to smaller, bigger and equal values of the fundamental frequency of the energy harvester, e.g.,

11 Hz, 15 Hz and 19 Hz, respectively.

Figure 5.22 presents the voltage variance curves depicted at the centre frequency of 11 Hz. In the case of the monostable configuration the peak response appears at a larger bandwidth as compared with that of the linear configuration, it indicates that the hardening-type nonlinearity of the monostable energy harvester starts to take effect because of the moderate level of the excitation. Conversely, a higher response presents at narrower bandwidths for the bistable case.

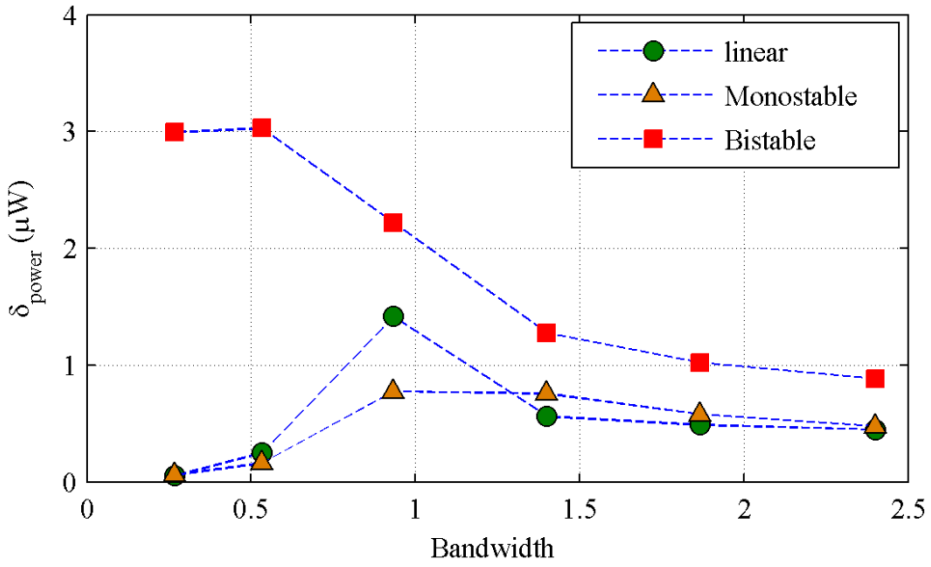

Figure 5.22. Variation of the experimental voltage variance with the excitation's bandwidth. ($\sigma_{acc}^2 = 2.49\,m^2s^{-4}$ centre frequency 11Hz)

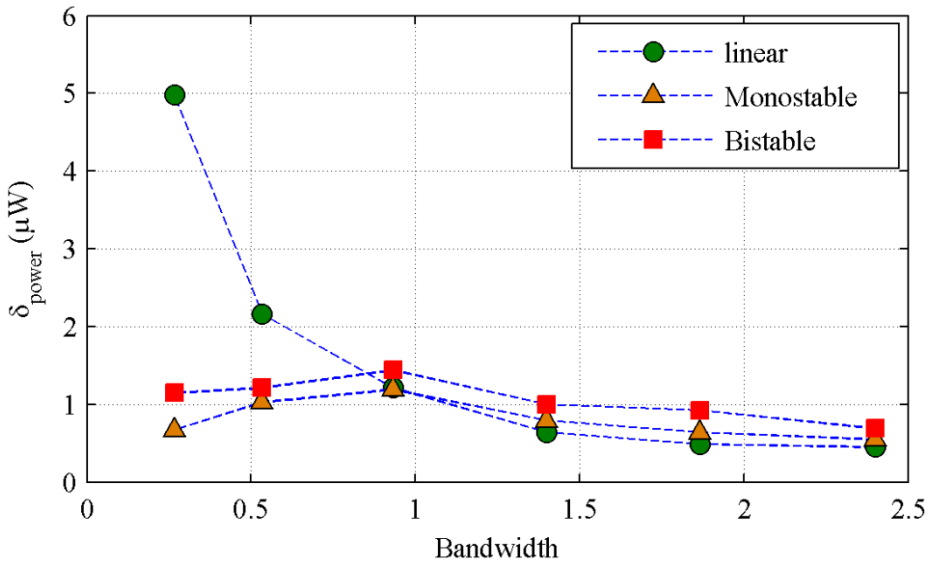

Figure 5.23. Variation of the experimental voltage variance with the excitation'sbandwidth.
($\sigma_{acc}^2 = 2.49\,m^2s^{-4}$ centre frequency $15\,Hz$)

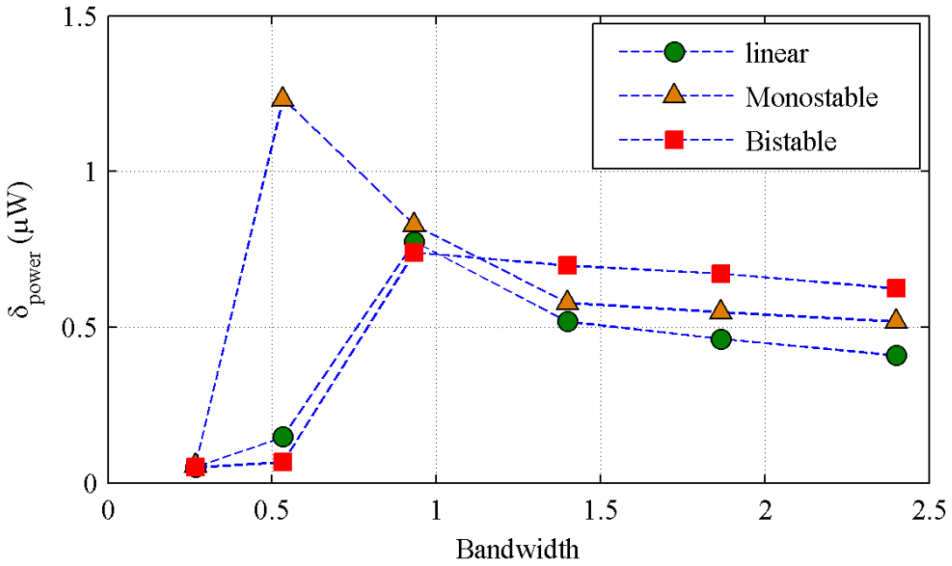

Figure 5.24. Variation of the experimental voltage variance with the excitation's bandwidth.
($\sigma_{acc}^2 = 2.49\,m^2s^{-4}$ centre frequency $19\,Hz$)

When the centre frequency is set at 15 Hz the peak output voltage variances are extended over wider bandwidths and the lowest voltage variance is observed in the monostable configuration in Figure 5.23. For the case when the centre of the noise excitation is around 19 Hz opposite trends can be seen from those of 11 Hz.

For all configurations and centre frequencies, as the bandwidth of the excitation increases to a large enough value the influence of the nonlinearity and centre frequencies decreases. It can be shown that the output voltage variance curves become insensitive, and the similar amplitude can be observed for different configurations when the bandwidth exceeds certain critical values.

- Comprehensive performance comparison

Figures 5.25 to 5.27 show the experimental output voltage variance as a function of the centre frequency and bandwidth of the noise excitation for the different configurations and under an excitation level of 2.49 m/s^2. For the monostable case the peak response can be observed at a higher fundamental frequency. For different centre frequencies the optimum bandwidth can be found, and this increases as the centre frequency shifts away from the peak point.

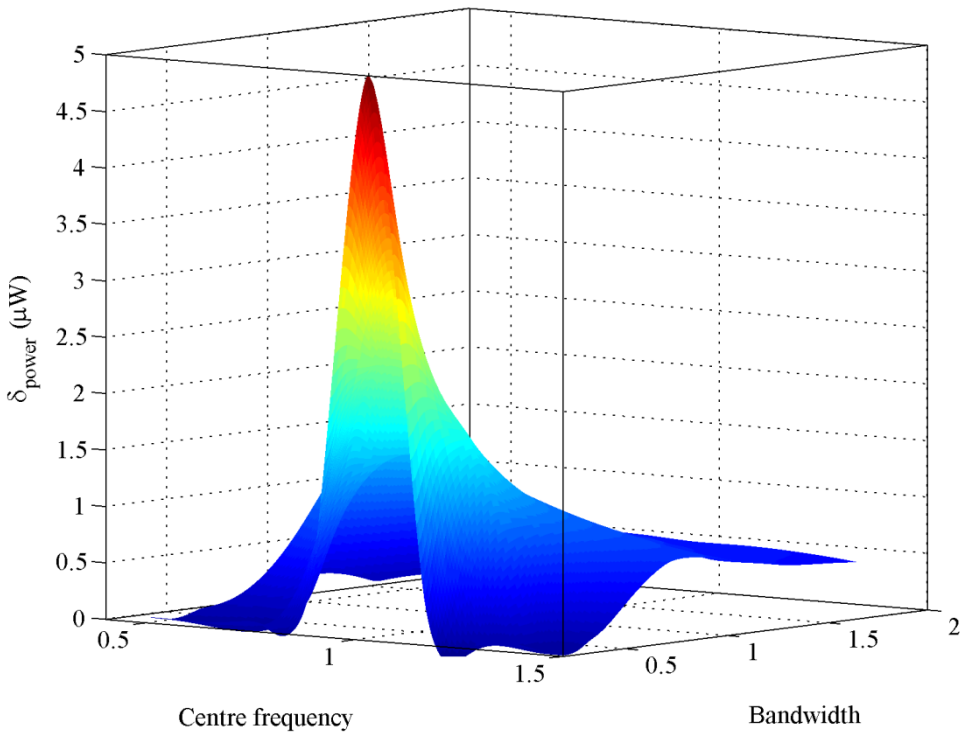

Figure 5.25. Variation of the experimental voltage variance with the excitation's bandwidth and centre frequency. ($\sigma_{acc}^2 = 2.49\,\mathrm{m^2 s^{-4}}$ linear oscillator)

For the linear energy harvester a foreseeable peak output can be noted at the fundamental frequency in Figure 5.25. The influence of the bandwidth shows a similar effect to the monostable nonlinear case. However an overall higher output can be observed for the linear energy harvester when compared with the monostable nonlinear case as shown in Figure 5.26, and this is different from the general impression due to the assumed advantages inherent in nonlinearity in this context.

Noting that it is different to the linear and monostable nolinear configurations, the bistable system result of Figure 5.27 shows that the peak voltage variance is obtained at a lower centre frequency than the fundamental frequency. The voltage variance obtained is much higher than that of the other configurations in most areas. It is confirmed that the bistable configuration is less susceptible to variations in the centre frequency and bandwidth of the noise excitation. However, it can also be noted that the peak value of the linear configuration is still greater than that of the bistable energy harvester.

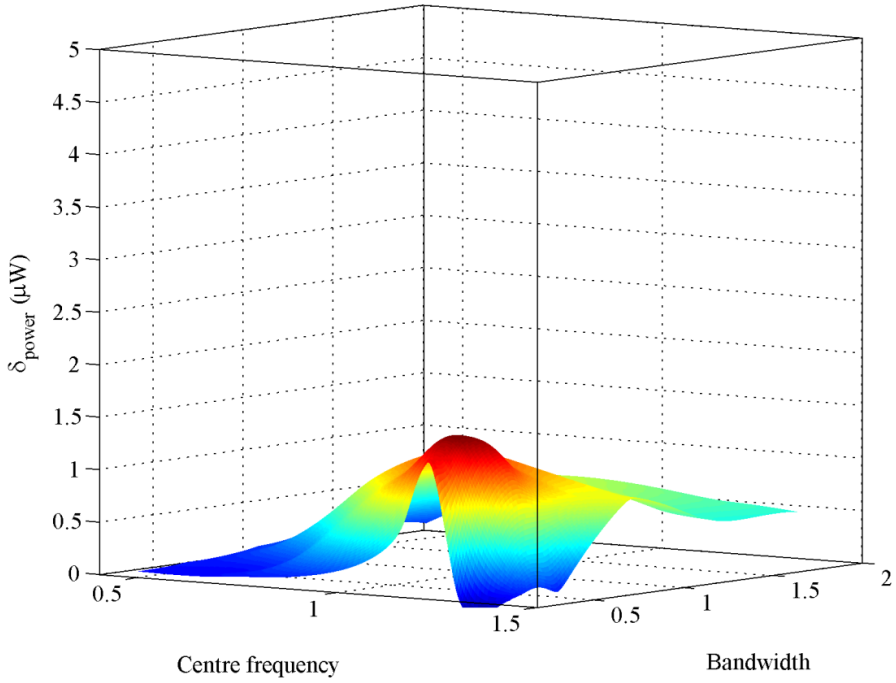

Figure 5.26. Variation of the experimental voltage variance with the excitation's bandwidth and centre frequency. ($\sigma_{acc}^2 = 2.49\,m^2s^{-4}$ hardening-type monostable oscillator)

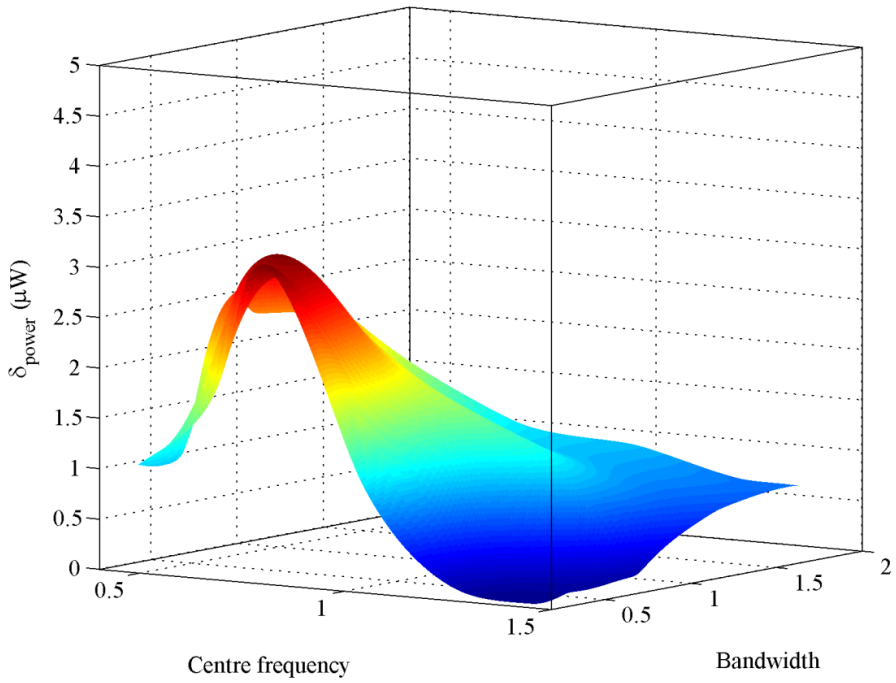

Figure 5.27. Variation of the experimental voltage variance with the excitation's bandwidth and centre frequency. ($\sigma_{acc}^2 = 2.49\,m^2s^{-4}$ bistable oscillator)

By using the same parameters in Table 5.2, it is simulated for comparison with the experimental results.

Figure 5.28 to 5.30 how the simulation results of the rms output power as a function of the centre frequency and bandwidth of the noise excitation for the different configurations and under an excitation level of 2.49 m/s^2. It can be seen that the simulation results confirm the experimental results.

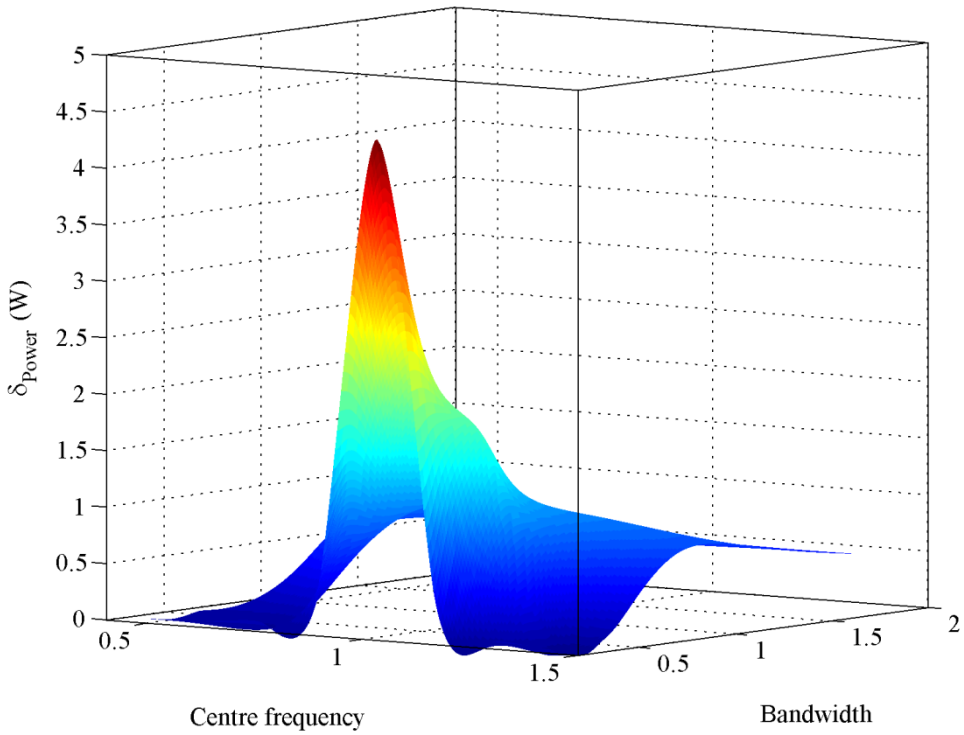

Figure 5.28. Variation of the rms output power with the excitation's bandwidth and centre frequency. ($\sigma_{acc}^2 = 2.49\,m^2s^{-4}$ linear configuration) (Numerical simulation)

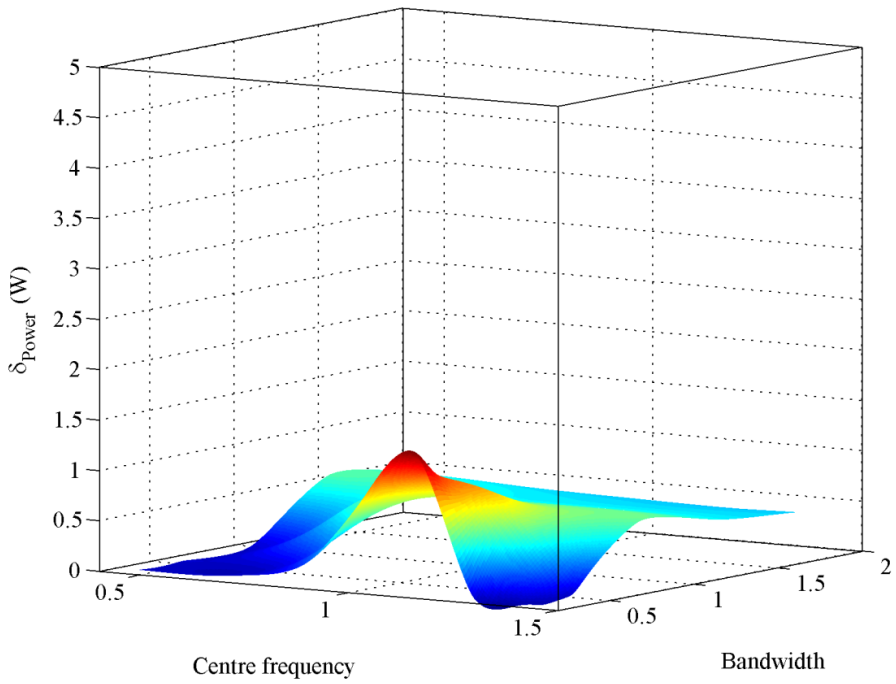

Figure 5.29. Variation of the numerical rms output power with the excitation's bandwidth and centre frequency. ($\sigma_{acc}^2 = 2.49\,m^2s^{-4}$ monostable configuration) (Numerical simulation)

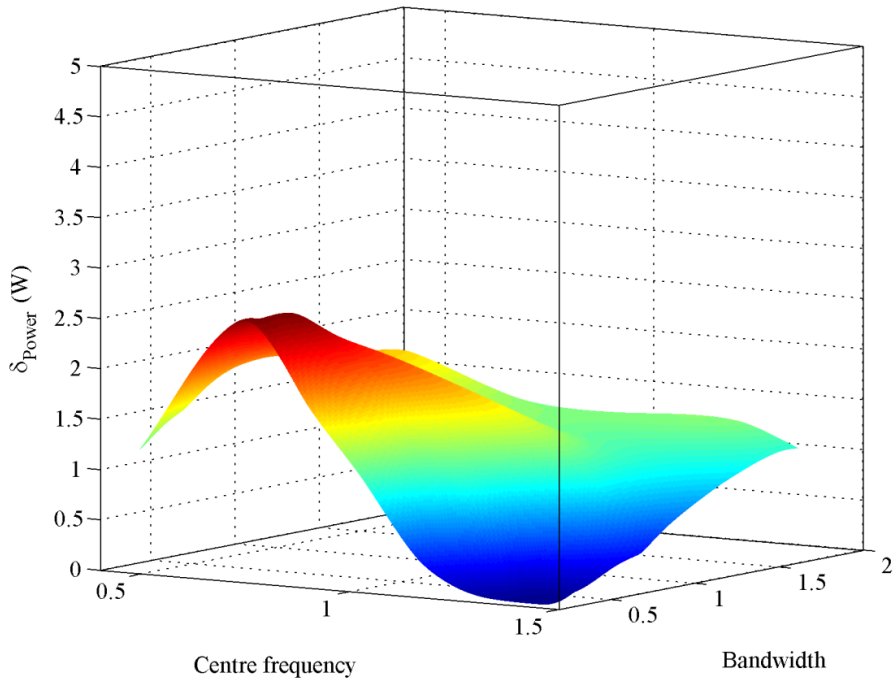

Figure 5.30. Variation of the numerical rms output power with the excitation's bandwidth and centre frequency. ($\sigma_{acc}^2 = 2.49\,m^2s^{-4}$ bistable configuration) (Numerical simulation)

5.3.2 Comparative analysis with optimised electrical damping

Thus far, the above discussion is the numerically and experimentally comparative investigation of different configurations under the constant electrical damping level, however, the optimised damping level is not taken into consideration. For further fair comparison, numerical simulations with the optimised electrical damping for each combination of the centre frequency and bandwidth are carried out. Considering the achievable higher electrical damping compared with the piezoelectric-type, the electromagnetic type transducer is adopted. The governing equation of the system is written as

$$m\ddot{x} + c\dot{x} \pm kx + \alpha x^3 = N(t) \tag{5.3}$$

where c is the total damping, and it is the sum of the mechanical damping c_m and the electrical damping c_e.

Table 5.3. Parameters used in the investigations of stiffness on the frequency response.

Parameter	Value	Unit
m	0.028	kg
c	0.036	Ns/m
k (monostable/linear)	248	N/m
k (bistable)	124	N/m
α (monostable)	2.5×10^8	N/m^3
α (bistable)	3.8×10^7	N/m^3

Table 5.3 shows the parameters for numerical simulations, which also the representative of the experimental setup. For each combination of the bandwidth and centre frequency, the electrical damping is varied to find the optimised value and get the maximum outputpower.

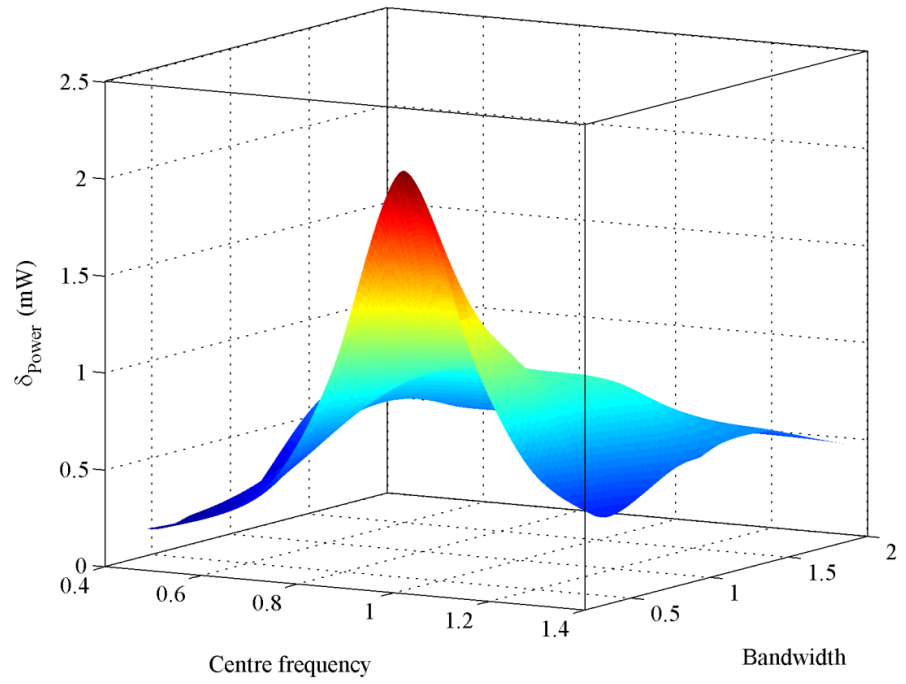

Figure 5.31. Variation of the rms power with the excitation's bandwidth and centre frequency. ($\sigma_{acc}^2 = 2.49\,\mathrm{m^2 s^{-4}}$ linear configuration)

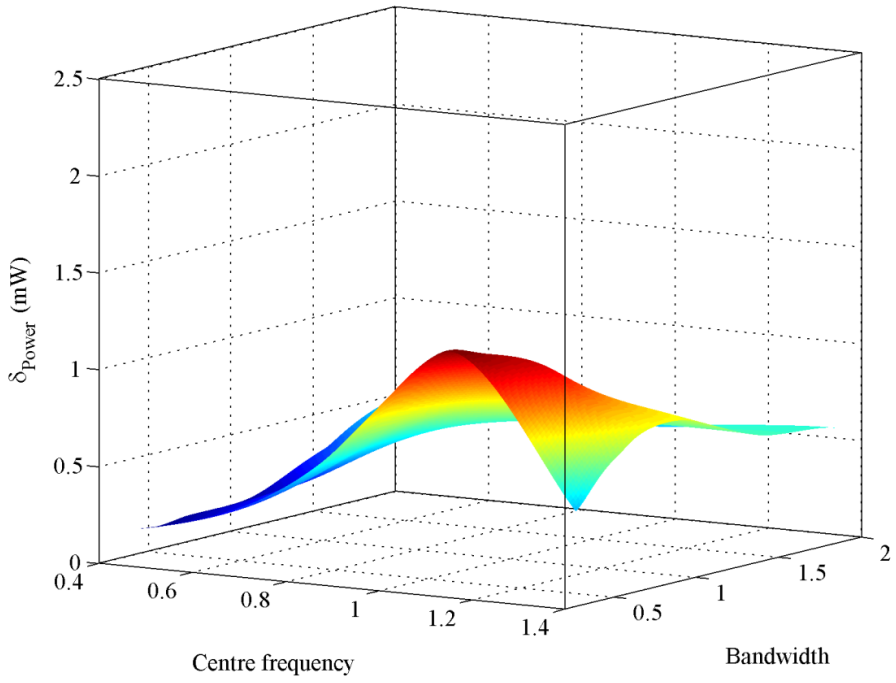

Figure 5.32. Variation of the rms power with the excitation's bandwidth and centre frequency. ($\sigma_{acc}^2 = 2.49\,\mathrm{m^2 s^{-4}}$, $\alpha = 2.5\times10^8\ \mathrm{N/m^3}$ hardening-type monostable configuration)

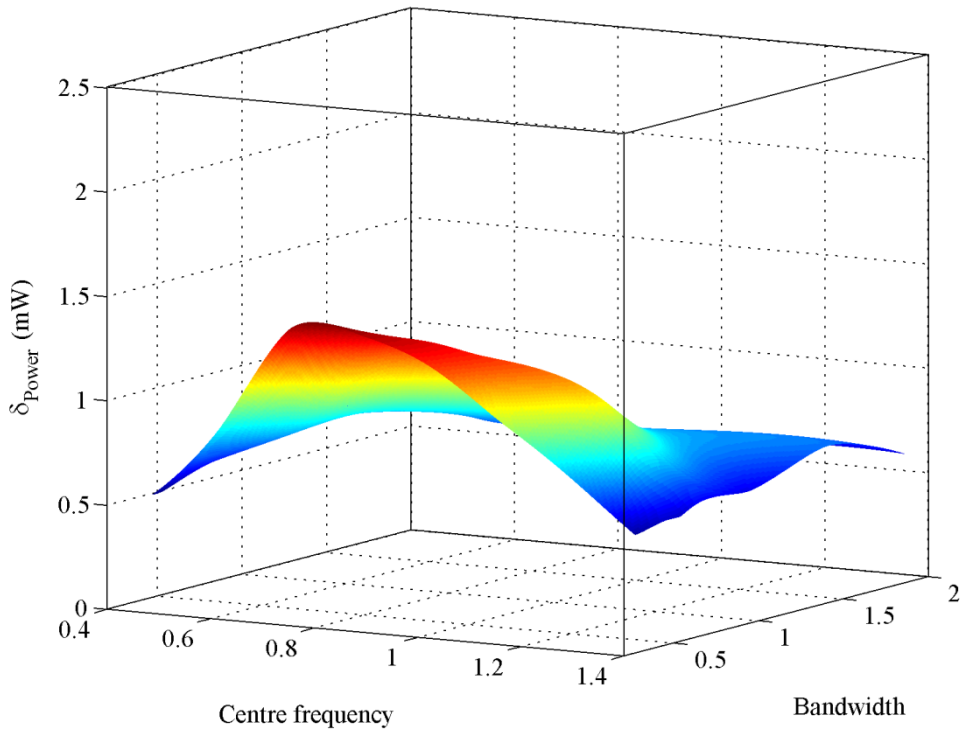

Figure 5.33. Variation of the rms power with the excitation's bandwidth and centre frequency. ($\sigma_{acc}^2 = 2.49\,m^2s^{-4}$ bistable configuration)

From Figure 5.31 to Figure 5.33, when the damping level is optimised, the similar responses to the experimental results can be observed, whatever the overall tendency or the quantitative analysis. Generally, the hardening-type monostable configuration does not show improvement compared with the linear case.

Moreover, from the comparison between Figures 5.31, 5.32 and 5.34, for the harden-type nonlinearity, it can be found that with the increasing of the nonlinear stiffness, the performance presents a decreasing tendency.

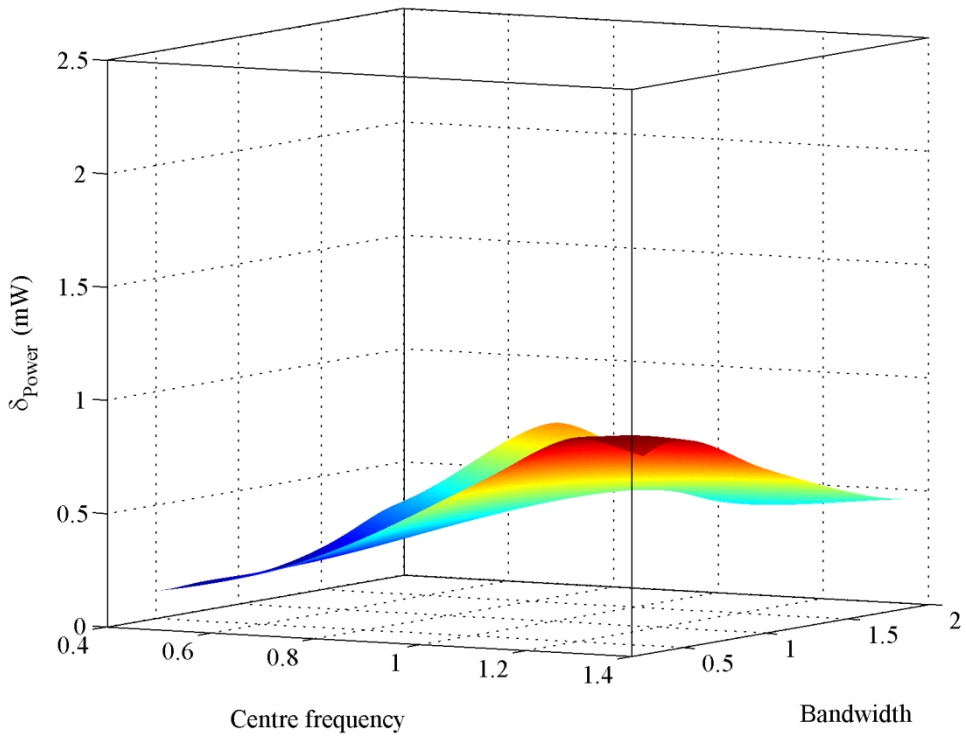

Figure 5.34. Variation of the rms power with the excitation's bandwidth and centre frequency. ($\sigma_{acc}^2 = 2.49\,\mathrm{m^2 s^{-4}}$, $\alpha = 1.2\times10^9\,\mathrm{N/m^3}$ hardening-type monostable configuration)

5.3.3 Comparative analysis constrained electrical damping

There are practical limits on the damping level because of the strength of the magnetic field, coil area and number of coil turns, etc [102]. Therefore, the conditions with the constrained electrical damping should be further investigated. The performance comparison under the constrained electrical damping is conducted and interpreted in this section.

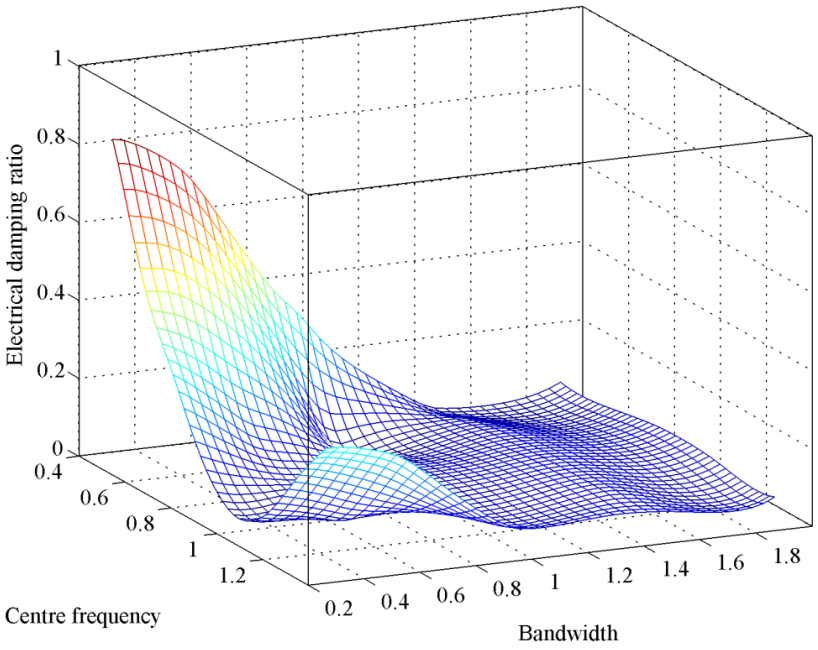

Figure 5.35. Variation of the optimised electrical damping with the excitation's bandwidth and centre frequency. ($\sigma_{acc}^2 = 2.49\,\mathrm{m^2 s^{-4}}$ linear configuration)

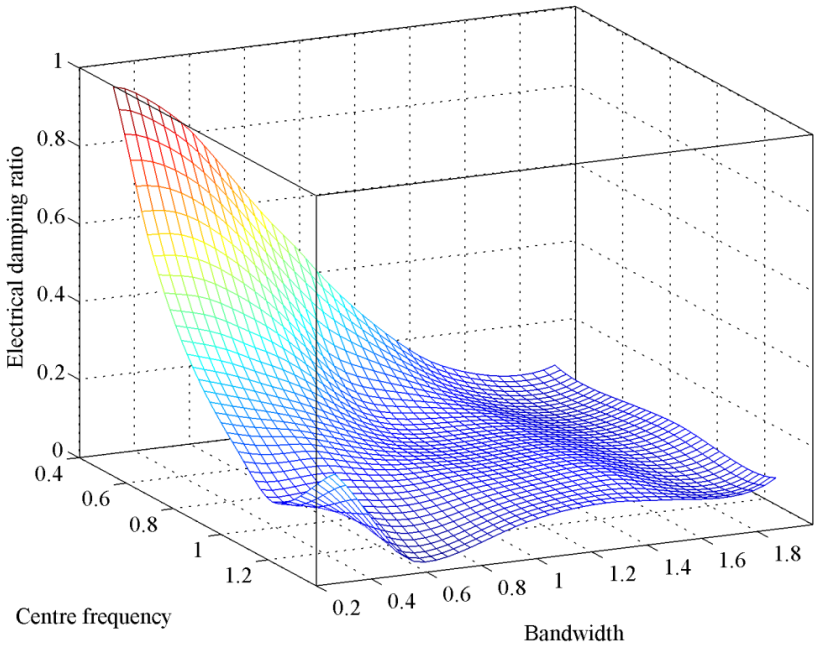

Figure 5.36. Variation of the optimised electrical damping with the excitation's bandwidth and centre frequency. ($\sigma_{acc}^2 = 2.49\,\mathrm{m^2 s^{-4}}$, $\alpha = 2.5\times10^8\ \mathrm{N/m^3}$ hardening-type monostable configuration)

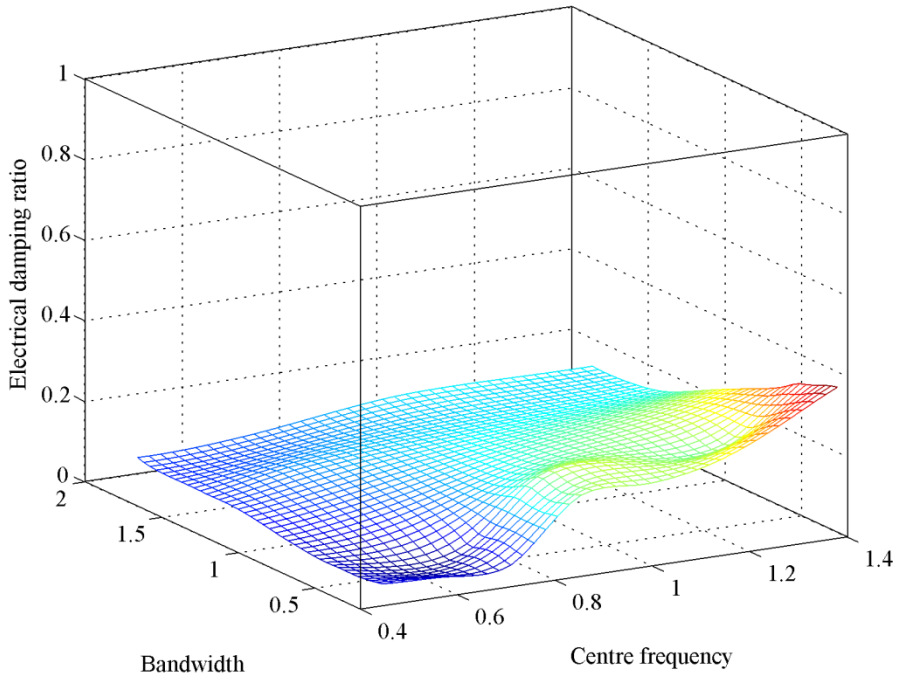

Figure 5.37. Variation of the optimised electrical damping with the excitation's bandwidth and centre frequency. ($\sigma_{acc}^2 = 2.49\,m^2s^{-4}$ bistable configuration)

Figures 5.35-5.37 show the distribution of the optimised electrical damping level, which corresponds to the rms output power of Figures 5.31-5.33. It can be noted that the hardening-type monostable energy harvester requires the overall highest electrical damping, while the bistable configuration presents the lowest damping level.

For the linear configuration in Figure 5.35 and the hardening-type monostable configuration in Figure 5.36, it is found that when the centre frequency moves far away from the fundamental frequency and with a relatively narrow bandwidth, the optimised electrical damping becomes much higher compared with that of the other areas. However, for the bistable configuration, it shows similar tendency only for the high centre frequency area.

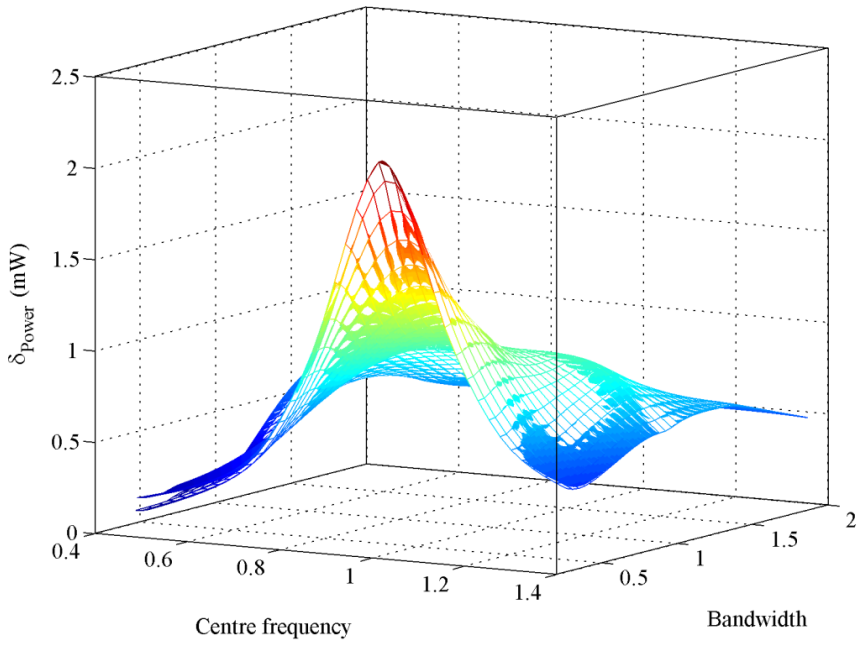

Figure 5.38. Comparison of the optimised output power. (grid surface: with limited damping ratio of 0.29; smooth surface: without damping limit $\sigma_{acc}^2 = 2.49\,m^2s^{-4}$ linear configuration)

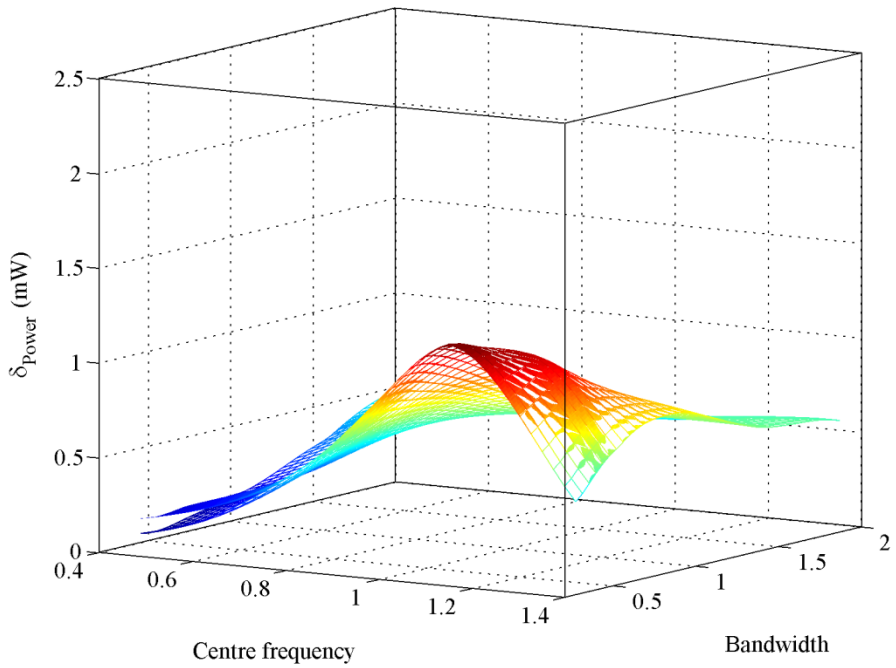

Figure 5.39. Comparison of the optimised output power. (grid surface: with limited damping ratio of 0.29; smooth surface: without damping limit $\sigma_{acc}^2 = 2.49\,m^2s^{-4}$ hardening-type monostable configuration)

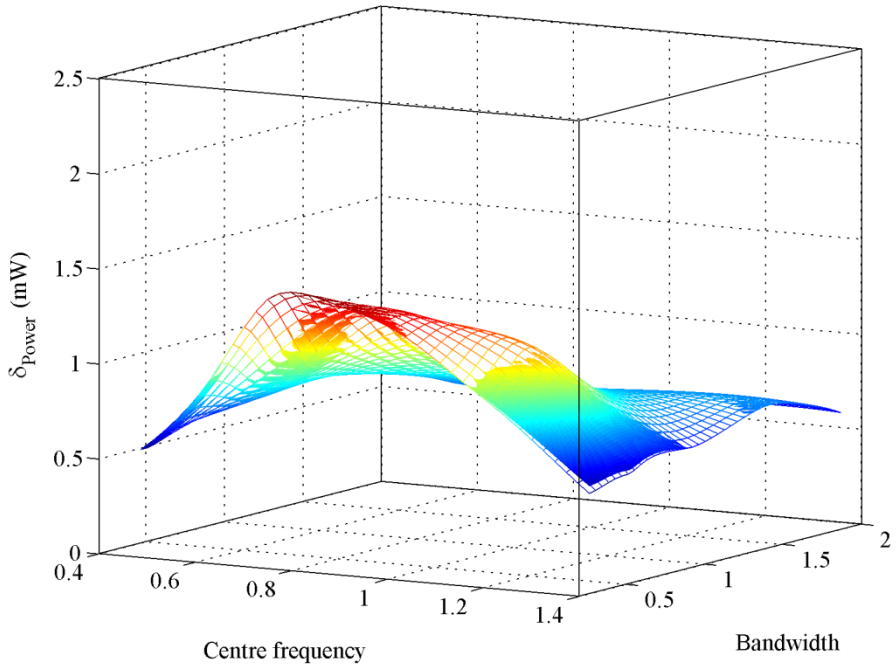

Figure 5.40. Comparison of the optimised output power. (grid surface: with limited damping ratio of 0.29; smooth surface: without damping limit $\sigma_{acc}^2 = 2.49\,m^2s^{-4}$ bistable configuration)

Figures 5.38 to 5.40 present the performance comparison of three different configurations when the electrical damping is constrained to be 1.5 Ns/m, which corresponds to the damping ratio of 0.29. It is shown that the performance of the linear energy harvester and the hardening-type monostable energy harvester present decrease of the performance, especially in the low centre frequency area. However, there is no obvious influence on that of the bistable configuration, except for slight decrease in the area of high centre frequency.

From those observations, it can be concluded that the bistable energy harvester generally requires smaller electrical damping for the maximum power output, compared with the linear- and monostable configurations, especially the low frequency area, which indicts the lower performance decrease when the electrical damping is limited. It provides an obvious benefit for the practical implementation.

5.3.4 Comparative analysis constrained displacement

Considering the practical energy harvester has limit of the stroke, the condition when the displacement of the mass is constrained to a certain value is investigated for further comparison of different configurations in this section.

It should be mentioned that a special characteristic of the bistable configuration is that it has two equilibrium points, which indicts that there is the displacement exists even if there is no excitation is applied to the system. For the performance comparison in Sections 5.3.2 and 5.3.3, the variance of the excitation acceleration is 2.49 m^2s^{-4}, where the displacement of the linear energy harvester cannot exceed the displacement of the equilibrium point of the bistable energy harvester for most cases. Thus, a higher excitation level of 15 $m^2s^{-4}$is used for performance comparison under constrained displacement.

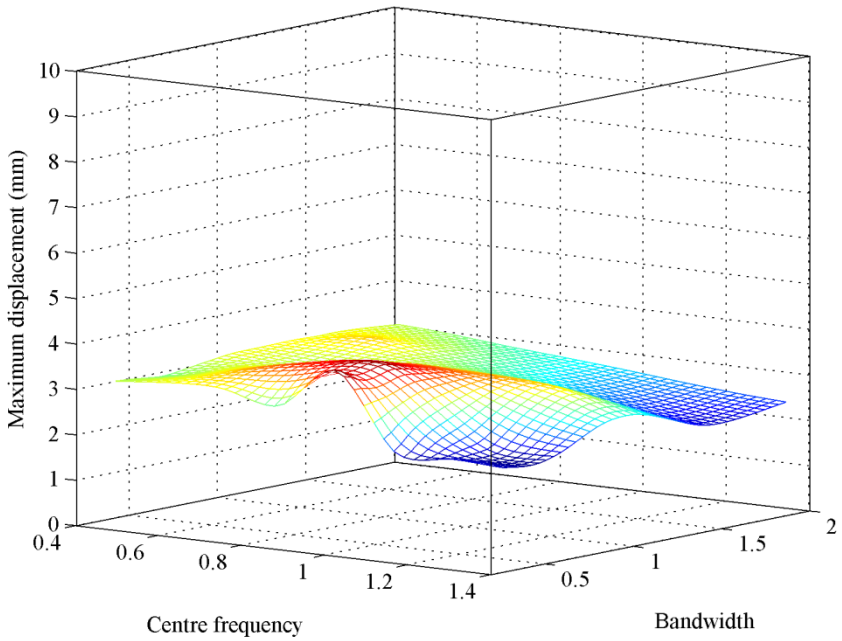

Figure 5.41. Variation of the maximum displacement with the excitation's bandwidth and centre frequency. ($\sigma_{acc}^2 = 15\,m^2s^{-4}$ bistable configuration)

Figure 5.41 shows the variation of the maximum displacement with the excitation's bandwidth and centre frequency for the bistansystem. Figure 5.42 presents the displacement response of the bistable energy harvester when the peak displacement occurs in Figure 5.41. In practice, because of the hardening effect of the bistable potential wells under large amplitude excitation, with the increase of the excitation level, the increasing of the displacement amplitude for the bisable configuration becomes lower compared with the linear energy harvester. Therefore, the displacement amplitude limit (4 mm) shown in Figure 5.42 (red dashed line) is set to be the displacement constraint of the linear energy harvester. The electrical damping level is tuned to meet this displacement constraint.

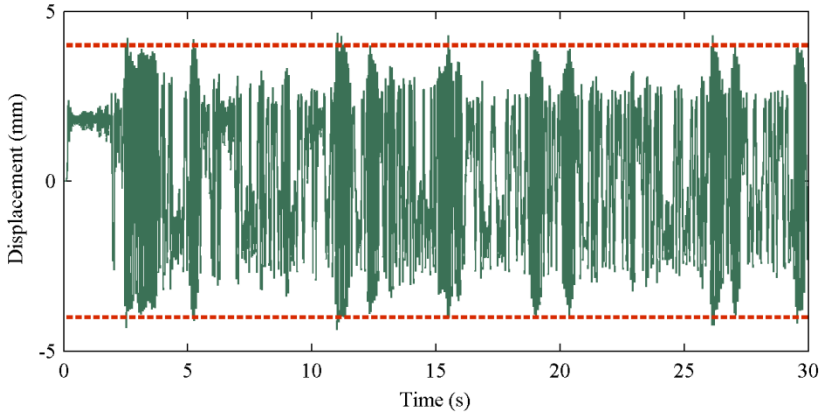

Figure 5.42. The largest displacement response of the bistable energy harvester with the optimised electrical damping.

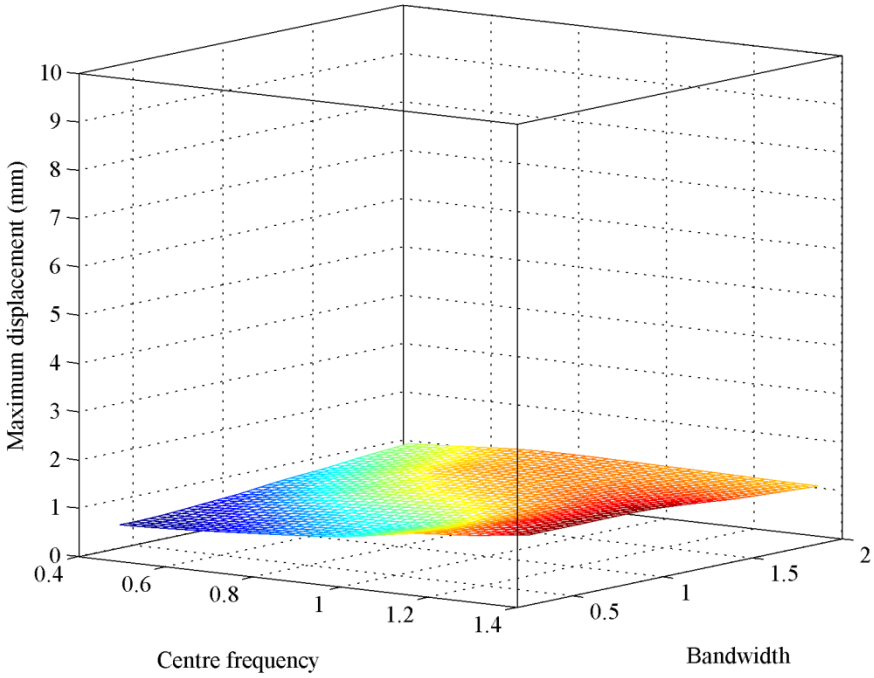

Figure 5.43. Variation of the maximum displacement with the excitation's bandwidth and centre frequency. ($\sigma_{acc}^2 = 15\,m^2s^{-4}$ hardening-type monostable configuration)

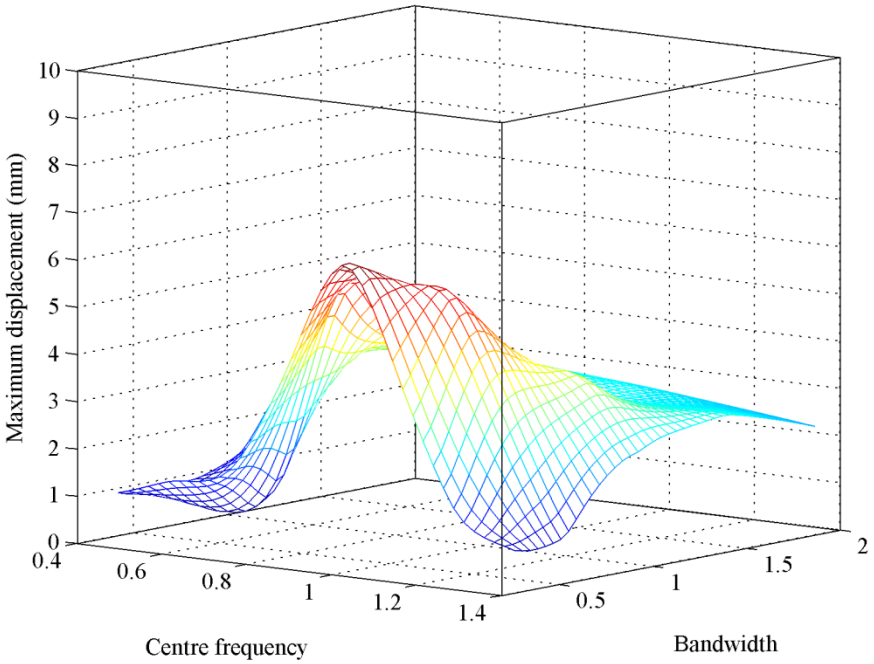

Figure 5.44. Variation of the maximum displacement with the excitation's bandwidth and centre frequency. ($\sigma^2_{acc} = 15\,m^2s^{-4}$ linear configuration)

Variation of the maximum displacement with the excitation's bandwidth and centre frequency for the mnostable and linear energy harvesters are shown in Figures 5.43 and 5.34, respectively. It can be noted that the displacement of the hardening-type configuration is smaller than the displacement constraint of 4 mm. However, for the linear configuration in Figure 5.34, the displacement response exceeds the limit for some areas.

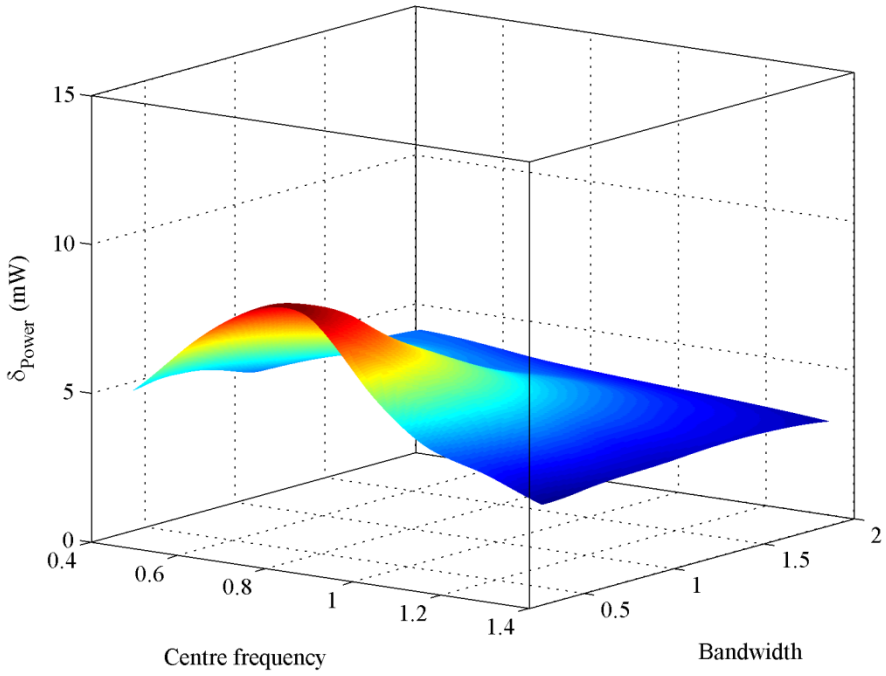

Figure 5.45. Variation of the rms output power with the excitation's bandwidth and centre frequency. ($\sigma_{acc}^2 = 15\,m^2s^{-4}$ bistable configuration)

Figures 5.45 and 5.46 show the rms output power under different centre frequencies and bandwidths for the bistable and hardening-type energy harvesters, respectively, where the displacement response is smaller than the constraint.

Moreover, Figure 5.47 shows the performance comparison of the linear energy harvester between the conditions that with displacement constraint (grid curve surface) and without the constraint (smooth curve surface). It can be noted that there is an obvious decrease of the output power around the peak response area.

To summarise, it is also predictable that if the displacement constraint is very closed to the equilibrium points of the bistable energy harvester, the performance of the bistable energy harvester will suffer an obvious decrease because it can only achieve the intra-well motion instead of the large amplitude inter-well motion because of the displacement constraint.

However, when the excitation level is large enough to make the displacement of the linear energy harvester exceed that of the bistable configuration, the linear energy harvester will present the decreased performance as shown in Figure 5.47, while there is little influence on the bistable energy harvester.

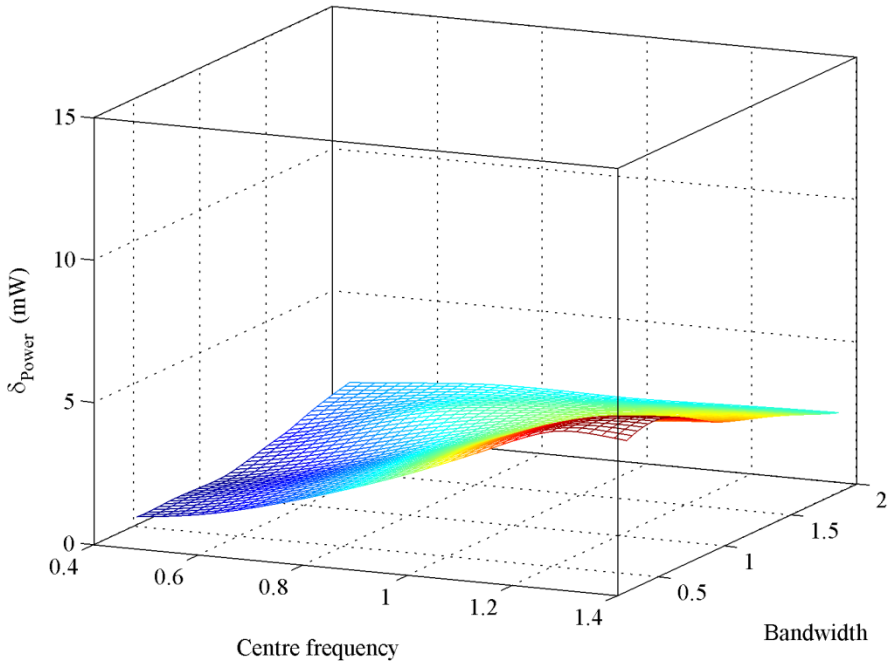

Figure 5.46. Variation of the rms output power with the excitation's bandwidth and centre frequency. ($\sigma_{acc}^2 = 15\,m^2s^{-4}$ hardening-type configuration)

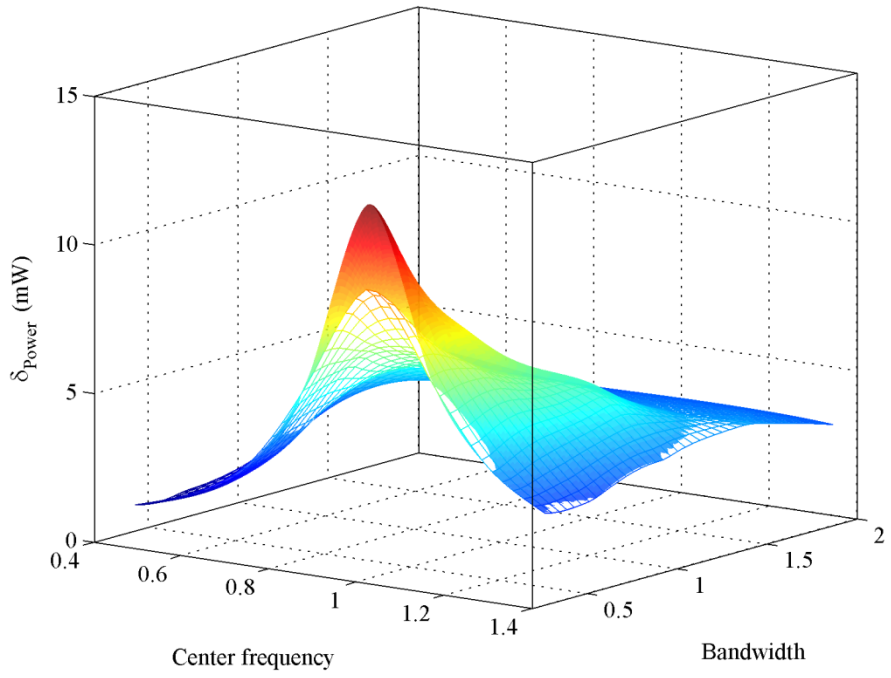

Figure 5.47. Comparison of the optimised output power. (grid surface: with displacement limit; smooth surface: without damping limit $\sigma_{acc}^2 = 15\,m^2s^{-4}$ linear configuration)

5.4 Summary

The comprehensive performance comparison was analysed for the linear, monostable and bistable hardening-type configurations, under different centre frequencies, bandwidths, and excitation levels. The general conclusions can be explained as follows.

(1) When the input excitation level is small the peak response can be observed around the fundamental frequencies, and it shows similar amplitude irrespective of the centre frequency in all configurations. This indicates that the nonlinearities of the monostable and bistable energy harvesters have little effect on the response.
(2) As the input acceleration is increased to a relatively high level the peak response shifts toward a higher centre frequency for the monostable nonlinear energy harvester, and the same tendency is seen as the excitation level is further increased to a higher level still because of the hardening nonlinearity effect. However the fact that the peak response of the bistable configuration moves to a lower centre frequency indicates the effect of the softening effect within the single potential as the excitation level is increased. Then the presented reversion effect demonstrates that the hardening phenomenon takes over when the large amplitude hopping oscillation between the potential wells becomes apparent.
(3) In contrast to the commonly held assumption that a hardening-type monostable nonlinear energy harvester shows a wider bandwidth of large amplitude voltages as compared to the linear variant, this study experimentally and numerically validate that the hardening-type nonlinearity does not provide enhancement, it should be avoided for the band-limited noised excited energy harvesting.
(4) For a given band-limited noise excitation with certain bandwidth and centre frequency, the linear configuration can be selected, and the fundamental frequency of the device should be around the centre frequency of the excitation frequency bandwidth. That's because it has been validated that the optimised condition for the hardening-type monostable and bistable energy harvesters is when the parameter is appropriately selected so that they are operated like a linear energy harvester.
(5) If the excitation presents the time-varying property of the frequency bandwidth or centre frequency, in other words, considering that sometimes the designed fundamental frequency of the system is excluded from excitation frequency range or becomes far away from the centre excitation frequency, the bistable configuration is the best candidate. That is because for most of the frequency and bandwidth range considered the bistable harvester outperforms the linear system but for area of the peak output power.
(6) The bistable energy harvester requires the overall lower electrical damping compared with

the linear and monostable configurations. If the maximum available damping is constrained, the linear and the hardening-type energy harvester will suffer energy loss at both the low and high centre frequency area when the excitation bandwidth is narrow.

(7) Because of the existence of the equilibrium point of the bistable energy harvester, there is a minimum stroke requirement for the bistable configuration. However, when the excitation level is large enough to make the displacement amplitude become bigger than that of the bistable energy harvester, the constrained displacement will cause the obvious performance decrease around the peak response area for the linear energy harvester.

Chapter 6

Enhancement for Random Excitation

6.1 Introduction

In this chapter, a bistable mechanism is designed to achieve the stochastic resonance, as an approach for energy harvesting following the fundamental theoretical work. A small-scale periodic input is provided to boost the response of the energy harvester. Moreover, another novel method, henceforth called square-wave-driven stochastic resonance, is also proposed with the advantaged that there is no need to determine the periodic excitation frequency based on the noise density and the physical parameters of the system. The feasibility of further increasing the available energy is validated from the random excitation source, which is different from the other investigations about the noise excited vibrational energy harvesting, in where only the performance study of several existing typical energy harvesters were conducted.

6.2 Enhanced energy harvesting

6.2.1 Apparatus illustration and modelling

A practical physical system may now be conjectured as shown in Figure 6.1, where there is a cantilever beam with an end mass magnet, a fixed magnet, and a non-contacting actuator. The system is excited by ambient noise source, $N(t)$, the effect of which may result in a nonlinear interaction between the beam and the magnets if the distance d between the two magnets is adjusted, and the non-contacting actuator is used to provide the periodic excitation.

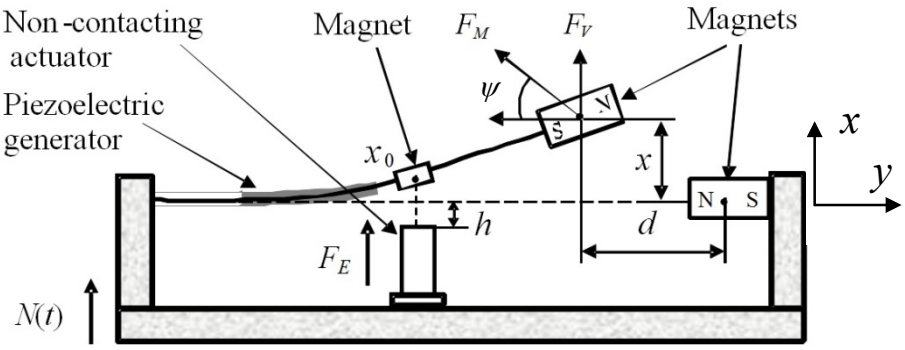

Figure 6.1. Schematic of a practical bistable system.

The repulsive force F_M acts between the tip magnet and its counterpart. While the two magnets are parallel in the central position, the horizontal component is maximised and tends to push the tip magnet away from the central position. After that the effect of the horizontal

component weakens and the vertical component predominates. Therefore, to avoid an over-complicated analysis only the vertical component is considered by appropriately simplifying the modelling of the device. The vertical component F_V can be written as [103][104]

$$F_V = F_M \sin\psi = \frac{F_M}{d} \frac{x}{\left[1+(x^2/d^2)\right]^{1/2}} \tag{6.1}$$

The above equation is expanded in the form of a Taylor series, computed around $x = 0$ and truncated to lead to

$$F_V \approx \frac{F_M}{d} x - \frac{F_M}{2d^3} x^3 \tag{6.2}$$

F_V is a nonlinear function of x and has the same overall form as a cubic polynomial. Moreover, the stiffness of an elastic cantilever beam can be approximated by a linear spring of stiffness k

$$k_c = \frac{3EI}{l^3} \tag{6.3}$$

where E is Young's modulus, I is the cross-section moment of inertia of the beam, and l is the length of the beam. Therefore the dynamics of the beam in Figure 6.1 can be represented in single degree of freedom form by the following simple differential equation of the form of Equation (6.4), where c represents the damping active in the system, noting that this can be measured and inserted later as a suitable numerical value.

$$m\ddot{x} + c\dot{x} + (k_c - \frac{F_M}{d})x + \frac{F_M}{2d^3} x^3 = N(t) \tag{6.4}$$

from which the potential $U(x)$ for the system is obviously of this form

$$U(x) = \frac{1}{2}(k_c - \frac{F_M}{d})x^2 + \frac{1}{4}\frac{F_M}{2d^3} x^4 \tag{6.5}$$

The distance d between the two magnets can be adjusted in Equation (6.5) and it is also

apparent that the value of $k_c - F_M/d$ can become negative and lead to the possibility of bistability. The condition is necessary and sufficient as a basic requirement for the occurrence of stochastic resonance.

6.2.2 Non-contacting actuator

In order to achieve stochastic resonance an electromagnet was used as a non-contacting actuator in conjunction with a further magnet fitted to the underside of the cantilever beam and positioned just above the electromagnet, so that a periodic force excites the cantilever beam when a periodic voltage is applied to the electromagnet coil. It should also be mentioned that the non-contacting actuator may excite higher modes, thereby reducing the performance of the harvester, even though the resonator is designed and modelled assuming that it mainly operates in the first mode. Referring to the schematic of Figure 6.1, h is defined as the distance from the electromagnet to the undeflected position of the cantilever beam, and x_0 as the displacement of the magnet attachment point on the beam. Therefore (h+x_0) defines the distance between the electromagnet and the beam when the system vibrates. F_E is the force between the electromagnet and the magnet.

F_E reduces nonlinearly as the distance between the electromagnet and the magnet increases, and in order to determine this relationship the calibration experiment for F_E was carried out by means of which the attractive force was measured over a distance of 1 mm to 16 mm. It was found that the force was inversely proportional to the square of the distance, so this relationship could be represented approximately by

$$F_E = \frac{\lambda}{(h + x_0)^2} \tag{6.6}$$

The quantity λ is a system dependent constant, and the calibration experiment showed that $\lambda = 28$ for an almost perfect fit between the observed results and those predicted by Equation (6.6). In general it is possible to write this as,

$$F_E = \frac{\lambda}{(h + x_0)^2}\cos(\omega t) = \frac{\lambda}{h^2}\frac{\left[1 - 2x_0/h + (x_0/h)^2\right]}{\left[1 - (x_0/h)^2\right]^2}\cos(\omega t) \tag{6.7}$$

where x_0 is the peak vibration displacement of the attachment point of the magnet on the beam which now has to be related to the beam displacement x at the location of the end mass. The

static deflection formula for a cantilever can readily be used to define this relationship since it is physically similar in shape to the first bending mode. The formula is given by

$$x_0(y,t) = \left(\frac{3y^2}{2l^2} - \frac{y^3}{2l^3} \right) x(l,t) \tag{6.8}$$

where x is the horizontal location along the beam axis, and l is the length of the beam. In the experimental system this relationship was found to be $x_0 = 0.25\,x$.

One can generally observe that when the cantilever beam vibrates x_0 is negligible when compared with h, namely that $x_0 << h$. Therefore, when the nonlinear term $(x_0/h)^2$ is neglected and $x_0 = 0.25\,x$ is applied to Equation (4.7) it can be simplified down to

$$F_E = \frac{\lambda}{h^2}(1 - 2\frac{x_0}{h})\cos(\omega t) = (\frac{\lambda}{h^2} - \frac{\lambda x}{2h^3})\cos(\omega t) \tag{6.9}$$

It is significant to note that one of the two terms representing the amplitude of the force F_E contains x, and that this will lead to a parametric excitation term in the equation of motion. Following on from this the equation of motion for the practical system can now be written in full,

$$m\ddot{x} + c\dot{x} + (k_c - \frac{F_M}{d})x + \frac{F_M}{2d^3}x^3 = N(t) + (\frac{\lambda}{h^2} - \frac{\lambda x}{2h^3})\cos(\omega t) \tag{6.10}$$

As mentioned above, conventionally the frequency of the small-scale periodic force required to achieve stochastic resonance is in a relationship with the Kramers rate [105]. When the system is lightly damped, it can be defined by

$$r_K = \frac{\omega_n}{2\pi}\exp\left(-\frac{k^2}{4\alpha D} \right) \tag{6.11}$$

where $\omega_n = \sqrt{2k/m}$ is the natural frequency around the equilibrium points. The value of the excitation frequency is clearly dependent upon the noise density D, stiffness coefficients k, and α.

It should be noted that when the excitation frequency is half the maximum value of the Kramers rate, stochastic resonance will occur by means of the definition already stated. Contrary to this, when the excitation frequency exceeds that value then stochastic resonance cannot occur. Therefore, the reference value of excitation frequency ω for stochastic resonance can be represented by,

$$\omega_{\lim} = 2\pi \frac{1}{2} r_{K\lim} = \frac{\omega_n}{2} \tag{6.12}$$

6.3 Further improvement

The study in Section 6.2 is based on the premise that the frequency of the periodic input must necessarily be determined by the Kramers rate, which is the transition frequency between the two potential wells of the bistable system. To calculate the value of the Kramers rate, the physical parameters, such as linear, nonlinear stiffness and noise density should be measured with the premise that the stiffness nonlinearity of the bistable device can be accurately modelled by a cubic polynomial. However, it is usually more applicable to characterize it using the higher order polynomial under practical conditions. Furthermore, the intensity of the noise excitation is rather difficult to measure in practice despite it being a necessary parameter for determining the value of the Kramers rate. To get round these problems, square-wave-driven stochastic resonance has been proposed. This approach differs fundamentally from the traditional method of directly adding a periodic modulating excitation to the random excited system and is based on the application of a simple closed-loop control law, thereby eliminating the need to determine excitation frequency by estimating the physical parameters and noise density.

6.3.1 Methodology

To achieve stochastic resonance without needing to determine the excitation frequency, that is, by measuring the physical parameters in Equation (6.11), another approach of square-wave-driven stochastic resonance is proposed by introducing an additional force as

$$\gamma(t) = G\,\mathrm{sgn}(\dot{x}) \tag{6.13}$$

where G is a positive constant. This force can be characterized by a square wave and follows the direction of the response velocity. In addition to the system being excited by the ambient vibration force, when the low-level additional force $\gamma(t)$, is applied, the system's dynamics is described as

$$m\ddot{x} + c\dot{x} - kx + \alpha x^3 - \gamma(t) = N(t) \tag{6.14}$$

The potential associated with the system described by Equation (6.14) can be correspondingly expressed as

$$U(x,t) = -\frac{1}{2}kx^2 + \frac{1}{4}\alpha x^4 - \gamma(t)x \tag{6.15}$$

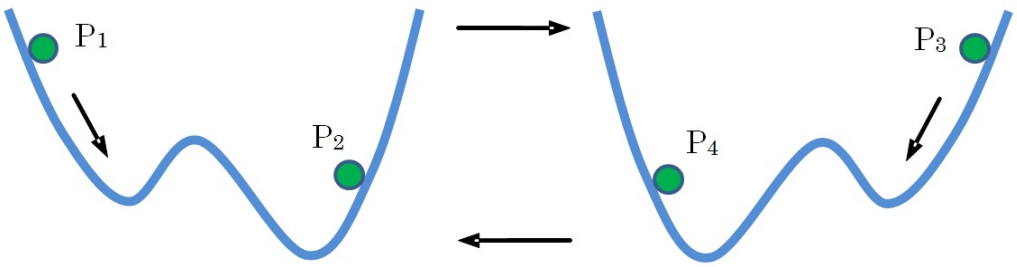

Figure 6.2. Changes in the double-well potential under the additional force.

The amplitude of the additional force $\gamma(t)$ can also be used to express the degree of asymmetry of the potential wells. There are two kinds of interpretation that can be applied to $\gamma(t)$. The intuitive physical explanation is that it is a force follows the direction of the response velocity of the mass in the bistable system, and that this helps the mass jump between the symmetrical wells of the potential. The other, albeit non-physical, explanation is simply that $\gamma(t)$ is a convenient means to modulate asymmetrically the shape of the potential. Figure 6.2 illustrates the variation in the potential arising from this additional force, $\gamma(t)$, showing the potential in two differently biased asymmetrical forms. The arrows represent the direction of movement of the magnetic end mass. Assuming that the mass is moving within the left well of the potential from point P_1 where $\gamma(t)$ equals G to point P_2 where $\gamma(t)$ is set to be $-G$, it

jumps to point P_3 changing instantaneously its potential whilst the displacement shows no change. Then, within the right well of the potential, the mass moves to point P_4 with $\gamma(t)$ equal to $-G$, and finally returns to the starting point P_1. However, in practice, mainly because of losses through mechanical damping and the efficiency of the electricity transducer, any excess in the input energy (provided by the additional force) cannot be completely dissipated by the electrical damper. Nevertheless, it is necessary to subtract the energy provided by the small-scale additional force to calculate the net energy. This will decrease the net energy that can be harvested from the external ambient vibration. Therefore, the amplitude of the additional force should be appropriately chosen to establish optimal conditions. To provide guidance for selecting such amplitude of the square wave force, we write the partial derivative of the potential in Equation (6.15) with respect to x and set it equals to zero as

$$\frac{\partial U(x,t)}{\partial x} = kx + \alpha x^3 - \gamma(t) = 0 \tag{6.16}$$

when Equation (6.16) has only two different roots, it shows that the system is in the transitional state between bistablity and monostablity. The threshold of the parameter $\gamma_a(t)$ can be given by

$$\gamma_a(t) = \pm\frac{2\sqrt{3}}{9}\sqrt{\frac{k^3}{\alpha}} \tag{6.17}$$

It should be mentioned that because the additional force is a square wave, it only has two values with opposite signs. The system maintains bistability when the amplitude of the additional force is smaller than $|\gamma_a(t)|$. Under this condition, the derivative of the potential wells has three roots and it denotes bistability. However, when the amplitude of the additional force is bigger than $|\gamma_a(t)|$, there is only one root, meaning a single potential well and the bistability disappears. The coefficient G should be smaller than $|\gamma_a(t)|$, because the mass can already switch between the potential wells even if only under the additional excitation, that becomes excessive.

6.3.2 Performance estimation

Different from the source of ambient random vibration that is inherent to the system to be harvested, the small-scale periodic input was manually added and should be subtracted from the total harvested energy for comparison. This particular work was not involved in the previous study. To assess the effectiveness of use of stochastic resonance for vibrational energy harvesting, the power dissipated by the damper is investigated. The net power under stochastic resonance should be compared with the case that the energy harvester is only excited by the random excitation. The net power dissipated by the damper will now be investigated. Equation (6.14) can be rewritten as

$$m\dot{x}\ddot{x} + c\dot{x}^2 - k\dot{x}x + \alpha\dot{x}x^3 = \gamma(t)\dot{x} - m\dot{x}\ddot{X} \tag{6.18}$$

and re-expressed as

$$\frac{d}{dt}\left(\frac{1}{2}m\dot{x}^2 - \frac{1}{2}k^2x + \frac{1}{4}\alpha x^4\right) + c\dot{x}^2 = \gamma(t)\dot{x} - m\dot{x}\ddot{X} \tag{6.19}$$

Equation (6.19) effectively describes the conversion of energy within the bistable system. The rate of change of the kinetic energy, $m\dot{x}^2/2$, and the potential of the mechanism, $-k^2x/2 + \alpha x^4/4$, equals the instantaneous external excitation and the additional force input [83]. Clearly, $c\dot{x}^2$ represents the instantaneous energy dissipated by the damper. The energy input of the additional small-scale force is expressed by $\gamma(t)\dot{x}$ and is always non-negative because $\gamma(t)$ is a force that follows the magnetic end mass. $-m\dot{x}\ddot{X}$ is the input energy from the external ambient vibration. To estimate the net power of the mechanism under stochastic resonance, the power provided by the additional force $\gamma(t)$ is subtracted from the total power. Therefore the instantaneous net power can be defined by

$$P_{net}(t) = P_d(t) - P_c(t) = c\dot{x}^2 - \gamma(t)\dot{x} \tag{6.20}$$

where $P_{net}(t)$ is the net power, $P_d(t)$ the total dissipated power by the damping, and $P_c(t)$ the power consumed by the additional force. The net energy during a period of duration t_0 is given by

$$E_{net} = \int_0^{t_0} P_{net}(t)dt \tag{6.21}$$

6.4 Numerical and experimental validation

6.4.1 Enhanced energy harvesting

- Parameter identification

To prepare the harvesting experiment, it is necessary to confirm three important parameters, which include the normal natural frequency of the cantilever beam, the frequency range of the periodic modulating excitation, and the distance between the magnets for bistability. Especially, when the predominant frequency of the ambient vibration is close to the normal natural frequency of the cantilever beam, the vibration will be enhanced correspondingly. In order to distinguish the effect stochastic resonance from the normal resonance it is necessary to analyse the normal natural frequency and the frequency range of the periodic modulating excitation for stochastic resonance, respectively. Therefore, in the first step, the normal resonance frequency of the cantilever beam was investigated in the monostable system without the counterpart magnet. Moreover, considering the influence of the end magnet on the cantilever beam the natural frequencies of the cantilever beam were measured with and without the ending magnet fitted, and the natural frequencies were processed by spectral analysis. The results of the natural frequencies of the cantilever beam were found to be 5.5 Hz and 5.0 Hz for the cases with and without the ending magnet fitted, respectively.

However, the frequency range of the periodic modulating excitation for stochastic resonance is different from the natural frequency of the cantilever beam. The parameter $k = k_c - F_M/d$ in Equation (6.2) changes while the beam vibrates because of the variation in F_M. The preliminary experiment showed that the maximum peak displacement of the cantilever beam was about 25 mm, so a force transducer could be used to measure the vertical elastic force F_V, and F_M can be given by,

$$F_M = F_V \cdot \frac{\sqrt{x^2 + d^2}}{x} \tag{6.22}$$

According to Equation (6.22), the corresponding minimum value for F_M is then F_M (x= 25 mm) = 2.83 N, and therefore a maximum numerical value for linear stiffness can be calculated as follows,

$$k_{\min} = (\frac{F_M}{d} - k_c) = \frac{2.83}{0.04} - 46.15 = 24.5 \tag{6.23}$$

Using the calculated value, the parametric excitation frequency was found to be 2.76 Hz for stochastic resonance, as predicted by Equation (6.12). When the system vibrates F_M will be the same as or a little bigger than F_M (x = 25mm), therefore the central value of the parametric excitation frequency should be around about, or just a little bigger than 2.76 Hz to ensure that stochastic resonance occurs.

In addition to this, a preliminary experiment was also carried out in order to determine the relatively optimal inter-magnet distance d for bistability. A harmonic ambient vibration of amplitude of 5 mm and frequency of 5 Hz was used to excite the experimental harvester, when the distance is 30 mm, 40 mm, and 50 mm, respectively. The experimental result indicated that the magnetic force drops almost to zero when d exceeds 50 mm, and the beam can only vibrate in one stable state and cannot then jump into the bistable state when it is less than 30 mm. It was observed that the system readily becomes bistable and the response is correspondingly stronger when d is 40 mm. Therefore, the 40 mm distance between the magnets was adopted in the following experiments.

- Experimental trials

The schematic diagram of the experimental system with the necessary instrumentation connected is shown in Figure 6.3. A signal generator (Iwatsu type SG-4105) was used to provide a harmonic voltage to drive the linear power amplifier which in turn drives the electromagnetic non-contact actuator. The ambient vibration was provided by a large-scale vibration generator (Mitsubishi, Japan), which could generate white noise and harmonic vibration over a range of amplitudes of 0 to 10 mm and, in the harmonic case, frequencies between 0 and 12 Hz.

A high-precision laser vibrometer (Kyence Types IL-300 and IL-1000) was used to measure the displacement of the cantilever beam together with an accelerometer. A Rion PV-08A piezoelectric accelerometer and a charge amplifier were used to measure the acceleration of the end magnet of the cantilever beam. The experimental data was all recorded on a computer.

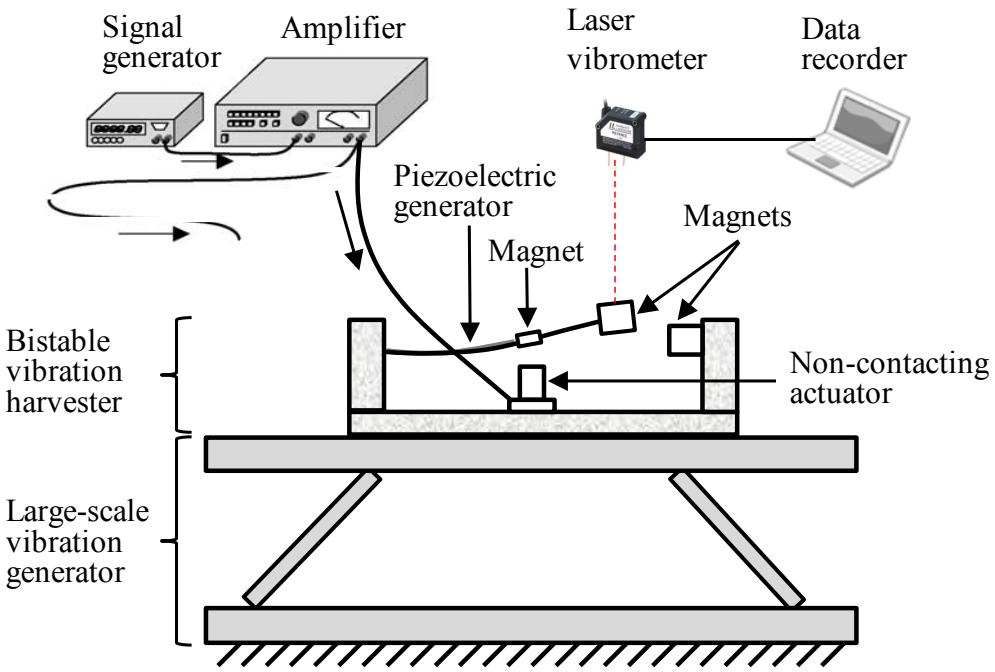

Figure 6.3. Schematic diagram of the experimental harvester with instrumentation.

A harvester was designed as shown in Figure 6.4. The harvester was constructed around a rigid aluminium frame sub-system of length 700 mm, width 280 mm, and height 120 mm, a cantilever beam of aluminium alloy, two magnets, and an electromagnetic non-contacting actuator for the provision of the periodic excitation.

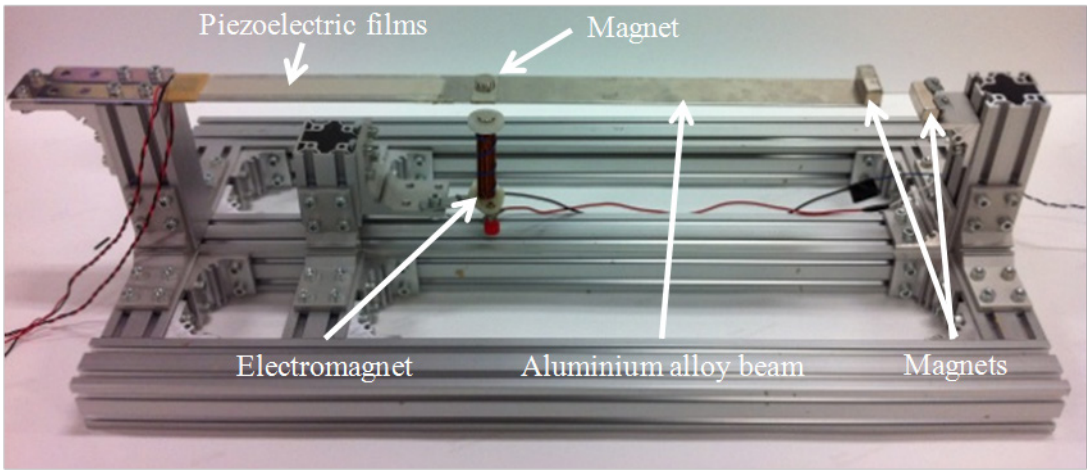

Figure 6.4. Bistable harvester for stochastic resonance.

A harmonic voltage applied by a linear power amplifier to the electromagnet coil generates a

corresponding force which can be accurately calibrated as a function of amplifier input voltage. The cantilever beam has a readily computable elastic characteristic, with suitable design specifications presented in Table 6.1. According to the design parameters in Table 6.1 the linear spring stiffness k in Equation (6.3) is calculated to be 46.15 N/m.

Table 6.1. Specifications of the cantilever beam.

Parameters	Values
Length	550 mm
Width	30 mm
Height	2 mm
Young's modulus	70 kN/mm^2
Area moment of inertia	20 mm^4
Density	2800 kg/m^3

Two square neodymium magnets of dimensions 30 mm × 10 mm × 10 mm were fitted to the system. One of the magnets was attached as a mass at the free end of the cantilever beam and the other was fixed to the frame side member, in order, as a pair, to provide the nonlinear magnetic force F_M. One of the most important factors underpinning the effectiveness of the magnets is the distance d between them, and a calibration experiment was carried out to check the optimal value of d for bistability.

As is shown in Figure 6.5, the ambient vibration from the vibration generator is Gaussian white noise defined by $N(t) = \sqrt{2D}g(t)$, with D = 6 mm and operating over a band width of 0 to 10 Hz. The signal amplifier provides a variable current gain and the electromagnetic actuator generates an adjustable frequency f for the periodic modulating excitation. A laser vibrometer was used to measure the displacement of the cantilever beam.

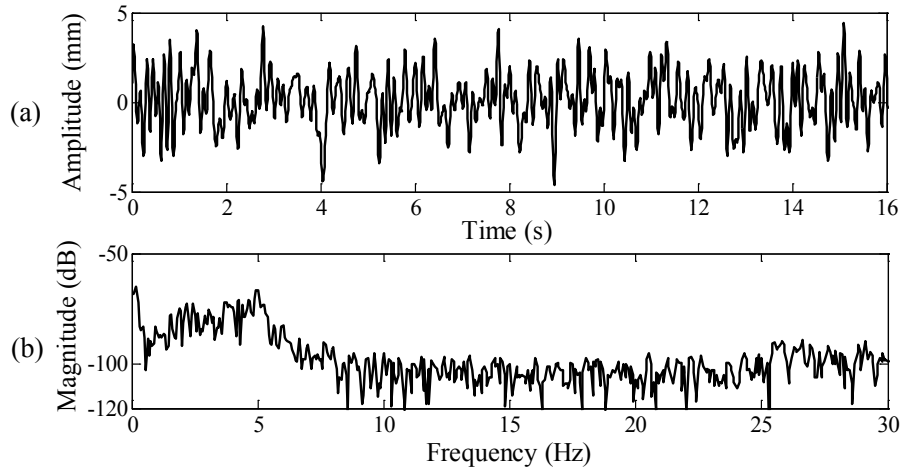

Figure 6.5. Random excitation characteristics of the ambient excitation: (a) displacement and (b) power spectrum.

In order to generate stochastic resonance the ambient excitation and the periodic modulating excitation must be input to the system together. A comparison was made between excitation only through the white noise ambient vibration and also for the case when only the modulating vibration is applied. A third set of results is provided for the case when both excitations are applied together. The response displacement of the end mass of the cantilever beam is shown in Figure 6.6 for the first case, and it can easily be observed that the cantilever beam is unable to jump periodically between the two potential wells.

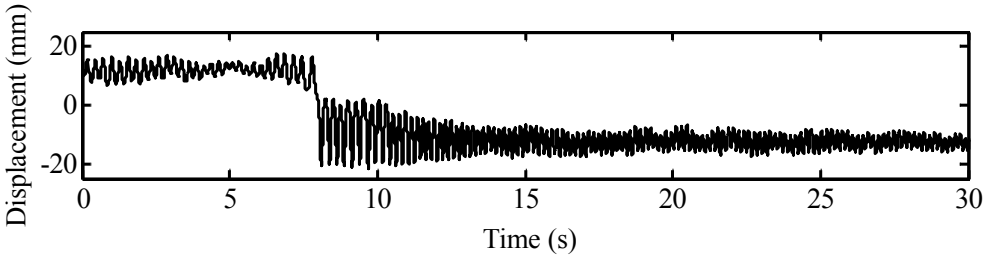

Figure 6.6. Response displacement solely under ambient vibration.

Conversely, Figure 6.7 presents the response displacement just for the periodic modulating excitation, operating at the discrete points of 0.2 Hz, 0.5 Hz, 1.0 Hz, 2.0 Hz, 3.0 Hz, 5.0 Hz and 6.0 Hz, respectively. It is observed that in the second case the periodic modulating excitation acting alone is also unable to push the cantilever beam into the bistable condition.

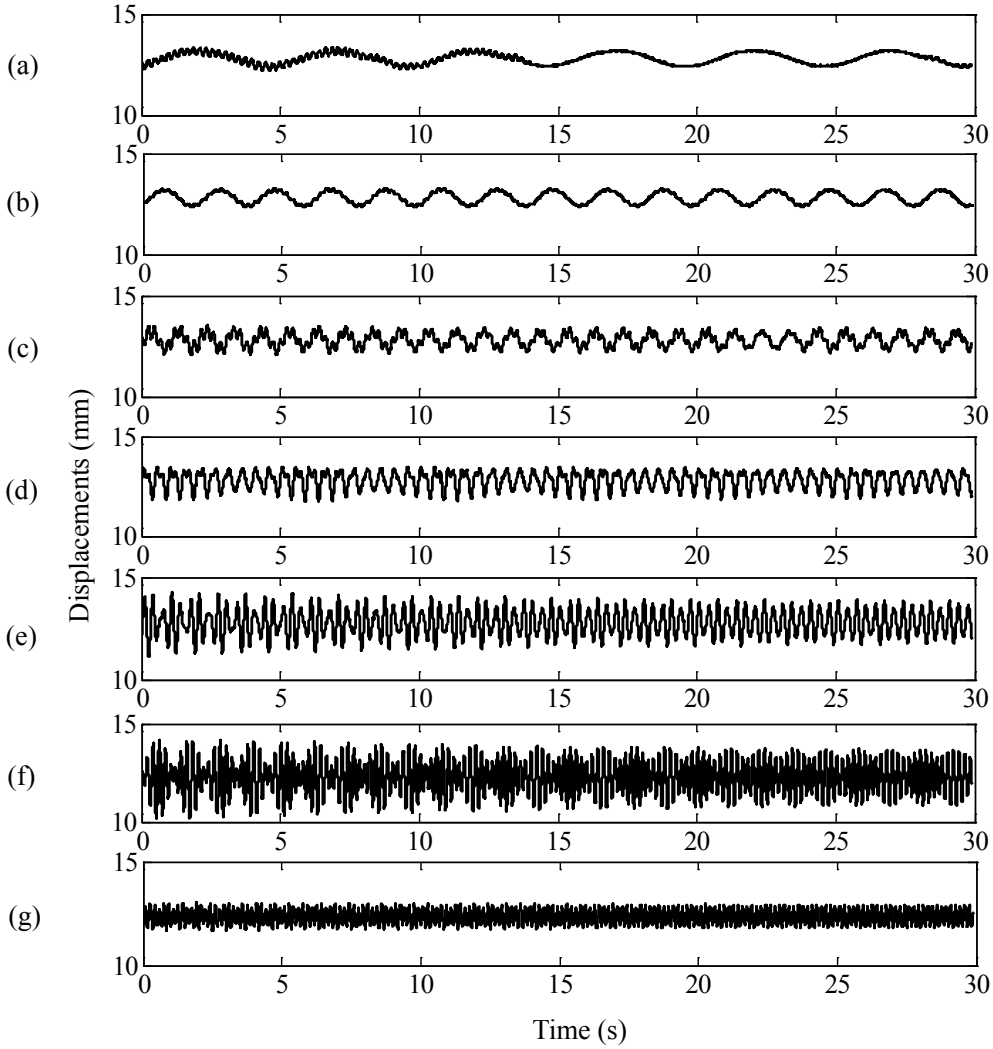

Figure 6.7. Response displacements solely under the periodic modulating excitation at different discrete frequencies: (a) 0.2 Hz, (b) 0.5 Hz, (c) 1.0 Hz, (d) 2.0 Hz, (e) 3.0 Hz, (f) 5.0 Hz, and (g) 6.0 Hz, respectively (Experimental results).

Figure 6.8 shows the response displacements of the cantilever beam under different frequencies of the periodic modulating excitation when simultaneously applied with the ambient noise vibration.

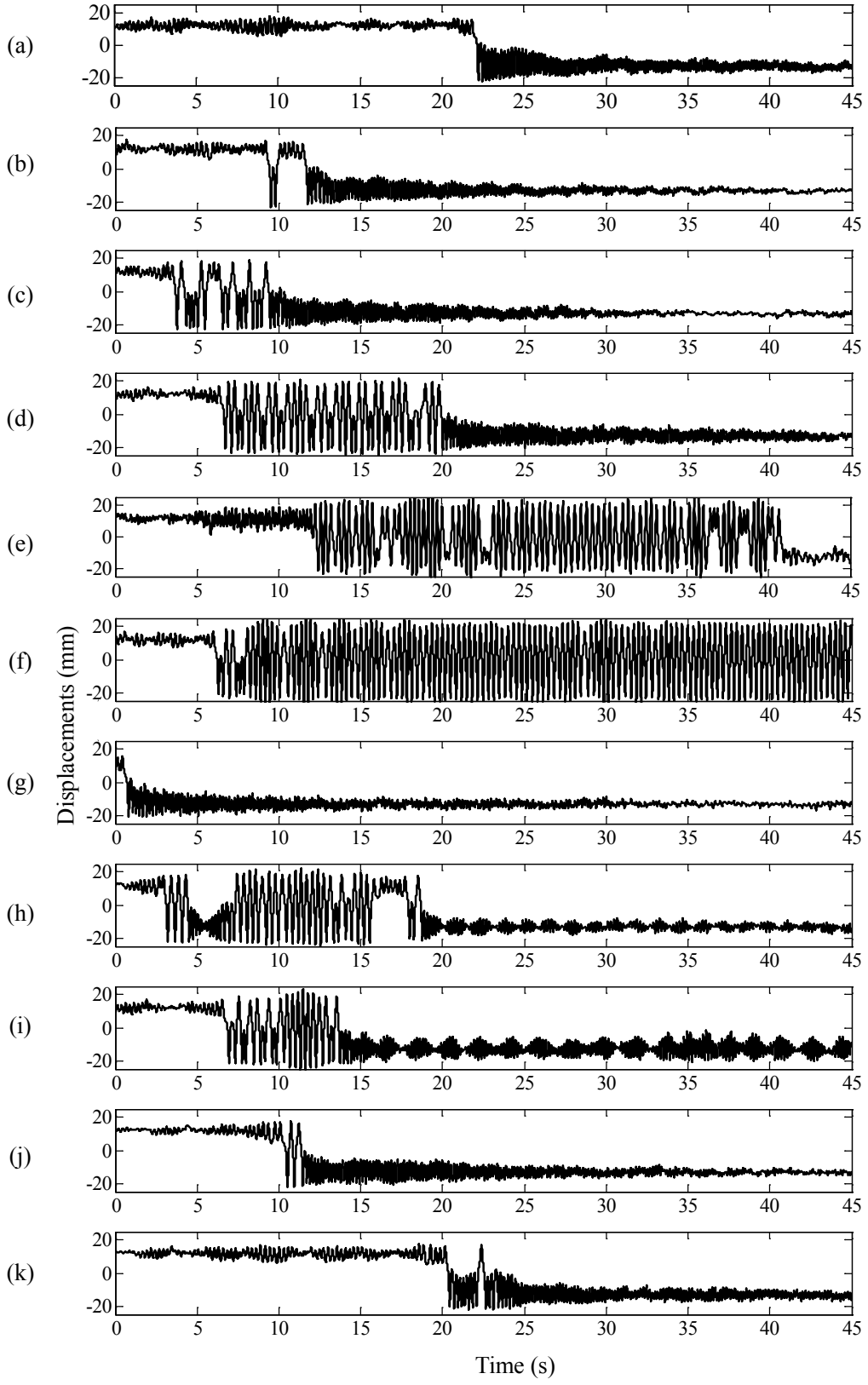
(a)
(b)
(c)
(d)
(e)
(f)
(g)
(h)
(i)
(j)
(k)
Displacements (mm)
20
0
-20
0 5 10 15 20 25 30 35 40 45
Time (s)

Figure 6.8. Response displacements under the ambient vibration together with the periodic modulating excitation applied at different frequencies: (a) 0.2 Hz, (b) 0.5 Hz, (c) 1.0 Hz, (d) 2.0 Hz, (e) 2.76 Hz, (f) 3.0 Hz, (g) 4.0 Hz, (h) 5.0 Hz, (i) 6.0 Hz, (j) 8.0 Hz, and (k) 10.0 Hz (Experimental results).

According to the results in Figure 6.8, when the frequency of the periodic modulating excitation is either 2.76 Hz or 3.0 Hz the response displacements of the cantilever beam are enhanced through clear progression into the bistable condition. However, when the frequency is shifted to 4.0 Hz, the amplitude of the response displacement decreases again. When the frequency of the periodic modulating excitation is 5.0 Hz (near to the natural frequency of damped vibration of the cantilever beam), the response displacement is more intense for a time than for 4.0 Hz but weaker than when it is at 2.76 Hz and 3.0 Hz. It becomes generally weaker again when the periodic modulating excitation frequency exceeds 6 Hz. Therefore it is considered that when the periodic modulating excitation frequency is in the region of 2.76 Hz to 3.0 Hz then stochastic resonance occurs, and the harvesting response of the system is considerably enhanced.

Table 6.2. Parameters used for simulation.

Parameter	Value	Unit
m	0.045	kg
c	0.019	Ns/m
k	24.5	N/m
α	1.45×10^{5}	N/m^3
Periodic force amplitude	0.0016	N

A series simulations under the same specifications are also conducted. Table 6.2 show the parameters used for simulation, which also represents the parameters of the experimental device.

Figure 6.9 presents the response displacement just for the periodic modulating excitation under different excitation frequencies. Similar results can be found to the experimental series, the cantilever beam only vibrate within one potential well.

Figure 6.10 shows the response displacements of the cantilever beam under different frequencies of the periodic modulating excitation with the action of the ambient noise vibration. It can be noted that stochastic resonance occurs when excitation frequency of the periodic excitation is in around 2.7 Hz to 3 Hz, which meets the experimental results.

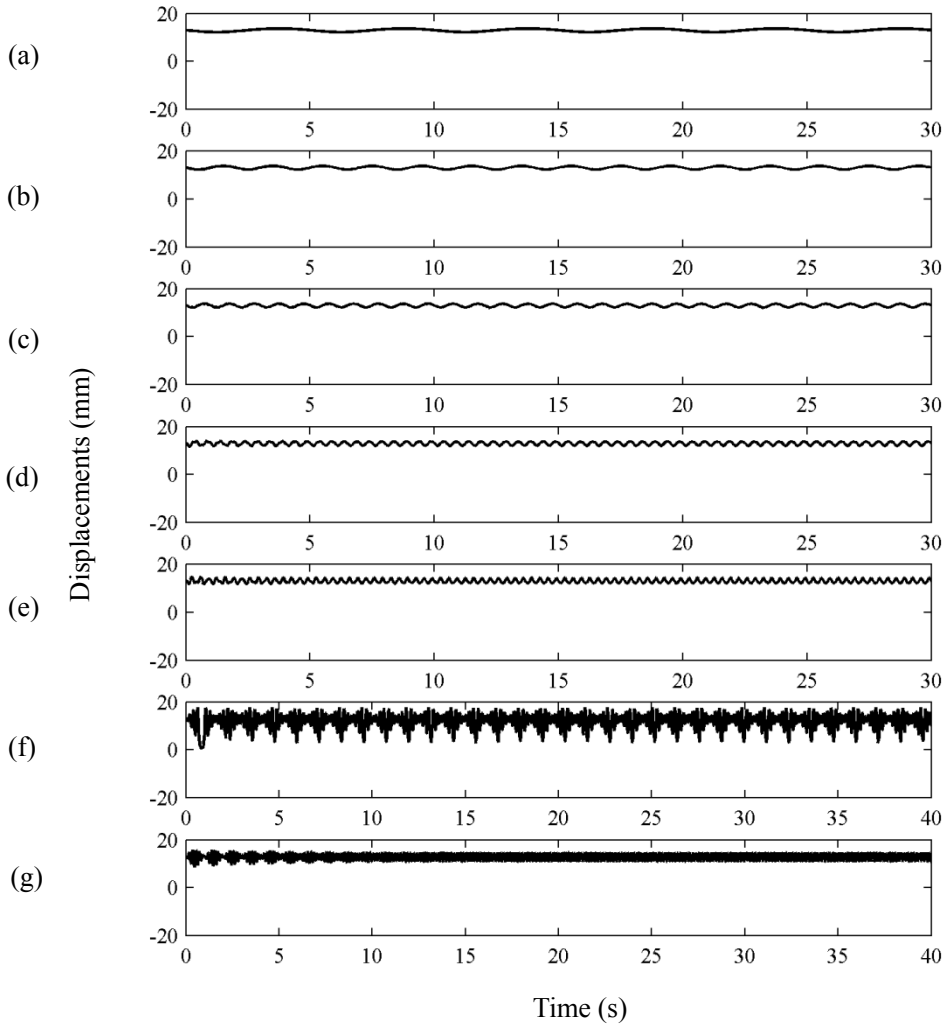

Figure 6.9. Response displacements solely under the periodic modulating excitation at different discrete frequencies: (a) 0.2 Hz, (b) 0.5 Hz, (c) 1.0 Hz, (d) 2.0 Hz, (e) 3.0 Hz, (f) 5.0 Hz, and (g) 6.0 Hz, respectively (Numerical simulation results).

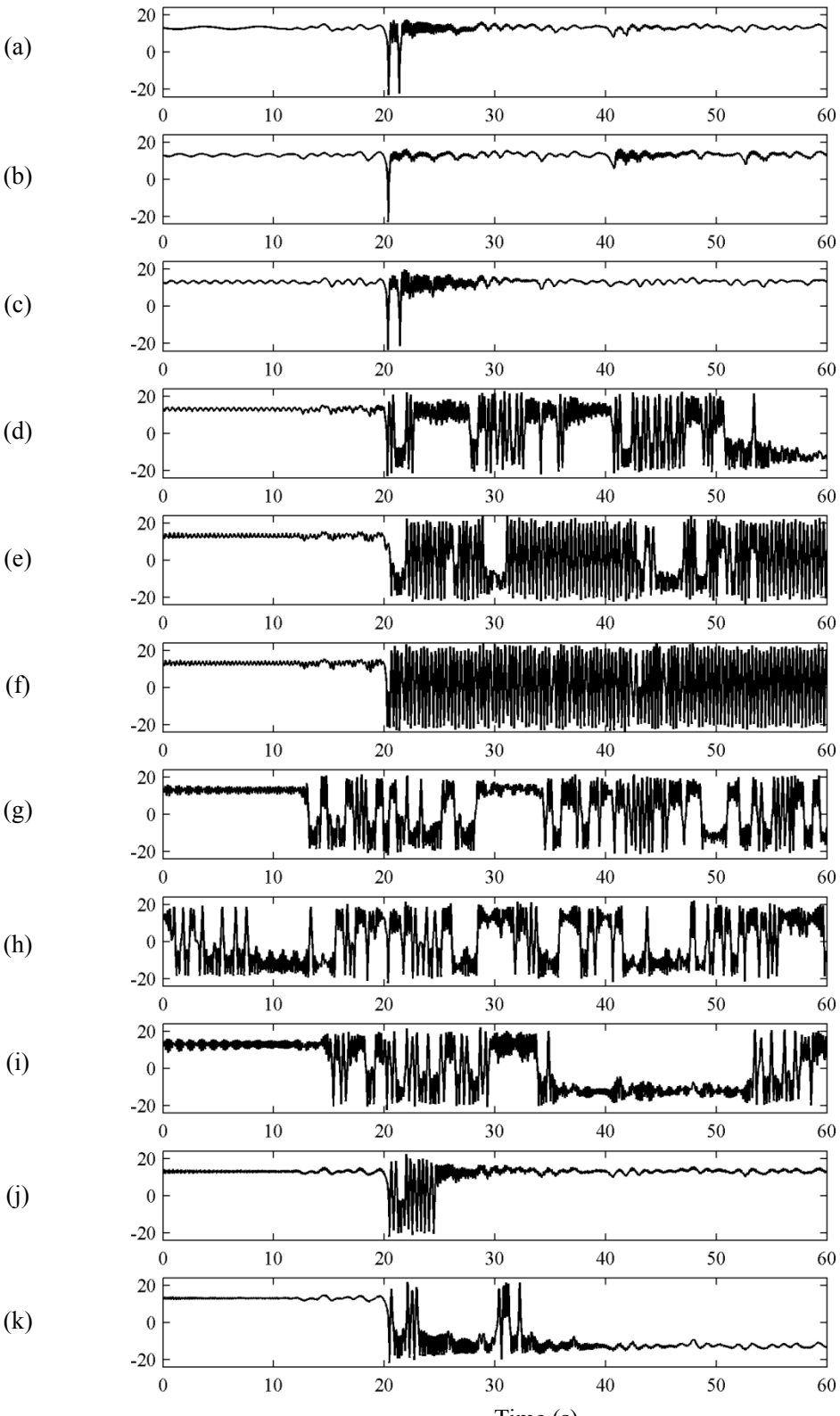
(a)
(b)
(c)
(d)
(e)
(f)
(g)
(h)
(i)
(j)
(k)
20
0
-20
0
10
20
30
40
50
60
Time (s)

Figure 6.10. Response displacements under the ambient vibration together with the periodic modulating excitation applied at different frequencies: (a) 0.2 Hz, (b) 0.5 Hz, (c) 1.0 Hz, (d) 2.0 Hz, (e) 2.76 Hz, (f) 3.0 Hz, (g) 4.0 Hz, (h) 5.0 Hz, (i) 6.0 Hz, (j) 8.0 Hz, and (k) 10.0 Hz (Numerical simulation results).

6.4.2 Further improvement

Another novel approach to achieve stochastic resonance is shown in this section, and a new energy harvester (Figure 6.11) is designed, three permanent magnets of the same parameters are arranged in an attractive configuration, although the 0.0225 kg magnetic end mass of the piezoelectric beam with length × width × thickness of 300 × 20 × 1 mm. is displaced horizontally by a small distance d with respect to the two vertically fixed permanent magnets (top and bottom magnets). These fixed magnets are symmetrically attached by sliders to a rail that allow distance h to be adjusted equally on either side of the end mass. Similarly the horizontal distance d between the small magnets and the magnetic end mass can also be adjusted. To achieve stochastic resonance two electromagnets are used as an actuator in conjunction with a small permanent magnet, which is attached to the beam at a distance 193 mm from the magnetic mass, so that an additional force excites the beam when a square wave voltage is applied to the electromagnets. The electromagnets are fitted symmetrically disposed at a distance of 31.7 mm either side of this small permanent magnet. The outer diameter and length of the coil are 13 and 40 mm, respectively.

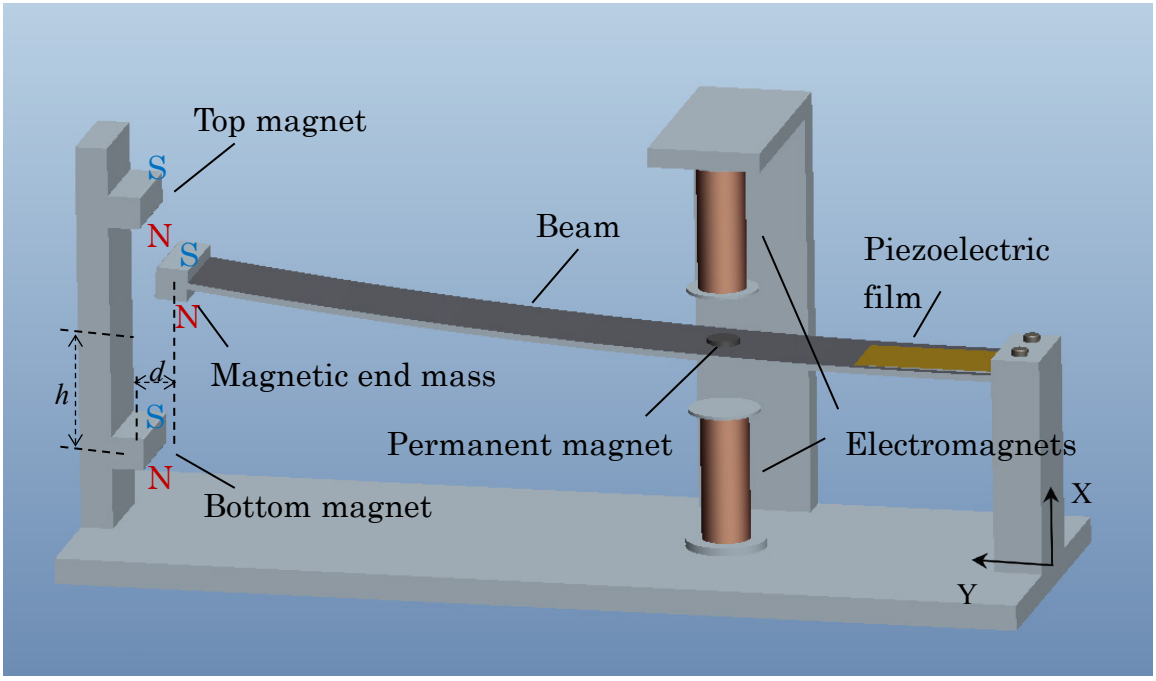

Figure 6.11. Schematic of the bistable vibrational energy harvester.

The potential energy of the magnetic end mass can be derived using the dipole model as

$$U_m = \frac{\mu_0 v^2}{4\pi}\big(\Phi(h+x)+\Phi(h-x)\big) \tag{6.24}$$

where $\mu_0 = 4\pi\times10^{-7}$ H/m is the permeability of free space, v the volume of each permanent magnet, and the function $\Phi(x)$ is defined by

$$\Phi(x) = -\frac{3\big(dM_{cy}+xM_{cx}\big)\big(dM_{fy}+xM_{fx}\big)}{\big(d^2+x^2\big)^{5/2}} + \frac{M_{fy}M_{cy}+M_{fx}M_{cx}}{\big(d^2+x^2\big)^{3/2}} \tag{6.25}$$

where M_{cx}, M_{fx}, M_{cy}, and M_{fy} are the magnetization amplitudes of the magnetic end mass and the fixed magnets in the directions x and y, respectively.

The values of d and h can be adjusted to change the corresponding value of the potential U_m for the permanent magnets. The corresponding magnetisation strengths were chosen for the fixed magnets and the magnetic end mass to be $M_{fx} = M_{cx} = -9\times10^5$ A/m. Note that M_{fx} and M_{cx} should be of the same sign, indicating polarity, so $M_{cy} = -M_{fy} = -8\times10^5$ A/m. Considering the role of the beam and choosing dimensions of length 30 mm, width 10 mm, and height 10 mm, by setting different values of distance d and h, the restoring force and potential energy can then be plotted against the displacement of the magnetic end mass (Figures 6.12 to 6.17).

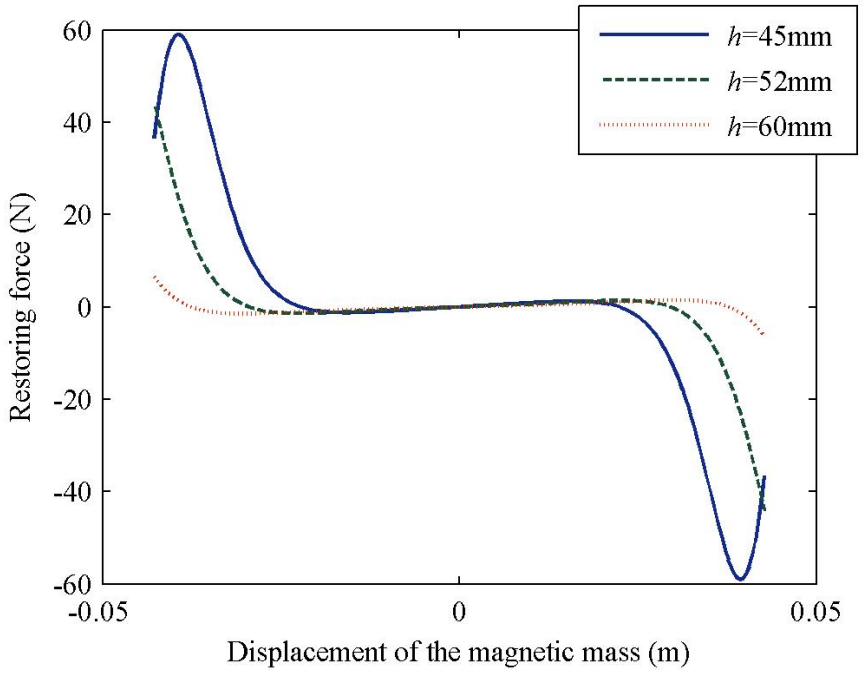

Figure 6.12. Restoring force against the displacement of the magnetic end mass (d =15mm).

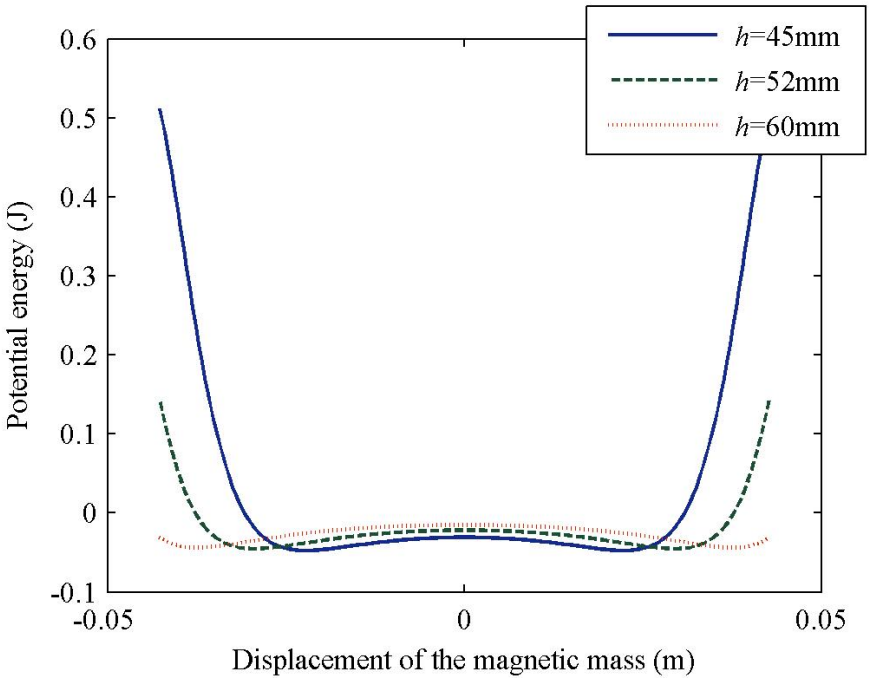

Figure 6.13. Potential energy against the displacement of the magnetic end mass (d =15mm).

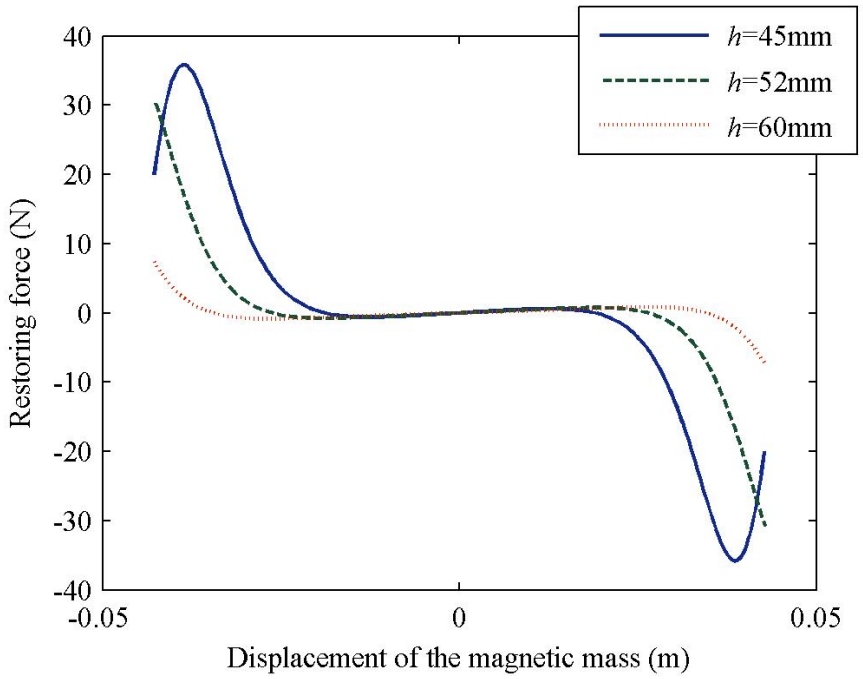

Figure 6.14. Restoring force against the displacement of the magnetic end mass (d =17mm).

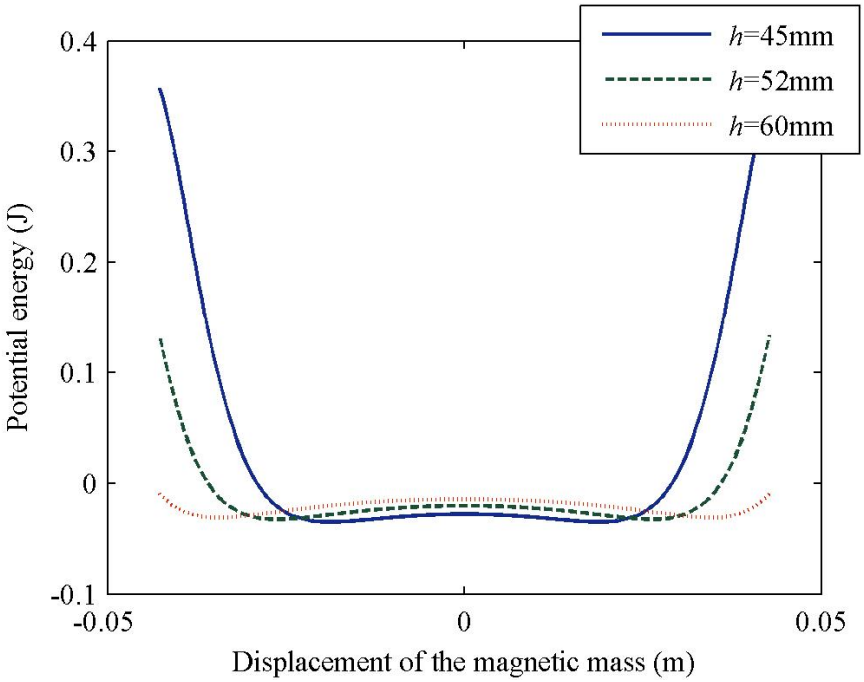

Figure 6.15. Potential energy against the displacement of the magnetic end mass (d =17mm).

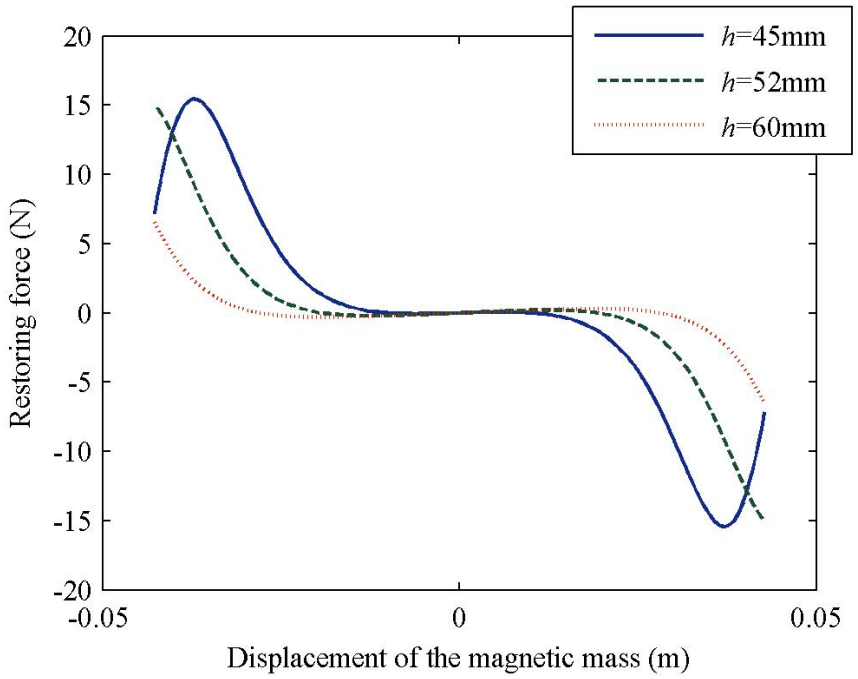

Figure 6.16. Restoring force against the displacement of the magnetic end mass (d =21mm).

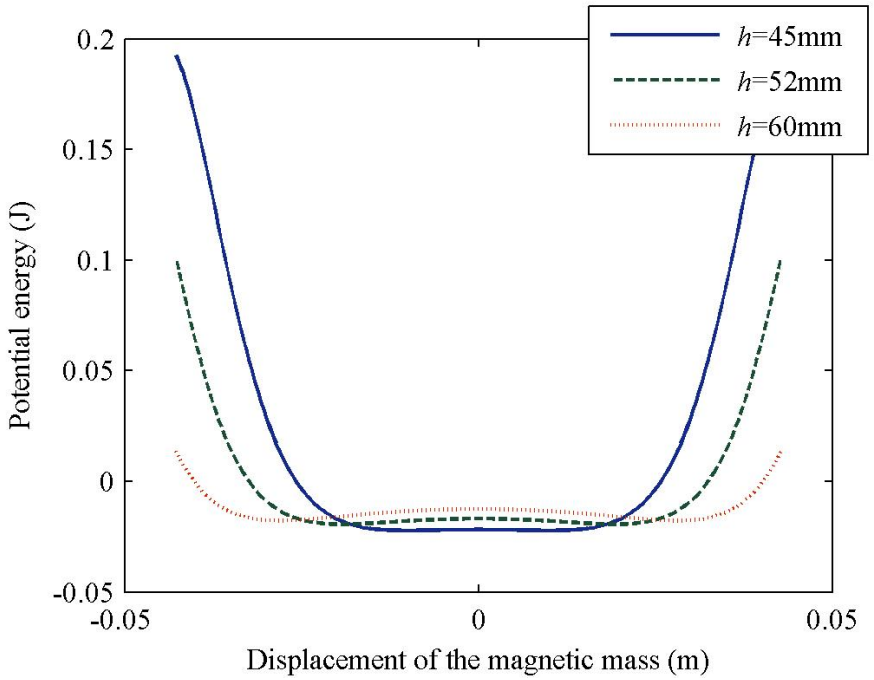

Figure 6.17. Potential energy against the displacement of the magnetic end mass (d =21mm).

In this work, two adjustable distances are set as $d = 17$ mm and $h = 52$ mm. Clearly, two stable equilibria exist, so it can reasonably be assumed that the magnetic end mass is initially in one of the two symmetric equilibria corresponding to one of the two available potential wells.

- Instrumentation and measurement

A laboratory-scale experimental device has been designed and fabricated to illustrate the theory described in Section 6.3 (see photo of the energy harvester in Figure 6.18). A modal shaker table (m060, IMV Corp., Japan) driven by an power amplifier (MA1, IMV Corp.) is used to provide the random excitation. The displacement and velocity of the magnetic end mass are measured using a (IL-300, KEYENCE Corp.) laser displacement sensor and a directly mounted (PV-08A, RION Corp.) velocity micro-sensor at the sample frequency of 100 Hz. The measured velocity signal is used as the feedback to control the electromagnets in real time based on the rule shown in Equation (6.13) by a dSPACE 1103 controller, and the output control signal is amplified by a linear power amplifier (LPA01, TOYO Corp.) to the electromagnets generate a corresponding force which can be accurately calibrated as a function of amplifier input voltage. Data is acquired using a midi data logger (GL900, Graphtec Corp.). An overview of the experimental setup is shown in Figure 6.19.

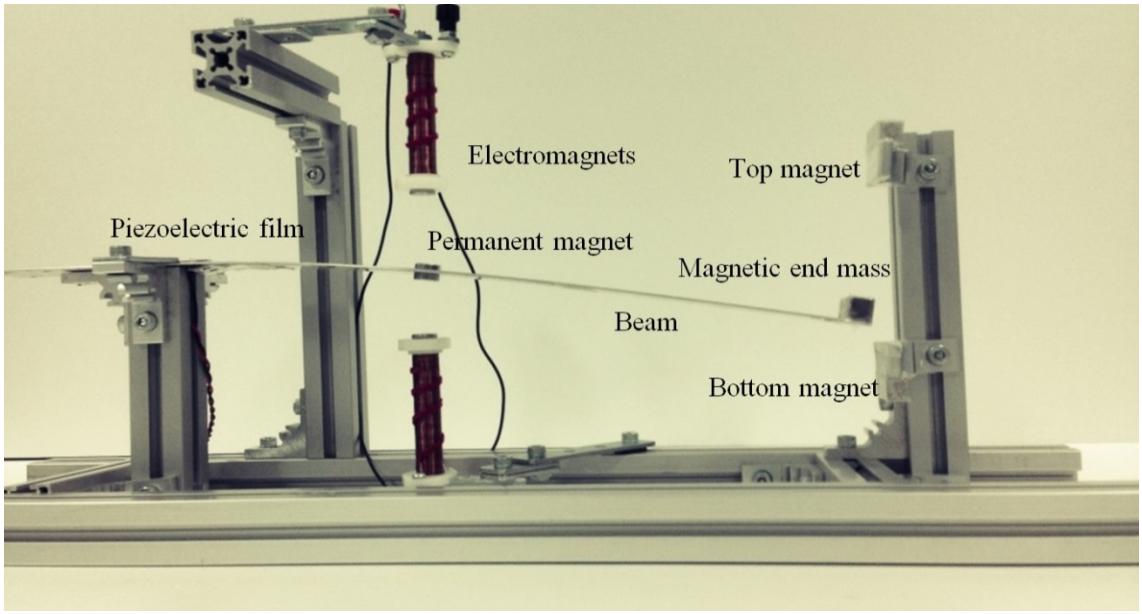

Figure 6.18. Photo of the experimental system.

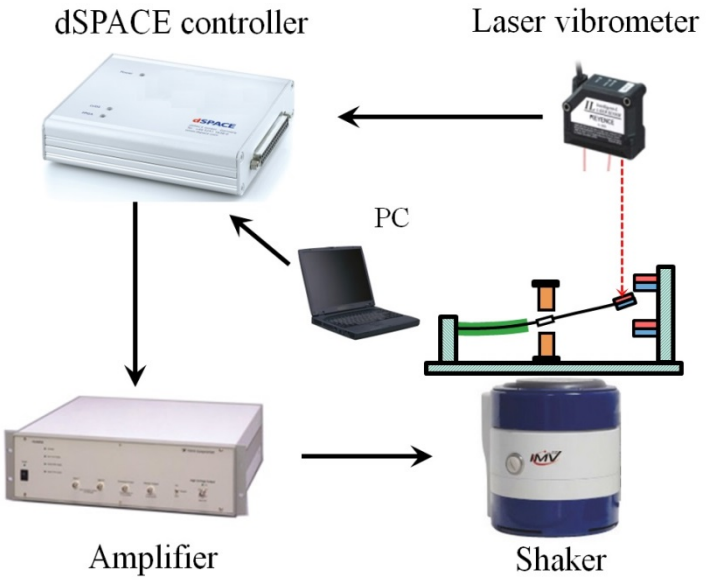

Figure 6.19. Schematic of the experimental setup used in tests.

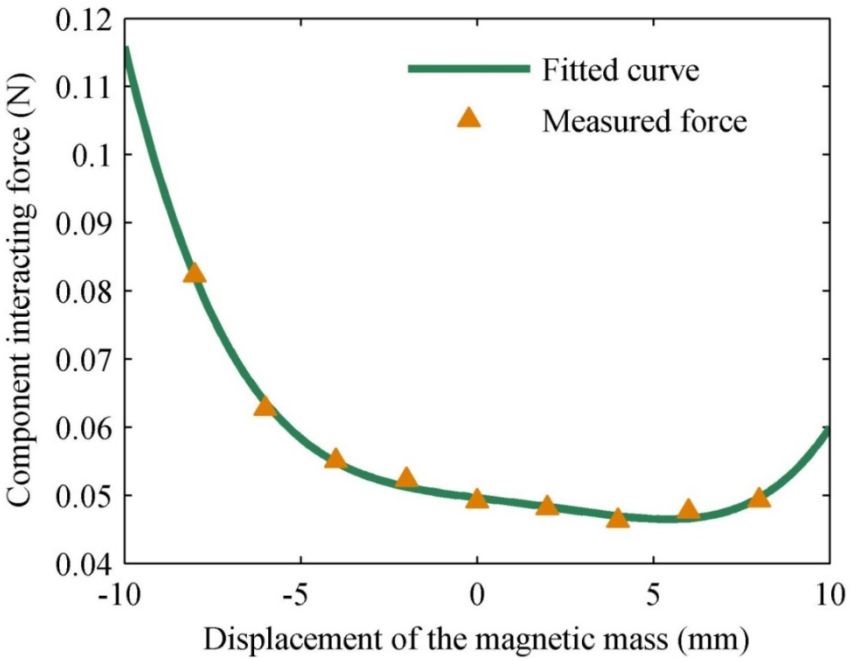

Figure 6.20. Fitted curve for the interaction force between the permanent magnet and the flux generated by the electromagnets.

The main aim of the experiment was to verify the possibility of achieving stochastic resonance using the proposed principle, and to compare the net available energy under the

condition of stochastic resonance with that available when only the random excitation is applied to the oscillator. The input to the electromagnets was calculated, mainly because of their relatively low efficiency. The two electromagnets are connected in series and operate with a supply voltage of 3 V. A fitted curve for the amplitude of the interaction force between the permanent magnet and the flux generated by the electromagnets is shown in Figure 6.20. The interaction force is measured by a digital force gauges. The best-fit force-displacement relationship used is given by

$$F_E(x) = 3.598\times10^{-6}x^4 - 2.157\times10^{-5}x^3 + 2.304\times10^{-5}x^2 - 6.413\times10^{-4}x + 0.04961 \quad (6.26)$$

This interaction force is not fully symmetrical because of the effect caused by the interaction force between the small permanent magnet and the iron cores of the electromagnets. It can also be noted that the amplitude of the force is not kept constant. However, small variation can be observed within certain displacement, thereby an approximate square wave is applied on the mass.

To evaluate the net energy from stochastic resonance, the energy input from the electromagnets should be subtracted from the total energy dissipated through damping in the system. However, when the mechanical quality factor is low, a considerable part of the mechanical energy is transformed into heat, and this just serves to decrease the available energy. Xu et al. [106] proposed, and experimentally confirmed, the power that can be delivered from a PZT-Stack system to a resistive load. In the quasi-static regime, 70% of the generated electrical power was delivered to a matched resistive load, with a 35% mechanical to electrical energy conversion efficiency. This result significantly exceeds that of other reports. However, it can still be seen that the conversion efficiency is still very low when both the mechanical and internal resistance losses are considered. Therefore the total damping, including both the mechanical and electrical damping effects, was measured to calculate the total dissipated energy.

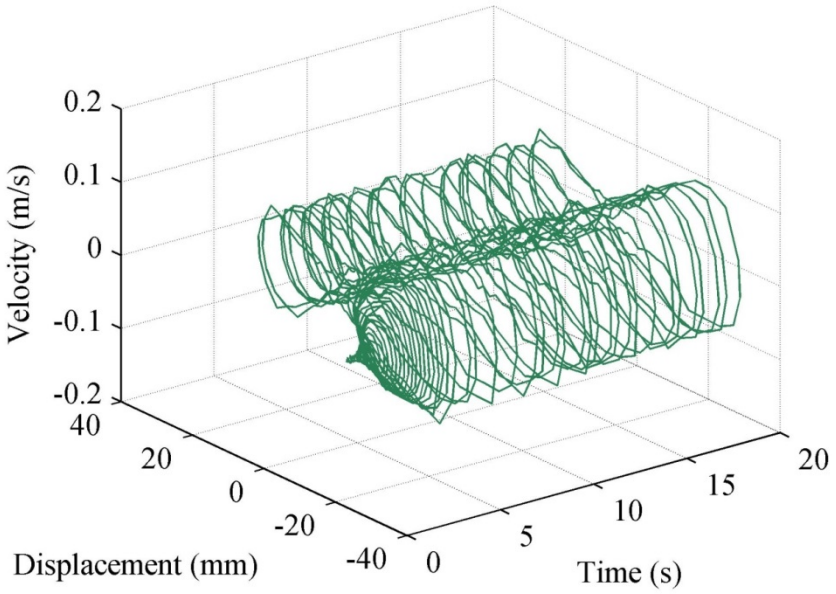

Figure 6.21. Velocity vs displacement phase trajectories of the magnetic end mass when only the additional force is applied to the device.

The method of conservation of energy was used to measure the total damping, as shown in Equation (6.27). All the energy input of the electromagnets is dissipated by the damping. In this method only the force provided by the electromagnets is applied to the oscillator without the noise excitation, and a very small perturbation is needed to start the oscillator off initially. Thus, portions of the time domain response of the magnetic end mass are shown in Figure 6.21. The total damping of this particular system is estimated to be $0.0401\,\mathrm{Ns/m}$.

$$\int_0^{t_0}\left(c\dot{x}^2-\gamma(t)\dot{x}\right)dt=0 \tag{6.27}$$

- Experimental results

The responses of the mechanism were investigated with and without the small-scale additional force. The external ambient force was provided throughout by random excitations. The corresponding comparison of the displacement vs velocity phase trajectories of the magnetic end mass is shown in Figure 6.22. Compared with the responses of the unforced condition, the mass is seen to fluctuate between the two potential wells in a state of stochastic

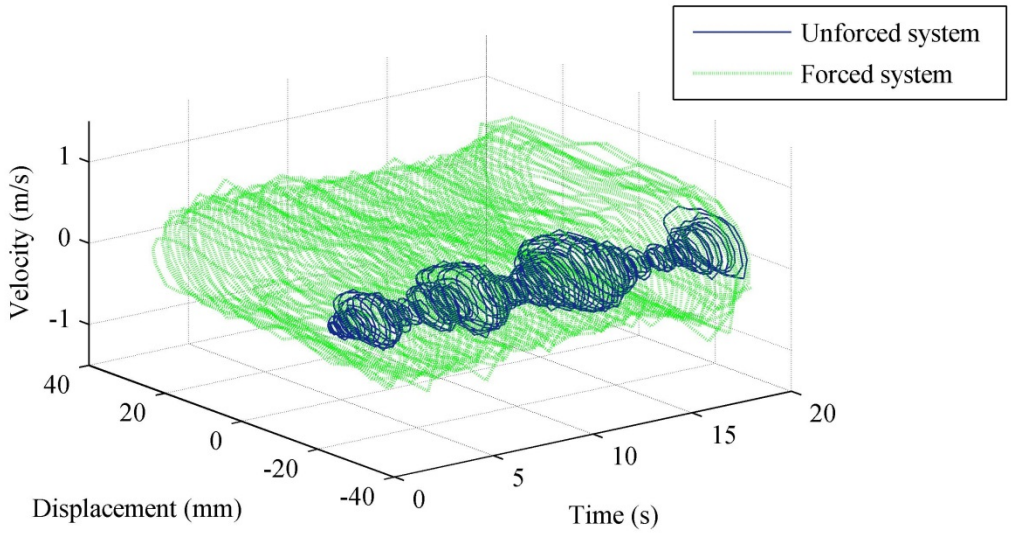

Figure 6.22. Velocity vs displacement phase trajectories of the magnetic end mass: unforced system (solid line) and forced system (dashed line).

resonance with large amplitude displacements and velocities. After adding the random excitation to the system, the vibration intensity also becomes much stronger when compared with that of Figure 6.22. Therefore the dissipated energy by the damper is greatly enhanced.

Figure 6.23 shows the instantaneous power dissipated by the damper with and without the additional force, and the net cumulative energy from both cases is also compared. Although the energy consumed by the additional force should be subtracted, under the additional forcing of $\gamma(t)$, the net energy from the external random excitation is still found to be several times greater than that of the unforced system. Note also that the presence of mechanical damping and internal resistance will decrease the energy that can be practically harvested. However, if more than 54.3% of the mechanical power can be delivered to a resistive load, then the practical harvested electrical energy under stochastic resonance will be noticeably higher than that of the unforced system.

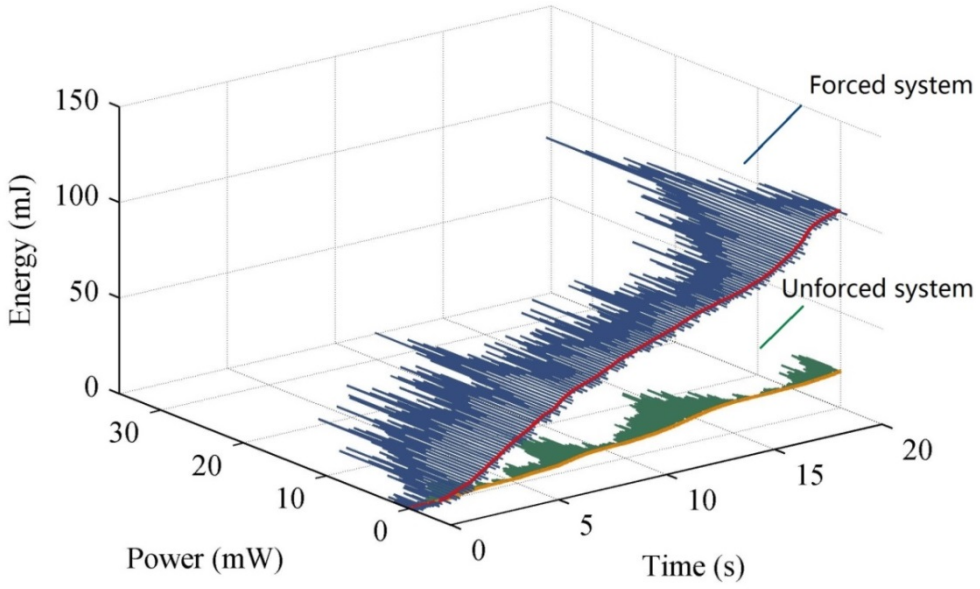

Figure 6.23. Instantaneous power and cumulative energy of the forced and unforced systems: dissipated power from the unforced system (green line), net power from the forced system (blue line), net cumulative energy available from the device with forcing (red line), and without forcing (yellow line).

It has been shown through experiment that the proposed method of square-wave-driven stochastic resonance can enhance the availability of harvestable energy from the external ambient vibration. It is a different approach to achieving stochastic resonance that uses a periodic modulating force, with the advantage that there is now no need to estimate the forcing frequency from the noise density using the Kramers rate. It is therefore a potentially easier method to apply.

However, it should be understood that the application of stochastic resonance for energy harvesting requires a relatively high efficiency of conversion from mechanical into electric energy, because an additional force is manually provided. Improvements to the intrinsic conversion efficiency of piezoelectric materials may well deliver a practical convenient solution to this requirement. The external mechanical energy loss is also a very important factor to be considered, manifested, for instance, as aerodynamic damping. More effective ways to apply the necessary additional force is to be further explored in future work. The theoretical and experimental work reported here provides a simple form of a precursor technology from which alternatives to achieving stochastic resonance can be developed further.

6.5 Summary

This chapter proposed a novel concept of enhancing the performance under random excitations by application of the theory of stochastic resonance. The occurance of the stochastic resonance is conventionally based on the theory of Kramers rate, which is used to determine the excitation frequency of the periodic force for achieving stochastic resonance. However, considering the difficulty of the parameters measurement and estimation, another approach of the square-wave-driven stochastic resonance is also proposed, and its principle is illustrated based on the experimental investigations. It is validated that both of the approaches is a effective method for enhancing randomly excited vibrational energy harvesting.

Chapter 7

Conclusions

7.1 Conclusions

Investigation on energy harvesting from ambient vibration has attracted the interest of many researchers in the last decade. Contributing to the hot topic, this thesis focused on various aspects of energy harvesting from ambient vibration, to enhance harvesting capacity of monostable and bistable Duffing nonlinear oscillators under harmonic and random excitations.

This paper begins with detailed reviews about various methods to broaden the bandwidth of the energy harvesters, and pay specific attentions on nonlinear energy harvesters. And, the performances are overviewed for the monostable and bistable energy harvesters under harmonic and random excitations.It was validated that the monostable nonlinear energy harvester hold wider response bandwidth under harmonic excitations, due to the coexisting high- and low-energy solutions. However, if the harvester's response happens to fall into the low-energy solution, the improved performance achieved by the nonlinear harvester will be significantly impaired. Hence, rational mechanism should be developed that can ensures stable high-energy solution regardless of initial conditions and disturbances, to achieve high performance of the nonlinear harvester.

In Chapter 3, an original model was proposed as a stiffness tuning method, in which the linear and nonlinear stiffness can be adjusted by changing the distance between the permanent magnets, which can result in shifting the frequency response curve and triggering the jump from low- to high-energy orbit, without changing the frequency or the amplitude of the excitation. Through a theoretical and experimental investigation, the monostable energy harvester can trigger a jump to the desirable state, accompanying with broadened bandwidth and boosted response. However, it consumes extra electrical energy for this method. Therefore, another approach with the damping variation is proposed with the advantage that it requires little energy consumption, which is a considerable benefit for the practical implementation of the energy harvester.

The stabilised operating point of the energy harvester on the high-energy orbit is just a precondition. It is still needed to optimise the parameters of the energy harvester for maximum power output. However, there is little literature on the optimisation of the nonlinear energy harvester. Therefore, in Chapter 4, the optimisation of the monostable energy harvester is investigated, and the optimisation principles under general conditions are concluded with the consideration of two kinds of electrical transducers, namely the inductive and piezoelectric types. Moreover, under practical conditions, both the stroke of the device and the available electrical damping of the damper are considerably limited; therefore, the optimisation work is also conducted under the constrained response displacement and electrical damping conditions.

The above work provides a detailed design principal for the practical implementation of the

monostable nonlinear energy harvester under harmonic excitations. When a Duffing-type monostable harvester is employed for energy harvesting under harmonic excitations, either the stiffness or damping tuning method can be used to ensure the operation of the high-energy orbit, then to maximise the output power according to the proposed optimisation rules. Although the stiffness tuning method consumes extra electrical energy, it can achieve the complete two-parameter optimisation. For the damping tunable method to stabilise the higher energy orbit, its apparent advantage is little energy consumption for the tuning process but also with a smaller frequency tuning range.

Given stochastic nature of ambient vibration sources, linear and nonlinear energy harvesters under random excitations had been investigated in the previous studies; however, their performance is still unclear with conflicting conclusions. In Chapter 4, a comprehensive investigation was processed for the monostable, bistable, and linear harvesters under the band-limited random excitations. In general, the bistable energy harvester can achieve higher performance than the linear configuration, when the time-varying of the excitation parameters is taken into consideration, while the monostable hardening-type energy harvester drops into the lowest performance. Therefore, the hardening-type monostable configuration should be avoided under band-limited random excitations. Conversely, the linear configuration is a preferable candidate for a given band-limited excitations with specific parameters.

For the band-limited noise excitation, the performance of different energy harvesters is also investigated, considering the influences of the constrained electrical damping and displacement. It is found that the bistable energy harvester requires overall lower optimised electrical damping, which is an obvious advantage for practical application. For the condition of constrained displacement, there is a minimum stroke requirement for the bistable system because the existence of the equilibrium points. However, the hardening effect of the bistable configuration under relatively larger excitation levels also tends to prevent the further increasing of the response displacement. Relative to the linear energy harvester, it is found that the higher performance around the fundamental frequency will be impaired because of the displacement constraint for the bistable configuration.

To further improve energy harvesting efficiency under random excitations, the theory of stochastic resonance is applied for a bistable energy harvesting device. By the theoretical and experimental validations, the proposed method can obviously enhance the availability of harvestable energy from the external random vibration. In this case, the energy harvesting capacity can be several times than that of the common bistable energy harvester, even though it is limited in the arrangement of weakly periodic signal and ambient noise for the nonlinear system.

7.2 Significance of this thesis

This thesis is actually the enhancement of architecture of the field of nonlinear vibrational energy harvesting, the significance of the work are:

(1) For harmonic-excited energy harvesting using the monostable nonlinear energy harvester, the thesis solves the problem of how to guarantee the operation of the energy harvester on the high-energy branch, especially the proposed damping tuning method in Chapter 3, it doesn't consume additional energy, which is an obvious benefit for improving the self-sustainable ability of the practical energy harvesting.

(2) This thesis outlined the optimisation principles for the monostable nonlinear energy harvesting, which can be applied for the practical design of the energy harvesting device. This work also revel one advantage of the nonlinear energy harvester: the frequency tuning can be achieved by modifying the electrical damping (load resistance), and without the need to employ reactive loads as required for the linear energy harvesters.

(3) For random-excited energy harvesting, this study processed a comprehensive parameter interpretation on the performances of three kinds of most typical configurations, including linear, monostable, and bistable harvesters; meanwhile, the design guidance was collected for the random-excited energy harvesting. Generally, for a given band-limited noised excitation, the linear energy harvester can present the highest performance. However, when the practical conditions, such as the limited electrical damping and stroke of the device, and the variation of the excitation frequency range are taken into consideration, the bistable becomes the best candidate, because it is less sensitive to the variation of the excitation parameters, especially the low frequency area, and the low requirement of the electrical damping, also the smaller response displacement under large enough excitation levels.

(4) This thesis also explores and validates the feasibility of actively increasing the available energy from the random vibration source using the theory of stochastic resonance. As long as the required additional force can be effectively applied, this approach can be a promising way to improve the energy harvesting performance under random excitations.

Reference

[1] L. Tang, Y. Yang, and C.K. Soh. Toward broadband vibration-based energy harvesting. Journal of Intelligent Material Systems and Structures, 21(18):1869-1897, 2010.

[2] R. Amirtharajah and A.P. Chandrakasan. Self-powered signal processing using vibration-based power generation. IEEE Journal of Solid-Sate Circuits, 33(5): 687-695, 1998.

[3] E.S. Leland and P.K. Wright. Resonance tuning of piezoelectric vibration energy scavenging generators using compressive axial preload. Smart Materials and Structures, 15(5):1413-1420, 2006.

[4] D.J. Morris, J.M. Youngsman, M.J. Anderson, and D.F. Bahr. A resonant frequency tunable, extensional mode piezoelectric vibration harvesting mechanism. Smart Materials and Structures, 17: 065021, 2008.

[5] V.R. Challa, M.G. Prasad, Y. Shi, and F.T. Fisher. A vibration energy harvesting device with bidirectional resonance frequency tunability. Smart Materials and Structures, 17: 015035, 2008.

[6] S.S. Rao. Mechanical vibrations, 3rd ed. Addison-Wesley, Reading, MA, 1995.

[7] A. Erturk and D.J. Inman. A distributed parameter electromechanical model for cantilever piezoelectric energy harvesters. Journal of Vibration and Acoustics, 130(4): 041002, 2008.

[8] V.R. Challa, M.G. Prasad, Y. Shi, and F.T. Fisher. A Vibration Energy Harvesting Device with Bidirectional Resonance Frequency Tunability. Smart Materials and Structures, 17:015035, 2008.

[9] W. Wu, Y. Chen, B. Lee, J. He, and Y. Peng. Tunable resonant frequency power harvesting devices. SPIE Proceedings, 6169:61690A, 2006.

[10] M. Wischke, M. Masur, F. Goldschmidtboeing, and P. Woias. Electromagnetic vibration harvester with piezoelectrically tunable resonance frequency. Journal of Micromechanics and Microengineering, 20(3):035025, 2010.

[11] C. Eichhorn, F. Goldschmidtboeing, and P. Woias. A frequency tunable piezoelectric energy converter based on a cantilever beam, Power MEMS 2008, Sendai, Japan, pp. 309-312, November, 2008.

[12] D. Zhu, S. Roberts, J. Tudor, S. Beeby, Closed Loop Frequency Tuning of a Vibration-based Microgenerator, Power MEMS 2008, Sendai, Japan, pp. 229–232, November, 2008.

[13] X. Wu, J. Lin, S. Kato, K. Zhang, T. Ren, and L. Liu. A frequency adjustable vibration

energy harvester. Power MEMS 2008, Sendai, Japan, pp. 245-248, November, 2008.

[14] S.M. Shahruz. Design of mechanical band-pass filters for energy scavenging, Journal of Sound and Vibration, 292(3-5): 987-998, 2006.

[15] S.M. Shahruz. Limits of performance of mechanical band-pass filters used in energy scavenging, Journal of Sound and Vibration, 292(1-2):449–461, 2006.

[16] J. Rastegar, C. Pereira, and H.L. Nguyen. Piezoelectric-based power sources for harvesting energy from platforms with low frequency vibration. SPIE Proceedings, 6171:617101, 2006.

[17] D. Lee, G. Carman, D. Murphy, and C. Schulenburg. Novel micro vibration energy harvesting device using frequency up conversion. Proceedings of 14th International Conference on Solid-State Sensors, Actuators and Microsystems, Lyon, pp. 871-874, June, 2007.

[18] H. Külah. Energy scavenging from low-frequency vibrations by using frequency up-conversion for wireless sensor applications. IEEE Sensors Journal, 8:3, 2008.

[19] H.D. Akaydin, N. Elvin and Y. Andreopoulos. The performance of a self-excited fluidic energy harvester. Smart Materials and Structures, 21: 025007, 2012.

[20] X. Gao. Vibration and flow energy harvesting using piezoelectric. PhD Thesis, Drexel University, 2008.

[21] J. Wang, J. Ran, and Z. Zhang. Energy harvester based on the synchronization phenomenon of a circular cylinder. Mathematical Problems in Engineering, 2014:567357, 2014.

[22] WB. H. Jr. Piezoelectric energy harvesting: vortex induced vibrations in plants, soap films, and arrays of cylinders. Master Thesis, Georgia Institute of Technology, 2010.

[23] Y. Han. Exploring the interaction of two self-excited energy harvesters. Master Thesis City University of New York, 2013.

[24] M.Y. Zakaria, M.Y. Al-Haik, and M.R. Hajj. Experimental analysis of energy harvesting from self-induced flutter of a composite beam. Applied Physics Letters, 107: 023901, 2015.

[25] E. Suwa, Y. Tsujiura, F. Kurokawa, H. Hida and I. Kanno. Airflow energy harvesters of metal-based PZT thin films by self-excited vibration. Journal of Physics: Conference Series, 557: 012029, 2014.

[26] J. Yu and A.S Ashwin. An auto-parametrically excited vibration energy harvester, Sensor Actuator A: Physical, 220: 69-75, 2014.

[27] S.G. Burrow, and L.R. Clare. A resonant generator with non-linear compliance for energy harvesting in high vibrational environments. IEEE International Electric Machines Drives Conference, IEMDC'07, 1: 715–720, 2007.

[28] D.A.W. Barton, S.G. Burrow, and L.R. Clare. Energy harvesting from vibrations with a nonlinear oscillator. Journal of Vibration and Acoustics, Transactions of the ASME, 132(2):0210091, 2010.

[29] B.P. Mann and N.D. Sims. Energy harvesting from the nonlinear oscillations of magnetic levitation, Journal of Sound and Vibration, 319(1-2) 515–530, 2009.

[30] D.D. Quinn, A.L. Triplett, L.A. Bergman, and A.F. Vakakis. Comparing linear and essentially nonlinear vibration-based energy harvesting. Journal of Vibration and Acoustics, Transactions of the ASME, 133(1): 011001, 2011.

[31] P.L. Green, K. Worden and N.D. Sims. On the identification and modelling of friction in a randomly excited energy harvester, Journal of Sound and Vibration, 332(19):4696-4708, 2013.

[32] S.C. Stanton, C.C. McGehee, and B.P. Mann. Reversible hysteresis for broadband magnetopiezoelastic energy harvesting. Applied Physics Letters, 95(17): 174103, 2009.

[33] B. Marinkovic and H. Koser. Demonstration of wide bandwidth energy harvesting from vibrations. Smart Materials and Structures, 21(6):065006, 2012.

[34] G. Manla, N.M. White, and M.J. Tudor. Numerical model of a non-contact piezoelectric energy harvester for rotating objects. IEEE Sensors Journal, 12(6):1785-1793, 2012.

[35] B. Marinkovic and H. Koser. Smart sand-a wide bandwidth vibration energy harvesting platform. Applied Physics Letters, 94(10): 103505, 2009.

[36] H. Liu, C. Lee, T. Kobayashi, C.J. Tay, and C. Quan. A new s-shaped mems PZT cantilever for energy harvesting from low frequency vibrations below 30 Hz. Microsystem Technologies, 18(4):497-506, 2012.

[37] G. Sebald, H. Kuwano, D. Guyomar, and B. Ducharne. Simulation of a Duffing oscillator for broadband piezoelectric energy harvesting, Smart Materials and Structures, 20(7): 075022, 2011.

[38] B. Marinkovic and H. Koser. Smart Sand—A wide bandwidth vibration energy harvesting platform. Applied Physics Letters, 94(10):103505, 2009.

[39] L.G.W. Tvedt, D.S. Nguyen, and E. Halvorsen, Nonlinear behavior of an electrostatic energy harvester under wide- and narrowband excitation. Journal of Microelectromechanical Systems, 19(2): 305–316, 2010.

[40] D. Miki, M. Honzumi, Y. Suzuki, and N. Kasagi. Large-amplitude MEMS electret generator with nonlinear springs. 2010 IEEE 23rd International Conference on Micro Electro Mechanical Systems (MEMS): 176–179, 2010.

[41] D.S. Nguyen, E. Halvorsen, G.U. Jensen, and A. Vogl. Fabrication and characterization of a wideband MEMS energy harvester utilizing nonlinear springs. Journal of Micromechanics and Microengineering, 20(12):125009, 2010.

[42] L. Gammaitoni, I. Neri, and H. Vocca. Nonlinear oscillators for vibration energy harvesting. Applied Physics Letters, 16:164102, 2009.

[43] M.F. Daqaq. Response of uni-modal Duffing-type harvesters to random forced excitations. Journal of Sound and Vibration, 329(18):3621-3631, 2010.

[44] P.L. Green, K. Wordena, K. Atallahb, and N.D. Sims. The benefits of Duffing-type nonlinearities and electrical optimisation of a mono-stable energy harvester under white Gaussian excitations, Journal of Sound and Vibration, 331(20):4504–4517, 2012.

[45] M.F. Daqaq. On intentional introduction of stiffness nonlinearitiesfor energy harvesting under white gaussian excitations. Nonlinear Dynamics, 69(3):1063–1079, 2012.

[46] E. Halvorsen. Fundamental issues in nonlinear wide-band vibration energy harvesting. Physical Review E, 87:042129, 2013.

[47] F. Cottone, H. Vocca, L. Gammaitoni, Nonlinear energy harvesting, Physical Review Letters, 102 :080601, 2009.

[48] R. Masana and M.F. Daqaq. Electromechanical modeling and nonlinear analysis of axially-loaded energy harvesters. Journal of Vibration and Acoustics, Transactions of the ASME, 133:011007, 2011.

[49] S.C. Stanton, C.C. McGehee and B.P. Mann. Nonlinear dynamics for broadband energy harvesting: Investigation of a bistable piezoelectric inertial generator, Physica D, 239 640-653, 2010.

[50] A. Erturk, D.J. Inman, Broadband piezoelectric power generation on high-energy orbits of the bistable Duffing oscillator with electromechanical coupling. Journal of Sound and Vibration, 330(10):2339-2353, 2011.

[51] F. C. Moon and P. J. Holmes. A magnetoelastic strange attractor. Journal of Sound and Vibration, 65(2):275-296, 2009.

[52] B.P. Mann, D.G. Gorman, B.A. Owens. Investigations of a nonlinear energy harvester with a bistable potential well, Journal of Sound and Vibration, 329(9):1215-1226, 2010.

[53] A. Erturk, J. Hoffmann, and D.J. Inman. A Piezomagnetoelastic structure for broadband vibration energy harvesting, Applied Physics Letters, 94(25):254102, 2009.

[54] S. Stanton, B. Owen, and B. Mann. Harmonic Balance analysis of the bistable piezoelectric inertial generator, Journal of Sound and Vibration, 331(15):3617–3627, 2012.

[55] R.L. Harne, M. Thota, and K.W. Wang. Concise and high-fidelity predictive criteria for maximizing performance and robustness of bistable energy harvesters, Applied Physics Letters, 102(5):053903, 2013.

[56] R. Masana and M.F. Daqaq. Relative performance of a vibratory energy harvester in mono- and bi-stable potentials, Journal of Sound and Vibration, 330(24):6036–6052,

2011.

[57] L. Gammaitoni, F. Cottone, I. Neri, and H. Vocca. Noise harvesting. ICNF 2009, AIP Conference Proceedings, 1129(1): 651-654, 2009.

[58] M.F. Daqaq. Transduction of a bistable inductive generator driven by white and exponentially correlated gaussian noise. Journal of Sound Vibration, 330(11):2254-2564, 2011.

[59] M.F. Daqaq, R. Masana, A. Erturk, and D.D. Quinn. On the Role of Nonlinearities in Vibratory Energy Harvesting: A Critical Review and Discussion. Transactions of the ASME Applied Mechanics Reviews, 66(4):040801-1, 2014.

[60] D. Meimukhin, N. Cohen, and I. Bucher. On the advantage of a bistable energy harvesting oscillator under bandlimited stochastic excitation. Journal of Intelligent Material Systems and Structures, 24(14):1736-1746, 2013.

[61] H.K. Joo and T.P. Sapsis, Performance measures for single-degree-of-freedom energy harvesters under stochastic excitation. Journal of Sound Vibration, 333(19):4695-4710, 2014.

[62] M.I. Friswell, J.E.T. Penny. The accuracy of jump frequencies in series solutions of the response of a Duffing oscillator. Journal of Sound and Vibration, 169(2): 261–269, 1994

[63] K. Worden. On jump frequencies in the response of a Duffing oscillator. Journal of Sound and Vibration, 198(4-5): 522-525, 1996.

[64] M.J. Brennan, I. Kovacic, A. Carrella, and T.P. Waters. On the jump-up and jump-down frequencies of the Duffing oscillator. Journal of Sound and Vibration 318(4-5):1250-1261, 2008.

[65] A. Carrella. Passive vibration isolators with high-static-low-dynamic-stiffness. PhD Thesis, University of Southampton, 2008.

[66] Z.K. Peng, Z.Q. Lang, S.A. Billings, and G.R. Tomlinson. Comparisons between harmonic balance and nonlinear output frequency response function in nonlinear system analysis. Journal of Sound and Vibration, 311: 56-73, 2008.

[67] K. Magnus. Vibrations, Blackie and Son, London, 1965.

[68] P. Hagedorn, Non-linear oscillations (Translated and edited by Wolfram Stadler), Clarendon Press, Oxford, 1981.

[69] J. Moehlis, B.E. DeMartini, J.L. Rogers, and K.L. Turner. Exploiting nonlinearity to provide broadband energy harvesting. ASME Dynamic Systems and Control Conference 2009, Hollywood, California, DSCC2009-2542, October, 2009.

[70] R. Ramlan, M.J. Brennan, B.R. Mace, and I. Kovacic. Potential benefits of a non-linear stiffness in an energy harvesting device. Nonlinear Dynamics, 59(4):545-558, 2010.

[71] R. Masana, R and M.F. Daqaq. Energy harvesting in the superharmonic frequency region

of a twin-well oscillator, Journal of Applied Physics, 111(4): 044501, 2012.

[72] D.S. Nguyen, E. Halvorsen, G.U. Jensen, and A. Vogl. Fabrication and characterization of a wideband mems energy harvester utilizing nonlinear springs. Journal of Micromechanics and Microengineering, 20(12):125009, 2010.

[73] M. Ferrari, V. Ferrari, M. Guizzetti, B. Ando, S. Baglio, and C. Trigona. Improved energy harvesting from wideband vibrations by nonlinear piezoelectric converters, Sensors and Actuators A, 162(2):425-431, 2010.

[74] G. Litak, M.I. Friswell, and S. Adhikari. Magnetopiezoelastic Energy Harvesting Driven by Random Excitations," Applied Physics Letters, 96(21):214103, 2010.

[75] N.A. Khovanova, and I.A. Khovanov. The role of excitations statistic and nonlinearity in energy harvesting from random impulsive excitations. Applied Physics Letters, 99(14):144101, 2011.

[76] G. Sebald, H. Kuwano, D. Guyomar, and B. Ducharne. Experimental Duffing oscillator for broadband piezoelectric energy harvesting. Smart Materials and Structures, 20(10):102001, 2011.

[77] R. Masana and M.F. Daqaq. Response of duffing-type harvesters to band-limited noise. Journal of Sound Vibration, 332(25):6755-6767, 2013.

[78] G.P. Harmer, B.R. Davis, and D. Abbott. A review of stochastic resonance: circuits and measurement. IEEE Transactions on Instrumentation and Measurement, 51(2):99-309, 2002.

[79] W. Korneta, I. Gomes, C.R. Mirasso, and R. Toral. Experimental study of stochastic resonance in a Chua's circuit operating in a chaotic regime. Physica D: Nonlinear Phenomena, 219:93–100, 2006.

[80] L. Gammaitoni, P. Hanggi, P. Jung and F. marchesoni. Stochastic resonance. Reviews of Modern Physics, 70:223-287, 1998.

[81] P. Hänggi, P. Talkner, and M. Borkovec. Reaction-rate theory: fifty years after Kramers, 62 (2):251-341, 1990.

[82] A. Cammarano, S.G. Burrow, D.A.W. Barton, Modelling and experimental characterization of an energy harvester with bi-stable compliance characteristics. Proceedings of the Institution of Mechanical Engineers, Part I: Journal of Systems and Control Engineering 225 (2011) 475-484.

[83] C.R. McInnes, D.G. Gorman, and M.P. Cartmell. Enhanced vibrational energy harvesting using nonlinear stochastic resonance. Journal of Sound and Vibration, 318(4-5):655–662, 2008.

[84] A. Masuda, A. Senda, T. Sanada, and A. Sone. Global stabilization of high-energy response for a Duffing-type wideband nonlinear energy harvester via self-excitation and

entrainment. Journal of Intelligent Material Systems and Structures, 24:1598-1612, 2013.

[85] Y. Li, H. Matsuhisa, and H. Utsuno. Semi-active vibration isolation system with variable stiffness and damping control, Journal of Sound and Vibration, 313(1-2):16–28, 2008.

[86] K. Nakano, Y. Suda. Combined type self-powered active vibration control of truck cabins. Vehicle System Dynamics, 41(6): 449-473, 2004.

[87] D. Su, K. Nakano, R. Zheng, M.P. Cartmell, Investigations of a stiffness tunable nonlinear vibrational energy harvester. International Journal of Structural Stability and Dynamics, 14(8): 1440023, 2014.

[88] B.P. Mann. Energy criterion for potential well escapes in a bistable magnetic pendulum, Journal of Sound and Vibration, 323(3-5):864-876, 2009.

[89] D. Su, K. Nakano, R. Zheng, and M. Cartmell. On electrical optimisation using a Duffing-type vibrational energy harvester. Journal of Mechanical Engineering Science, 2014, In press.

[90] K. Nakano, S.J. Elliott and E. Rustighi. A unified approach to optimal conditions of power harvesting using electromagnetic and piezoelectric transducers. Smart Materials and Structures, 16:948–958, 2007.

[91] S. Priya and D.J. Inman. Energy harvesting Technologies. Spinger, New York, USA, 2009.

[92] D.R. Johnso, R.L. Harne, and K.W. Wang. A disturbance cancellation perspective on vibration control using a bistable snap-through attachment, Journal of Vibration and Acoustics, Transactions of the ASME, 136: 031006, 2014.

[93] M. Hendijanizadeh, M. Moshrefi-Torbati, and S.M. Sharkh. Constrained design optimization of vibration energy harvesting devices, Journal of Vibration and Acoustics, Transactions of the ASME, 136: 021001, 2014.

[94] K. Nakano, Y. Suda, and S. Nakadai. Self-powered active vibration control using a single electric actuator. Journal of Sound and Vibration, 260(2):213-235, 2003.

[95] S. Choi, M. Seong, and K. Kim. Vibration control of an electrorheological fluid-based suspension system with an energy regenerative mechanism. Journal of Automobile Engineering, 223(4): 459-469, 2009.

[96] M. Hendijanizadeh, S.M. Sharkh, S.J. Elliott, and M. Moshrefi-Torbati. Output power and efficiency of electromagnetic energy harvesting systems with constrained range of motion, Smart Materials and Structures, 22(12): 125009, 2013.

[97] N.G. Stephen. On energy harvesting from ambient vibration. Journal of Sound and Vibration, 293: 409-425, 2006.

[98] THK CO.,LTD. Ball screw transmission efficiency. Available at : https://tech.thk.com/en/products/thkdlink.php?id=861. (accessed April 10 2014).

[99] http://www.chiltrix.com/chiller-fan-coil.html. (accessed July 25 2015).

[100] A. Carrella, M.J. Brennan, and T.P. Waters. Static analysis of a passive vibration isolator with quasi-zero-stiffness characteristic. Journal of Sound and Vibration 301(3-5):678-689, 2007.

[101] M.A. AL-Shudeifat. Highly efficient nonlinear energy sink. Nonlinear Dynamics, 76(4):1905-1920, 2014.

[102] P.D. Mitcheson, T.C. Green, E.M. Yeatman, A.S. Holmes. Architectures for vibration-driven micropower generators. Journal of Microelectromechanical Systems, 13 (3):429-440, 2004.

[103] H. Hu, K. Nakano, and M.P. Cartmell. An experimental study of stochastic resonance in a bistable mechanical system. Journal of Physics: Conference Series, 382(1):012024, 2012.

[104] R. Zheng, K. Nakano, H. Hu, D. Su and M.P. Cartmell. An application of stochastic resonance for energy harvesting in a bistable vibrating system. Journal of Sound and Vibration, 333(12):2568-2587, 2014.

[105] F. Moss and P. V. E. McClintock. Noise in Nonlinear Dynamical Systems Volume 2, Theory of Noise Induced Processes in Special Applications. Cambridge University Press, 1989.

[106] T.B. Xu, E.J. Siochi, J.H. Kang, and L. Zuo, L.W. Zhou, X. Tang, and X.N. Jiang. Energy harvesting using a PZT ceramic multilayer stack. Smart Materials and Structures, 22: 065015, 2013.

List of Publications

Paper of Academic Journals

1. **Dongxu Su**, Kimihiko Nakano, Rencheng Zheng and Matthew P Cartmell. On square-wave-driven stochastic resonance for energy harvesting in a bistable system. AIP advances, 4:1171401, 201 4.
2. **Dongxu Su**, Kimihiko Nakano, Rencheng Zheng and Matthew P Cartmell. On electrical optimisation using a Duffing-type vibrational energy harvester. Proceedings of the Institution of Mechanical Engineers, Part C: Journal of Mechanical Engineering Science, 2014, doi: 10.1177/0954406214563736. (Copyright @ 2014 SAGE Publications)
3. **Dongxu Su**, Kimihiko Nakano, Rencheng Zheng, Matthew P Cartmell, Investigations of a stiffness tunable nonlinear vibrational energy harvester. International Journal of Structural Stability and Dynamics, 14(8): 1440023, 2014. (Copyright @ 2014 World Scientific Publishing Co Pte Ltd.)
4. **Dongxu Su**, Rencheng Zheng, Kimihiko Nakano and Matthew P Cartmell. Stabilisation of the high-energy orbit for a nonlinear energy harvester with variable damping. Proceedings of the Institution of Mechanical Engineers, Part C: Journal of Mechanical Engineering Science, 2015, doi: 10.1177/0954406215590169. (Copyright @ 2015 SAGE Publications)
5. Rencheng Zheng, Kimihiko Nakano, Honggang Hu, **Dongxu Su**, Matthew P Cartmell, An application of stochastic resonance for energy harvesting in a bistable vibrating system. Journal of Sound and Vibration, 333(12):568–2587, 2014. (Copyright @ 2014 Elsevier B.V.)

Proceeding of International Conference

1. **Dongxu Su**, Kimihiko Nakano, Honggang Hu, Matthew P Cartmell, Masanori Ohori and Rencheng Zheng. Further Application of Stochastic Resonance for Energy Harvesting. ASME 2013 Dynamic Systems and Control Conference, Palo Alto, California, USA, October 21–23, 2013.
2. **Dongxu Su**, Kimihiko Nakano, Rencheng Zheng, and Matthew P Cartmell. Stiffness tunable nonlinear vibrational energy harvester with damping control. Conference on Motion and Vibration Control, Sapporo, Japan, August 3-7, 2014.